

AD-A186 611

DTIC FILE COPY

Bulletin 52  
(Part 5 of 5 Parts)

2

# THE SHOCK AND VIBRATION BULLETIN

Part 5  
Mathematical Modeling and  
Structural Dynamics

MAY 1982

DTIC  
SELECTED  
NOV 19 1987  
S D  
C&D

A Publication of  
THE SHOCK AND VIBRATION  
INFORMATION CENTER  
Naval Research Laboratory, Washington, D.C.



Office of  
The Under Secretary of Defense  
for Research and Engineering

Approved for public release; distribution unlimited.

87 10 28 018

## **SYMPOSIUM MANAGEMENT**

### **THE SHOCK AND VIBRATION INFORMATION CENTER**

Henry C. Pusey, Director

Rudolph H. Volin

J. Gordan Showalter

Jessica Hileman

Elizabeth A. McLaughlin

### **Bulletin Production**

Publications Branch, Technical Information Division,  
Naval Research Laboratory

**Bulletin 52**  
**(Part 5 of 5 Parts)**

# **THE SHOCK AND VIBRATION BULLETIN**

**MAY 1982**

A Publication of  
**THE SHOCK AND VIBRATION  
INFORMATION CENTER**  
Naval Research Laboratory, Washington, D.C.

Accession For	
NTIS	CRAAG <input checked="" type="checkbox"/>
DTIC	TAB <input type="checkbox"/>
Unprocessed	<input type="checkbox"/>
Justification	
By	
Organization	
Availability Codes	
DAI	Availability of Document
A-1	

The 52nd Symposium on Shock and Vibration was held at the Monteleone Hotel, New Orleans, LA on October 26-28, 1981. The Defense Nuclear Agency, Washington, D.C. and the U.S. Army Waterways Experiment Station, Vicksburg, MS were Co-Hosts.



Office of  
The Under Secretary of Defense  
for Research and Engineering

## CONTENTS

### PAPERS APPEARING IN PART 5

#### Mathematical Modeling

DAMPED STRUCTURE DESIGN USING FINITE ELEMENT ANALYSIS ; M. F. Kluesener and M. L. Drake, University of Dayton Research Institute, Dayton, OH	1
DETERMINATION OF NORMAL MODES FROM MEASURED COMPLEX MODES ; S. R. Ibrahim, Old Dominion University, Norfolk, VA	13
THE EFFECT OF JOINT PROPERTIES ON THE VIBRATIONS OF TIMOSHENKO FRAMES ; I. Yaghmai, Sharif University of Technology, Tehran, Iran and D. A. Frohrib, University of Minnesota, Minneapolis, MN	19
SOIL STRUCTURE INTERACTION AND SOIL MODELS ; J. M. Ferritto, Naval Civil Engineering Laboratory, Port Huememe, CA	29
FINITE ELEMENTS FOR INITIAL VALUE PROBLEMS IN DYNAMICS ; T. E. Simkins, U.S. Army Armament Research and Development Command, Watervliet, NY	39

#### Structural Dynamics

A PROCEDURE FOR DESIGNING OVERDAMPED LUMPED PARAMETER SYSTEMS ; D. J. Inman, State University of New York at Buffalo, Buffalo, NY and A. N. Andry, Jr., Lockheed California Company, Burbank, CA	49
ON THE OPTIMAL LOCATION OF VIBRATION SUPPORTS ; B. P. Wang and W. D. Pilkey, University of Virginia, Charlottesville, VA	55
DYNAMIC BUCKLING OF PINNED COLUMNS ; J. M. Ready, David W. Taylor Naval Ship Research and Development Center, Bethesda, MD	59
LARGE DEFLECTION RANDOM RESPONSE OF SYMMETRIC LAMINATED COMPOSITE PLATES ; K. R. Wentz and D. B. Paul, Air Force Wright Aeronautical Laboratories, Wright-Patterson AFB, OH and C. Mei, Old Dominion University, Norfolk, VA	99
DYNAMIC CHARACTERISTICS OF A NON-UNIFORM TORPEDO-LIKE HULL STRUCTURE ; A. Harari, Naval Underwater Systems Center, Newport, RI	113
VIBRATION AND ACOUSTIC RADIATION FROM POINT EXCITED SPHERICAL SHELLS ; E. H. Wong, Naval Ocean Systems Center, San Diego, CA and S. I. Hayek, The Pennsylvania State University, University Park, PA	135
DAMPING OF SHALLOW-BURIED STRUCTURES DUE TO SOIL-STRUCTURE INTERACTION ; F. S. Wong and P. Weidlinger, Weidlinger Associates, Menlo Park, CA and New York, NY	149

### PAPERS APPEARING IN PART 1

#### Welcome

#### WELCOME

Colonel Tilford Creel, Commander/Director, U.S. Army Waterways Experiment Station, Vicksburg, MS

#### Keynote Address

#### KEYNOTE ADDRESS

Marvin Atkins, Director, Offensive and Space Systems, Office of the Under Secretary of Defense  
Research Engineering, Department of Defense, Washington, DC



#### Invited Papers

##### **EQUIPMENT SURVIVABILITY ON THE INTEGRATED BATTLEFIELD**

Charles N. Davidson, Technical Director, U.S. Army Nuclear and Chemical Agency, Springfield, VA

##### **NAVAL OPERATIONS IN A NUCLEAR ENVIRONMENT**

Captain Donald Alderson, U.S.N., Acting Chief, Tactical Nuclear Weapons Project Office (PM-23)  
Department of the Navy, Washington, DC

##### **SURVIVABILITY REQUIREMENTS FOR FUTURE AIR FORCE SYSTEMS**

Henry F. Cooper, Deputy for Strategic and Space Systems, Assistant Secretary of the Air Force  
(Research, Development and Logistics), Washington, DC

##### **NUCLEAR HARDNESS VALIDATION TESTING**

Edward Conrad, Deputy Director (Science and Technology), Defense Nuclear Agency, Washington, DC

##### **ELIAS KLEIN MEMORIAL LECTURE — THE CHANGING DIMENSIONS OF QUALIFICATION TESTING**

H. Norman Abramson, Vice-President, Engineering Sciences, Southwest Research Institute, San Antonio, TX

##### **REQUIRED DEVELOPMENTS IN STRUCTURAL DYNAMICS**

Ben K. Wada, Jet Propulsion Laboratory, Pasadena, CA

##### **EFFECT OF SEALS ON ROTOR SYSTEMS**

David P. Fleming, NASA, Lewis Research Center, Cleveland, OH

##### **MACHINERY VIBRATION EVALUATION TECHNIQUES**

R. L. Eshleman, The Vibration Institute, Clarendon Hills, IL

##### **SHAFT VIBRATION MEASUREMENT AND ANALYSIS TECHNIQUES**

Donald E. Bently, President, Bently Nevada Corporation, Minden, NV

#### Rotor Dynamics and Machinery Vibration

##### **SPIN TEST VIBRATIONS OF PENDULOUSLY SUPPORTED DISC/CYLINDER ROTORS**

F. H. Wolff and A. J. Molnar, Westinghouse Research and Development Center, Pittsburgh, PA

##### **MODAL ANALYSIS AS A TOOL IN THE EVALUATION OF A TURBINE WHEEL FAILURE**

A. L. Moffa and R. L. Leon, Franklin Research Center, Philadelphia, PA

##### **CONTRIBUTION TO THE DYNAMIC BEHAVIOUR OF FLEXIBLE MECHANISMS**

E. Imam, J. Der Hagopian and M. Lalanne, Institut National des Sciences Appliquées, Villeurbanne, France

##### **SELF-EXCITED VIBRATION OF A NONLINEAR SYSTEM WITH RANDOM PARAMETERS**

R. A. Ibrahim, Texas Tech University, Lubbock, TX

#### **PAPERS APPEARING IN PART 2**

#### Invited Papers

#### Space Shuttle Loads and Dynamics

##### **SPACE SHUTTLE MAIN ENGINE (SSME) POGO TESTING AND RESULTS**

J. R. Fenwick, Rockwell International, Rocketdyne Division, Canoga Park, CA and  
J. H. Jones and R. E. Jewell, NASA, Marshall Space Flight Center, Huntsville, AL

##### **SPACE SHUTTLE SOLID ROCKET BOOSTER WATER ENTRY CAVITY COLLAPSE LOADS**

R. T. Keefe and E. A. Rawls, Chrysler Corporation, Slidell, LA and  
D. A. Kross, NASA, Marshall Space Flight Center, Huntsville, AL

##### **SPACE SHUTTLE SOLID ROCKET BOOSTER REENTRY AND DECELERATOR SYSTEM LOADS AND DYNAMICS**

R. Moog, Martin Marietta/Denver Division, Denver, CO and D. Kross, NASA,  
Marshall Space Flight Center, Huntsville, AL

##### **INVESTIGATION OF SIDE FORCE OSCILLATIONS DURING STATIC FIRING OF THE SPACE SHUTTLE SOLID ROCKET MOTOR**

M. A. Behring, Thiokol Corporation/Wasatch Division, Brigham City, UT

#### Space Shuttle Data Systems

##### DEVELOPMENT OF AN AUTOMATED PROCESSING AND SCREENING SYSTEM FOR THE SPACE SHUTTLE ORBITER FLIGHT TEST DATA

D. K. McCutchen, NASA, Johnson Space Center, Houston, TX, J. F. Brose, Lockheed Engineering and Management Services Company, Inc., Houston, TX and W. E. Palm, McDonnell Douglas Corp., Houston, TX

##### DEVELOPMENT OF A VIBROACOUSTIC DATA BASE MANAGEMENT AND PREDICTION SYSTEM FOR PAYLOADS

F. J. On, NASA, Goddard Space Flight Center, Greenbelt, MD and W. Hendricks, Lockheed Missiles and Space Company, Sunnyvale, CA

##### AUTOMATION OF VIBROACOUSTIC DATA BANK FOR RANDOM VIBRATION CRITERIA DEVELOPMENT

R. C. Ferebee, NASA, Marshall Space Flight Center, Huntsville, AL

##### THE DEVELOPMENT AND VERIFICATION OF SHUTTLE ORBITER RANDOM VIBRATION TEST REQUIREMENTS

M. C. Coody, NASA, Johnson Space Center, Houston, TX, H. K. Pratt, Rockwell International Corporation, Downey, CA and D. E. Newbrough, Management and Technical Services Corporation, Houston, TX

##### SPACE SHUTTLE ORBITER ACOUSTIC FATIGUE CERTIFICATION TESTING

R. A. Stevens, Rockwell International, Downey, CA

#### Space Shuttle Thermal Protection Systems

##### STRUCTURAL CHARACTERISTICS OF THE SHUTTLE ORBITER CERAMIC THERMAL PROTECTION SYSTEM

P. A. Cooper, NASA, Langley Research Center, Hampton, VA

##### SHUTTLE TILE ENVIRONMENTS AND LOADS

R. J. Muraca, NASA, Langley Research Center, Hampton, VA

##### DYNAMIC AND STATIC MODELING OF THE SHUTTLE ORBITER'S THERMAL PROTECTION SYSTEM

J. M. Housner, G. L. Giles and M. Vallas, NASA, Langley Research Center, Hampton, VA

##### BUFFET LOADS ON SHUTTLE THERMAL PROTECTION SYSTEM TILES

C. F. Coe, NASA, Ames Research Center, Moffett Field, CA

##### UNSTEADY ENVIRONMENTS AND RESPONSES OF THE SHUTTLE COMBINED LOADS ORBITER TEST

P. H. Schuetz, Rockwell International, Downey, CA and L. D. Pinson and H. T. Thornton, Jr., NASA, Langley Research Center, Hampton, VA

#### Space Shuttle Main Engine Dynamics

##### VIBRATION MATURITY OF THE SPACE SHUTTLE MAIN ENGINES

E. W. Larson and E. Mogil, Rockwell International/Rocketdyne Division, Canoga Park, CA

##### STRUCTURAL RESPONSE OF THE SSME FUEL FEEDLINE TO UNSTEADY SHOCK OSCILLATIONS

E. W. Larson, G. H. Ratekin and G. M. O'Connor, Rockwell International/Rocketdyne Division, Canoga Park, CA

#### PAPERS APPEARING IN PART 3

#### Environmental Testing and Simulation

##### DIGITAL CONTROL OF A SHAKER TO A SPECIFIED SHOCK SPECTRUM

J. F. Unruh, Southwest Research Institute, San Antonio, TX

##### GUNFIRE VIBRATION SIMULATION ON A DIGITAL VIBRATION CONTROL SYSTEM

J. Ches, Hewlett-Packard Company, Paramus, NJ

##### MEASUREMENT OF ALL COMPONENTS OF STRAIN BY A 3-D FIBER OPTIC STRAIN GAGE

S. Edelman and C. M. Davis, Jr., Dynamic Systems, Inc., McLean, VA

##### REGISTRATION OF THREE SOIL STRESS GAGES AT 0 THROUGH 28 MPa (4000 psi)

C. R. Welch, U.S. Army Engineer Waterways Experiment Station, Corps of Engineers, Vicksburg, MS

**CABLE PROTECTION FOR GROUND SHOCK INSTRUMENTATION IN SEVERE ENVIRONMENTS --  
RESULTS OF AN EVALUATION TEST**

C. R. Welch, U.S. Army Engineer Waterways Experiment Station, Corps of Engineers, Vicksburg, MS

**STRUCTURAL RESPONSE OF HEPA FILTERS TO SHOCK WAVES**

P. R. Smith, New Mexico State University, Las Cruces, NM and W. S. Gregory, Los Alamos National Laboratory, Los Alamos, NM

**A TECHNIQUE COMBINING HEATING AND IMPACT FOR TESTING REENTRY VEHICLE IMPACT  
FUZES AT HIGH VELOCITIES**

R. A. Benham, Sandia National Laboratories, Albuquerque, NM

**USE OF A DROPPED WEIGHT TO SIMULATE A NUCLEAR SURFACE BURST**

C. R. Welch and S. A. Kiger, U.S. Army Engineer Waterways Experiment Station, Corps of Engineers, Vicksburg, MS

**ANALYSIS AND TESTING OF A NONLINEAR MISSILE AND CANISTER SYSTEM**

R. G. Benson, A. C. Deerhake and G. C. McKinnis, General Dynamics/Convair Division, San Diego, CA

**BIO-DYNAMIC RESPONSE OF HUMAN HEAD DURING WHOLE-BODY VIBRATION CONDITIONS**

B. K. N. Rao, Birmingham Polytechnic, Perry Barr, England

**Flight Environments**

**YC-15 EXTERNALLY BLOWN FLAP NOISE**

Capt. L. G. Peck, Flight Dynamics Laboratory, Air Force Wright Aeronautical Laboratories, Wright-Patterson AFB, OH

**DETERMINATION OF THE DYNAMIC ENVIRONMENT OF THE F/FB-111 TAIL POD ASSEMBLY**

J. Chinn and P. Bolds, Air Force Wright Aeronautical Laboratories, Wright-Patterson AFB, OH

**AN ASSESSMENT OF THE A-10's CAPABILITY TO OPERATE ON ROUGH SURFACES**

T. G. Gerardi and D. L. Morris, Air Force Wright Aeronautical Laboratories, Wright-Patterson AFB, OH

**SUBCRITICAL FLUTTER TESTING USING THE FEEDBACK SYSTEM APPROACH**

C. D. Turner, North Carolina State University, Raleigh, NC

**TOMAHAWK CRUISE MISSILE FLIGHT ENVIRONMENTAL MEASUREMENT PROGRAM**

E. S. Rosenbaum and F. L. Gloyne, General Dynamics/Convair Division, San Diego, CA

**TEST PROGRAM TO DEVELOP VIBROACOUSTICS TEST CRITERIA FOR THE GALILEO BUS**

D. L. Kern and C. D. Hayes, Jet Propulsion Laboratory, California Institute of Technology, Pasadena, CA

**SLV-3 FLIGHT VIBRATION ENVIRONMENT**

S. A. Palaniswami, G. Muthureman and P. Balachandran, Aerospace Structures Division, Vikram Sarabhai Space Centre, Trivandrum, India

**PAPERS APPEARING IN PART 4**

**Fatigue and Random Loading**

**FATIGUE LIFE PREDICTION FOR VARIOUS RANDOM STRESS PEAK DISTRIBUTIONS**

R. G. Lambert, General Electric Company, Aircraft Equipment Division, Utica, NY

**FATIGUE LIFE EVALUATION, STOCHASTIC LOADING AND MODIFIED LIFE CURVES**

M. El Mensoufy, H. H. E. Leipholt and T. H. Topper, University of Waterloo, Waterloo, Ontario, Canada

**THE EFFECTS OF ENDURANCE LIMIT AND CREST FACTOR ON TIME TO FAILURE  
UNDER RANDOM LOADING**

A. J. Curtis and S. M. Molte, Hughes Aircraft Company, Culver City, CA

**SINGLE POINT RANDOM MODAL TEST TECHNOLOGY APPLICATION TO FAILURE DETECTION**

W. M. West, Jr., NASA, Johnson Space Center, Houston, TX

**FORCED VIBRATIONS OF A LARGE DAMPED MECHANICAL SYSTEM**

D. W. Nicholson, Naval Surface Weapons Center, White Oak, Silver Spring, MD

**INDIRECT FOURIER TRANSFORM (IFT) AND SHOCK RESPONSE — A DETAILED  
PRESENTATION OF BASIC THEORY**  
C. T. Morrow, Encinitas, CA

**Control, Isolation and Damping**

**ACTIVE VIBRATION CONTROL OF LARGE FLEXIBLE STRUCTURES**

T. T. Soong and J. C. H. Chang, State University of New York at Buffalo, Buffalo, NY

**FORCE OPTIMIZED RECOIL CONTROL SYSTEM**

P. E. Townsend, U.S. Army Armament Research and Development Command, Dover, NJ,  
R. J. Radkiewicz, U.S. Army Armament Research and Development Command, Rock Island, IL and  
R. F. Gartner, Honeywell, Inc., Edina, MN

**PERFORMANCE ANALYSIS OF HIGH-SPEED HYDRAULIC SUSPENSION SYSTEMS IN  
MULTIPLE WHEELED LAND TRANSPORTERS**

P. Woods, Martin Marietta Corporation, Denver, CO

**NONLINEAR ANALYSIS OF PNEUMATIC FORCE GENERATORS USED FOR VIBRATION CONTROL**

S. Sankar, Concordia University, Montreal, Quebec, Canada, R. R. Guntur, Union College, Schenectady, NY,  
and S. G. Kalumbar, Electronic Associates, Inc., West Long Branch, NJ

**REDUCTION OF HYDRAULIC LINE OSCILLATING PRESSURES INDUCED BY PUMP CAVITATION**

G. Druhak, P. Marino and M. Bernstein, Grumman Aerospace Corporation, Bethpage, NY

**RUBBER ISOLATORS FOR THE ADATS MISSILE**

J. Frottler, Oerlikon-Buehler Werkzeugmaschinenfabrik, Zurich, CH and  
C. F. O'Hearne, Martin Marietta Orlando Aerospace, Orlando, FL

**TIME AND TEMPERATURE EFFECTS ON CUSHIONS**

G. S. Mustin, Naval Sea Systems Command, Washington, DC

**EXTRANEUS EFFECTS IN DAMPING MEASUREMENT**

R. J. Hooker, University of Queensland, Queensland, Australia and  
S. Prasertan, Prince of Songkla University, Hat-yai, Thailand

**DYNAMIC ANALYSIS OF A LARGE STRUCTURE WITH ARTIFICIAL DAMPING**

Q. L. Tian, D. K. Liu, Y. P. Li and D. F. Wang, Institute of Mechanics,  
The Chinese Academy of Sciences, Beijing, China

**AN EXPERIMENTAL STUDY OF THE NONLINEAR BEHAVIOUR OF A STRANDED CABLE  
AND DRY FRICTION DAMPER**

C. S. Chang and Q. Tian, Institute of Mechanics, The Chinese Academy of Sciences, Beijing, China

**RESPONSE OF PNEUMATIC ISOLATOR TO STANDARD PULSE SHAPES**

M. S. Hundal, The University of Vermont, Burlington, VT

**TITLES AND AUTHORS OF PAPERS PRESENTED IN THE  
SHORT DISCUSSION TOPICS SESSION**

**NOTE:** These papers were only presented at the Symposium. They are not published  
in the Bulletin and are only listed here as a convenience.

**TRANSFER FUNCTION ANALYSIS OF LARGE STRUCTURES**

H. J. Weaver, Lawrence Livermore National Laboratory, Livermore, CA

**SHOCK HARDENED STRUCTURAL ATTACHMENTS FOR HONEYCOMB BULKHEADS**

P. W. Buermann, Gibbs & Cox, Inc., New York, NY

**DISCOVERING THE THIRD (AND SECOND) DIMENSION**

B. Meeker, Pacific Missile Test Center, Point Mugu, CA

**A MICROPROCESSOR BASED ADAPTIVE ISOLATION AND DAMPING OF A VIBRATING STRUCTURE**

A. S. R. Murty, Indian Institute of Technology, Kharagpur, India

- HARMONIC RESPONSE OF A STRUCTURE INCLUDING A DRY FRICTION DAMPER**  
J. Der Hagopian and M. LaLanne, Institut National des Sciences Appliquees, Villeurbanne, France
- RATIONALE FOR VIBRATION TESTING IN MIL-STD-810D (DRAFT)**  
H. J. Caruso, Westinghouse Electric Corporation, Baltimore, MD
- VIBRATION ISOLATION OF SENSITIVE IUS COMPONENTS REQUIRING THERMAL CONDUCTION**  
F. W. Sparrn, Eosong Aerospace Company, Seattle, WA
- FINITE ELEMENT ANALYSIS OF SHOCK AND VIBRATION FIXTURES**  
L. G. Smith, Hughes Aircraft Company, Fullerton, CA
- A UNIQUE METHOD FOR VIBRATION TESTING FAR BELOW THE NORMAL AMBIENT NOISE LEVEL OF ELECTRODYNAMIC SHAKERS**  
H. D. Camp, Jr., U.S. Army; ERADCOM, Fort Monmouth, NJ
- BOLTS AND FASTENER TIGHTENING TO BROCHURE IDEALNESS THROUGH VIBRATION SIGNATURES**  
A. S. R. Murty, Indian Institute of Technology, Kharagpur, India
- COST EFFECTIVE METHODS OF INCREASING DATA RECORDING CAPACITY**  
M. Dowling, Franklin Research Center, Philadelphia, PA
- PIEZOELECTRIC FORCE GAUGE WITH HIGH SENSITIVITY**  
R. R. Bouche, Bouche Laboratories, Sun Valley, CA
- PYROTECHNIC SHOCK ENVIRONMENTS MEASURED ON INERTIAL UPPER STAGE (IUS)**  
C. J. Beck, Jr., Boeing Aerospace Company, Seattle, WA
- USE OF BAND-SELECTABLE HANNING SMOOTHING TO IMPROVE TRANSIENT WAVEFORM REPRODUCTION ON SHAKERS**  
D. O. Smallwood and D. L. Gregory, Sandia National Laboratories, Albuquerque, NM
- SHAKER SHOCK TEST DATA - BASED ON OPTIMIZED PRE AND POST PULSES**  
R. T. Fandrich, Harris Corporation, Melbourne, FL
- PROGRESS ON THE EDESS MACHINES**  
F. J. Szama, Naval Surface Weapons Center, Silver Spring, MD
- MULTI-AXIS RANDOM VIBRATION TESTER FOR AVIONICS**  
D. Everett, Pacific Missile Test Center, Point Mugu, CA and G. Greanias, UCLA, Los Angeles, CA
- ACOUSTIC FACILITY FOR CRUISE MISSILE TESTING**  
O. H. Moore, Jr., General Dynamics/Convair, San Diego, CA
- EFFECT OF FRICTION AND MISTUNING ON THE RESPONSE OF A BLADED DISK DISCRETE MODEL**  
A. Muszynska, University of Dayton and Bently Nevada Corp., Minden, NV
- CURRENT DEVELOPMENTS IN HUMAN VIBRATION RESEARCH**  
J. C. Guignard, Naval Biodynamics Laboratory, New Orleans, LA

## MATHEMATICAL MODELING

### DAMPED STRUCTURE DESIGN USING FINITE ELEMENT ANALYSIS

Matthew F. Kluesener

and

Michael L. Drake

University of Dayton Research Institute  
Dayton, Ohio 45469

As the performance requirements and the life cycle costs for jet engines and aircraft increase the need for functional high cycle fatigue (HCF) control is evident. The purpose of this paper is to present the methodology of using finite element analysis to evaluate viscoelastic damping treatments for HCF control. Steps for analyzing passive damping treatments are presented. Design criteria used to evaluate the damping applications, as well as two methods of calculating the structural loss factor are discussed. The results from analyses of a stiffened panel and turbine blade are also presented.

#### INTRODUCTION

As the performance requirements and the life cycle costs for jet engines and aircraft fuselage increase, the need for functional high cycle fatigue (HCF) control is evident. A major concern in jet engines is the HCF failure of turbine blades. Blade failures cause frequent maintenance overhauls resulting in high life cycle costs. Another concern is the reliability of these components under war time conditions, where the operation time would be greatly increased and the operational environment would be more severe. Blade redesign efforts have proven somewhat effective; however, they are extremely expensive and often result in performance losses. Likewise, the design of aircraft fuselage structures is often governed by sonic fatigue. In these cases, high sound pressure levels cause the structure to vibrate at its natural frequencies, resulting in very high resonant stresses which cause HCF problems. Current design methods to reduce the high stresses include strengthening the structures or decreasing frame and stringer spacing, resulting in weight penalties affecting aircraft performance.

A weight efficient method to reduce HCF is to dissipate vibratory energy through the use of viscoelastic damping

materials. Viscoelastic damping materials in the form of free layer and constrained layer damping treatments (sometimes called passive damping) to increase the damping in structures have been used for sometime [1,2,3] Figure 1 shows the types of damping treatments.

In recent year, vibration damping technology has been successfully applied to numerous structures to control resonant vibration at both high and low temperatures [4,5,6].

Most applications of damping treatments on structures to date have been "fixes" for existing vibration problems. A more prudent approach is to consider passive damping in the initial design stage. This requires sophisticated structural analysis programs to verify conceptual designs reducing the number of prototypes that need to be constructed. A finite element program which can predict the response of damped structures has been developed which meets this need [7,8]. The purpose of this paper is to present the methodology of using this finite element analysis approach to evaluate viscoelastic damping treatments for high cycle fatigue control. The results of analyses on a skin stringer panel and a high temperature turbine blade will also be presented.

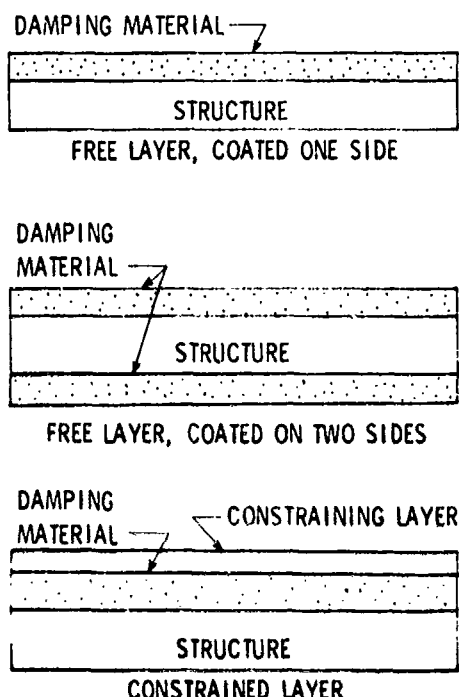


Fig. 1 - Types of Viscoelastic Damping Treatments.

#### APPROACH TO DAMPING DESIGN BY FINITE ELEMENT METHOD

When considering passive damping in the initial design process, the analysis can be used to evaluate the design concepts by one of several criteria. In the case of a fatigue problem, the criteria may be a maximum stress level during resonance. However, in the design of a structure requiring small vibration levels, another criteria may be a required maximum displacement at resonance. Both criteria are based on the fact that damping limits the response during resonance. Both criteria follow the same basic steps in the analysis.

In the past, constrained layer damping treatments applied to a structure usually consisted of a thin layer of self-adhesive damping material covered by a thin layer of metal foil (the constraining layer). In the initial design stage, it is possible and advantageous to design the structure as a composite (sandwich) consisting of equal thicknesses of metal serving as the base layer and constraining layer, bonded together with damping material. This would be the same as the damped sheet steel which is commercially available.

Our approach to evaluating the effect of a damping treatment on the

response involves several steps (also see Figure 2):

(1) The first step is to determine the natural frequencies and mode shapes of the undamped structure. Once the natural frequencies are established, the mode or modes of interest in the frequency band of excitation can be chosen. Since the loss factor and modulus of the damping material are frequency and temperature dependent, the natural frequency is needed to select the properties of the damping material. It is also important at this time to establish the temperature range over which damage or high cycle fatigue is likely to occur. Note that this temperature range most probably will be narrower than the broad temperature range that the component will see.

An alternative to determining the properties of the damping material based on temperature and frequency at this point, is to choose a typical value of modulus and loss factor of a material where it has peak damping. It then becomes necessary to find a material that has these properties at the required temperature and frequency.

(2) The second step in the analysis procedure is to do a forced harmonic response of the undamped structure. This is done by applying a vibrating or harmonic load to the structure. The load can be applied at the natural frequency of interest from which displacement and/or stress is calculated. Alternatively, the load can be applied at discrete frequencies in a small bandwidth about the natural frequency, to yield an amplitude versus frequency response plot (receptance plot). From this response plot the structural damping can be determined by the half-power bandwidth method. A small amount of damping is included in the base structure to simulate the actual inherent structural damping and to keep the response at the natural frequency from becoming infinite. It should be noted that the damping determined from the response plot will be the same as the inherent damping specified, and the step may be deleted. The reason the damping will be the same as the inherent damping, can be seen by referring to the equation for system loss factor by the Strain Energy Method in Figure 3. For the undamped case with a small amount of inherent damping,  $\eta_1 = \eta_2 = \dots = \eta_n$  (where  $\eta_i$  is the loss factor for the  $i$ th element), and  $\eta_0$  will therefore be the loss factor specified for the material. Thus, the response and stress level are determined during resonance for the undamped

case, giving a reference by which to measure the effect of the damping treatment.

(3) The third step is to determine the natural frequencies of the damped structure. The natural frequencies of the damped structure are going to differ from the undamped structure because the damping material and constraining layer change the section properties of the structure, thereby changing its natural frequencies. This is especially true if the damped structure is a sandwich composite where damping material is sandwiched between two metal layers that are each one-half the thickness of the undamped structure. It should be noted that the loss factor or damping ratio of the damping material does not enter into the natural frequency calculation. That is, the natural frequency determined is not the damped natural frequency. The natural frequency is based solely on the geometry of the layers and the stiffness or modulus of the materials.

(4) The fourth step is to do a forced harmonic response of the damped structure. The same harmonic loading as in step (2) is again applied to the structure. The loss factor of the material does enter into the calculations in this step. The increased damping in the structure shifts the damped resonant frequency slightly higher than the undamped resonant frequency. Usually the shift is small, on the order of one percent or less. The exact resonant frequency for the damped structure is determined by performing the forced harmonic response analysis at discrete frequencies in the neighborhood of the expected natural frequency, and noting that frequency which yields the maximum displacement for a specific point on the structure. Once the damped natural frequency is determined, a forced response analysis at the damped natural frequency is performed to determine the stresses at the damped resonance.

With this information, the designer can now compare the damped structure to the undamped structure on the basis of stress or displacement, depending on which criteria was selected. If the damped structure meets the design criteria, it may be wise at this point to determine the loss factor or stress in the structure during resonance at different temperatures to see how the damping varies versus temperature. The properties of the damping material are determined at the new temperature and an estimation of the new frequency, and steps (3) and (4) above are repeated. The frequency of the damped structure at the new temperature will be differ-

ent, because the modulus of the damping material will be different at the new temperature. Although the damping material is temperature and frequency dependent, it is not as dependent on frequency as it is on temperature. Therefore, a close approximation of the natural frequency at the new temperature should be adequate.

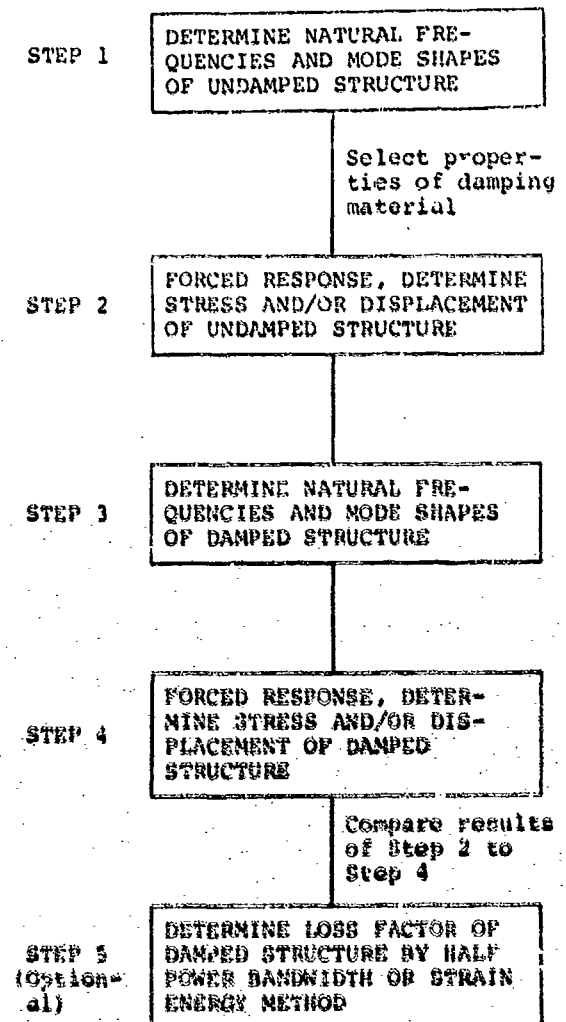


Fig. 2 - Steps to Evaluate Damping Treatment by Finite Element Analysis.



$$\eta_s = \frac{\eta_1 \times SE_1 + \eta_2 \times SE_2 + \eta_3 \times SE_3 + \dots}{\sum_{i=1}^n SE_i}$$

WHERE  $SE_i$  IS THE STRAIN ENERGY FOR THE  $i^{th}$  ELEMENT

STRAIN ENERGY METHOD

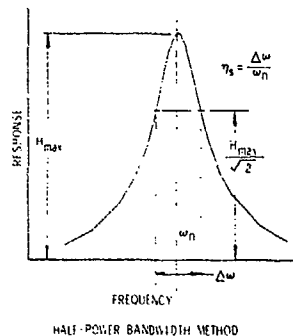


Fig. 3 - Determination of System Loss Factor.

The fifth and last step in the analysis is optional. If the system loss factor for the damped structure is desired, it can be calculated in two ways. The first method is to do a forced vibration analysis at discrete frequencies about the natural frequency and the plot the response amplitude versus frequency. Note that part of this was already done in order to determine the damped natural frequency. The loss factor is then determined by the half-power bandwidth method, as shown in Figure 3. The second approach is to use the strain energy method. In the strain energy method the loss factor is determined as the ratio of the energy dissipated to the total strain energy stored. The energy dissipated is equal to the sum over all the elements of the loss factor of each element times the strain energy stored in each element (see Figure 3).

Two recent projects on which damping treatments were analyzed will be presented in the following sections as examples of using this methodology.

#### EXAMPLES OF DAMPED STRUCTURE DESIGN

##### Damped Skin Stringer Panel

The purpose of the investigation of a skin stringer structure was to lower the stresses in the resonant condition by the use of viscoelastic constrained layer damping. The method and analysis are not limited to aircraft fuselage structures, but are also representative of any general class of structures consisting of stiffened skins or panels.

When analyzing a complex structure such as an aircraft fuselage, it is impractical to model the whole fuselage or even a sub-section of the fuselage. The number of nodes and elements necessary for accurate dynamic predictions would be enormous. Therefore, a representative section of the structure is modeled (see Figure 4). However, by imposing the proper boundary conditions, two of the edges can be treated as lines of symmetry. The effect of this is to give the model the same flexibility as if four sections were modeled (see Figure 5). It does, however, restrict the natural frequencies that can be extracted to the odd-odd modes such as the 1,1 mode, 1,3 mode, 3,3 mode, 1,5 mode, etc. Other symmetry conditions would yield even-even or even-odd modes (see Figure 6).

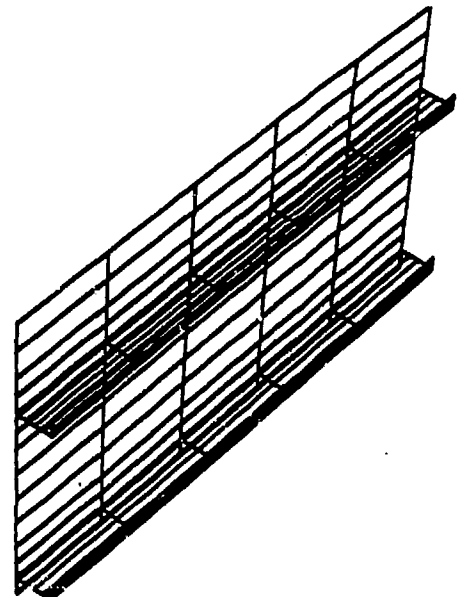


Fig. 4 - Finite Element Model of Stiffened Panel.

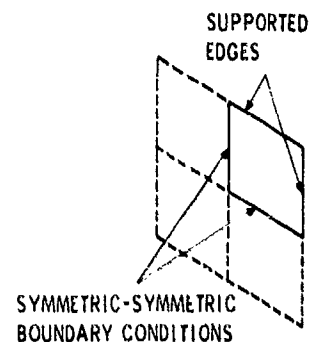


Fig. 5 - Boundary Conditions.

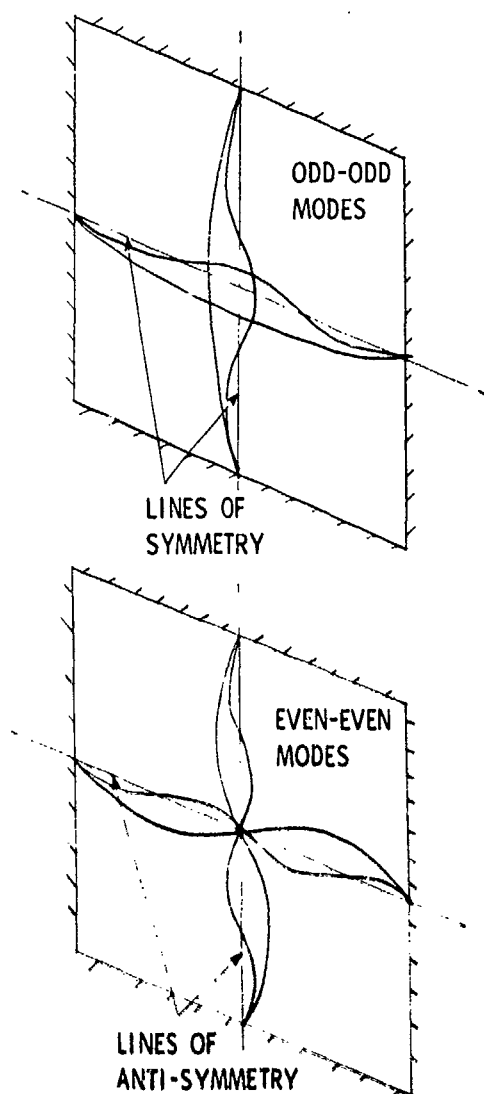


Fig. 6 - Mode Shapes for Various Symmetry Conditions.

The model shown in Figure 4 consists of 285 elements and 828 nodes, for a total of almost 2,500 degrees of freedom. With the boundary conditions chosen, a panel 1,524-mm (60-inches) long by 813-mm (32-inches) wide was modeled. The distance between stiffening ribs was 254-mm (10-inches). The cross-section of the structure is shown in Figure 7, from which it is easy to identify the various layers in the model.

The ribs and damping material layer were modeled with solid elements, which are shear deformable. It is important that the damping layer is modeled with shear deformable elements, since a constrained layer damping treatment dissipates energy through shear deformation.

The constraining layer and panel were modeled with thin-shell elements. The panel, ribs, and constraining layer were aluminum.

The stiffeners were 51-mm (2-inches) high, and all sections of the stiffeners were 1.5-mm (0.060-inch) thick. The panel directly under the stiffener web was 2.2-mm (0.035-inch) thick. From this point under the web, the panel tapered to a thickness of 1.5-mm (0.060-inch), in a distance of 25-mm (1-inch). The taper was actually very shallow, and not abrupt as it appears in Figure 7. This taper represented a two-step chem-milled panel.

In between the stiffener web and the panel, a very thin element, 0.13-mm (0.005-inch) was incorporated. This element could be used as a faying surface damping treatment. A faying surface damping treatment is a damping layer applied where two surfaces fit together and where relative motion or fretting between the surfaces might occur. For the undamped runs this thin element was given the material properties of aluminum, and it contributed little stiffness to the ribs.

The approach to evaluate this constrained layer damping treatment varied slightly from the steps outlined earlier. The "undamped" structure actually included the damping and constraining layers. The stresses for the undamped forced vibration analysis were obtained by giving the damping material a very low loss factor, 0.006, the same loss factor as was used for the aluminum panels and ribs. For the damped forced vibration analysis, the damping material was given its normal loss factor of approximately 0.9 at the temperature and frequency of interest, and new stresses were obtained.

The first five modes of the panel for the symmetric-symmetric boundary conditions are listed in Table 1. Our investigation centered about the third mode, the 3,3 mode at 120.1 Hz, as shown in Figure 8.

In the undamped and damped forced vibration analysis, the force was a harmonic pressure loading normal to the surface of the panel. The pressure corresponded to an acoustic sound pressure level of 165 dB. A small amount of inherent damping is included in the base structure (loss factor = 0.006) to simulate actual structural damping and to keep the response at the natural frequency for the undamped case from becoming infinite. The constrained layer damping treatment consists of

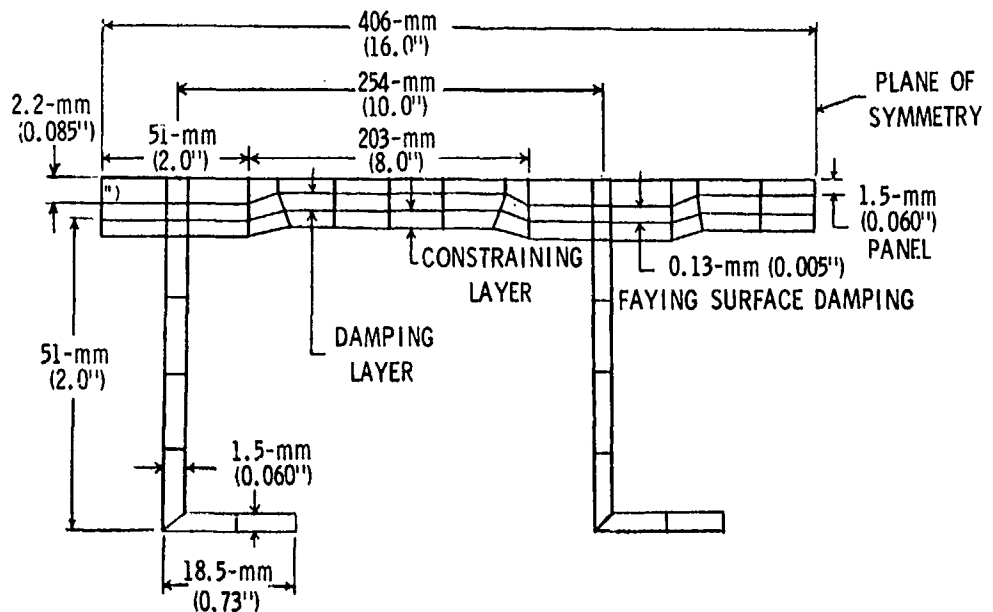


Fig. 7 - Cross Section of Panel Model.

TABLE 1  
MODES OF UNDAMPED SKIN STRINGER PANEL

Mode	Frequency (Hz)
1,1	48.8
1,3	68.9
3,3	120.1
1,5	149.7
3,5	159.2

0.35-mm (0.014-inch) of 3M Company's SD 112 damping material (properties chosen at 29°C [85°F] and 120 Hz) and 0.2-mm (0.008-inch) of aluminum constraining layer. The complex modulus data for the damping material are shown in the reduced temperature monograph in Figure 9.

The results for the undamped and damped panel are given in Table 2. With an inherent loss factor of 0.006, the stress in the undamped panel was 263 MPa (38,100 psi). With the addition of 0.35-mm (0.014-inch) damping layer and a 0.2-mm (0.008-inch) constraining layer, the loss factor increased to 0.029. Stress was reduced by 80 percent to 48.5 MPa (7,030 psi). The addition of the damping treatment represents only a 10 percent increase in weight of the structure.

#### Damped Turbine Blade

As another example of using finite elements to analyze damping designs, the results of analyses on a turbine blade are presented. The purpose of the

analyses was to determine the effect of damping treatments on the blade airfoil on the modal loss factor of the blade. The forced harmonic response (magnitude and phase angle) of the first bending mode of the blade was studied for the following cases: (1) undamped blade; (2) blade with free layer damping treatment; (3) blade with constrained layer damping treatment; and (4) rotating blade with constrained layer damping treatment.

The model, shown in Figure 10, consists of 234 elements. The axial length was divided into six sections, giving 39 elements per section. The cross-section of the blade is also shown in Figure 10. The damping treatment consisted of a 0.25-mm (0.010-inch) layer of Corning 8463 glass covered by a 0.13-mm (0.005-inch) layer of nickel. The glass layer was modeled by twelve elements per section, the nickel by twelve elements per section, and the blade by fifteen elements per section. The boundary condition used in the analysis was the base of the airfoil fully constrained in the x, y and z directions. The platform and root of the blade were not modeled, because coordinate data was not available for those portions of the blade. The frequencies determined by the finite element model were higher than the frequencies of the actual blade. This is because the root and platform contribute flexibility to the blade. However, for the purpose of analyzing damping treatments on the airfoil section of the blade, this is not a serious limitation.

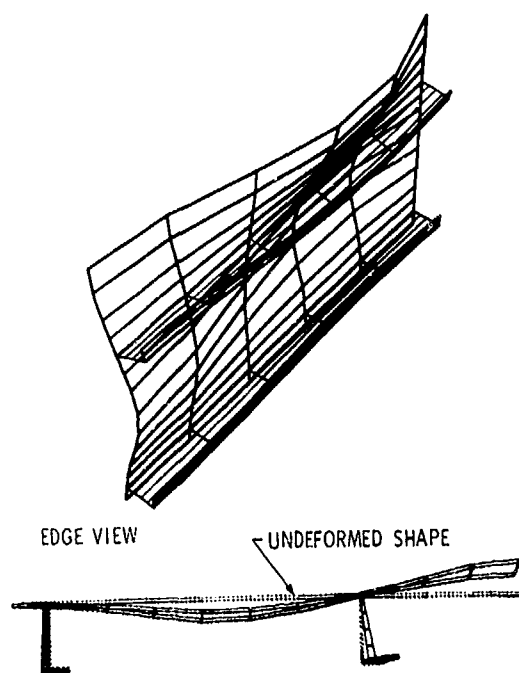


Fig. 8 - Mode 3,3 of Stiffened Panel.

The analysis of the turbine blade followed the four steps outlined previously. That is, the natural frequency search and forced harmonic response were performed on the undamped blade and then repeated for the damped blade.

The purpose of the force harmonic response analysis in this example was not to determine absolute stresses and absolute displacements, but was used to show the relative decrease in response with damping as compared to the undamped response, given the same loading condition. This is best illustrated by an amplitude-frequency plot, which can be generated by calculating the response at discrete frequencies in the neighborhood of the resonant frequency of interest. From this plot, one can identify the half-power bandwidths and then compute the structural loss factor for that particular mode, as discussed earlier. Thus, the end results of the forced harmonic response analysis is the structural loss factor, which is independent of the load applied. The loading condition for the forced harmonic response was a point load applied at the tip of the blade.

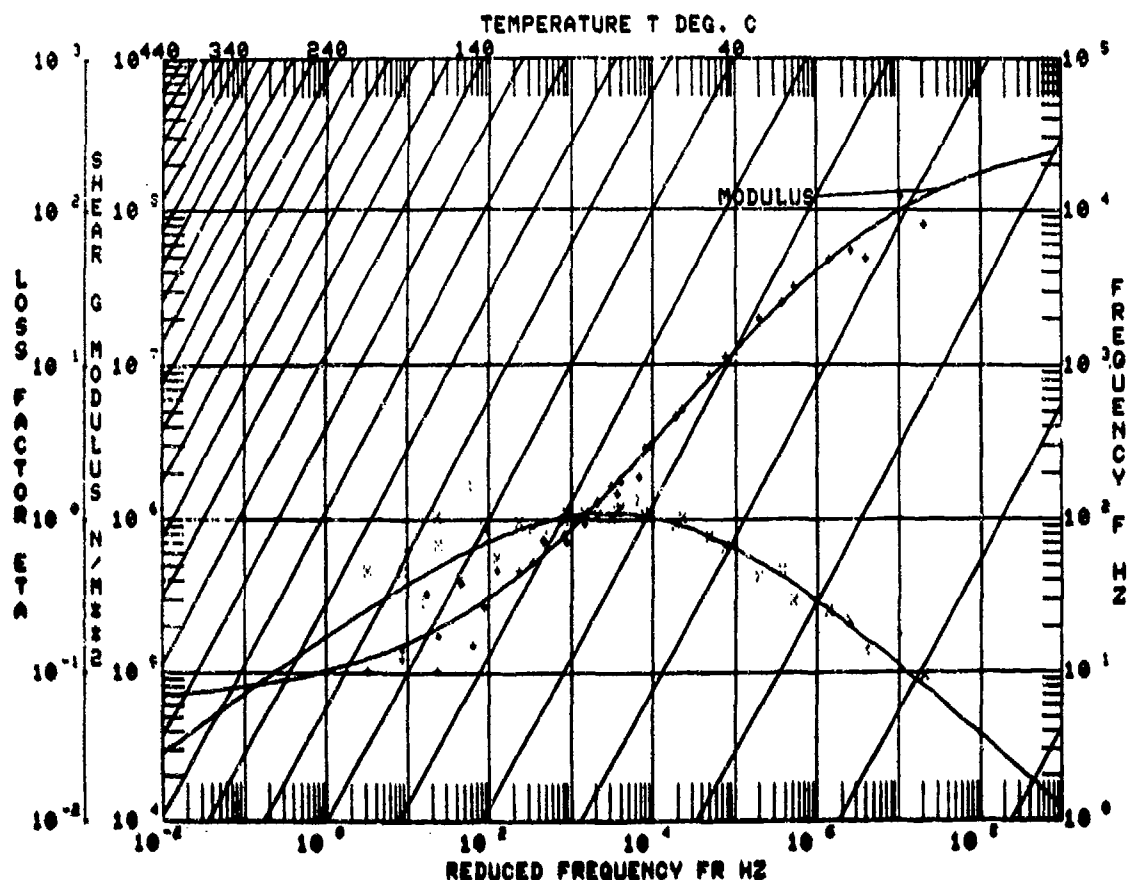
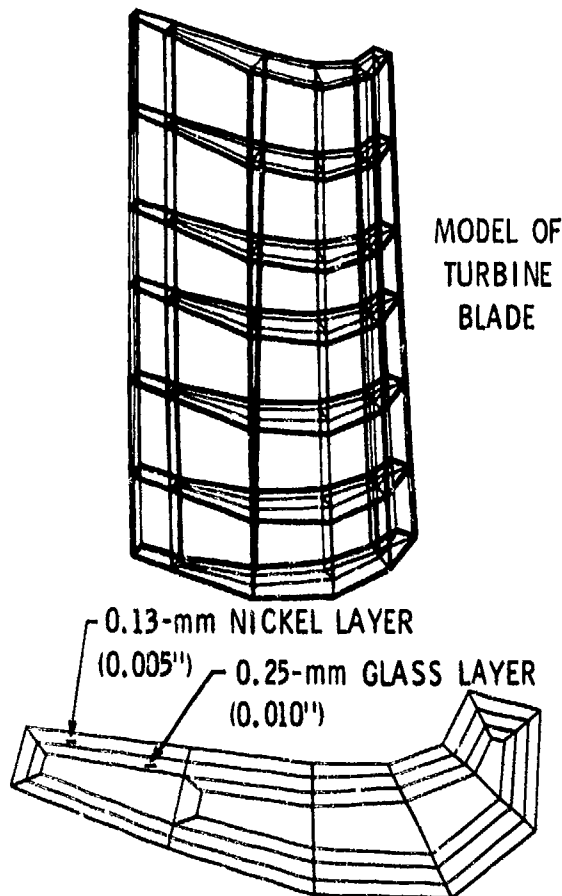


Fig. 9 - Reduced Temperature Nomograph for 3M ISD-112.

TABLE 2  
RESULTS FOR UNDAMPED AND DAMPED PANEL

Condition	Frequency	Mode	Damping	Stress	% Stress Reduction	% Weight Increase
1.5-mm (0.060") Panel, Undamped	120.1	3,3	0.006	263 MPa (38,100 psi)	0	0
1.5-mm (0.060") Panel, 0.35-mm (0.014") damping layer, 0.2-mm (0.008") constraining layer	120.3	3,3	0.029	48.5 MPa (7,030 psi)	80	10



CROSS-SECTION OF TURBINE BLADE

Fig. 10 - Finite Element Model of Turbine Blade.

A total of eight configurations and sets of conditions were analyzed by the finite element method. The seven non-rotating cases and the one rotating case are shown in Table. 3.

Figure 11 shows cases 1, 2, and 3 on the same plot for comparison purposes. Cases 1 and 2 were the undamped blade at room temperature and 496°C (925°F), respectively. Comparison of these two plots shows the downward shift in first mode frequency due to the higher temperature; the change in frequency was approximately 0.8 percent. Comparison of case 3 with case 2 illustrates the increased first mode frequency of the damped blade which was due primarily to the stiffness of the nickel overcoat. Of course the most obvious feature is the marked decreased in response of the damped blade compared to the undamped blade.

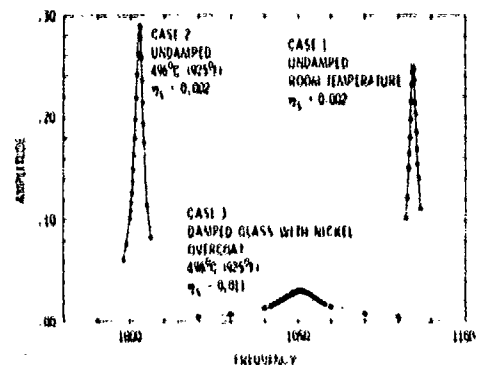


Fig. 11 - Comparison of Damped and Undamped Response.

TABLE 3  
ANALYSES OF TURBINE BLADE

Case	Description	First Three Modes (Hz)	Composite Loss Factor
1	Bare, undamped blade, all material properties at room temperature	1,085.1 1,972.0 3,010.4	0.002*
2	Bare, undamped blade, all material properties at 925°F (496°C)	1,002.7 1,822.6 2,782.0	0.002*
3	Damped blade, full blade glass coating with nickel overcoat, material properties at 925°F (496°C)	1,050.7 2,847.4 4,032.9	0.011
4	Damped blade, full glass coating, all material properties at 925°F (496°C)	920.6 1,660.8 2,845.7	0.008
5	Damped blade, full glass coating, all material properties at 800°F (427°C)	940.6 1,690.7 2,917.3	0.0022
6	Damped blade, full glass coating, all material properties at 1,000°F (538°C)	907.3 1,641.0 2,792.2	0.0044
7	Damped blade, full blade glass coating with nickel overcoat, all material properties at 925°F (496°C), 7500 rpm	1,082.4 2,870.6 4,037.5	0.0083**
8	Damped blade, full blade coating, with nickel overcoat, all material properties at 925°F (496°C), glass layer modeled with solid elements	1,058.7 2,874.5 3,999.2	0.0122

\*Blade material is assumed to have an inherent loss factor of 0.002.

\*\*The loss factor is approximate because the peak is non-symmetric; loss factor was estimated by using the left side of the peak and multiplying bandwidth by two. Analysis includes blade rotation effects.

A series of analyses was completed for a non-rotating blade with an 0.25-mm (0.010-inch) glass free layer coating (full blade coverage) at 427, 496, 538°C (800, 925, 1,000°F). The peak structural loss factor occurred at the temperature of 496°C (925°F), at which the loss modulus was also at a maximum. The complex modulus data for Corning 8463 glass are shown in the reduced temperature nomograph in Figure 12. The amplitude-frequency response for the three temperatures is shown in Figure 13. This plot shows the reduced response amplitude of the blade at the optimum temperature. The shift in the first mode frequency with temperature can also be seen. The structural loss factors at 427, 496, and 538°C were 0.0022, 0.008, and 0.0044, respectively.

In a structure with a free layer damping treatment, the damping is proportional to the loss modulus. The loss modulus (modulus  $\times$  loss factor) of Corning Glass 8463 versus temperature is shown in Figure 14. Superimposed on this graph is the structural loss factor of the blade with full glass coating. From this plot it can be seen that the loss factor predicted by the finite element analysis has the same temperature profile as the loss modulus. For a free layer damping application, these are the trends expected. Also shown on this plot is the experimentally measured structural loss factor for a blade with a half-blade glass coating; the peak structural loss factor is higher and occurs at a lower temperature.

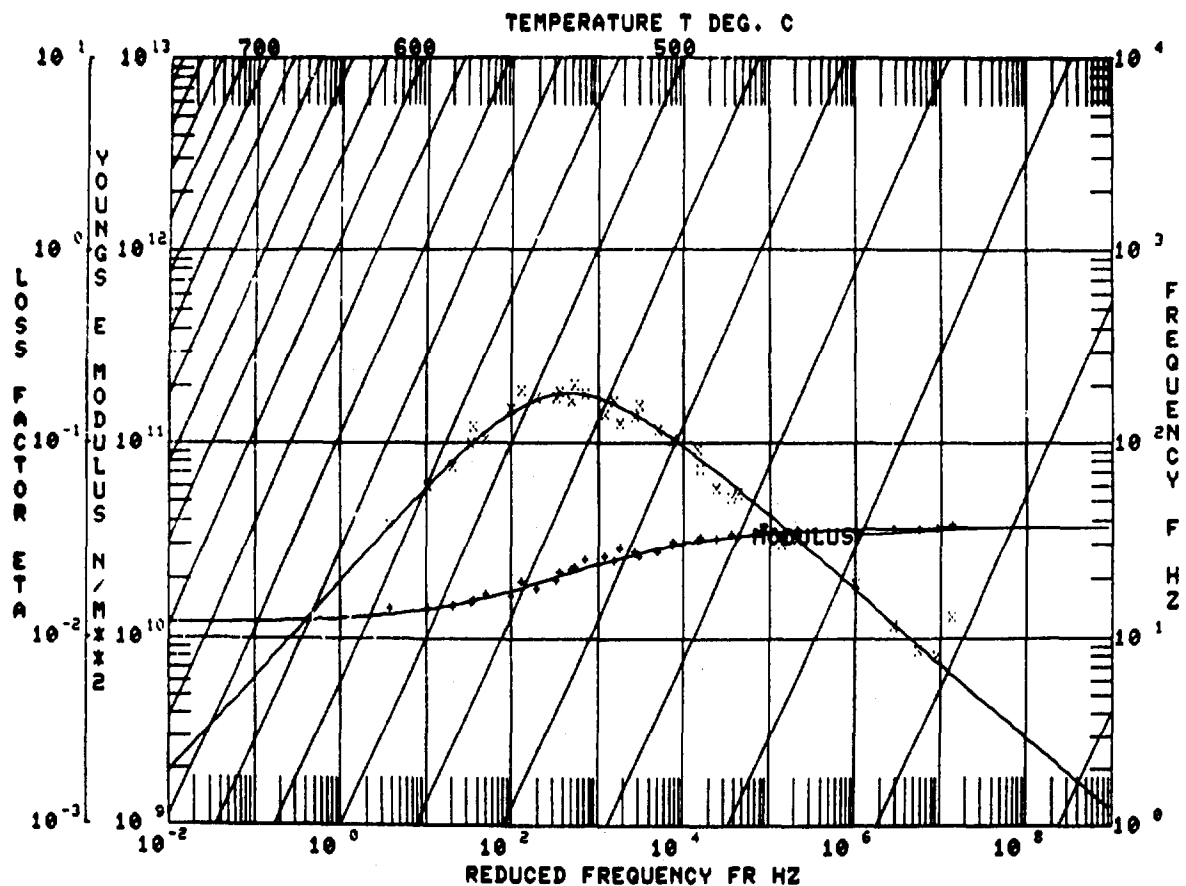


Fig. 12 - Reduced Temperature Nomograph for Corning 8463 Glass.

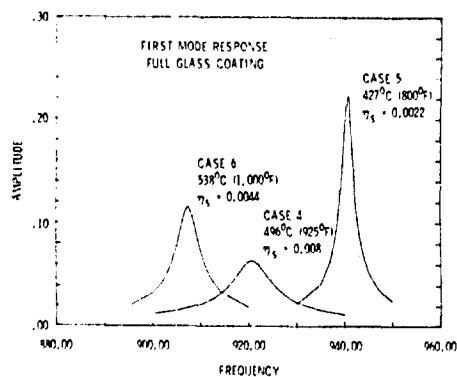


Fig. 13 - Response with Full Glass Coating at Three Temperatures.

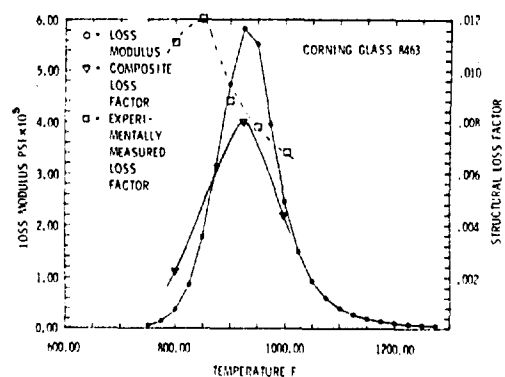


Fig. 14 - Loss Modulus and Structural Loss Factor Versus Temperature.

Figure 15 shows cases 3 and 4 together for comparison purposes. The damped blade with glass coating and nickel overcoat exhibited a lower response than the blade with just a glass coating. Case 4 had a lower first mode frequency because the glass coating added mass loading to the blade, but contributed very little stiffness since its modulus was an order of magnitude lower than the modulus of the blade material or nickel overcoat.

Results were obtained for an initially stressed damped blade (case 7, glass coating with nickel overcoat). The initial stress was caused by rotation at 7,500 rpm. The shift in first mode frequency due to rotation can be seen by comparing the rotating and non-rotating cases in Figure 16. The width of the peaks in each case are approximately the same, indicating that each has about the same level of damping.

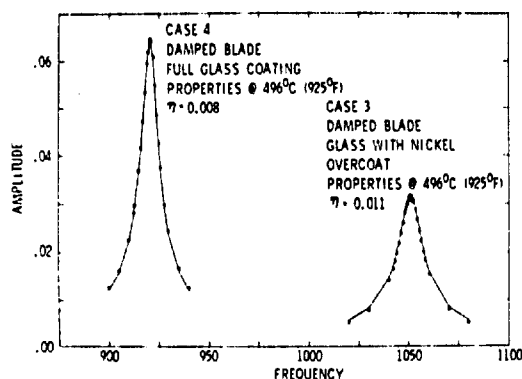


Fig. 15 - Comparison of Blade with Glass and Glass and Nickel.

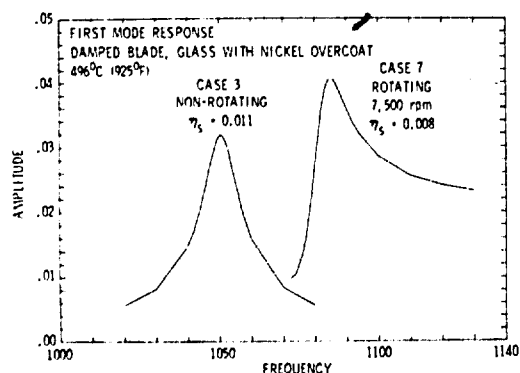


Fig. 16 - Damped Blade Response, Rotating and Non-Rotating.

#### SUMMARY

Concise steps were presented describing the process by which a damping treatment can be analyzed. Design

criteria used to evaluate the passive damping treatments were set forth, as were two methods of calculating the structural loss factor. The example of the skin stringer panel demonstrated the superior weight effectiveness of optimally designed damping treatments for reducing stress. A ten percent increase in weight yielded an 80 percent reduction in stress. This reduction in stress compares favorably to the results of several successful damping treatments shown in Figure 17. The analysis of the damped turbine blade demonstrated the effect of temperature on damping performance (see Figure 13) and shows a good comparison between predicted and experimental results (see Figure 14).

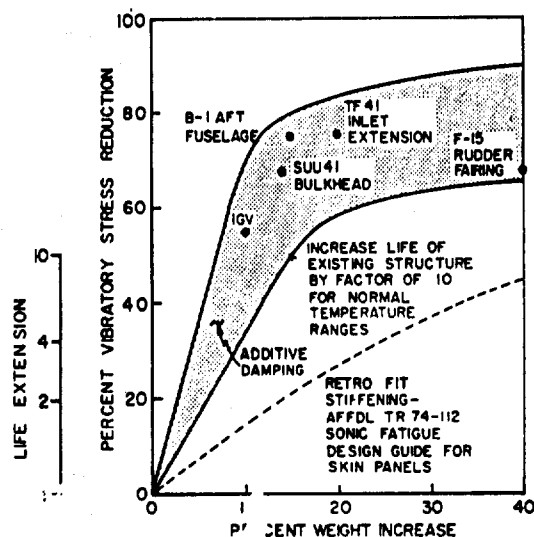


Fig. 17 - Damping as a More Weight Efficient Procedure.

#### ACKNOWLEDGEMENTS

The authors wish to acknowledge M.L. Soni and R. A. Brockman for their assistance in using the finite element program, and to Charlene Thompson for typing the manuscript.

#### REFERENCES

- [1] Ross, D., Ungar, E. E., and Kerwin, Jr., E. M., "Damping of Plate Flexural Vibrations by Means of Viscoelastic Laminates," *Structural Damping*, ed. J. E. Ruzicka, Proc. ASME Colloq., 1959.
- [2] Ungar, E., "Loss Factors of Viscoelastically Damped Beam Structures," *J. Acoustical Society*, Vol. 34, No. 8, pp. 1082-1089, August 1962.



- [3] Oberst, H., "Reduction of Noise by the Use of Damping Materials," Royal Aero. Soc., Vol. 263, pp. 411-453, 1968.
- [4] Jones, D. I. G. and Cannon, C. M., "Control of Gas Turbine Stator Blade Vibrations by Means of Enamel Coatings," J. Aircraft, Vol. 12, No. 4, pp. 226-230, April 1975.
- [5] Henderson, J. P. and Drake, M. L., "Investigation of the Effect of Damping Treatment on the Response of Heated Fuselage Structure," Proc. of NOISEXPO 76, National Noise and Vibration Control Conference and Exposition, New York, March 1976.
- [6] Rogers, L. C. and Parin, M. L., "A Thoroughly Engineered Application of Damping Technology to Jet Engine Inlet Guide Vanes," Conf. in Aerospace Polymeric Viscoelastic Damping Technology for the 1980's, AFFDL-TM-78-FBA, July 1978.
- [7] Bogner, F. K. and Soni, M. L., "Finite Element Analysis of Damped Structures," Proc. 22nd Structures, Dynamics, and Materials Conference, April 1981.
- [8] Soni, M. L., "Finite Element Analysis of Viscoelastically Damped Sandwich Structures," Shock and Vibration Bulletin, 51, pp. 97-108, May 1981.

#### DISCUSSION

Voice: Where did you get your viscoelastic properties from? Were they assumed?

Mr. Kluesener: We do a lot of testing on the viscoelastic properties of materials at the University of Dayton, so we get them from our data bank. We used a reduced temperature nomogram for the material.

Mr. Glazer (Rockwell International): The first model that you analyzed was a panel; did you run an acoustic test to verify your analysis?

Mr. Kluesener: No, we didn't. We used some test results to use that assumed loss factor. We had some test data that said the undamped loss factor was about .006. That is where we got the assumed inherent damping from. We didn't compare the predicted stress to a test.

# DETERMINATION OF NORMAL MODES FROM MEASURED COMPLEX MODES

S. R. Ibrahim  
Department of Mechanical Engineering and Mechanics  
Old Dominion University  
Norfolk, VA 23508

## ABSTRACT

A technique is presented to compute a set of normal modes from a set of measured complex modes. The number of elements in the modal vectors, which is equal to the number of measurements, can be larger than the number of modes under consideration. It is also shown in this paper that the practice of normal mode approximation to complex modes can lead to very large errors when the modes are too complex. A numerical example and a simulated experiment are presented to illustrate the concepts discussed and to support the theory presented.

## NOMENCLATURE

- [C] : Damping matrix.
- [c] : Modal damping matrix (diagonal).
- f : Frequency in Hz.
- $I_j$  : Imaginary part of the  $j$ th element of a complex modal vector.
- [K] : Stiffness matrix.
- [k] : Modal stiffness matrix (diagonal).
- [M] : Mass matrix.
- [m] : Modal mass matrix (diagonal).
- $R_j$  : Real part of the  $j$ th element of a complex modal vector.
- $\alpha_1, \alpha_2$  : Two angles defining sign ( $\pm$ ) boundaries for the approximated normal mode elements.
- $\beta_j$  : Phase angle of the  $j$ th element of a modal vector ( $0.0^\circ$  or  $180.0^\circ$ ).
- $\theta_j$  : Phase angle of the  $j$ th element of a complex modal vector.
- $\phi_j$  :  $j$ th element of the normal modal vector.
- $\{\phi\}_j$  :  $j$ th normal modal vector.
- $\phi_j$  :  $j$ th element of the complex modal vector.
- $\{\phi\}_j$  :  $j$ th complex modal vector.

$\lambda_j$  :  $j$ th characteristic root.

$\omega$  : Natural frequency (rad/sec.).

$\xi$  : Damping factor.

[ ]<sup>T</sup> : Transpose of a matrix.

[ ]<sup>-1</sup> : Inverse of a matrix.

## INTRODUCTION AND BACKGROUND

Modal vibration tests are carried out to experimentally determine a set of modal parameters for the structure under test. These modal parameters are usually used to verify, determine or improve some analytical model of the structure, [1-8].

Most of the approaches that use experimentally determined modal parameters for dynamic modeling of structures use one or more of the following equations:

$$[M]^{-1}[K]\{\phi\} = \omega^2\{\phi\} \quad (1)$$

$$\{\phi\}^T[M]\{\phi\} = [m] \quad (2)$$

$$\{\phi\}^T[K]\{\phi\} = [k] \quad (3)$$

$$\{\phi\}^T[C]\{\phi\} = [c] \quad (4)$$

In all these equations,  $\{\phi\}$ 's are the normal modes even though, in practice, the measured modes are the complex modes, which in some cases can be very different from normal modes. As a matter of fact, in vibration testing and analysis work it is frequently assumed that damping levels are very small and/or the damping matrix is proportional to either the mass or stiffness matrices, an assumption that is not valid for many of today's structures. Such assumptions and the lack of differentiation between normal and complex modes may be attributed to the lack of a tool to measure or compute the normal modes.

With the introduction of computer technology to modal identification in the early seventies, in both frequency domain [9,10] and time domain [11-15] techniques, the question of normal versus complex modes started to persist for answers. In frequency domain approaches, even with light damping and well spaced modes, users frequently encountered a scatter of the phase angles associated with the measured modal vector, [12]. Some researchers and users even went to the extent of questioning the test and data analysis procedures when the phase angles were not within  $\pm 10^\circ$  from  $0.0^\circ$  or  $180.0^\circ$ .

In some cases, the scatter of the phase angles of the modal vectors was due to the fact that the damping is nonproportional, and hence the mode shapes are complex. Time domain approaches to modal identification, which contains no assumptions regarding the level or proportionality of damping, also indicated that structures, in many cases, possess complex modes.

#### Normal Mode Approximation to Complex Modes

Normal modes are defined as modal vectors whose phase angles are either  $0.0^\circ$  or  $180.0^\circ$ . Such modes exist for extremely simple structures, that do not need any testing anyway. They also exist for structures with no damping or structures tailored with proportional damping, none of which represents today's complex structures.

Unlike normal modes, complex modes may possess any phase angle distribution. Each element of the modal vector is described by a real and imaginary part of an amplitude and phase angle relative to the arbitrary element. A scatter in the phase angles of as much as  $\pm 90.0^\circ$  from  $0.0^\circ$  or  $180.0^\circ$  is not uncommon.

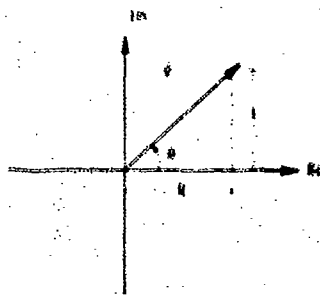
Recognizing the phase angle scatter for measured (complex) modes, and the need for normal modes for use in equations such as (1), (2), (3) and (4), researchers and users have frequently used normal modes approximation to complex modes.

Figure 1 (a) shows an element of a complex modal vector  $\psi_j$ , which is complex and can be expressed as:

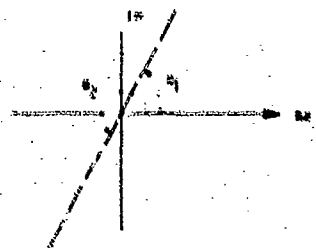
$$\psi_j = R_j + iI_j \quad (5)$$

The approximate normal mode element  $\phi_j$  corresponding to  $\psi_j$  is:

$$\phi_j = \pm \sqrt{R_j^2 + I_j^2} \quad (6-a)$$



(a) Complex modal element



(b) Approximates to complex modal element

Fig. 1 - Normal mode approximation to complex modes

where the assignment of a positive or negative sign which is equivalent to  $0.0^\circ$  or  $180.0^\circ$  phase angle, depends on the angle  $\theta_j (\theta_j = \tan^{-1} I_j / R_j)$  of the complex modal element and its relation to some arbitrary angles  $\alpha_1$  and  $\alpha_2$  as shown in Figure 1 (b). In other words, the phase angle  $\beta_j$  for the approximated normal mode element  $\phi_j$  is assigned according to the equations:

$$\beta_j = 0.0^\circ \quad \alpha_2 < \theta_j < \alpha_1 \quad (6-b)$$

$$\beta_j = 180.0^\circ \quad \alpha_1 < \theta_j < \alpha_2 \quad (6-c)$$

It is enough to state that, irrespective of the choice of  $\alpha_1$  and  $\alpha_2$ , it is unacceptable to assign two different signs to two elements of the approximated normal modal vector because the phase angles of the corresponding elements of the complex modal vector differ by a fraction of a degree.

Such approximation can lead to erroneous and misleading results and conclusions. An example is the orthogonality check where the orthogonality of the measured modes with respect to the mass matrix is tested. Large off-diagonal terms may result not only because of errors in the mass matrix or inaccuracies in the identification process, but because of the normal mode approximation to complex modes.

#### NUMERICAL EXAMPLE

The purpose of this example is to show that even though all the parameters used are exact:

1. Complex modes can be very different from normal modes, even for lightly damped modes and small nonproportionality in the damping matrix.
2. Large errors may result from assuming that normal modes approximated from complex modes are orthogonal with respect to the mass matrix.

The system used in this example is a ten degree-of-freedom system. This system was constructed (simulated) by analytically generating ten normal modes at ten measurement stations of a simply supported beam, ten undamped natural frequencies and a stiffness matrix for the system. The natural frequencies were selected corresponding to 10.0, 12.0, 15.0, 20.0, 24.0, 30.0, 36.0, 43.0, 46.0 and 50.0 Hz. Then, a proportional damping matrix (equivalent to 1.0% modal damping factor for all the ten modes) and the mass matrix were computed from the assumed information.

To make the damping matrix nonproportional, the damping elements  $C(3,3)$ ,  $C(4,4)$ ,  $C(3,4)$  and  $C(4,3)$  were doubled. Complex modes, damping factors, and damped natural frequencies were computed for the system. Damping factors changed from 1.0% for all modes for proportional damping case to 2.6, 1.3, 1.2, 1.2, 1.1, 1.8, 2.9, 3.8, 1.7, and 1.0 percent for the nonproportional damping case. These damping factors are relatively small but nevertheless, some modes showed high levels of complexity. Table 1 shows the two most complex mode shapes, modes 9 and 10, listed with the corresponding normal modes. Phase angles of as much as  $98.9^\circ$  and  $74.8^\circ$  for modes 9 and 10 are noticed respectively. Also large differences in amplitudes exist between normal and complex modes.

To illustrate the large errors that may result from normal modes approximation to complex modes, approximated normal modes were used in checking their orthogonality with

Table 1 — Comparison of Theoretical Complex and Normal Modes

9 <sup>th</sup> MOD			10 <sup>th</sup> MOD		
NORMAL	COMPLEX		NORMAL	COMPLEX	
$\zeta = 0.0\% \quad f = 46.00 \text{ Hz}$	$\zeta = 1.75\% \quad f = 45.83 \text{ Hz}$		$\zeta = 0.0\% \quad f = 50.00 \text{ Hz}$	$\zeta = 1.02\% \quad f = 49.99 \text{ Hz}$	
$\pm \text{AMPL.}$	AMPL.	PHASE	$\pm \text{AMPL.}$	AMPL.	PHASE
100.00	100.00	0.0	100.00	100.00	0.0
26.00	53.27	64.3	-56.00	57.95	175.1
-136.00	144.46	-155.5	-0.00	9.94	-72.9
168.00	167.74	-0.3	56.00	54.65	7.3
-98.00	144.19	136.7	-100.00	102.48	176.0
-26.00	113.55	-98.9	114.00	119.47	7.9
136.00	135.26	3.3	-98.00	102.24	172.3
-168.00	220.22	143.3	56.00	55.70	0.3
98.00	187.99	-54.8	-0.00	9.73	-74.6
26.00	36.38	48.7	-56.00	58.25	172.9

respect to the exact mass matrix. The results are shown in Figures 2(a) and 2(b) for different values of  $\alpha_1$  and  $\alpha_2$ . In Figure 2(a),  $\alpha_1$  and  $\alpha_2$  were chosen as  $90^\circ$  and  $270^\circ$ , while in Figure 2(b), they are  $135^\circ$  and  $315^\circ$ . Errors in the offdiagonal terms are as high as 23.29% for the first case and 35.49% for the second case.

#### THEORY: COMPUTATION OF NORMAL MODES FROM COMPLEX MODES

In this section, two approaches are presented to compute normal modes from a measured set of complex modes. The required data are a set of modal parameters such as may be identified from a modal survey test. These modal parameters are namely a set of complex modes  $\{\psi\}_i, i = 1, \dots, m$  and a set of corresponding characteristic roots  $\lambda_i, i = 1, \dots, m$  (and their complex conjugates). The modal vectors have  $n$  elements

where  $n > m$ , which is a typical test situation. To compute the normal modes from this given set of complex modes, one of the following two approaches may be used.

##### Approach 1. Using an Oversized Mathematical Model

From the given modal parameters, displacement velocity and acceleration responses are formed according to the equations:

$$\{x(t)\} = \sum_{i=1}^{2m} \{\psi\}_i e^{\lambda_i t} + \{n_1(t)\} \quad (7-a)$$

$$\{\dot{x}(t)\} = \sum_{i=1}^{2m} \lambda_i \{\psi\}_i e^{\lambda_i t} + \{n_2(t)\} \quad (7-b)$$

$$\{\ddot{x}(t)\} = \sum_{i=1}^{2m} \lambda_i^2 \{\psi\}_i e^{\lambda_i t} + \{n_3(t)\} \quad (7-c)$$

where  $n_1(t), n_2(t), n_3(t)$  are added random noise of uniform distribution. These responses are then used in the state vector equation:

$$\begin{Bmatrix} \dot{x}(t) \\ \ddot{x}(t) \end{Bmatrix} = \begin{bmatrix} 0 & I \\ -M^{-1}K & -M^{-1}C \end{bmatrix} \begin{Bmatrix} x(t) \\ \dot{x}(t) \end{Bmatrix} \quad (7)$$

or

$$\{\dot{X}\} = [A]\{X\} \quad (8)$$

where  $\{X\}$  and  $\{\dot{X}\}$  contain responses measured at  $2n$  time instants. From equation (8), the  $[A]$  matrix can be identified as:

$$[A] = \{\dot{X}\} \{X\}^{-1} \quad (9)$$

Naturally, without any noise, the matrix  $\{X\}$  is singular since the number of degrees-of-freedom is larger than the number of modes present in the responses. A small amount of noise makes the inversion of  $\{X\}$  possible, for the purpose of extracting modal information. For example, noise to signal ratios of as little as 0.00001 were used, [14], to invert a  $600 \times 600$  matrix of a rank of 4 without signs of ill-conditioning on a 60-bit word computer. Higher levels of noise may be needed for computers with less accuracy.

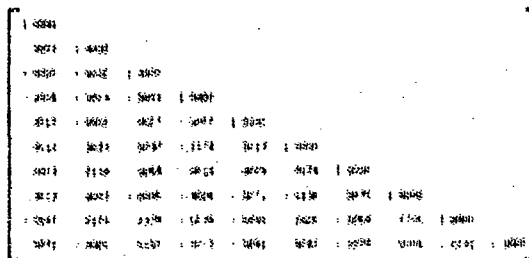


Fig. 2(a) — Orthogonality check using approximated complex modes ( $\alpha_1 = 90^\circ, \alpha_2 = 270^\circ$ )

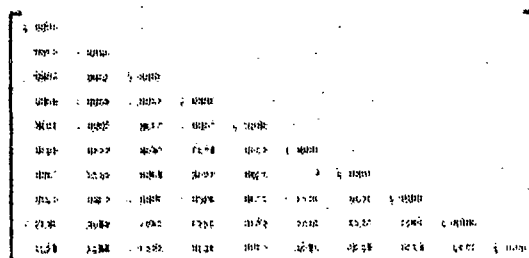


Fig. 2(b) — Orthogonality check using approximated complex modes ( $\alpha_1 = 135^\circ, \alpha_2 = 315^\circ$ )

By computing matrix  $[A]$ , the  $[M^{-1}K]$  matrix gives normal modes according to the eigenvalue equation:

$$[M^{-1}K] \phi = \omega^2 \phi \quad (10)$$

#### Approach 2. Using Assumed Modes

The given set of complex modal parameters satisfy the equation:

$$[M^{-1}K \ M^{-1}C] \begin{Bmatrix} \psi_i \\ \lambda_i \psi_i \end{Bmatrix} = \{-\lambda_i^2 \psi_i\} \quad (i = 1, \dots, m) \quad (11)$$

Since we only have  $m$  modes and the system has  $n$  degrees of freedom, equation (11) cannot be solved for  $[M^{-1}K \ M^{-1}C]$ . Let us assume that there exists a set of vectors  $\{P_j\}$  and a set of characteristic roots  $s_j$ ,  $j = m + 1, m + 2, \dots, n$ . This set of assumed parameters are selected such that:

$$\lambda_i \neq s_j \quad (12-a)$$

$$\{P\}_j \neq [\psi_1 \psi_2 \dots \psi_m] \{a\} \quad (12-b)$$

where  $\{a\}$  is any vector of coefficients. The second equation (12-b) implies that  $\{P\}_j$  and  $\{\psi\}_i$  for all  $i$ 's and  $j$ 's form a linearly independent set of vectors. In such a case, it can be written that

$$[M^{-1}K \ M^{-1}C] \begin{Bmatrix} P_j \\ s_j^2 P_j \end{Bmatrix} = \{-s_j^2 P_j\} \quad (j = m + 1, m + 2, \dots, n) \quad (13)$$

and equations (11) and (13) can be solved for  $[M^{-1}K \ M^{-1}C]$  from which normal modes are computed according to equation (10).

It is extremely important to point out that  $[M^{-1}K]$  and  $[M^{-1}C]$  obtained from either approach are not unique since they are functions of the introduced noise of the assumed modes. However the set of normal modes, corresponding to the set of given complex modes, was found to be independent of the introduced small levels of noise or the assumed modes, [14].

#### SIMULATED EXPERIMENT

To test the validity of the theories presented in this paper, the ten degrees-of-freedom system previously discussed in the section "NUMERICAL EXAMPLE" is used here as a simulated test structure. Response time histories containing contributions from the last four modes measured at the ten stations were generated. The last four modes were selected because the last two modes show a high level of complexity. Simulated measurement noise was added to these responses, with a noise/signal r.m.s. ratio of 20%, to represent conditions in a real test. From these responses, the complex modes and characteristic roots were identified, using the time domain approach [11]. Normal modes were computed using the two approaches presented here. The assumed modes approach produced results identical to those of the oversized math model approach.

Table 2-A and 2-B list the identified complex modes and the computed normal modes for the last two modes. A close examination of the computed normal modes, in comparison with the theoretical ones, indicate the validity of the approaches presented.

Table 2-A — Identified Complex Mode and Normal Mode  
(Mode No. 9)

THEORETICAL			IDENTIFIED		
NORMAL	COMPLEX		NORMAL	COMPLEX	
$\zeta = 0.05 \quad f = 46.0 \text{ Hz}$	$\zeta = 1.755 \quad f = 45.8 \text{ Hz}$		$\zeta = 0.05 \quad f = 46.0 \text{ Hz}$	$\zeta = 2.65 \quad f = 45.93 \text{ Hz}$	
AMPL.	AMPL.	PHAS.	AMPL.	AMPL.	PHAS.
100.00	100.00	0.0	100.00	100.00	0.0
25.0	53.27	64.3	25.18	64.93	59.0
-136.00	144.46	-155.5	-136.76	152.62	-154.0
168.00	167.75	-0.3	170.00	164.89	-2.2
-98.00	144.19	136.7	-97.65	135.86	132.6
-24.00	113.55	-98.9	-36.95	107.75	-129.2
136.00	125.26	3.3	145.63	140.38	-0.3
-164.00	222.22	143.1	-167.51	202.69	143.7
98.00	109.09	-54.8	94.81	164.94	-54.7
25.00	36.38	48.7	28.32	36.51	47.5

Table 2-B — Identified Complex Mode and Normal Mode  
(Mode No. 10)

THEORETICAL			IDENTIFIED		
NORMAL	COMPLEX		NORMAL	COMPLEX	
$\zeta = 0.05 \quad f = 50.0 \text{ Hz}$	$\zeta = 1.041 \quad f = 50.0 \text{ Hz}$		$\zeta = 0.05 \quad f = 50.0 \text{ Hz}$	$\zeta = 1.748 \quad f = 50.0 \text{ Hz}$	
AMPL.	AMPL.	PHAS.	AMPL.	AMPL.	PHAS.
100.00	100.00	0.0	100.00	100.00	0.0
-55.00	57.95	175.1	-5.07	57.27	170.7
3.0	9.94	-72.9	0.39	13.54	-74.4
56.00	54.85	7.3	54.08	53.19	8.4
-101.00	102.48	174.0	-94.95	97.74	175.6
114.00	119.61	-7.9	129.92	118.18	-9.6
-93.00	107.24	172.3	-95.82	94.78	171.5
54.00	55.70	0.3	53.42	58.61	-1.1
-0.00	9.71	-74.8	-0.44	4.61	-48.1
-54.00	58.77	173.0	-54.36	57.71	170.9

Figure 3 shows the orthogonality check matrices. In Figures 3(a) and 3(b), approximated normal modes were used with  $(90^\circ, 270^\circ)$  and  $(135^\circ, 315^\circ)$  for  $(\alpha_1, \alpha_2)$  respectively. In Figure 3(c) the computed normal modes were used. Errors of 21% and 48% are noticed in the off-diagonal terms for cases a and b respectively, while the error for case c was only 5%.

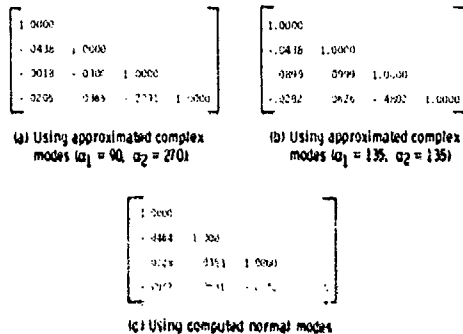


Fig. 3 - Orthogonality check matrix using identified modes

## CONCLUSIONS

It is shown in this paper that even for low levels of damping for structures with nonproportional damping, complex modes can be very different from normal modes. In such cases, normal mode approximation to complex modes may lead to large errors in orthogonality checks or in any use of these approximated modes as normal modes.

A technique is presented to compute normal modes from measured complex modes. Computed normal modes eliminate any errors that may result from using normal mode approximation to complex modes produced by non-proportional damping.

## ACKNOWLEDGEMENT

This work was partially supported by a grant from NASA's Langley Research Center.

## REFERENCES

1. Young, J. P. and Oh, F. J.: "Mathematical Modeling Via Direct Use of Vibration Data." SAE National Aeronautic and Space Engineering and Manufacturing Meeting, Los Angeles, California, Oct. 1969.

2. Thoren, A. R.: "Derivation of Mass and Stiffness Matrices from Dynamic Test Data." AIAA/ASME/SAE 13th SDM Conference, San Antonio, Texas, April 1972.
3. Berman, A.: "System Identification of a Complex Structure." AIAA/ASME/SAE 16th SDM Conference, Denver, Colorado, May 1975.
4. Potter, R. and Richardson, M.: "Mass Stiffness and Damping Matrices from Measured Modal Parameters." International Instrumentation - Automation Conference, New York, October 1974.
5. Berman, A.: "Mass Matrix Correction Using an Incomplete Set of Measured Modes." AIAA J., Vol. 17, No. 10, October 1979.
6. Chen, J. C. and Garba, J. A.: "Matrix Perturbation for Analytical Model Improvement." AIAA/ASME/ASCE/AHS 20th SDM Conference, St. Louis, Mo., April 1979, Paper No. 79-0831.
7. Easuck, M.: "Optimization Procedure to Correct Stiffness and Flexibility Matrices Using Vibration Tests." AIAA J., Vol. 16, No. 4, April 1978.
8. Berman, A., Wei, F. S. and Rao, K. W.: "Improvement of Analytical Models Using Modal Test Data." AIAA/ASME/ASCE/AHS 21st SDM Conference, Seattle, Washington, May 1980, Paper No. 80-800.
9. Klosterman, A. and Zimmerman, R.: "Modal Survey Activity Via Frequency Response Functions." SAE Paper 751068, 1975.
10. Brown, D. L., Allemang, R. J., Zimmerman, R., and Mergeay, M.: "Parameter Estimation Techniques for Modal Analysis." SAE Paper 790221, Feb. 1979.
11. Ibrahim, S. R. and Mikulek, E. C.: "A Method for the Direct Identification of Vibration Parameters from the Free Response." Shock and Vibration Bulletin 47(4): 47(4):183-198, Sept. 1977.
12. Hanks, B. R., Miserentino, R., Ibrahim, S. R., Lee, S. H., and Wada, B. K.: "Comparison of Modal Test Methods on the Voyager Payload." SAE Paper 781044, Nov. 1978.
13. Pappa, R. S. and Ibrahim, S. R.: "A Parametric Study of Ibrahim Time Domain Modal Identification Technique." Shock and Vibration Bulletin 51, June 1981.
14. Ibrahim, S. R. and Pappa, R. S.: "Large Modal Survey Testing Using the Ibrahim Time Domain (ITD) Identification Technique." AIAA Paper 81-0523-CP.
15. Andrew, L. V.: "An Automated Application of Ibrahim's Time Domain Method to Responses of the Space Shuttle." AIAA Paper 81-0528-CP.

## THE EFFECT OF JOINT PROPERTIES ON THE VIBRATIONS OF TIMOSHENKO FRAMES

I. Yaghmai

Department of Mechanical Engineering  
Sharif University of Technology  
Tehran, Iran

and

D. A. Frohrib

Department of Mechanical Engineering  
University of Minnesota  
Minneapolis, Minnesota 55455

Mechanical support fixtures comprised of short beams and joints have natural frequencies which may differ appreciably from predictions based on slender beam theory and which neglect joint properties. This paper presents information on the role of Timoshenko effects and joining properties on the first several natural frequencies of frame structures. The interaction between these properties and the number of vertical bays of the structure is also portrayed.

### INTRODUCTION

Frame structures are regularly used to support equipment in a vibrational environment, such as shock and vibration test stands and rotary equipment mountings. As resonant-free supports are desired in such settings, compact structures composed of stiff beams tend to be used. Then, the size of the joints and short beam effects play important roles in the natural frequencies of the frame.

Frames are typically constructed of standard beam members fabricated with welded, riveted, or bolted joints, which represent flexible arrays; often, their size is not small compared to the length of the members of which they are constructed.

This paper presents information on the vibration of plane rectangular frame structures with flexible joints. Because there is interest in a large spectrum of natural frequencies for supporting structures, the beams and columns were retained as distributed parameter models represented by Timoshenko Beam Theory (1). Joints are modelled as end connections with both axial and bending/shear flexibility, and with geometric size.

The deformation of joints connecting structural members has been studied, primarily using experimental methods (2-11). Joint flexibility can have significant effects on internal forces and moments within the structure and hence, on its natural frequency, as demonstrated by Lionberger, et al. (12), who studied

only joint effects in slender beam structures, using lumped mass models.

In this paper, joints are considered as independent structural elements with mass, geometric size, and flexibility. Joint deformation is characterized as a sum of rotational and translational components as described by Fielding (13), Figure 1. Five types of planar joint displacement and deformation are included:

- 1) rigid body rotation,
- 2) rigid body translation,
- 3) bending deformation,
- 4) shear deformation,
- 5) axial deformation.

To place the combined effects of short beams and joints in the context of application, the effect of the number of bays, or vertically-connected cells, of the frame was included in the prediction of natural frequencies. These correlations are valuable when automated procedures, such as finite element methods, are used to determine natural frequencies, as the role of joint properties can then be understood when modelling the structure.

### MATHEMATICAL REPRESENTATION

As vibrational amplitudes are regarded as small, static and dynamic coupling, and coupling between transverse and longitudinal beam vibration in the continuum equations are neglected. However, transverse and longitudinal coupling occurs through the boundary conditions, or joints.

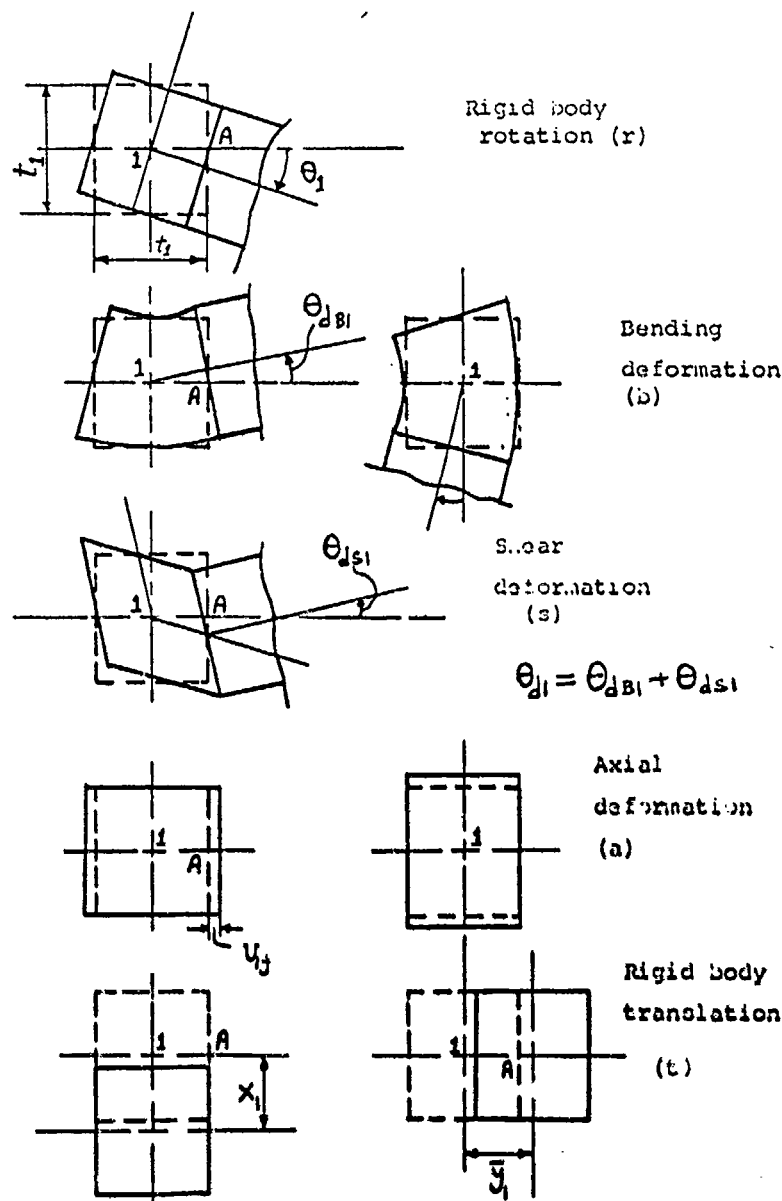


Figure 1: Joint Deformations and Displacements

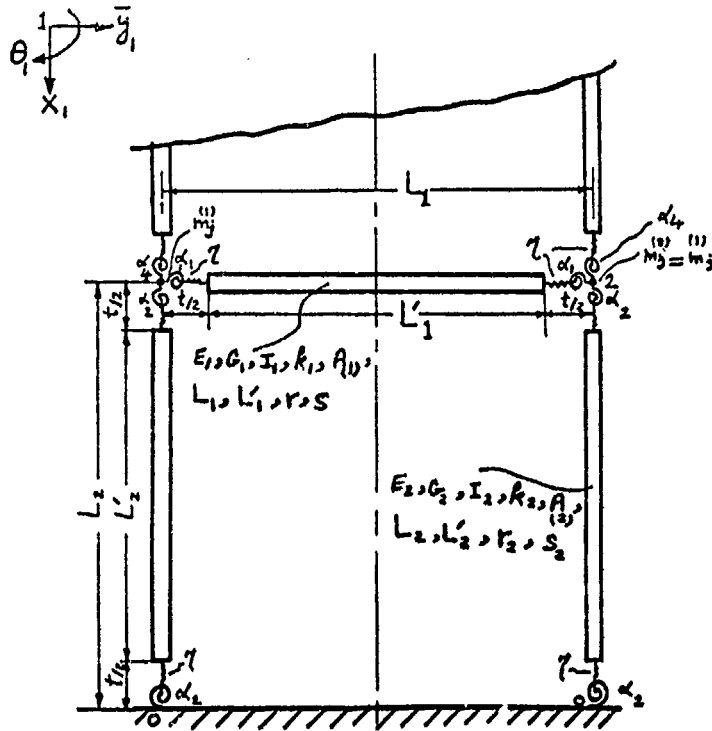
The mathematical frame model composed of Timoshenko beams and inertial/flexible joints, is described in Figure 2. Joint inertia ( $m_j$ ), axial stiffness ( $k$ ), and combined bending and shear stiffness ( $k_s$ ) are included. Joint size is included by beam length ( $L'$ ) of size less than center-to-center joint length ( $L$ ). The solution is formulated by applying the method of Wang and Kinsman 14, where dynamic moment and shear slope-deflection equations were developed for Timoshenko beams with rigid ends. The non-dimensionalized forms of the equations are:

$$\frac{d^4 y}{d \zeta^4} + b^2(r^2 + s^2) \frac{d^2 y}{d \zeta^2}$$

$$- b^2(1 - b^2 r^2 s^2) y =$$

$$(1 - b^2 r^2 s^2) Q L^4 / EI$$





$$t_1 = t(N_0) = t$$

$$t' = \frac{t}{L_1}$$

Figure 2: General Model of Combined Frame and Joint Properties

$$\frac{d^4 \psi}{ds^4} + b^2 (r^2 + s^2) \frac{d^2 \psi}{ds^2} - b^2 (1 - b^2 r^2 s^2) \psi = 0,$$

$$- b^2 (1 - b^2 r^2 s^2) \psi = 0,$$

where symbols are identified in the nomenclature. The solution of these equations for the boundary conditions described in Figure 1 are lengthy, and are presented by the authors in reference (15). The associated two boundary conditions are:

Rotational:

$$\left( \frac{d\psi}{ds} \right) (0) - \alpha_1 L' \left( \frac{d\psi}{ds} \right) (0) = L' \theta_1$$

$$\left( \frac{d\psi}{ds} \right) (1) + \alpha_2 L' \left( \frac{d\psi}{ds} \right) (1) = L' \theta_2$$

Translational:

$$V(0) - (t_1/2) \alpha_1 \left( \frac{d\psi}{ds} \right) (0) = V_1 + (t_1/2) \theta_1$$

$$V(1) - (t_1/2) \alpha_2 \left( \frac{d\psi}{ds} \right) (1) = V_2 - (t_2/2) \theta_2$$

The axial problem wherein boundary tensions are related to boundary axial motions, can be regarded as an uncoupled problem, as shown in reference (15).

The use of dynamic force-deflection equations implements the solution by permitting dynamic equilibrium equations to be derived which relate beam boundary loads to required joint loads for dynamic equilibrium of the isolated joints. The resulting dynamic equilibrium relationships for deflections of the entire structure of  $N$  bays form a  $3N \times 3N$  tri-diagonal matrix, whose determinant provides the charac-

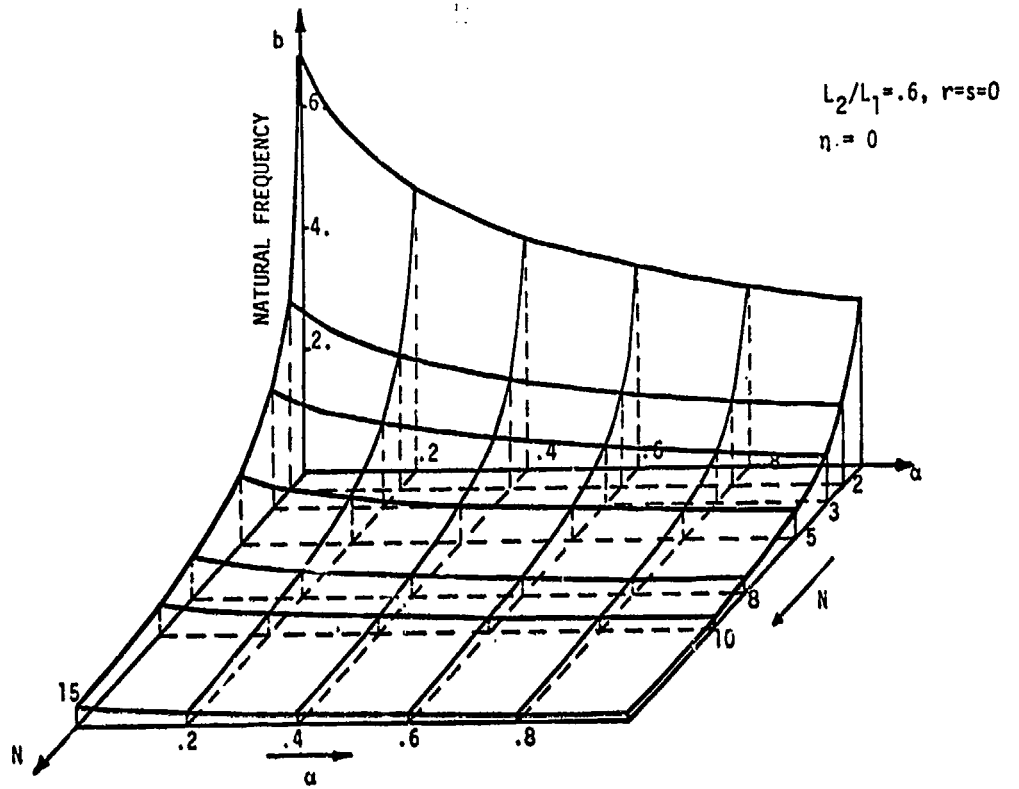


Figure 3: Effect of Joint Flexibility and Number of Stories on Frame Fundamental Frequency

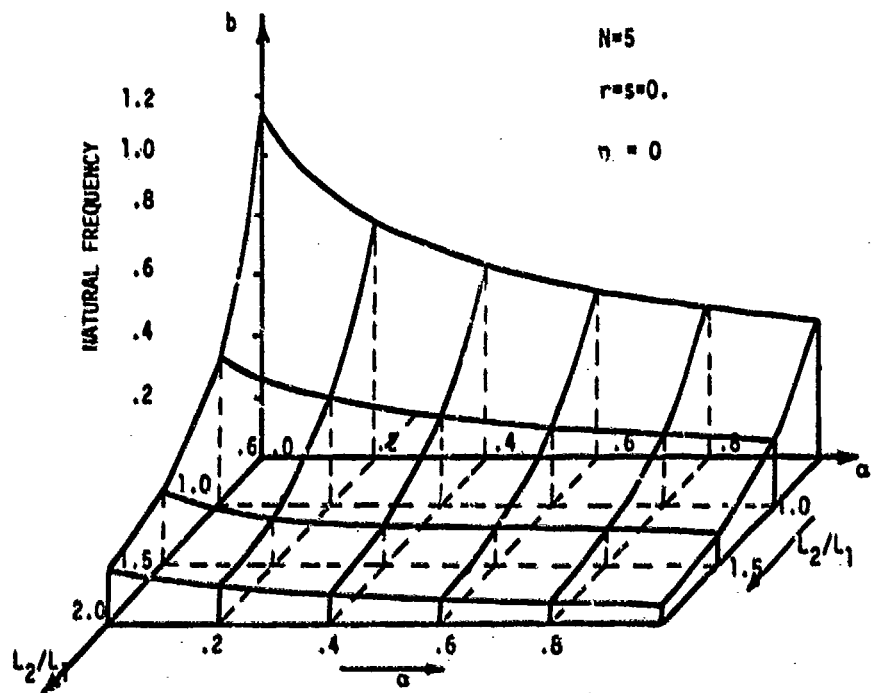


Figure 4: Effect of Joint Flexibility and  $L_2/L_1$  on Frame Fundamental Frequency

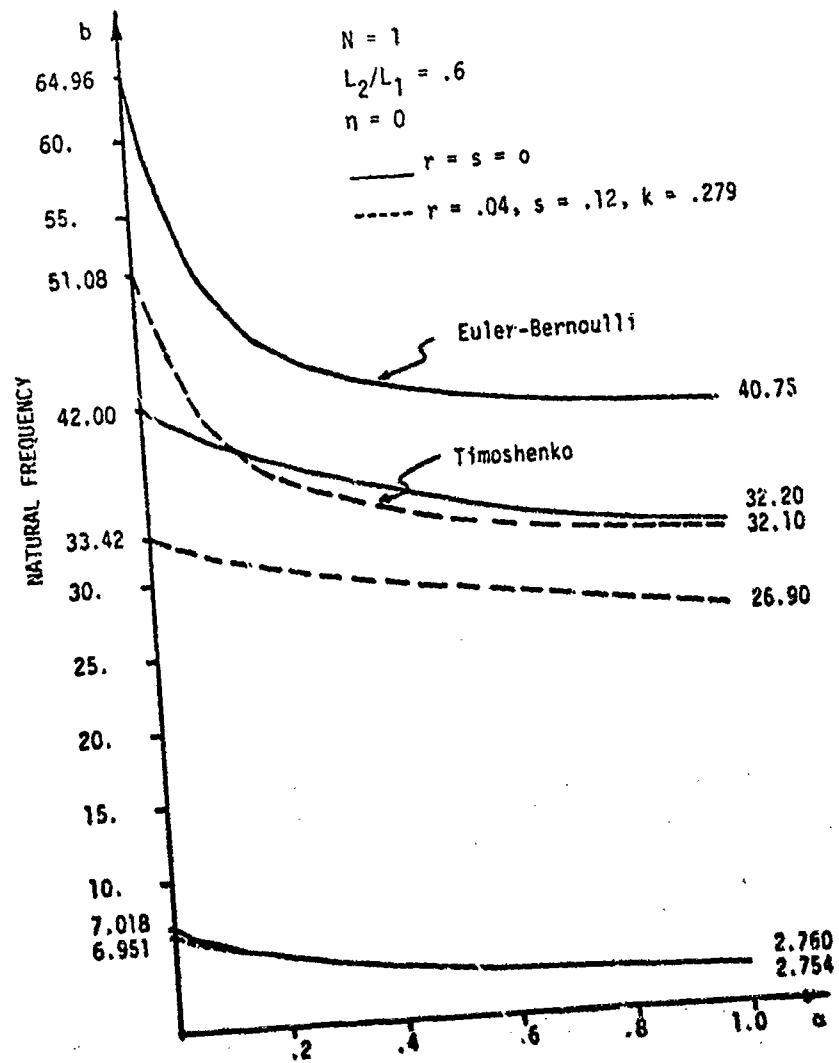


Figure 5: Effect of Rotatory Inertia and Shear Deformation on the Natural Frequencies of a One-Story Frame with Flexible Joints

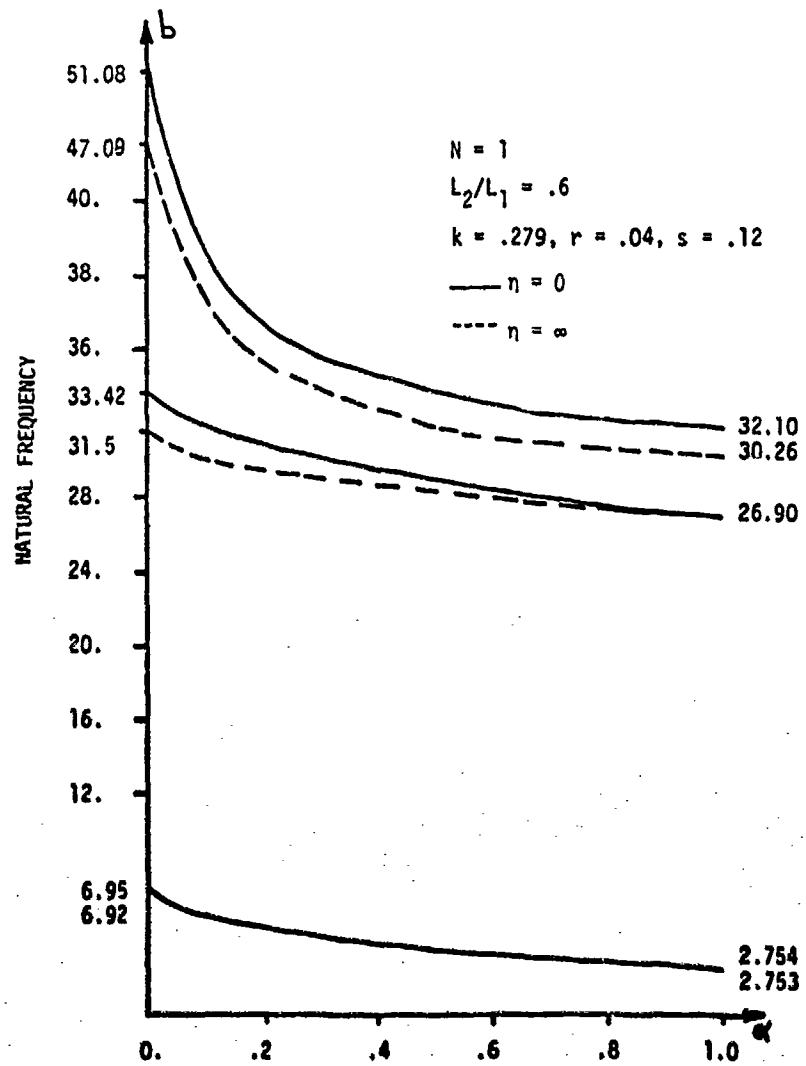


Figure 6: Effect of Axial Deformation of Beams and Columns on Natural Frequencies of a One-Story Frame with Flexible Joints

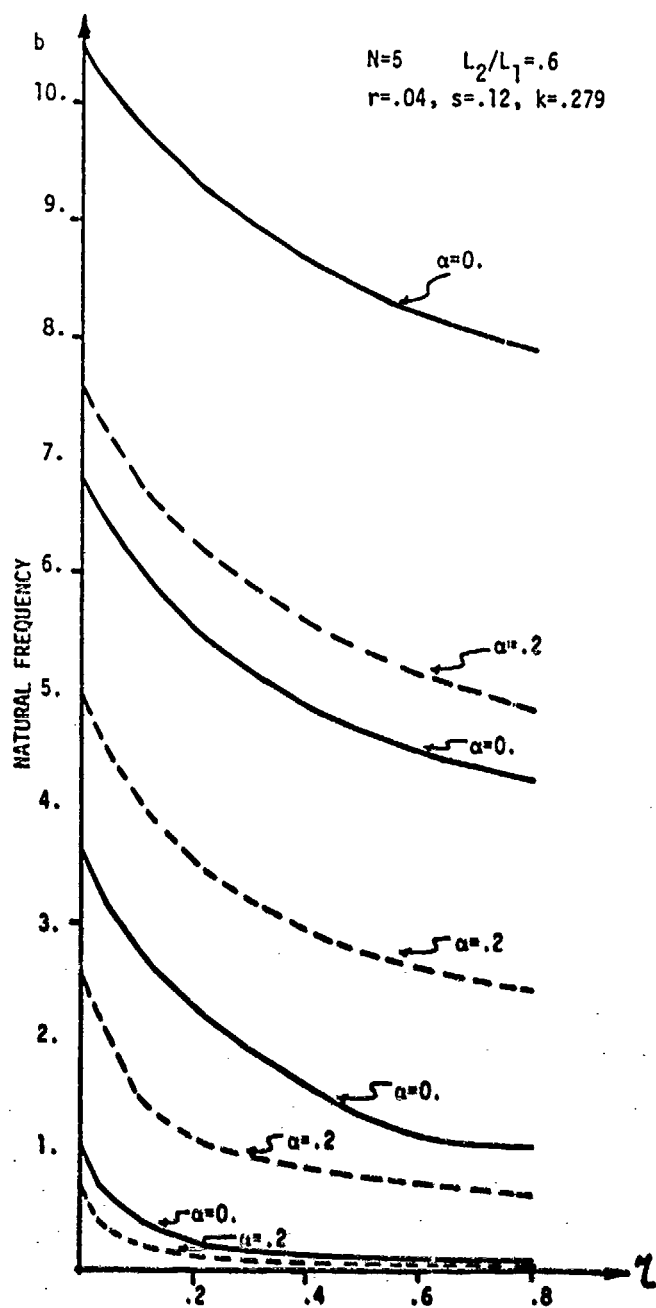


Figure 7: Effect of Axial Flexibility at the Joints on Natural Frequencies of a Five-Story Frame with Rotary Flexible Joints

teristic equation from which natural frequencies are calculated. Computer programs (FREOF2, MODEF2, RESP2, FREQS2) are given in pages 168-192 of reference [15].

## RESULTS AND INTERPRETATION

An initial perspective of the role of joint flexibility on the fundamental natural frequencies of multi-bay structures is provided in Figure 3. There, Timoshenko effects are neglected ( $r = s = 0$ ). As the number of bays (or cells),  $N$ , increases, the role of joint rotary stiffness,  $\alpha$ , becomes of lesser consequence. However, for one or two bays, the role of joint flexibility is a dominant factor. The effects of

slenderness ratio ( $\frac{L}{l}$ ) of the frame bay geo-

metry, interactive with joint flexibility ( $\alpha$ ) are depicted in Figure 4. The fundamental natural frequency is significantly affected by joint stiffness for all slenderness ratios.

Whereas Figures 3 and 4 depict the sensitivity of the fundamental structural natural frequency to bay numbers, joint stiffness, and slenderness geometry for classical slender beams, it is important to understand the relevance of Timoshenko rotary inertia and shear effects on natural frequency. This perspective is supplied by Figures 5 through 7.

Figure 5 illustrates the dramatic effect of flexure parameters on several of the lowest structural natural frequencies of a one-bay frame. Here, axial stiffness is infinite, while joint shear and bending stiffnesses are represented by a common parameter,  $\alpha$ . The departure from slender (Bernoulli-Euler) beam theory is progressively greater as the mode number increases. The second mode, symmetric about the structure's center, demands greater joint relative motion, and consequently at low joint stiffness levels ( $\alpha$ ), that effect is responsible for greater deviation of second natural frequency values for slender and Timoshenko beams.

The role of axial deformation of both joints and beams is depicted in Figure 6. Two extreme cases are graphed: for axially infinitely stiff members ( $\eta = \infty$ ) and for non-existent axial stiffness ( $\eta = 0$ ). Again, the effect of axial stiffness is progressively evident as the mode number increases. In addition, the role of axial stiffness is more pronounced for any mode for infinitely stiff joints in bending ( $\alpha = 0$ ). Under this condition, the compatibility laws relating the kinematics at the joint boundaries demand greater axial motion if joint internal rotary distortion is prevented. Naturally, the structure then becomes more sensitive to axial flexibility, as reflected in the variance between dashed and solid curves for each mode number at  $\alpha = 0$ .

Another important manifestation of axial

flexibility arises as the number of structural bays increases. The combined role of both axial and bending deformation of the joints for such a case is illustrated in Figure 7. Here, as a number of bays ( $N = 5$ ) exists, the mode shapes associated with the higher mode numbers demand progressively more severe relative motions between bays for higher mode numbers. This contrasts with greater curvature within beam members at higher modes of a one-bay frame. Consequently, with several bays, the joints are worked progressively harder as the mode number increases, and the natural frequencies are of pronounced difference for a given mode for two typical values of bending stiffness,  $\alpha$ . These frequencies are somewhat insensitive to axial stiffness for the low modes unless bending stiffness is very high ( $\alpha \rightarrow 0$ ).

## CONCLUSIONS

The role of computational systems to study the dynamic response of multi-degree-of-freedom systems has permitted the analysis of vibratory response inconceivable two decades ago. The quality of answers naturally resides in the decisions introduced in modelling effort which generates inputs to these algorithms. This paper demonstrates that frame-like structures of practical shape have natural frequency properties quite sensitive to end fixity (joint) conditions. Whereas joints may be difficult to model, methods have become available to do so, and deliberate thought should be given to proper characterization of their contributions. The difference between fact and fiction in computer output may rely on adroit effort in this regard.

## NOMENCLATURE

$b$	dimensionless natural frequency; $b^2 = \frac{\omega^2 \alpha A l^4}{E I G}$
$k$	shear coefficient (shape coefficient)
$m_j$	mass of $j^{\text{th}}$ joint
$r$	dimensionless radius of gyration of beam or column cross-section; $r^2 = I/A L^2$
$s$	$\sqrt{E I / (k A G l^2)}$
$t_1, t_2$	joint width, 1, 2.
$x$	position coordinate along beam or column axis
$A$	beam or column cross-sectional area
$E$	modulus of elasticity
$G$	shear modulus
$I$	beam or column cross-sectional moment of inertia

L'	beam or column length exclusive of joints
L	beam or column length, center-to-center of joints
M	moment at a joint
N	number of bays, or cells
Q	external transverse dynamic load/length on beam/column
T	axial force at beam end
$U_{ij}$	axial distortion of joint
$X_1$	vertical translation of joint
$Y_1$	transverse translation of joint
Y	transverse motion of beam or column incremental element
$\alpha$	dimensionless combined bending and shear flexibility of a joints, $\theta_d/M$
$\gamma$	weight per unit volume
n	dimensionless joint axial flexibility = $\frac{UEA}{TL}$
$\theta_1, \theta_2$	rigid body rotation of joints 1, 2
$\theta_{dB}$	relative bending distortion angle
$\theta_{dSN}$	relative shear distortion angle
$\theta_d$	relative distortion angle = $\theta_{dSN} + \theta_{dB}$
$\zeta$	$X/L'$
$\omega$	angular frequency
$\psi$	rotation of beam cross-section

#### BIBLIOGRAPHY

1. Timoshenko, S.; Vibration Problems in Engineering; D. Van Nostrand Company; 1928.
2. Wilson, W. M. and H. F. Moore; Tests to Determine the Rigidity of Riveted Joints of Steel Structures; University of Illinois, Eng. Experiment Station, Bulletin No. 104, Urbana; 1917.
3. Batho, C. and H. C. Rowan; Investigations on Beam and the Stanchion Connections; Second Report, Steel Structures Research Committee, Department of Scientific and Industrial Research of Great Britain, H. M. Stationery Office, London; 1934; pp. 61-139.
4. Batho, C. and S. D. Lash; Further Investigations on Beam and Stanchion Connections; Final Report, Steel Structures Research Committee, Department of Scientific and Industrial Research of Great Britain, H. M. Stationery Office, London; 1936; pp. 276-

- 363.
5. Rathbun, J. C.; "Elastic Properties of Riveted Connections"; ASCE Transactions; 1936; Vol. 101, pp. 524-536.
6. Lyse, I. and G. J. Gibson; "Welded Beam-Column Connections"; Jr. AWS, Vol. 15, No. 10; October 1936; pp. 34-40.
7. Johnston, B. and L. F. Green; "Flexible Welded Angle Connections"; Jr. AWS, Vol. 19, No. 10; October 1940; Welding Research Supplement; pp. 402-408.
8. Johnston, B. and E. H. Mount; "Analysis of Building Frames with Semi-Rigid Connections"; ASCE Transactions, Vol. 107; 1942; pp. 993-1018.
9. Brands, J. L. and R. M. Mains; "Reports of Tests of Welded Top-Plate and Seat Building Connections"; Jr. AWS, Vol. 23; March 1944; Welding Research Supplement; pp. 146-165.
10. Pray, R. F. And C. Jensen; "Welded Top Plate Beam-Column Connections"; Jr. AWS, Vol. 35, No. 7; July 1956; Welding Research Supplement; pp. 338-347.
11. Munse, W. H., W. G. Bell, and E. Chesson; "Behavior of Beam-To-Column Connections"; ASCE Transactions, Vol. 126, Part II; 1961; pp. 729-740.
12. Lionberger, S. R. And W. Weaver; "Dynamic Response of Frames with Nonrigid Connections", Journal of the Engineering Mechanics Division, ASCE; February 1969; pp. 95-113.
13. Fielding, D. J.; Structural Behavior of Welded Beam-To-Column Connections; Ph.D. Thesis; Lehigh University, Bethlehem; 1972.
14. Wang, T. M. and T. A. Kinsman; "Vibrations of Frame Structures According to Timoshenko Theory"; Journal of Sound and Vibration; 1971; 14(2); pp. 215-227.
15. Yaghmai, I. and D. A. Frohrib; "A Sensitivity Analysis of the Effects of Interconnection Joint Size, Flexibility, and Inertia on the Natural Frequencies of Timoshenko Frames"; Journal of Sound and Vibration; 1981; 75(3), pp. 329-346.

## SOIL STRUCTURE INTERACTION AND SOIL MODELS

John M. Ferritto  
Naval Civil Engineering Laboratory  
Port Hueneme, California

### ABSTRACT

Soil-structure interaction effects can significantly alter the computed seismic behavior of a structure. The accurate characterization of the nonlinear soil behavior is important in considering seismic amplification and attenuation. A detailed discussion of soil models, fitting of parameters and comparison of results is presented. A comparison is given of linear and nonlinear example data.

### INTRODUCTION

Soil-structure interaction effects can significantly alter the seismic loading that reaches a structure. This greatly influences the response of the structure. To complicate the problem, the Navy has unique, complex structures such as piers, drydocks, power plants, control towers, and fuel tanks. Advanced techniques for analysis of these structures are of interest. One tool in wide usage is the finite element technique. The finite element method has an advantage over other methods in that structural elements and structures themselves can be easily modeled. However, the semi-infinite soil field has to be modeled by finite soil elements with prescribed boundary conditions. The selection of proper material characterizations of the nonlinear soil behavior is important in considering seismic amplification/attenuation.

Recent earthquakes, particularly those in Alaska, Japan, and Chile, have emphasized the high damage threat the soil liquefaction phenomenon poses to waterfront structures. These experiences have shown that both the nature of waterfront facilities, such as earth-retaining structures, and the depositional environment of the coastal marine soil contribute to major liquefaction damage. A study conducted by the Office of Naval Research (Ref 1) recognized a

major liquefaction hazard existing at West Coast Naval stations. A more recent investigation at the Naval Air Station (NAS) North Island, CA, (Ref 2), concluded that liquefaction under design earthquake levels could result in destruction of such critical structures as aircraft carrier berths, aviation fuel tank farms, and underground utility service lines. Unfortunately, almost all previous studies of the liquefaction problem have been concerned with either conventional building foundations or with analyses of dams, and procedures for analysis are not available for specialized Navy structures.

The effective stress model is of major significance since the Navy must locate in areas where the water table is high. Even if liquefaction (a loss of shear stress from a loss of effective confining stress) does not occur, a buildup of pore pressure is probable both in sands and clays. This pore pressure buildup can be of major significance to structural behavior.

The Navy has a drydock certification program in progress. These structures are examples of situations where a structure is surrounded by soil, often with a high water table. A brief review of certification reports shows that high liquefaction potential, flota-



tion, and floor and wall failures are possible. Drydocks are critical Navy structures; however, present analytical techniques reflect the state-of-the-art as of 1950. Basically, static structural analysis procedures are used with estimates of the soil pressure. The drydock illustrates the significance of the soil-structure interaction. Soil loading causes wall deflections which, in turn, alter the soil load. The effective stress soil model is a critical tool for use on waterfront structures. Dynamic analysis techniques are essential for a realistic assessment of drydock safety. Drydocks are only one application; others include quaywalls, bulkheads, retaining walls, ocean floor structures, etc.

Two points are significant: (1) the Navy needs a dynamic analysis capability to accurately evaluate structural safety of facilities such as drydocks, and (2) presently no such capability exists.

There are procedures in use mainly in support of analysis of nuclear power plants. Codes such as SHAKE or SLAVE are used to compute amplification of vertical shear waves. Material parameters are strain dependent and linear. Two-dimensional programs, such as FLUSH, perform linear strain dependent analysis with quiet boundaries (do not reflect earthquake loading wave). TRI-SAC is a similar code using elastic material properties. TRANAL is a nonlinear finite element code and STEALTH is a finite difference code. None of these considers effective stresses in the soil-structure problem (Ref 3).

The state-of-the-art of soil-structure analysis is limited. The influence of surface features is uncertain. Undulating subsurface layers can create problems in modeling. There is a frequency dependence of response spectra relative to the dynamic properties of the soil. Limitations of the present procedures are becoming more apparent as technology improves. Since ground motion is so dependent on soil filtering, specification of motion levels should be at the surface since bedrock motions are not measured or known with certainty. Horizontal propagation of motion, not considered in most analyses, creates rotational excitations as a result of variation of ground motion across a foundation. The resulting rocking and torsional excitation may increase translations depending upon the phase of the motions. Although three-dimensional techniques have not been used, only three-dimensional techniques can capture radiation damping effects.

The structure resting on a soil field is excited by a dynamic inertial force, resulting in displacements of both. The shaking structure disturbs the ground motion, creating secondary waves. These secondary waves travel through the finite element spatial grid (mesh) and reach a boundary. The boundary is a limitation of the analysis and does not exist in the actual case. The presence of the boundary can cause a reflection of the wave. When linear material properties are used, reflections can be minimized for shear waves by use

of springs and dampers. These then form transmitting boundaries (reducing reflection). The solution of the true soil-structure interaction is obtained by superimposing the free-field solution with the structure-soil solution. If nonlinear soil properties that affect the stiffness and damping are used, superposition is no longer valid. A possible solution to the nonlinear problem is to impose the free-field solution at depths along the boundary. If the boundaries are taken a sufficient distance from the structure, effects can be minimized.

This paper will present results of evaluations of material models and an approach for a soil-structure analysis.

#### COMPARISON OF MATERIAL MODELS

Reference (4) gives an in-depth discussion of the material laws studied presenting significant amount of individual model evaluation, including background development, parameter studies, and fitting procedures. Three models were selected for study:

1. Sandler CAP75 model (Ref 5)
2. Prevost effective stress model (Ref 6)
3. Zienkiewicz LIQU model with Mohr-Coulomb and critical state formulations (Ref 7)

The CAP75 model is a plasticity model defined by a nonsoftening convex yield surface and a plastic strain rate vector that is normal to the yield surface in stress space. The yield surface is defined by means of a failure envelope and a hardening cap.

$$\text{Failure envelope} \quad J_2 = F_F(J_1)$$

$$\text{Cap} \quad J_2 = F_C(J_1)$$

Figure 1 shows the yield surfaces. The failure envelope must be a decreasing function of the  $J_1$  axis to the failure envelope; the yield surface must be continuous.

Within the yield surface the material behavior is isotropic elastic defined by the bulk and shear moduli (Figures 2 and 3), which are of the form:

$$K = K(J_1, k)$$

$$G = G(\sqrt{J_2}, k)$$

The hardening parameter,  $k$ , is defined as the functional of the plastic volumetric strain. The plastic volumetric strain is defined in terms of material parameters  $W$  and  $D$  (Figure 4),

$$c_{xx} P = W \{ \exp [D X(k)] - 1 \}$$

$$\text{where } X(k) = K - R I_p(k)$$

$$X = \text{material parameter}$$

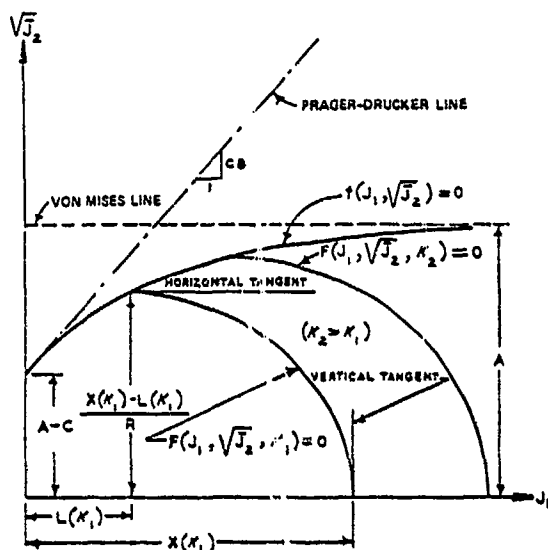


Figure 1. Proposed yield surfaces for the elastic-plastic strain-hardening model.

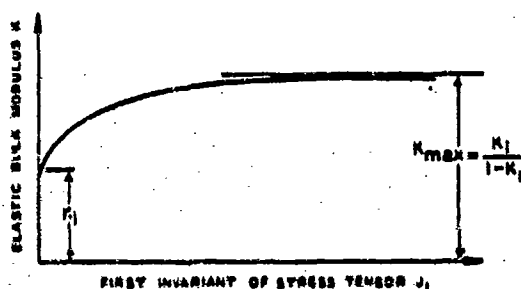


Figure 2. Elastic bulk modulus versus first invariant of the stress tensor.

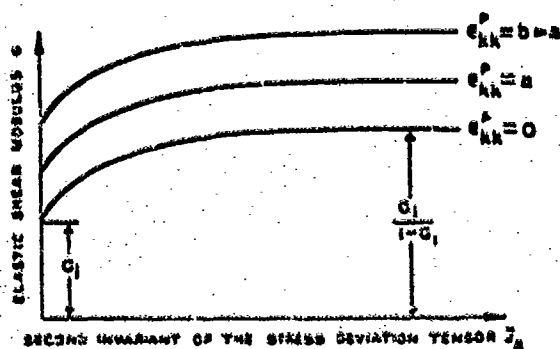


Figure 3. Elastic shear modulus versus second invariant of the stress deviation tensor and plastic volumetric strain.

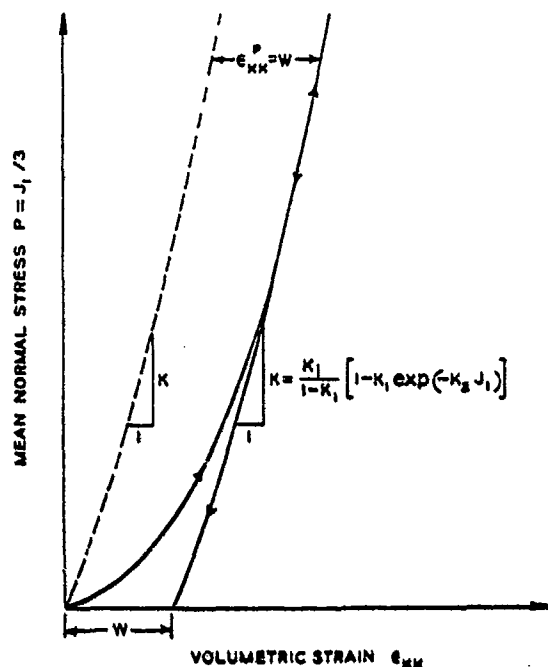


Figure 4. Proposed relationship for isotropic compression test.

The cap is a consequence of the stability requirements and is prevented from acting as a softening yield surface. If dilatancy occurs, the shrinking of the cap is limited to ensure it remains finite. A tension cutoff is included based on hydrostatic stress. The model is a total stress model.

In the Prevost, Figure 5, soil model the soil is viewed as a multiphase medium consisting of an inelastic porous skeleton and viscous fluids. The model is a general analytical model that describes the nonlinear, anisotropic, elasto-plastic, stress and strain dependents, and strength properties of the skeleton when subjected to a three-dimensional loading. Prevost develops the coupled field tensor equations for a saturated soil consisting of a perfect fluid and a piecewise-linear, time-independent porous skeleton where the pore fluid and the solid grains are incompressible. The general formulation of the field equations can be reduced for the following conditions:

1. Undrained
2. Fully drained
3. Fully drained steady state

The elastic and plastic components of deformation are separated and it is assumed the elasticity of the material is isotropic and linear in shear. Shear nonlinearity and anisotropy result from the material's plasticity. The elastic components are related by a generalized Hooke's law in which the shear modulus is

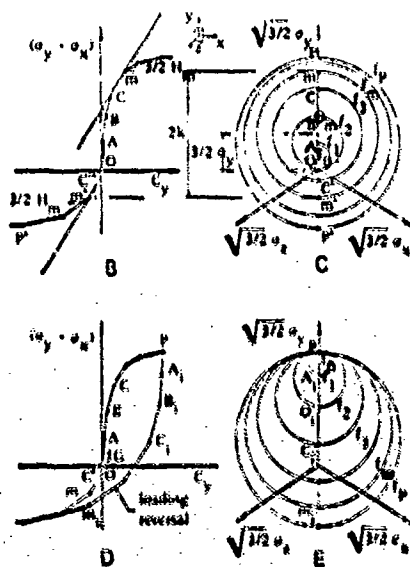
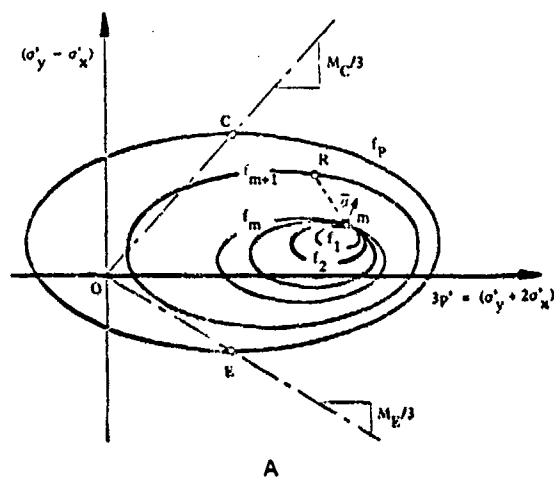


Figure 5. Prevost model.

constant and the bulk modulus is assumed to be a function of the effective mean normal stress. The model uses a series of yield surfaces with a normality flow rule of plasticity. The rule of isotropic plastic hardening is not adequate for soils in general since under unloading and loading reversal it implies elastic behavior exclusively until the stress is fully reversed. Test data show both elastic and plastic deformations occur well before the stress is fully reversed. To account for this combination, isotropic and kinematic plastic hardening rule is used to allow the yield surfaces to be translated in stress space as well as to change in size. The yield surfaces' initial position and size reflect the past stress-strain history. The outermost "boundary" surface is a "volumetric" yield surface whose size, position, and movement are functions of material

density. Points C and E (Figure 5a) define the critical state conditions for triaxial compression and extension and the slopes of lines OC and OE remain constant. An associative flow rule is used on the yield surface,  $f_p$ , to compute plastic strain rate vector components. A plastic modulus is associated with the inner yield surfaces and varies along the yield surface. Projections of the yield surface onto the deviatoric subspace define regions of constant plastic shear moduli. A nonassociative flow rule is used on the yield surface. The plastic deviatoric strain rate vector, however, remains normal to the projection of the yield surface onto the deviatoric subspace. All the yield surfaces may translate in stress space, touch and push each other, but they cannot intersect. When the stress loading point reaches yield surface all the yield surfaces are tangent to each other at the contact point. If a stress rate is then applied such that the stress rate vector points outward, the plastic strain rate vectors are given by the nonassociative flow rule. The yield surfaces translate together and remain together based on the stress path. Overlapping of the yield surfaces is prevented by restricting contact to points only having the same outward normal. The pore pressure is related through the bulk modulus to the plastic potential.

The Zienkiewicz soil model Figures 6, 7 and 8 is formulated in terms of a plasticity model. An elastic limiting yield surface can be formulated in terms of an effective stress tensor and a hardening parameter which is a function of plastic strain. Elastic straining occurs below the yield surface and both elastic and plastic strain occur on the yield surface. The direction of plastic strain is defined by the plastic potential function. A flow rule for plastic strain can be written relating stress to plastic strain. The total, stress-dependent, strain increment can be divided into elastic and plastic parts.

#### MODEL RESULTS

Figures 9a-c present a comparison of the models under triaxial loading with 50 psi consolidation pressure. Test data are taken from references 8, 9 and 10. All models are satisfactory in evaluating both shear and volumetric loading. The Prevost model gives the best fit to the experimental data. The calculation was repeated for a triaxial loading with 100 psi consolidation pressure. Data for the CAP75 and OCZ models are used directly, only changing the consolidation pressure. Data for the Prevost model are scaled by a technique discussed in reference 4. Performance of the models was similar to the previous test results.

Using the drained isotropic material properties, undrained tests were simulated using the Zienkiewicz critical state model and the Prevost model. Results are shown in Figure 10 for different consolidations. Both tests exhibit good agreement in stress-strain

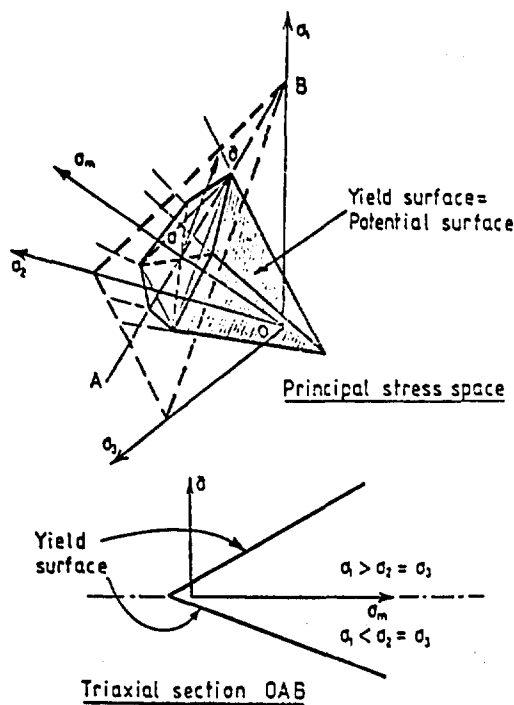


Figure 6. The Mohr-Coulomb failure surface in principal stress space representing the yield surface of an associated plastic model (Model A).

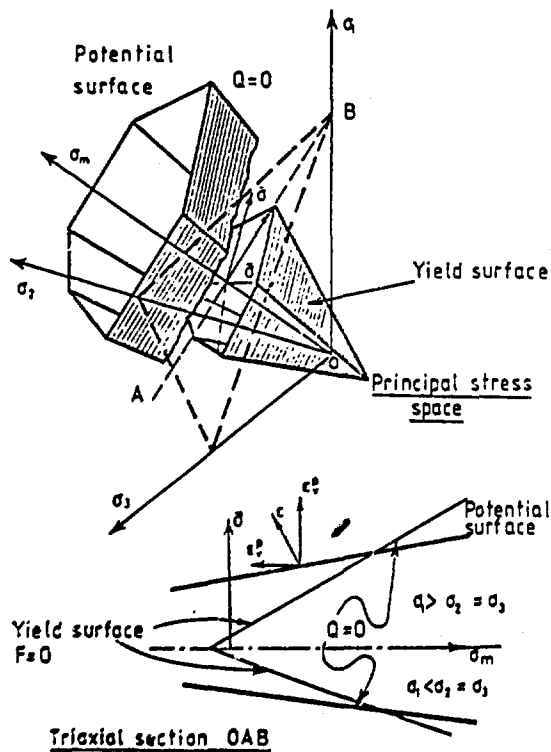


Figure 7. A non-associated ideal plastic model with potential and yield surfaces of similar, Mohr-Coulomb, form (Model B).

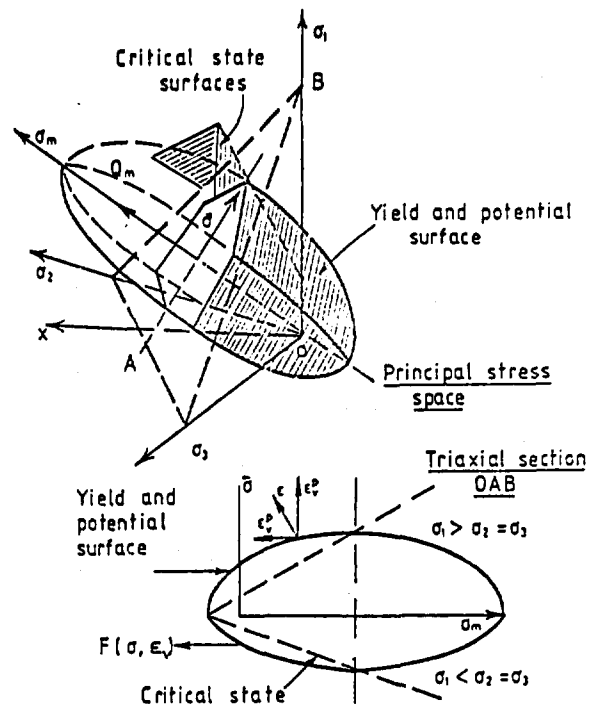


Figure 8. The critical state model (with a Mohr-Coulomb critical surface) (Model C).

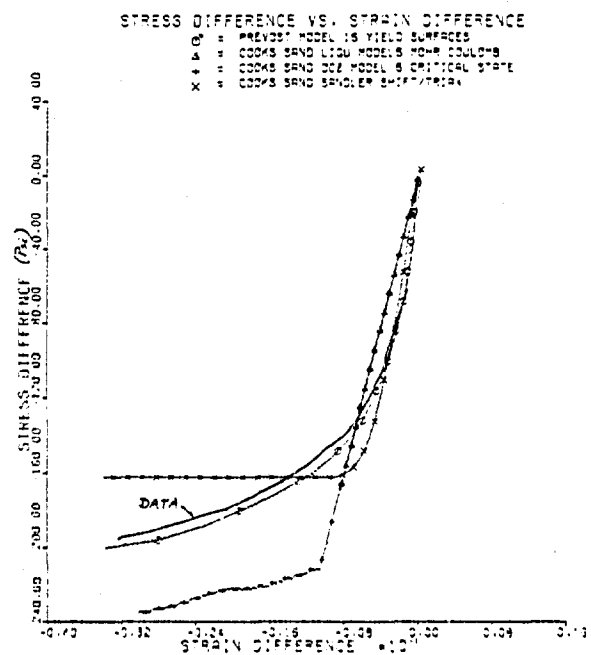


Figure 9. Cook's sand 50 pmi triaxial test.

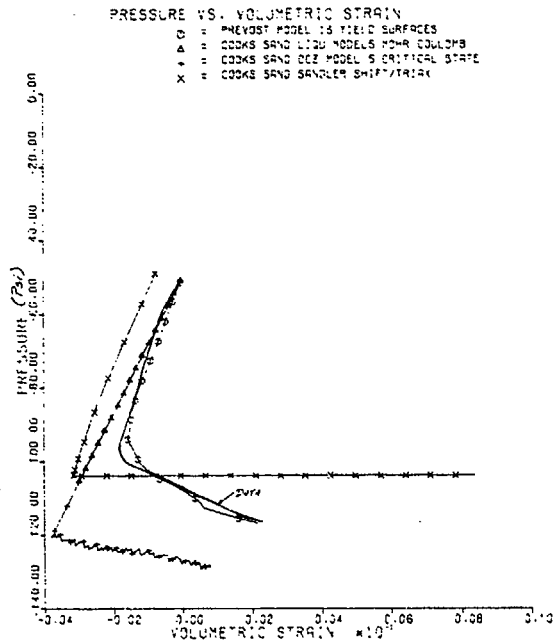


Figure 9b. Cook's sand 50 psi triaxial test.

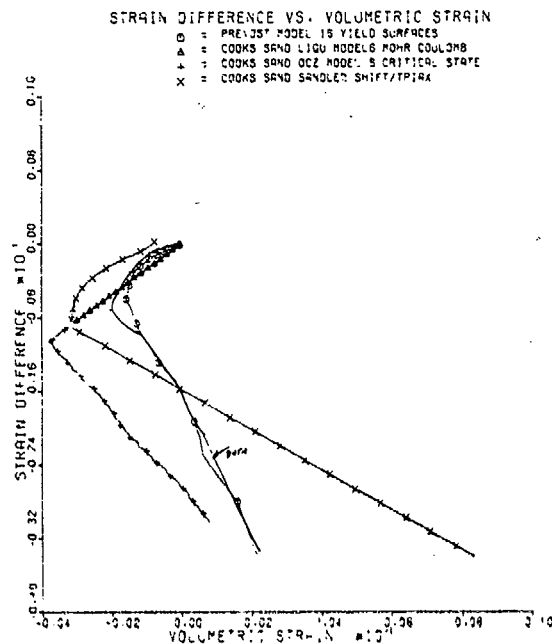


Figure 9c. Cook's sand 50 psi triaxial test.

behavior and poor agreement in stress path (stress-stress) tracking. The fitting of the critical state model parameters, although simple in concept, did not allow the model to match the volumetric data closely. This is thought to be the major cause of the problem. The best fit parameters force the model to overcompact (densify) the sand, resulting in high pore pressure and loss of strength. The

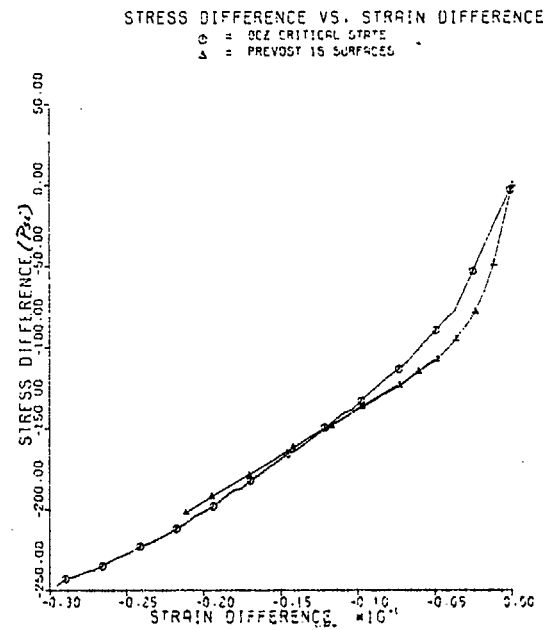


Figure 10a. Cook's sand undrained triaxial test, 100 psi confinement.

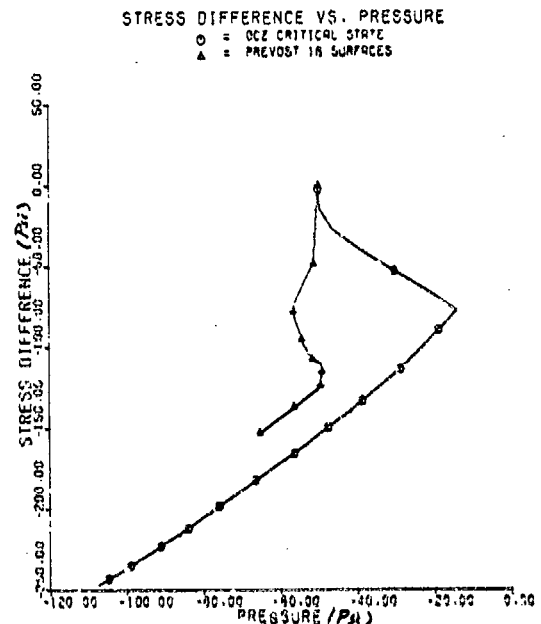


Figure 10b. Cook's sand undrained triaxial test, 100 psi confinement.

extent of pore pressure generation is very sensitive to the fluid modulus. This may be tuned by matching test data. The model exhibits pore pressure buildup both in loading and unloading. This, although crude in approach, does show cyclic degradation effects. Cyclic degradation effects are not presently included in the Prevost model.

## STATIC LOADS

Dynamic analysis requires the correct transmission of the exciting wave. The determination of correct stress amplification or attenuation is dependent on the material characterization. Most studies in the past have characterized the earthquake soil structure problem using strain-dependent elastic properties. One aspect of this task was to evaluate stress attenuation using nonlinear material properties. This effort is directly related both to the earthquake soil structure problem as well as to shock/blast analysis work.

In the nonlinear representation of a soil, traditional superposition of elastic static and dynamic solutions is no longer valid. The initial static stress state determines the ambient conditions for the dynamic loading. Consider a building sitting on a soil field. The stress state from the structure load imposes a different stress state on the soil from that of the free field. One approach is to calculate a uniform gravity on the soil field then "birth" the structure (have portions of the structure enter the calculation at different time steps). This stress state would then be the start for the dynamic solution. The CAP75 model has a gravity pressure, which is essentially a shift along the  $J_z$  axis.

This loads the element hydrostatically rather than with an appropriate  $K_z$  value for horizontal stress. To allow for a simplified starting point, the basic material model was modified to allow both a gravity shift and a  $K_z \neq 1.0$  condition to be represented. This imposed a nonzero value of  $J_z$ , which required that the cap be moved outward such that the starting point would be on the failure surface.

The ADINA restart option was used for dynamic analysis; it is not possible to first perform a vertical gravity analysis and then a horizontal shaking analysis since the boundary conditions would be different. Results from a typical static gravity analysis can be used as the basis for material property shift, then the static structure stresses and boundary displacement can be calculated. These static (structure load) displacements are reapplied at prescribed boundaries, repeating the static load case. The solution is then restarted, applying horizontal boundary displacements based on the dynamic shaking.

To summarize the procedure:

1. Calculate gravity shift.
2. Perform static analysis of soil and structure, evaluating structure weight displacements. Boundary conditions are horizontally restrained and vertically free. Determine boundary displacements.
3. Perform a dynamic soil column study to evaluate dynamic boundary horizontal displacements from shaking.
4. Perform a dynamic soil structure analysis to repeat soil-structure with displacements prescribed. First quasi-static (dynamic with long time steps) for gravity; then restart with shortened steps for dynamic shaking.

## ELASTIC ANALYSIS

Using the approach outlined above, a soil column mesh was excited with an earthquake to simulate free-field motion at various depths. Cook's sand (strain-dependent) properties were utilized in this analysis. Horizontal boundary node displacement, velocity, and acceleration histories were computed. A static analysis was performed using the mesh shown in Figure 11. Gravity loading was used to apply the structure and soil gravity loading to the soil. Figure 12 shows the static response. Time functions were constructed using the vertical mesh boundary displacements from the static analysis and the horizontal dynamic shaking displacement of the soil column. These displacement functions were applied to drive the horizontal and vertical mesh boundaries, first repeating the "static analysis" using large time steps then restarting with a smaller dynamic time increment. Results are shown in Figure 13. The soil column response indicates some amplification of the base motion. There is considerable reduction of motion under the structure as shown by the time histories beneath the structure when compared with free-field response. This is shown clearly by the contour plots of acceleration and velocity which give vector magnitudes at a particular time. The results shown are for the conditions of this problem and are not meant to express general conclusions.

## NONLINEAR ANALYSIS

The previous analysis was repeated using the nonlinear CAP75 material model and Cook's sand properties. The nonlinear results show faster propagation and higher load levels. This is a result of higher modulus values at depth than were estimated by the elastic analysis.

The static stress results for the mesh (Figure 11) are shown in Figure 14. The results are similar to the results of the elastic analysis. The overall levels of motion in the inelastic analysis are greater than those of the elastic analysis. The same base displacement function was used for both. Yielding in the nonlinear soil increased motions. However, attenuation of motion was noted beneath the structure relative to the free field as was noted in the elastic analysis. Figure 15 shows the response at step 50,  $t = 1.25$  seconds. Since the response is shown for a specific time and the nonlinear characteristics cause the time histories to differ from the elastic analysis, a direct comparison of stress states at that instant in time is not possible.

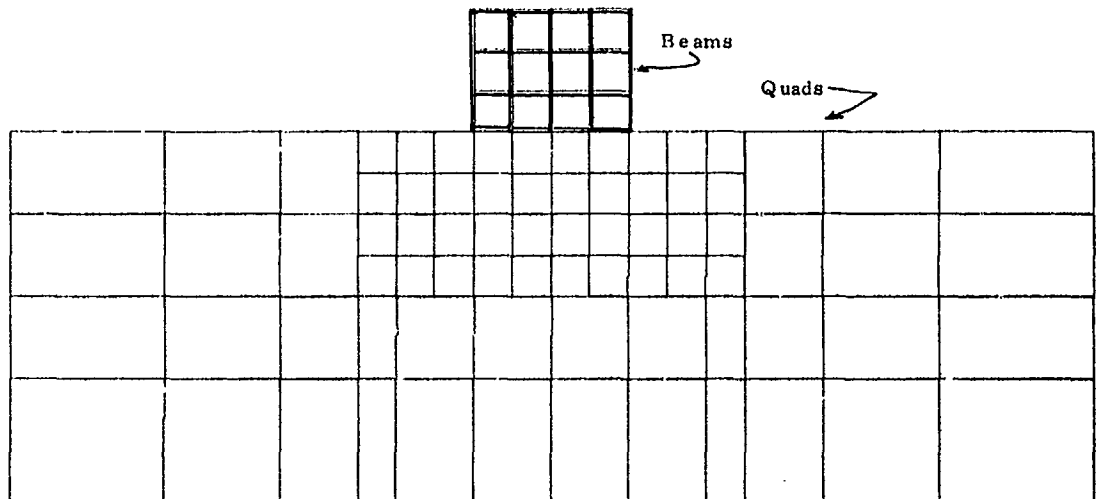


Figure 11. Finite element mesh.

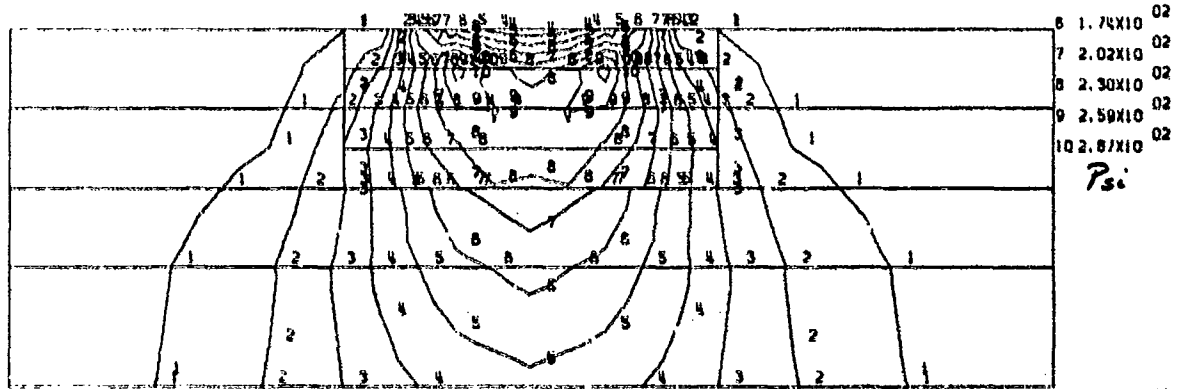


Figure 12. Static maximum shear stress, elastic analysis.

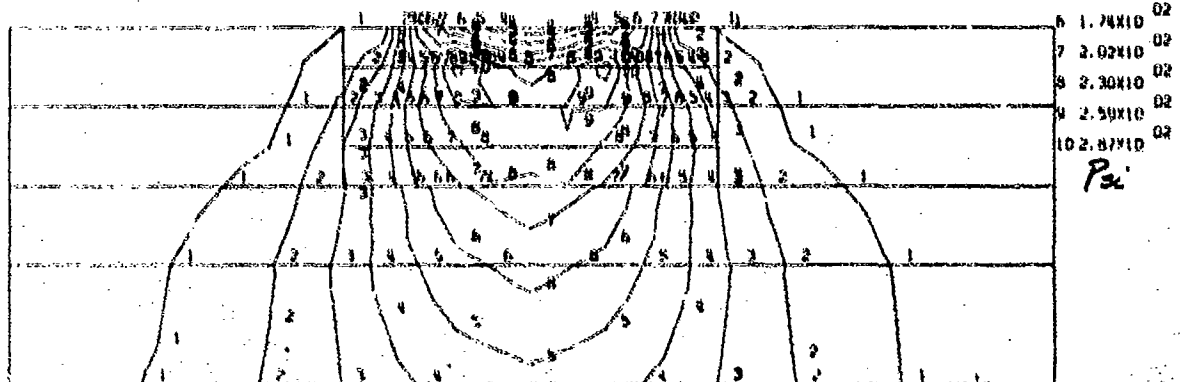


Figure 13. Maximum shear stress, elastic analysis, time 1.25 sec.

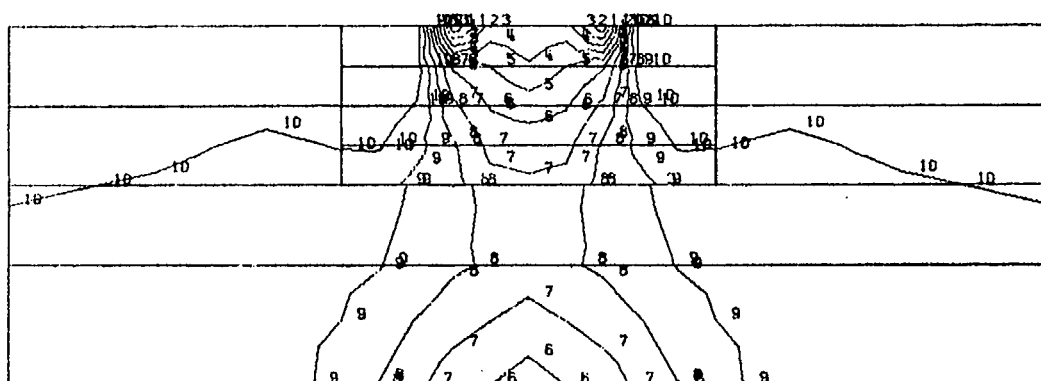


Figure 14. Static maximum stress, inelastic analysis.

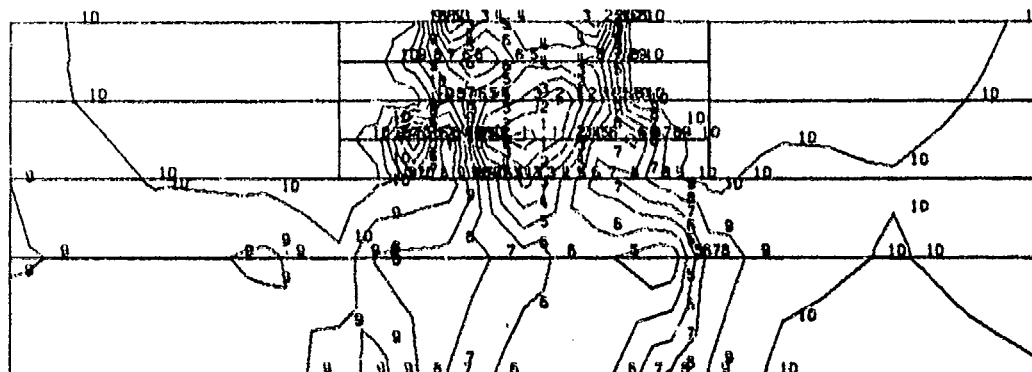


Figure 15. Maximum stress, inelastic analysis, time 1.25 sec.

The random cyclic loading is a severe test of the CAP model, having loading and unloading occurring both spatially in nearby sections of the mesh and in time with rapid reversals. These cause sudden changes in the stiffness of the elements. Often the state of stress may vary from the tension cutoff region, to cap region, to envelope region in a relatively small distance or time. This is particularly true beneath the outer edge of the structure where high shears are present. Rocking of the structure causes uplift and reduced stiffness of the soil. This greatly exaggerates the acceleration. Pockets of high acceleration occur. This problem can be corrected by reducing the time step and solving the wave propagation problem more exactly. However, from an engineering point of view, this is not the intent of the analysis, and the reduced time step would economically preclude an analysis of long duration. Displacement and stresses are not significantly affected by the acceleration sensitivity to changes in stiffness. Acceleration spatial plots are not accurate since they are influ-

enced by localized high spots, and acceleration results should not be expected unless the time step is reduced to track the wave propagation rather than stress response. This is clearly evident from satisfactory acceleration performance in the elastic analysis, which did not have rapid stiffness variation.

#### CONCLUSION

A detailed study has been made evaluating soil material models. A test case of a simplified structure on a soil field was studied. The analysis shows it is feasible to excite a soil column using base masses and a force/acceleration function; this motion can then be transferred to a large soil mesh through a displacement function. Mesh size and time step must be selected to ensure adequate preservation of the input motion. The material yielding and rapid changes in stiffness cause localized pockets of high acceleration. Static and dynamic loadings were satisfactorily imposed upon the mesh through utilization of static, quasi-static, and dynamic restarts.



Future work will further develop the concepts presented herein. Additional demonstration case studies are required to develop a generalized appreciation for mesh size and time step parameters. The use of nested surface material law concepts to more accurately track the wave propagation problem will be evaluated. The cumulative strain degradation effect on soil should be incorporated into the Prevost soil model to allow the model to track cyclic pore pressure generation.

#### REFERENCES

1. Office of Naval Research, "General Review of the Seismic Hazard to Selected U. S. Navy Installations", by ONR National Hazards Review Panel, Washington, D. C., Jan 1974.
2. Civil Engineering Laboratory, Technical Report R-847, "An Earthquake Analysis of the Liquefaction Potential at the Naval Air Station North Island", by J. M. Ferritto and J. B. Forrest, Port Hueneme, CA, Sep 1976.
3. Nuclear Regulatory Agency, Contract Report NUREG CR 0693, "Seismic Input and Soil Structure Interaction", Pittsburg, PA., D'Appolonia Consulting Engineers, Feb 1979 (Contract No. NCR 03-77-179).
4. Naval Civil Engineering Laboratory Technical Manual 51-81-12, "Effective Stress Soil Models", by J. M. Ferritto, Port Hueneme, CA, Aug 1981.
5. I. S. Sandler and D. Rubin, "An Algorithm and a Modular Subroutine for the CAP Model", International Journal for Numerical and Analytical Methods in Geomechanics, Vol 3, May 1979, pp 173-186.
6. J. Prevost and T. Hughes, "Mathematical Modeling of Cyclic Soil Behavior", Earthquake Engineering and Soil Dynamics, New York, N. Y., American Society of Civil Engineers, Jun 1979.
7. Zienkiewicz, O. C., Chang, C. T. and Hinton, E., "Nonlinear Seismic Response and Liquefaction, Int. J. Num. and Analytical Meth. in Geomechanics, 1978, 2, Issue No. 4, 381-404.
8. U. S. Department of Transportation, Federal Aviation Administration, FAA RD-76-206, "Experimental Relationships Between Moduli for Soil Layers Beneath Concrete Pavements", by J. B. Forrest et al, Washington, D. C., Jun 1977.
9. Weidlinger Associates, "Dynamic Analysis of Buried Structures Including Catastrophic Failure", by J. Isenberg, G. Wojeik, and N. Nikooyeh. Menlo Park, CA, Dec 1979.
10. Civil Engineering Laboratory Technical Memorandum 51-77-5, "Mighty Epic Pre-Test Analysis", by J. Crawford, et al., Port Hueneme, CA, Mar 1977.

## FINITE ELEMENTS FOR INITIAL VALUE PROBLEMS IN DYNAMICS

T. E. Simkins, Ph.D.  
U.S. Army Armament Research and Development Command  
Large Caliber Weapon Systems Laboratory  
Benet Weapons Laboratory  
Watervliet, NY 12189

The complete dynamic analysis of shock and vibration problems usually requires the solution of one or more hyperbolic partial differential equations involving space and time as independent variables. Many times a numerical solution is attempted by first eliminating the spatial dependency through the substitution of Ritz type approximations into a variational formulation of the problem, thus generating a corresponding set of ordinary differential equations in time, i.e., the Euler-Lagrange equations for the problem. The solution of these equations can sometimes be tedious owing to the hyperbolic nature of the problem. Instability may result unless the time step is sufficiently small and for problems involving rapidly changing loads or material properties, the smallness of the time step required may lead to unacceptably long computation time. When true shock conditions are encountered, there may result no solution at all. For such problems advantage may be gained by continuing the variational formulation into the time domain, dispensing altogether with the Euler-Lagrange equations and the need to solve them. While there exists a considerable choice of variational principles for eliminating the space variables (virtual work, minimum potential energy, etc.), the only physically based variational principle extending to the time domain is Hamilton's principle which, however, is unsuitable for the solution of initial-value problems in dynamics because of constraints placed on the variational quantities at the end points of the interval of time-integration. A way around this restriction is to employ instead Hamilton's Law of Varying Action which only becomes Hamilton's principle if the end point constraints are applied. Unlike Hamilton's principle, the Law of Varying Action is not a true variational principle in the sense of the calculus of variations, yet this in no way impedes its application to problems in dynamics. When piecewise basis functions (finite-elements) are employed as Ritz-approximations in the Law of Varying Action, however, convergence to the proper solution does not follow in a straightforward manner. The difficulties encountered and their logical resolution leading to a workable finite element formulation for the time domain is the main topic of this paper. A few demonstrations of the utility of finite elements in time are also given.

### INTRODUCTION

According to Finlayson and Scriven [1] it is not variational notation or even the concept of a varied path which is the key criterion of a true variational 'principle' but rather the existence of a functional which when varied and set to zero, generates the governing equations and constraints for a given class of problems. In this sense, certain fundamental principles of mechanics such as d'Alembert's Principle do not truly qualify as variational principles. That is to say, these mechanical principles or 'laws' cannot be posed as central problems of the calculus of variations. On the other hand there

are others, such as Hamilton's principle which do qualify as true variational principles. Yet it is d'Alembert's Principle which forms a basis for all analytical mechanics [2] and it follows, therefore, that the vanishing of the first variation of some functional is not a necessary condition for the scalar formulation of any mechanics problem - however elegant or convenient this may be. Whether a true variational principle or a more fundamental variational statement is used to obtain a numerical solution to a dynamics problem, an important argument is that well established laws such as d'Alembert's Principle or true principles such as Hamilton's, are physically based and avoid the arbitrariness inher-

ent in general weighted residual methods and contrived variational principles. Moreover, only those variational principles which are also maximum or minimum principles appear to offer any special advantage for obtaining approximate solutions - mainly through their ability to provide bounds on the variational integral. Even then the system treated must be positive-definite and the upper and lower bounds are often too far apart to be of practical value. In brief, there seems to be little point in contriving a variational principle in preference to a variational law of mechanics despite the more primitive status of the latter. Indeed the many solutions to initial value dynamics problems achieved by C. Bailey [3] by applying the Ritz method to Hamilton's 'law of varying action' demonstrate the usefulness of variational formulations not qualifying as 'principles'. Thus motivated, the work herein explains the numerical difficulties encountered in attempting to generalize Bailey's formulations according to the method of finite elements.

Zienkiewicz [4] has expressed serious reservations concerning the use of finite elements in the time domain. Indeed, when the functions involved are sufficiently smooth, the number of time steps required to integrate a set of ordinary differential equations may not be great and it may require roughly as many finite elements to produce a solution of comparable accuracy. In view of the increased storage required, the use of time-finite elements to solve such systems is questionable. There are many other cases, however, in which conventional algorithms for step-by-step integration may call for a very large number of time steps. This is especially true when dealing with the (hyperbolic) equations of structural dynamics should the excitation and/or material properties change rapidly in time. A physically based variational method, with its inherent stability and physical origin, may lower the computational effort considerably.

The many solutions achieved by C. Bailey were generated by the Ritz method [3] using a power series approximation in which globally defined polynomials are the basis functions. Ultimately the length of interval over which solutions may be generated as well as the detail to be provided in any subinterval will be limited by the degree of polynomial used as a basis. The pitfalls of using higher powered polynomials are well documented [6] and partially account for the use of locally (piecewise) defined basis functions (finite elements) to solve problems in many branches of mathematical physics. The extraordinary accuracy and simplicity of procedure attained by Bailey, however, are not to be understated.

Apart from avoiding the problems which can arise when higher powered polynomials are employed as basis functions, finite element formulations have other advantages when used to

solve problems in continuum mechanics. Even though the principal motivation for their use has been the need to handle complicated boundary shapes (non-existent in the time domain) time-finite elements are also well suited to handle sudden changes in load functions, extending the interval of solution indefinitely without restart, and providing great detail to the solution in any subinterval. Two examples which exploit the advantages afforded by the finite-element discretization of time are given in Section 5.

Since 1977, several investigators have publications dealing with the use of finite elements to modify or replace conventional integration methods. Hughes and Liu [7], and Belytschko and Mullen [8] are notable examples. One also notes the work of Serbin, Dougalis, and Gunzberger who have recently begun a computational and theoretical study of finite element methods for hyperbolic equations [9]. Thus despite the reservations expressed by Zienkiewicz, the extension of the finite element method to the solution of transient field problems is well motivated and was first reported by Argyris and Sharpf [10], later by Fried [11], and most recently by Baruch and Riff [12,13]. All of these works attempt to use Hamilton's principle as a starting point for the finite element formulation of initial value problems. As will be pointed out in the following section, this cannot be accomplished without some logical inconsistency when bringing the initial data into the formulation. In the sequel it will be shown that the use of Hamilton's 'law', rather than Hamilton's 'principle', makes possible the logical incorporation of the initial conditions into the variational formulation.

## 2. HAMILTON'S PRINCIPLE - A CONSTRAINED VARIATIONAL PRINCIPLE

The following equation is known as the generalized principle of d'Alembert [14]:

$$\sum_{i=1}^N (\mathbf{F}_i - \dot{\mathbf{p}}_i) \cdot \delta \mathbf{r}_i = 0 \quad ; \quad (\dot{\phantom{x}}) = d/dt \quad (1)$$

This equation applies to any system of  $N$ -particles, the  $i$ th particle having a position  $\mathbf{r}_i$ , a momentum  $\mathbf{p}_i$ , and subject to a resultant applied force  $\mathbf{F}_i$ .

Under the assumption that the virtual work of the applied forces is derivable from a scalar  $V$ , a time integration of equation (1) leads to Hamilton's law of varying action [15,16]:

$$\delta \int_{t_1}^{t_2} (T - V) dt - \sum_{i=1}^N m_i \dot{\mathbf{r}}_i \cdot \delta \mathbf{r}_i \Big|_{t_1}^{t_2} = 0 \quad (2a)$$

$T$  is the kinetic energy of the system

$$T = 1/2 \sum_{i=1}^N m_i \dot{\mathbf{r}}_i \cdot \dot{\mathbf{r}}_i$$

and  $V$  is the potential energy of the forces impressed on the  $N$ -particles. The existence of  $V$  makes little difference as far as numerical calculations are concerned. In the event  $V$  does not exist, equation (2a) can be written:

$$\int_{t_1}^{t_2} (\delta T + \delta \bar{W}) dt - \sum_{i=1}^N m_i \bar{r}_i \cdot \delta \bar{r}_i \Big|_{t_1}^{t_2} = 0 \quad (2b)$$

The bar signifies that in general the virtual work of the applied forces cannot be derived from any scalar function of the generalized coordinates. Either of equations (2) can be used as a basis for a Ritz approximation to a dynamics problem.

If the  $\bar{r}_i$  are constrained to take on specified values at  $t_1$  and  $t_2$ , then  $\delta \bar{r}_i(t_1)$  and  $\delta \bar{r}_i(t_2)$  vanish in equation (2a) and the result is Hamilton's principle:

$$\delta \int_{t_1}^{t_2} (T - V) dt = 0 \quad (3)$$

Since the vanishing of the displacement variations at the end points is not the only means by which the partial sum in equation (2a) may vanish, equation (3) may not always represent Hamilton's principle in the strict sense. Should equation (3) be used as a basis for the numerical solution of a dynamics problem without the requirement that all of the  $\delta \bar{r}_i$  vanish at  $t_1$  or  $t_2$ , zero momentum conditions will prevail instead as natural boundary conditions on those displacements whose variations are free. This aspect of variational principles is covered very clearly in many references (cf. ref. [17]). An observation to be made here is that equation (3) corresponds to a system of boundary value problems - not initial value problems - since the partial sum can only vanish through boundary (endpoint) constraints either natural or imposed. Thus equation (3) cannot, with complete logic, be used to formulate any system of initial value problems of dynamics. The introduction of initial data has in fact always been the obstacle preventing the use of Hamilton's principle for the variational formulation of initial value problems [18,19].

Since equation (3) is a valid physical statement of mechanics only when the boundary constraints are such that the partial sum vanishes, it is proper to refer to this equation as a 'constrained variational principle' as opposed to equations (2) which are unconstrained variational laws of mechanics, suitable for the application of arbitrary constraint conditions.

### 3. GLOBAL AND PIECEWISE RITZ APPROXIMATIONS

Equations (2) and (3) differ only in the presence or absence of boundary terms. For the case of a single particle ( $N=1$ ) having only one degree of freedom  $u(t)$ , the Ritz procedure when

applied to either of equations (2) leads to a scalar relation of the form:

$$\delta U^T [(K-B)U-F] = 0 \quad (4)$$

whereas for equation (3):

$$\delta U^T [KU-F] = 0 \quad (5)$$

As yet, none of the  $U_i$  are specified so that all of the  $\delta U_i$  are arbitrary quantities. Equations (4) and (5) result from the Ritz procedure whereby the displacement function  $u(t)$  is approximated as:

$$u(t) = a^T(t)U \quad (6)$$

The relation (6) applies to the entire interval of solution when globally defined basis functions are used or to a particular subinterval thereof when piecewise functions (finite elements) are employed. When a global power series approximation is used  $U$  is a vector of generalized coordinates, the first two of which are identifiable as  $u(t_1)$  and  $\dot{u}(t_1)$ . The 'shape function',  $a(t)$ , in this case is simply:

$$a^T(t) = [1, t, t^2, \dots, t^n] \quad , \quad t_1 < t < t_2 \quad (7)$$

If piecewise cubic Hermite polynomials are used instead, the components of  $U$  are local values of  $u$  and  $\dot{u}$  defined at the endpoints of a particular subinterval, and

$$a^T(t) = [2\tau^3 - 3\tau^2 + 1, h(\tau^3 - 2\tau^2 + \tau), 3\tau^2 - 2\tau^3, h(\tau^3 - \tau^2)] \quad (8)$$

where  $\tau = t/h$ ,  $h$  being the length of the particular subinterval. Referring first to equation (5), it is noted that  $K$  should tend in the limit to be singular or degenerate one if the system is semi-definite and nonsingular for positive-definite systems. For example, the degeneracy of  $K$  for the simplest semi-definite system ( $m\ddot{u}=0$ ) represents the possibility that neither  $u(t_1)$  or  $u(t_2)$  has been specified. That is, if neither  $\delta u(t_1)$  or  $\delta u(t_2)$  vanishes, then  $m\ddot{u}$  must vanish at both endpoints as natural boundary conditions. Under these conditions  $u(t)$  may only be determined to within an arbitrary constant. Thus in equation (5)  $K$ , if singular, may only be reduced to a nonsingular matrix by specifying values for  $u(t_1)$  and/or  $u(t_2)$  so that the variations of one or both of these quantities vanish. As we are only interested in initial value problems, the essence of the discussion which follows is not changed if, it is henceforth assumed that  $u(t_1)$  has been specified. This is known as a 'geometric' or 'imposed' constraint. Because  $\delta U_1 = \delta u(t_1) = 0$  multiplies the first row of  $K$  in equation (5), this row is effectively removed from the formulation. Since the remaining variations are arbitrary the final set of equations to be solved is then:

$$\sum_{j=2}^n K_{ij} U_j = F_i - K_{i1} U_1, \quad i = 2, 3, \dots, n \quad (9)$$

where  $U_1 = u(t_1)$  is the specified value and  $n \times n$  is the dimension of  $K$ . Whether these equations derive from a global power series approximation or from one based on finite elements, one may readily verify that as  $n$  is increased their solutions do indeed converge to the exact solution of the corresponding two point time-boundary value problem. That is, when  $u(t_2)$  is also specified and the corresponding  $\delta U$  quantity set to zero, equation (9) converges to the proper solution. Should one wish a solution to an initial value problem, however, equation (4) must be used instead of equation (5). In this case, specifying values for  $u(t_1)$  and  $u(t_2)$  cause  $\delta U_1$  and  $\delta U_2$  to vanish thereby deleting the first two equations of this set. The resulting system of equations to be solved is thus:

$$\sum_{j=3}^n (K_{ij} - B_{ij}) U_j = F_i - (K_{i1} - B_{i1}) U_1 - (K_{i2} - B_{i2}) U_2, \quad i = 3, 4, \dots, n \quad (10)$$

In all cases attempted to date, solutions to equations (10) have been observed to converge to the exact solution if these equations are derived using a global power series approximation but not if they are formulated by finite elements. An example of this anomaly will be given in the next section. As the only difference between equations (4) and (5) is a subtraction of  $B$  in the former, and in as much as convergence is achieved when equation (4) derives from a power series approximation, one suspects that it is the finite element representation of the matrix  $B$  which is somehow at fault. It is therefore of interest to know in more detail just how the subtraction of  $B$  is supposed to affect the coefficient matrix of the system.

In contrast to the matrix  $K$ , the matrix  $K-B$  must tend to be singular of degeneracy two - no constraints having been assumed a priori. Thus when  $u(t_1)$  is specified and the first row of  $K-B$  is deleted, the remaining equations still must possess one degeneracy in the limit as the number of basis functions becomes infinite. Thus the effect of subtracting  $B$  must be to free the natural boundary condition at  $t_2$  (inherent in equation (5)) and to introduce a degeneracy. This remaining degeneracy can only be removed by specifying the value of  $u(t)$  at a time other than  $t_1$  or a value for  $\dot{u}$ , resulting in the deletion of another row of  $K-B$ .

#### 4. ANOMALOUS BEHAVIOR OF FINITE ELEMENT FORMULATIONS

The degree to which the subtraction of the matrix  $B$  from  $K$  can both free the natural boundary condition at  $t_2$  and introduce a degeneracy differs with the type of approximation employed. When global power series approximations are used the  $B$  matrix is quite full and the subtraction

affects many rows of  $K$ . When locally defined Hermite polynomials are used, however,  $B$  is very sparse and in fact contains only two non-zero components. Moreover, one of these appears in the first row of  $B$  which is deleted when  $u(t_1)$  is specified. In this case freeing the natural boundary condition and introducing a degeneracy depends on the subtraction from a single component of  $K$ . Even though both effects may actually be produced in the limit as the number of elements becomes infinite, the degree to which they are approximated for any finite number of elements is evidently insufficient and the solutions do not converge to the correct result. This is exemplified in Figure 1. The problem represented is that of a free oscillator of unit mass and stiffness (a positive-definite system), subject to the prescribed initial constraints of zero displacement and unit velocity. For this case, equation (2a) reads:

$$\int_0^\pi (\dot{u} \delta \dot{u} - u \delta u) dt - \dot{u} \delta u \Big|_0^\pi = 0 \quad (11)$$

or simply,

$$\int_0^\pi (u + \dot{u}) \delta u dt = 0 \quad (12)$$

The finite element results of Figure 1 were obtained using piecewise cubic Hermite polynomials. (Higher ordered Hermite polynomials yield similar results.) It is observed that the solutions tend to diminish from the exact solution,  $\sin(t)$ , as the number of elements is increased. Using only two finite elements the finite element matrix formulation (equation (4)) for this problem is as follows:

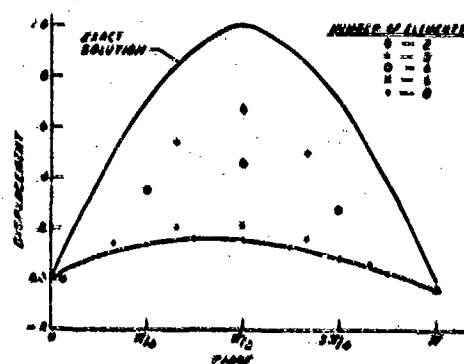


Fig. 1 - Divergent finite element solutions to free oscillator problem

\*Note that Eq. (12) would also result from application of the Galerkin procedure, implying that the Galerkin method has some physical justification for problems in dynamics.

$$0 = \delta U^T [K-B] U = [\delta U_1 \delta U_2 \delta U_3 \delta U_4 \delta U_5 \delta U_6] \cdot$$

$$\begin{bmatrix} k_{11} & k_{12} & k_{13} & k_{14} & 0 & 0 \\ k_{21} & k_{22} & k_{23} & k_{24} & 0 & 0 \\ k_{31} & k_{32} & k_{33}+k_{11} & k_{34}+k_{12} & k_{13} & k_{14} \\ k_{41} & k_{42} & k_{43}+k_{21} & k_{44}+k_{22} & k_{23} & k_{24} \\ 0 & 0 & k_{31} & k_{32} & k_{33} & k_{34} \\ 0 & 0 & k_{41} & k_{42} & k_{43} & k_{44} \end{bmatrix} - \begin{bmatrix} 0 & -1 & 0 & 0 & 0 & 0 \\ 0 & 0 & 0 & 0 & 0 & 0 \\ 0 & 0 & 0 & 0 & 0 & 0 \\ 0 & 0 & 0 & 0 & 0 & 0 \\ 0 & 0 & 0 & 0 & 0 & 1 \\ 0 & 0 & 0 & 0 & 0 & 0 \end{bmatrix} \cdot \begin{bmatrix} U_1 \\ U_2 \\ U_3 \\ U_4 \\ U_5 \\ U_6 \end{bmatrix} \quad (13)$$

Using expression (8), the element matrix  $k$  is calculated in terms of the element length  $h$  as:

$$k = \int_0^h (\dot{a}a^T - aa^T) dt = \begin{bmatrix} \frac{6}{5h} - \frac{13h}{35} & \frac{1}{10} - \frac{11h^2}{210} & -\frac{9h}{70} - \frac{6}{5h} & \frac{13h^2}{420} + \frac{1}{10} \\ & \frac{2h}{15} - \frac{h^3}{105} & -\frac{13h^2}{420} - \frac{1}{10} & \frac{h^3}{140} - \frac{h}{30} \\ & & & & -\text{SYMM.} & \\ & & & & & \frac{6}{5h} - \frac{13h}{35} & \frac{11h^2}{210} - \frac{1}{10} \\ & & & & & & \frac{2h}{15} - \frac{h^3}{105} \end{bmatrix}$$

Since  $U_1$  is specified the first row of  $K-B$  is deleted. As the subtraction of  $B$  only affects one row of the reduced system, the only way in which a degeneracy can be introduced is for the next to last row to join the space defined by the rows remaining. Thus rows two through six in equation (13) ideally would become linearly dependent. This dependency among rows must be quite general as specification of any other of the  $U_i$  must remove it.

One suspects that a simple subtraction of unity from  $K_{55}$  in equation (13) may not do the best job of introducing a degeneracy or of freeing the natural boundary condition at  $t_2 = \tau$ . One can gain some idea of how 'close' this subtraction brings the fifth row into the space of rows 2, 3, 4 and 6 by comparing it with its projection onto this space. Substituting  $\tau/2$  for  $h$ , the fifth row of equation (13) calculates to be:

$$\begin{bmatrix} 0.0 & 0.0 & -0.96590326 & -0.17637194 \\ & & 0.18050597 & -0.970753175 \end{bmatrix}$$

whereas its projection is:

$$\begin{bmatrix} 7.8567183E-3 & -8.5978979E-3 & -0.974496335 \\ -0.184380835 & 0.172642875 & -0.96178340 \end{bmatrix}$$

Further calculations show that if the interval of solution remains fixed and the number of finite elements is allowed to increase, closer agreement between the next to last row vector and its projection is observed but this is not accompanied by a convergence of the solution vector toward the exact solution to the problem. While the exact reasons for this instability are not known it is apparent that the rate at which the next to last row tends to become dependent is important. It stands to reason, therefore, that should one invoke the limit condition without actually proceeding to the limit, a convergent sequence may result and indeed this proves to be the case.

Asserting that the row vectors two through six are linearly dependent allows the fifth row (equation) of equations (13) to be replaced by a linear combination of the others. For example, let

$$R_5 = a_2 R_2 + a_3 R_3 + a_4 R_4 + a_6 R_6 \quad (14)$$

where  $R_i$  denotes the  $i$ th row of  $K-B$ . After imposing the second initial constraint,  $U_2 = 1$ , equations (13) can be written:

$$\begin{aligned} \delta U_3 R_3 \cdot U + \delta U_4 R_4 \cdot U + \delta U_5 (a_2 R_2 + a_3 R_3 + a_4 R_4 + a_6 R_6) \\ \cdot U + \delta U_6 R_6 \cdot U = 0 \end{aligned} \quad (15)$$

Since all variations in equation (15) are arbitrary, there results the following system of equations for solution:

$$0 = \underline{R}_3 \cdot \underline{U} = \underline{R}_2 \cdot \underline{U} = \underline{R}_4 \cdot \underline{U} = \underline{R}_5 \cdot \underline{U} \quad (16)$$

Thus the second equation (row) which was originally deleted through the specification of  $U_2$ , is brought back into the formulation in place of the fifth in a logical and consistent manner. Equations (16) are the same set as would result from following the procedure of Argyris and Scharpf. These authors, however, started with Hamilton's principle which requires that  $\delta U_1 = \delta U_5 = 0$ . This would delete the first and fifth equations from the set. Further specification of  $U_2$  should then delete the second equation as well, overspecifying the problem. Argyris and Scharpf [20] allow this equation to remain without justification. Moreover, no explanation is given as to why  $\delta U_5$  should vanish as  $U_5$  is never specified in an initial value problem. All of these inconsistencies derive from the fact that Hamilton's principle corresponds only to boundary value problems - never to initial value problems.

In summary, the work of this section shows that Hamilton's law of varying action, unlike Hamilton's principle, is an unconstrained variational statement permitting the introduction of arbitrary constraints including data ordinarily given for initial value problems. When piecewise Hermite cubic polynomials are used as a basis for a finite element formulation, the singular state of the resulting coefficient matrix in the limit justifies retention of the second equation of the system in preference to the next to last when typical initial values for

displacement and velocity are specified. Following this procedure, convergent solutions are then obtained for the problem of the free oscillator considered in this section. These results are presented in Table 1 for formulations based on one, two, and six finite elements.

Note that the replacement of the fifth row of  $[K-B]$  by a linear combination of rows two, three, four, and six in accordance with equation (14) does not have to be carried out in practice when seeking the solution to the homogeneous problem ( $F = 0$ ) as this procedure is entirely equivalent to replacing the fifth equation by the second. This equivalence, in general, does not apply to the nonhomogeneous problem ( $F \neq 0$ ) however, since  $F_2$  would then replace  $F_5$ . In general,  $F_5 \neq \alpha_2 F_2 + \alpha_3 F_3 + \alpha_4 F_4 + \alpha_6 F_6$  except when the original load function  $f(t)$  is a constant. Nevertheless, the replacement of the next to last equation by the 2nd will lead to convergent solutions in many cases. In some very important cases however, such as when  $F_2$  is zero and  $F_{n-1}$  is not, the procedure will fail. (For example  $f(t)$  might be concentrated at an end point of the time interval.) Thus to be perfectly consistent with equations (2) the substitution of the second row for the next to last should be confined to the matrix  $[K-B]$ . In this case the  $\alpha_i$  must be determined and will figure in the final solution. Since the  $\alpha_i$  are easily determined from the solution vector to the homogeneous problem these quantities are readily available. The proper substitution for the fifth equation of the nonhomogeneous counterpart of equation (13) can be shown to be

$$\underline{R}_2 \cdot \underline{U} = (F_5 - \alpha_3 F_3 - \alpha_4 F_4 - \alpha_6 F_6) / \alpha_2$$

in place of the original equation  $\underline{R}_5 \cdot \underline{U} = F_5$ .

TABLE 1. SOLUTIONS TO FREE OSCILLATOR PROBLEM (DISPLACEMENT/VELOCITY)  
 $0 \leq t \leq \pi$

$6t/\pi$	One Element	Two Elements	Six Elements	Exact Solution
0	0.0* 1.0*	0.0* 1.0*	0.0* 1.0*	0.0 1.0
1			0.49978005 0.86602547	0.5 0.86602541
2			0.86564452 0.50000025	0.86602541 0.5
3		0.97817298 2.02985945E-4	0.99956036 4.4572957E-7	1.0 0.0
4			0.86564496 -0.49999948	0.86602541 -0.5
5			0.499780823 -0.86602502	0.5 0.86602541
6	0.0166099781 -1.00079414	3.9845105E-4 -1.00000946	8.9130273E-7 -0.99999999	0.0 -1.0

\*Imposed values.

## 5. APPLICATIONS

### Example 1. Linear Oscillator Subjected to Discontinuous Forces

A linear oscillator of unit mass and stiffness is subjected to a force  $f(t)$ . Two cases are considered:

$$(a) f(t) = H(t-1/2)$$

$$(b) f(t) = \delta(t-0.4)$$

$H$  and  $\delta$  are the Heaviside and Dirac functions respectively and for either of these cases equation (2) reads:

$$\int_{t_1}^{t_2} [u\ddot{u} + (f(t)-u)\dot{u}]dt - u\dot{u} \Big|_{t_1}^{t_2} = 0$$

For case (a) four finite elements of equal length are used to approximate  $u(t)$  over the solution interval  $(0,2)$ . The element polynomial shape function is Hermite cubic and an element length of one half takes advantage of the specific shape of the forcing function. Table 2 compares the calculated displacements and velocities with those computed from the exact solution.

TABLE 2. SOLUTION TO  $\ddot{u} + u = H(t-1/2)$   
 $0 \leq t \leq 2.0$

t	Computed		Exact	
	Displacement	Velocity	Displacement	Velocity
0.0	0.0*	1.0*	0.0	1.0
0.5	0.47932149	0.87708716	0.47942555	0.877582565
1.0	0.96370936	1.0199163	0.96388844	1.01972786
1.5	1.45700388	0.91238744	1.45719267	0.91220819
2.0	1.83836447	0.5805616	1.83836024	0.58134814

\*Imposed values.

In case (b) a discontinuity in velocity can be expected in the solution. As the use of cubic shape functions enforces continuity of velocity throughout, a better solution might be expected when linear shape functions are employed. Table 3 compares the exact solution on the interval  $(0,1)$  with that obtained using ten such elements of equal length.

The two problems considered in this example demonstrate the manner in which the type of element and its points of attachment (i.e., the 'nodes' or 'grid points') may be varied to suit specified transient events.

TABLE 3. SOLUTION TO  $\ddot{u} + u = \delta(t-0.4)$   
 $0 \leq t \leq 1$

t	Computed Displacement	Exact Displacement
0.0	0.0*	0.0
0.1	0.1*	0.099833416
0.2	0.199001664	0.19866933
0.3	0.296016622	0.295520213
0.4	0.390076343	0.38941834
0.5	0.58007539	0.57925896
0.6	0.76428335	0.76331182
0.7	0.94086118	0.93973791
0.8	1.10804607	1.10677443
0.9	1.26416892	1.26275246
1.0	1.40767112	1.40611348

\*Imposed values.

### Example 2. Response of a Beam to a Moving Mass

A concentrated mass is assumed to move at constant velocity  $v$  along the length of a uniform Euler beam, simply supported at each of its ends and having zero displacement and velocity at  $t = 0$ . Under suitable definitions for  $k$  and  $m$ , the representative equations may be written [21]:

$$y^{iv} + ky + f(x,t) = 0$$

$$y(0,t) = y''(0,t) = y(1,t) = y''(1,t)$$

$$= y(x,0) = \dot{y}(x,0) = 0 \quad (18)$$

The function  $f(x,t)$  consists of a sum of inertial terms:

$$f(x,t) = m(y + 2vy' + g + v^2y'')\delta(x-vt) \quad (19)$$

where  $g$  denotes the gravitational constant and  $\delta$  is the Dirac function. This problem is particularly interesting in that the conventional use of piecewise cubic shape functions to discretize the space variable only, introduces forces which are discontinuous functions of time into the resulting ordinary differential equations.



These discontinuities are associated with the beam curvature load term appearing in the expression (19). Since the piecewise cubic polynomials are discontinuous in the second derivative at the element attachments, the term  $mv^2y''\delta(x-vt)$  - when multiplied by the shape function  $a(x)$  and integrated over the element length - will produce functions of time which are discontinuous whenever the moving mass arrives at any point of attachment. Clearly these discontinuities have nothing to do with the physics of the problem and are certain to invite trouble when one attempts to numerically integrate the time dependent equations via established algorithms. It is possible, of course, to use shape functions of higher degree to discretize the space variable thus eliminating the discontinuities at the onset but this is hardly consistent with the finite element method which should permit the use of even linear shape functions if need be. One is tempted to somehow 'smooth' these discontinuities, yet this should not be done in a purely arbitrary fashion. Integrating the effects of these forces throughout the time domain through the use of Hamilton's law of varying action provides a consistent way to handle this problem.

While it is possible to handle the space and time finite element discretizations in one operation, the amount of computation and computer programming tend to become inordinately large. Moreover, there exist any number of finite element codes (e.g. NASTRAN) which can quickly accomplish much of the space discretization. It seems more efficient, therefore, to apply the finite element method in two steps, by first discretizing the space variable and then applying Hamilton's law to the resulting system of ordinary differential equations in time. For the case at hand, the differential equations governing the motion of the  $i$ th beam element turn out to be:

$$\begin{aligned} (p + m_1)u + m_2\ddot{u} + \\ (q + m_3)u + m_4(vt) = 0 \end{aligned} \quad (20)$$

$p$  and  $q$  are proportional to the usual mass and stiffness matrices for beam elements and have been evaluated many times in the literature. Here all of the beam elements are of the same length  $l$ , and the displacement within the  $i$ th element is interpolated from  $u^i(t)$ , a vector of end point displacements and velocities, i.e.,

$$y(x,t) = a^T(\xi)u^i(t) \quad 0 \leq \xi \leq 1 \quad (21)$$

where  $\xi(x) = x/l - (i-1)$ , a nondimensional element coordinate.

The  $g$  matrices in equations (20) correspond to transverse, Coriolis, and centrifugal accelerations respectively and are defined for the  $i$ th element as follows:

$$\begin{aligned} c_1 &= a(\xi^1) a^T(\xi^1)|_{x=vt} \\ c_2 &= 2va(\xi^1) a^T(\xi^1)|_{x=vt} \\ c_3 &= v^2 a(\xi^1) a^T(\xi^1)|_{x=vt} \end{aligned} \quad (22)$$

It is noted that  $c_3$  will be discontinuous at  $\xi^1 = 0$  and  $\xi^1 = 1$ . The function  $\hat{m}$  takes on the value of  $m$  only when the concentrated mass lies within the  $i$ th element, otherwise  $\hat{m}$  is zero.

The element equations (20) are combined in the usual way to form  $N$  equations of motion for the combined structure. Symbolically:

$$M(t)\ddot{U} + C(t)\dot{U} + K(t)U = F(t) \quad (23)$$

Each of the matrices in equation (23) can be viewed as a conventional matrix of constant coefficients plus a time variant set of components which are active in a band along its main diagonal as the moving mass traverses the beam in time. For this system of equations Hamilton's law of varying action can be written:

$$\sum_{i=1}^N \sum_{j=1}^N \left\{ \int_{t_1}^{t_2} (\delta U_i M_{ij} \dot{U}_j + \delta U_i [(M_{ij} - C_{ij}) \dot{U}_j - K_{ij} U_j + F_{ij}] dt - \delta U_i M_{ij} U_j \right\} = 0 \quad (24)$$

It is interesting to observe the accuracy of solution which can be obtained from equation (24) using only two finite elements in space and two in time. A formulation using two elements in space results in a system of  $N=4$  ordinary differential equations in time once the geometric support constraints have been applied. A two element formulation of these four equations for the time domain, followed by the application of all initial constraints in the manner summarized in Section 4, gives a final system of sixteen linear algebraic equations for solution. Figure 2 compares this solution with the experimental results of Ayre, Jacobsen, and Hsu [22] and a conventional finite element solution using three elements in the space domain followed by a time-integration of the equations (28) by Hamming's predictor-corrector algorithm [23]. The mass velocity in this case is  $v = v^*/2$ , where  $v^*$  is the lowest velocity to cause resonance when the load is a moving weight only and the magnitude assigned to the moving mass is 25% of the total mass of the beam. (Other parametric values are the same as those in reference [22].) The displacements have been normalized with respect to the maximum deflection produced if the weight was applied statically at midspan and  $L$  is the total beam length. In particular one notes that the conventional solution obtained via three finite elements in space only, produces non-physical discontinuities in the slope of the solution curve at  $vt/L = 1/3, 2/3$ . (The continuous data for generating this curve is obtained by interpolating the solution to equation (23) using equation (21).) These discontinuities cause greatly increased compu-

tational effort for conventional integration algorithms but not when finite elements in space and time are employed. Improved agreement with the experimental results is also observed.

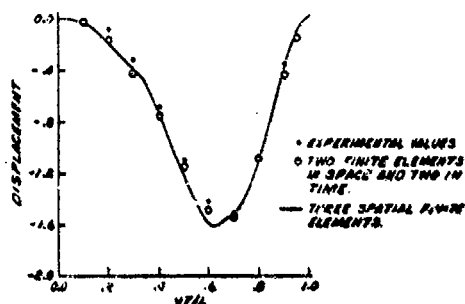


Fig. 2 - Displacement of beam at location of moving mass

#### ACKNOWLEDGMENTS

The author is especially grateful for the interest and assistance of Mr. Royce Soanes of the Benet Computer Science Laboratory.

All mathematics herein were performed using the MACSYMA [24] (Project MAC's SYmbolic MANipulation) system developed by the Mathlab Group of the MIT Laboratory for Computer Science.

#### REFERENCES

1. Vinlayson, B. A. and Scriven, L. E., "On the Search for Variational Principles," Int. J. Heat Mass Transfer, Vol. 10, 1967, pp. 799-821.
2. Lanczos, C., The Variational Principles of Mechanics, 3rd ed., University of Toronto Press, Toronto, 1966, pp. 70-72.
3. Bailey, C. D., "The Method of Ritz Applied to the Equation of Hamilton," Computer Methods in Applied Mechanics and Engineering, Vol. 7, 1976, pp. 233-247.
4. Zienkiewicz, O. C., The Finite Element Method, 3rd ed., McGraw-Hill, New York, 1977, pp. 369-70.
5. Kantorovich, L. V., and Krylov, V. I., Approximate Methods of Higher Analysis, 3rd ed., Interscience Publishers, Inc., The Netherlands, 1964, pp. 258-303.
6. Conte, S. D., and de Boor, C., Elementary Numerical Analysis: An Algorithmic Approach, 2nd ed., McGraw Hill, New York, 1972, pp. 231-233.
7. Hughes, T. J. R. and Liu, W. K., "Implicit-Explicit Finite Elements in Transient Analysis: Stability Theory," Journal of Applied Mechanics, Vol. 45, 1978, pp. 371-374.
8. Belytschko, T. and Mullen, R., "Mesh Partitions of Explicit-Implicit Time Integration," Formulations and Computational Algorithms in Finite Element Analysis, K. J. Bathe, J. T. Oden and W. Wunderlich (Eds.), M.I.T. Press, Cambridge, MA, 1977.
9. Personal communication from S. Serbin, University of Tennessee, March 1981.
10. Argyris, J. N., and Scharpf, D. W., "Finite Elements in Time and Space," Nuclear Engineering and Design, Vol. 10, 1969, pp. 456-464.
11. Fried, I., "Finite-Element Analysis of Time-Dependent Phenomena," AIAA Journal, Vol. 7, No. 6, pp. 1170-1172.
12. Riff, R., Weiler, T., and Baruch, M., "Space-Time Finite Elements for Structural Dynamic Analysis," TAE Report No. 343, Technion, Israel Institute of Technology, Department of Aero. Eng., Nov. 1978.
13. Riff, R., and Baruch, M., "Hamilton's Principle, Hamilton's Law, 6 Correction Formulation," TAE Report No. 403, Technion, Israel Inst. of Technology, Dept. of Aero Eng., March 1980.
14. Mierovitch, L., Methods of Analytical Dynamics, 1st ed., McGraw-Hill, New York, 1970, p. 65.
15. Bailey, C. D., "Application of Hamilton's Law of Varying Action," AIAA Journal, Vol. 13, No. 9, pp. 1154-1157.
16. Hamilton, W. R., "Second Essay on a General Method in Dynamics," Philosophical Transactions of the Royal Society of London, 1835, pp. 95-144.
17. Courant, R., "Variational Methods for the Solution of Problems of Equilibrium and Vibrations," Bulletin of American Mathematical Society, Vol. 49, 1943, pp. 1-23.
18. Tiersten, H. F., "Natural Boundary and Initial Conditions From a Modification of Hamilton's Principle," J. of Math. Physics, Vol. 9, No. 9, Sept. 1968, pp. 1445-1450.

19. Gurtin, M. E., "Variational Principles for Linear Elastodynamics," Archive Ratl. Mech. Anal., Vol. 16, 1964, pp. 34-50 (1964).
20. Argyris, J. H., and Scharpf, D. W., "Finite Elements in Time and Space," Nuclear Engineering and Design, Vol. 10, 1969, pp. 459.
21. Simkins, T. E., "Unconstrained Variational Statements for Initial and Boundary-Value Problems," AIAA Journal, Vol. 16, No. 6, June 1978, pp. 559-563.
22. Ayre, R. S., Jacobsen, L. S., and Hsu, C. S., "Transverse Vibration of One and of Two Space Beams Under the Action of a Moving Mass Load," Proceedings of First National Congress on Applied Mechanics, June 1951, pp. 81-90.
23. Ralston and Wilf, Mathematical Methods For Digital Computers, Wiley and Sons, NY, London, 1960, pp. 95-109.
24. Bogen, R. and Golder, J., MACSYMA Reference Manual, M.I.T., Cambridge, MA, 1977.

## STRUCTURAL DYNAMICS

### A Procedure for Designing Overdamped Lumped Parameter Systems

Daniel J. Inman  
Department of Mechanical and Aerospace Engineering  
State University of New York at Buffalo  
Buffalo, NY 14260

Albert N. Andry, Jr.  
Lockheed California Company  
Burbank, California 91520

The concept of overdamping common to a single degree of freedom damped linear system is extended to multidegree of freedom damped linear systems. Inequalities involving the mass, damping and stiffness parameters are derived to form a system with a free response which is overdamped in each mode. A general method for designing systems to be overdamped in each mode is indicated. The method is applied to a four degree of freedom model of a Darrieus wind turbine and a design solution for overdamping is presented.

#### Introduction

It is often desired to limit the oscillation in mechanical systems by using the effects of viscous damping. In a linear one degree of freedom spring, mass and dashpot arrangement, the selection of the proper values of mass stiffness and damping constants to produce an overdamped or critically damped system is trivial. The solution of a constant coefficient second order ordinary differential equation shows that if  $c \geq 2mk$ , where  $m$ ,  $c$  and  $k$  are the mass, damping and stiffness coefficients respectively, then the system will not oscillate. The work presented here yields similar inequalities for nonoscillation of multiple degree of freedom systems.

The systems considered here are those that can be modeled by the matrix differential equation

$$M\ddot{x}(t) + C\dot{x}(t) + Kx(t) = 0 \quad (1)$$

where  $x(t)$  is an  $n$ -dimensional vector of displacements and  $M$ ,  $C$  and  $K$  are  $n \times n$  symmetric matrices containing the physical parameters of mass, damping and stiffness constants. It is further assumed that  $M$  and  $K$  are positive definite and that  $C$  is at least positive semidefinite. The design procedure presented here takes advantage of newly derived matrix conditions [1] to generate non-linear algebraic inequalities in the physical parameters of the system. When the parameters are chosen to satisfy these inequalities, the resulting

transient response will be overdamped in each mode. The inequalities are stated directly in terms of the mass, damping and stiffness constants of the system.

The exact relations for overdamping are derived for a two degree of freedom system. Once the design criterion is satisfied the results are used to calculate the eigenvalues of the system to illustrate that the designed system is in fact overdamped in each mode. The design of a specific four degree of freedom model of a drivetrain is also given to illustrate the problems encountered in more practical design situations. The generalization to a degree of freedom is obvious from these examples.

#### Background

In [1] it is shown that if, in addition to the restrictions listed above, the matrices  $M$ ,  $C$  and  $K$  are such that the matrix

$$M^{-1/2}CM^{-1/2} - 2(M^{-1/2}KM^{-1/2})^{1/2}$$

is positive definite then all of the eigenvalues of (1) will be negative real numbers and each mode of (1) will be overdamped. Since  $M$  is symmetric and positive definite, it possesses a unique positive definite square root,  $M^{1/2}$ , with inverse  $M^{-1/2}$ . Using the transformation

$$x = M^{-1/2}y,$$

equation (1) is reduced to

$$\ddot{y} + A\dot{y} + By = 0 \quad (2)$$

where  $A = M^{-1/2}CM^{-1/2}$  and  $B = M^{-1/2}KM^{-1/2}$ . The condition for overdamping in each mode for (2) becomes that the matrix  $A-2B^{1/2}$  must be positive definite. Since the square root of a matrix is, in general, harder to compute than the square of a matrix, it is tempting to use the matrix  $A^2-4B$  in design work. Fortunately, it has been shown [3] that if  $A^2-4B$  is positive definite, then so is  $A-2B^{1/2}$ . Thus, requiring the matrix  $A^2-4B$  to be positive definite insures that each mode of (2) will be decaying non-oscillating (overdamped) function of time.

If it is desired to make the solution of (2) overdamped in each mode for arbitrary initial conditions, then it suffices to choose the physical constants  $m_1$ ,  $c_1$  and  $k_1$  so that  $A^2-4B$  is positive definite.

## 2 Degree of Freedom

To illustrate the above ideas consider the two mass arrangement in Fig. 1. The appropriate matrices for the equations of motion are:

$$M = \begin{bmatrix} m_1 & 0 \\ 0 & m_2 \end{bmatrix} \quad C = \begin{bmatrix} c_1+c_2 & -c_2 \\ -c_2 & c_2 \end{bmatrix}$$

$$\text{and } K = \begin{bmatrix} k_1+k_2 & -k_2 \\ -k_2 & k_2 \end{bmatrix}$$

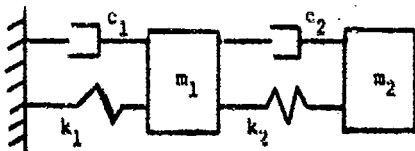


Fig. 1 Two degree of freedom system.

The matrix  $M^{-1/2}$  is:

$$M^{-1/2} = \begin{bmatrix} 1/\sqrt{m_1} & 0 \\ 0 & 1/\sqrt{m_2} \end{bmatrix}$$

Denoting the  $i-j$ th element of a generic matrix  $A$  by  $A_{ij}$  and forming the matrix  $A^2-4B$  yields

$$(A^2-4B)_{11} = \frac{(c_1+c_2)^2}{m_1^2} + \frac{c_2^2}{m_1 m_2} - 4 \frac{k_1+k_2}{m_1}$$

$$(A^2-4B)_{12} = \frac{-c_1 c_2 - c_2^2}{m_1 \sqrt{m_1 m_2}} - \frac{c_2^2}{m_2 \sqrt{m_1 m_2}} + \frac{4k_2}{\sqrt{m_1 m_2}}$$

$$= (A^2-4B)_{21}$$

$$(A^2-4B)_{22} = \frac{c_2^2}{m_2^2} + \frac{c_2^2}{m_1 m_2} - 4 \frac{k_2}{m_2}$$

It is desired to choose  $m_1$ ,  $c_1$  and  $k_1$  so that the matrix  $A^2-4B$  is positive definite. A necessary and sufficient condition for a matrix  $D$  to be positive definite is for each of its leading principal minors to be positive. In particular, a real  $2 \times 2$  matrix  $D$  is positive definite if and only if

$$D_{11} > 0$$

and

$$D_{11}D_{22} - D_{12}D_{21} > 0.$$

Applying these inequalities to  $(A^2-4B)$  yields

$$\frac{(c_1+c_2)^2}{m_1^2} + \frac{c_2^2}{m_1 m_2} > 4 \frac{k_1+k_2}{m_1} \quad (3)$$

$$\left[ \frac{(c_1+c_2)^2}{m_1^2} + \frac{c_2^2}{m_1 m_2} - 4 \frac{k_1+k_2}{m_1} \right] \times$$

$$\left[ \frac{(c_1+c_2)^2}{m_1^2} + \frac{c_2^2}{m_1 m_2} - 4 \frac{k_2}{m_2} \right] >$$

$$\left( \frac{1}{m_1 m_2} 4k_2 - \frac{c_1 c_2 + c_2^2}{m_1} - \frac{c_2^2}{m_2} \right)^2$$

If the parameters  $m_1$ ,  $c_1$  and  $k_1$  are now chosen to satisfy (3) (along with the physical constraints that  $m_1$ ,  $c_1$  and  $k_1$  are all positive) then (1) will be overdamped in each mode and will not oscillate when perturbed from equilibrium. In total the six parameters must satisfy eight inequalities [5,6].

The approach taken here was to simply fix the values of  $m_1$  and  $k_1$  and choose values of  $c_1$  to satisfy (3). For example the values

$$m_1 = 1 \quad m_2 = 1$$

$$c_1 = 4 \quad c_2 = 5$$

$$k_1 = 1 \quad k_2 = 2$$

satisfy (3). In order to verify that this set of values implies overdamping, we solve the eigenvalue problem using these parameters. This yields the characteristic polynomial

$$\lambda^4 + 13\lambda^3 + 24\lambda^2 + 13\lambda + 2 = 0.$$

with eigenvalues

$$\lambda_1 = -0.2662$$

$$\lambda_2 = -0.3323$$

$$\lambda_3 = -1.2941$$

$$\lambda_4 = -10.9074$$

Thus, the design procedure yields an overdamped response, since each eigenvalue is a negative real number.

#### Design Application

The process described here may be useful in enhancing the survivability of certain structures by designing them to have an overdamped free response. In order to illustrate this in a design context, we consider the drive train of a Darrieus wind turbine. A model, excluding damping, of the DOE/Sandia, 60 KW, vertical axis wind turbine and drive train is provided by Rueter [7-8] and is reproduced here with the addition of damping (see Figure 2). The numerical values for inertia and stiffness are listed in the appendix along with the definition of each parameter.

In order to produce a C matrix which would allow inequalities similar to (3) to be formulated, some mechanism must be available for adding damping to the system. For non-rotational systems this may be accomplished by use of shock absorbers or linear actuators. For rotational systems, devices such as Houdaille dampers may be useful. Figure 2 indicates the addition of such dampers to an existing system (i.e.,  $c_1, c_2, c_3, c_5$  and  $c_6$ ).

$$M = \begin{bmatrix} J_1 & 0 & 0 & 0 \\ 0 & J_2 & 0 & 0 \\ 0 & 0 & J_3 & 0 \\ 0 & 0 & 0 & J_4 \end{bmatrix}$$

$$C = \begin{bmatrix} c_1 & -c_1 & 0 & 0 \\ -c_1 & c_1+c_2 & -c_2 & 0 \\ 0 & -c_2 & c_2+c_3 & -c_3 \\ 0 & 0 & -c_3 & c_3+d_4 \end{bmatrix}$$

$$K = \begin{bmatrix} k_1 & -k_1 & 0 & 0 \\ -k_1 & k_1+k_2 & -k_2 & 0 \\ 0 & -k_2 & k_2+k_3 & -k_4 n_1 n_2 \\ 0 & 0 & -k_4 n_1 n_2 & k_4 \end{bmatrix}$$

where the  $J_i$  are the various values of inertia, the  $c_i$  are added damping constants,  $d_4$  is the damping constant due to the induction generator,  $k_1$  and  $k_2$  are shaft stiffness constants and  $k_3$  and  $k_4$  are stiffness constants associated with the transmission and pulley system. The transmission has a gear ratio  $n_1$  and the timing belt has a ratio of  $n_2$ . Forming the matrix  $A^2-4B$  yields:

$$(A^2-4B)_{11} = \frac{(c_1+c_5)^2}{J_1^2} + \frac{c_2^2}{J_1 J_2} - 4 \frac{k_1}{J_1}$$

$$(A^2-4B)_{12} = (A^2-4B)_{21} = -\frac{c_2(c_1+c_3)}{J_1 \sqrt{J_1 J_2}} - \frac{c_2(c_1+c_2+c_6)}{J_2 \sqrt{J_1 J_2}}$$

$$(A^2-4B)_{13} = (A^2-4B)_{31} = \frac{c_2^2}{J_2 \sqrt{J_1 J_3}}$$

$$(A^2-4B)_{14} = (A^2-4B)_{41} = 0$$

$$(A^2-4B)_{22} = \frac{c_2^2}{J_1 J_2} + \frac{(c_1+c_2+c_6)^2}{J_2^2} + \frac{c_2^2}{J_2 J_3} - 4 \frac{k_1+k_2}{J_2}$$

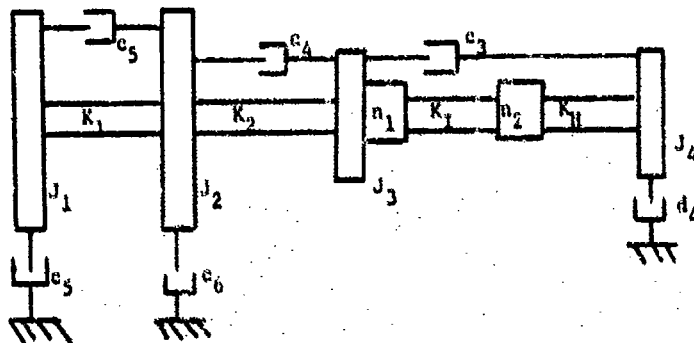


Fig. 2 Schematic of turbine and drive train components

$$(A^2-4B)_{23} = -\frac{c_2(c_1+c_2)}{J_2\sqrt{J_2J_3}} - \frac{c_2(c_2+c_3)}{J_3\sqrt{J_2J_3}} + 4\frac{k_2}{\sqrt{J_2J_3}}$$

$$= (A^2-4B)_{32}$$

$$(A^2-4B)_{24} = (A^2-4B)_{42} = \frac{c_2c_3}{J_3\sqrt{J_2J_4}}$$

$$(A^2-4B)_{33} = \frac{c_2^2}{J_2J_3} + \frac{(c_2+c_3)^2}{J_3^2} + \frac{c_3^2}{J_3J_4} - 4\frac{k_2+k_3}{J_3}$$

$$(A^2-4B)_{34} = -\frac{c_3(c_2+c_3)}{J_3\sqrt{J_3J_4}} - \frac{c_3(c_3+d_4)}{J_4\sqrt{J_3J_4}} + 4\frac{n_1n_2k_4}{\sqrt{J_3J_4}}$$

$$= (A^2-4B)_{43}$$

$$(A^2-4B)_{44} = \frac{c_3^2}{J_3J_4} + \frac{(c_3+d_4)^2}{J_4^2} - 4\frac{k_4}{J_4}$$

The addition of  $c_1$ ,  $c_2$ ,  $c_3$ ,  $c_4$  and  $c_6$  is necessary to make  $A^2-4B$  positive definite. Requiring the four leading principal minors of the  $4 \times 4$  matrix  $A^2-4B$  to be positive, yields four inequalities in the inertia, damping and stiffness parameters. Using the values from [7] and [8] for  $J_1$  and  $k_1$  (listed in the appendix) and choosing the  $c_i$  to satisfy the inequalities yields:

$c_1 = 12.0000 \times 10^4$	N-m sec/rad
$c_2 = 5.8653 \times 10^4$	" "
$c_3 = 1.4700 \times 10^5$	" "
$d_4 = 3.5300 \times 10^5$	" "
$c_5 = 18.0000 \times 10^4$	" "
$c_6 = 7.1347 \times 10^4$	" "

as one possible solution for the added damping constants.

The characteristic polynomial for this system is

$$2.024397 \times 10^{-5} \lambda^8 + 9.003867 \times 10^{-3} \lambda^7 + 1.36778 \lambda^6$$

$$+ 83.34538 \lambda^5 + 1.973763 \times 10^3 \lambda^4$$

$$+ 1.581429 \times 10^4 \lambda^3 + 2.502764 \times 10^4 \lambda^2$$

$$+ 8.958851 \times 10^3 \lambda + 2.105979 = 0,$$

which has roots:

$$\lambda_1 = -.152, \lambda_2 = -.328,$$

$$\lambda_3 = -.334, \lambda_4 = -.461$$

$$\lambda_5 = -1.75 \times 10^5, \lambda_6 = -1.03 \times 10^5,$$

$$\lambda_7 = -2.47 \times 10^4, \lambda_8 = -2.61 \times 10^4.$$

## Conclusion

A method for eliminating oscillation in  $n$ -degree of freedom lumped parameter systems by increasing the amount of viscous damping in the system has been presented. Examples of two and four degree of freedom systems indicate the complexity of the process and its level of applicability.

Another method available to produce total overdamping is given in [2] for two degree of freedom systems. Unfortunately to extend the process in [2] to  $n$ -degrees of freedom requires a closed form solution of polynomials of degree  $(n-1)$ . However, the method here requires only the numerical solution of non-linear equalities. Also, for the two degree of freedom case, the method presented in [2] allows only the parameters  $c_1$  and  $c_2$  to be adjusted. As an alternative, the method presented here allows all of the parameters  $n_i$ ,  $c_i$  and  $k_i$  to be adjusted. Thus it seems that the method presented here may be more computationally useful in design work.

## Acknowledgement

The authors wish to thank the reviewers for their helpful criticisms. The first author acknowledges the support of the Research Foundation of SUNY.

## References

1. Inman, D.J. and Andry, A.N., Jr. 'Some Results on the Nature of Eigenvalues of Discrete Damped Linear Systems', J. Appl. Mech. 47(4), pp. 927-930 (1980).
2. Beakos, D.E. and Boley, M.A. 'Critical Damping in Linear Discrete Dynamic Systems', J. Appl. Mech., 47(3) pp. 627-630 (1980) see also tech. rep., ONR Grant/Contract #N00014-74-C-1042.
3. Bellman, R., 'Some Inequalities for the Square Root of a Positive Definite Matrix', Linear Algebra and its Applications, 1, pp. 321-324 (1968).
4. Bellman, R., Introduction to Matrix Analysis, 2nd ed. McGraw Hill (1970).
5. Brent, R., 'Some Efficient Algorithms for Solving Systems of Nonlinear Equations', SIAM J. Numer. Anal., 10 pp. 327-344 (1973).
6. Byrne, G., and C. Hall, 8ds. Numerical Solution of Systems of Nonlinear Algebraic Equations, Academic Press, New York 1973.
7. Reuter, R.C., Jr., 'Torque Ripple in a Barrius, Vertical Axis Wind Turbine', ASME paper No. 80-WA/202-12 (1980).

8. Reuter, R.J., Jr., and Worstell, M.H., 'Torque Ripple in a Vertical Axis Wind Turbine', Sandia Nat. Lab. Rep. No. SAND 78-0577 (1978).

Appendix Parameter values of the DOE/SANDIA WIND TURBINE (values taken from [7]) for the case of tip speed ratio of 2 and turbine rotational speed of 50.6 RPM

$$J_1 = J_2 = 1/2 \text{ of turbine motor inertia} = 1.65 \times 10^4 \text{ N-sec}^2\text{-m} \quad (1.46 \times 10^4 \text{ lb-sec}^2\text{-in})$$

$$J_3 = \text{transmission inertia} = 2.43 \times 10^3 \text{ N-sec}^2\text{-in} \quad (2.15 \times 10^3 \text{ lb-sec}^2\text{-in})$$

$$J_4 = \text{generator inertia} = 3.06 \text{ N-sec}^2\text{-in} \quad (27.1 \text{ lb-sec}^2\text{-in})$$

$$n_1 = \text{transmission gear ratio} = 35.6$$

$$n_2 = \text{pulley gear ratio} = \frac{1800}{(35.6)(50.6)} = .999$$

$$k_1 = \text{rotor tower stiffness} = 1.65 \times 10^6 \text{ N-m/rad} \quad (1.46 \times 10^6 \text{ lb-in/rad})$$

$$k_2 = \text{shaft stiffness} = 2.69 \times 10^6 \text{ N-m/rad} \quad (2.39 \times 10^6 \text{ lb-in/rad})$$

$$K_I = \text{transmission shaft stiffness} = 1.41 \times 10^6 \text{ N-m/rad} \quad (1.25 \times 10^6 \text{ lb-in/rad})$$

$$J_H = \text{generator shaft stiffness} = 2.10 \times 10^5 \text{ m-m/rad} \quad (1.86 \times 10^4 \text{ lb-in/rad})$$

$$k_3 = \frac{n_1^2 n_2^2 K_I K_H}{k_1 + n_2^2 K_H} = 2.62 \times 10^6 \text{ N-m/rad} \quad (2.39 \times 10^6 \text{ lb-in/rad})$$

$$k_4 = \frac{k_3}{n_1^2 n_2^2} = 2.07 \times 10^5 \text{ N-m/rad} \quad (1.83 \times 10^4 \text{ lb-in/rad})$$



# On the Optimal Location of Vibration Supports

B. P. Wang, W. D. Pilkey  
University of Virginia  
Charlottesville, Virginia 22901

The problem of optimal positioning of vibration supports to raise the fundamental natural frequency of a system is studied. It is proposed that possible locations of the supports can be compared by studying the corresponding antiresonant frequencies. It is contended that a near optimal location is achieved by locating the supports such that the corresponding lowest antiresonant frequency is a maximum and a criterion is proposed. Numerical examples are used to illustrate this criterion.

## INTRODUCTION

Intermediate supports are often introduced in engineering structures to increase the resonant frequencies of the system as well as to support weights. These supports, when realized by actual structural components, are elastic supports. Thus, the problem of designing vibration supports to raise the fundamental frequency involves finding both the location and the required stiffness of the supports.

In an earlier paper, Besler and Curreri (1) studied the design of vibration supports for piping systems. They used the transformatrix method to study a spring supported cantilever beam and a spring supported L bend. They found the optimum spring location, i.e., the most effective location to put a spring to increase the fundamental frequency, from numerical experimentation. They concluded that a nearoptimal position for a flexible spring is at a node of the second mode. For a rigid support this would be the optimal location.

In the present paper, a criterion for selecting the optimal spring locations will be derived. This criterion can also be used to compare the relative effectiveness of sets of proposed support locations.

## PROBLEM FORMULATION

For a multiple-degree-of-freedom, undamped system with a spring rate of  $k$  introduced at dof  $J$ , the frequency equation is

$$\frac{1}{k} + R_{JJ}(\omega) = 0 \quad (1)$$

where  $R_{JJ}(\omega)$  is the receptance of dof  $J$ . Equation (1) can be derived using the receptance method [2]. Alternatively, it can be found by considering the addition of a spring to a system as a local modification [3,4,5]. The receptance  $R_{JJ}(\omega)$  can be expressed in modal summation form as

$$R_{JJ}(\omega) = \sum_{i=1}^n \frac{\rho_{Ji}^2}{G_i(\omega_i^2 - \omega^2)} \quad (2)$$

where  $\omega_i$  is the natural frequency of the  $i$ th mode of the unsupported system,  $(\rho_i)$  is the corresponding eigenvector,  $\rho_{Ji}$  is the  $J$ th component of  $(\rho_i)$ ,  $n$  is the number of modes utilized, and  $G_i = (\rho_i)^T [m] (\rho_i)$  is the generalized mass of the  $i$ th mode. Thus, for any given spring rate  $k$ , Eq. (1) along with Eq. (2) can be used to solve for the new frequencies  $\omega$ . The natural frequencies of the supported system increase as the spring rate increases. In the limit, as  $k$  approaches infinity, i.e., as the support becomes ideally rigid, the frequency equation becomes

$$R_{JJ}(\omega) = 0 \quad (3)$$

Denote the lowest  $\omega$  that satisfies Eq. (3) as  $\omega^{(J)}$ . Then  $\omega^{(J)}$  is the lowest antiresonant frequency of dof  $J$ . That is,  $\omega^{(J)}$  is the highest fundamental frequency achievable when the support at dof  $J$  becomes rigid. It follows from the eigenvalue separation property [6],

that  $a^{(J)} < \omega_2$ , where  $\omega_2$  is the second natural frequency of the unsupported system. Thus, by choosing dof J for a rigid support as a node in the second mode of the unsupported system, we have  $a^{(J)} = \omega_2$ , which is the maximum obtainable fundamental frequency. This result has been known for some time [1].

Now consider the case of introducing springs at dof  $J_1, J_2, \dots, J_s$ . Following the procedure of Ref. [5], the frequency equation of the supported system is given by

$$\det([I] + [\hat{R}][\Delta K]) = 0 \quad (4)$$

where  $[I]$  is an  $s \times s$  identity matrix  
 $[\hat{R}]$  is the receptance matrix associated with the dof  $J_1, J_2, \dots, J_s$ , i.e.,

$$\hat{R}_{ij} = R_{J_i J_j} \quad (5)$$

$$[\Delta K] = \begin{bmatrix} \Delta k_1 & & \\ & \Delta k_2 & \\ & & \ddots \\ & & & \Delta k_s \end{bmatrix} = \text{an } s \times s \text{ diagonal matrix}$$

$\Delta k_j$  is the spring rate of the support at dof j.

In the limiting case when all  $\Delta k_j \rightarrow \infty$ , Eq. (4) becomes

$$\det[\hat{R}] = 0 \quad (6)$$

Let  $a^{(J)}$  be the lowest root of Eq. (6). Then the optimal rigid support locations will be where

$a^{(J)}$  is a maximum. We are now in a position to propose a criterion for near optimal flexible support locations.

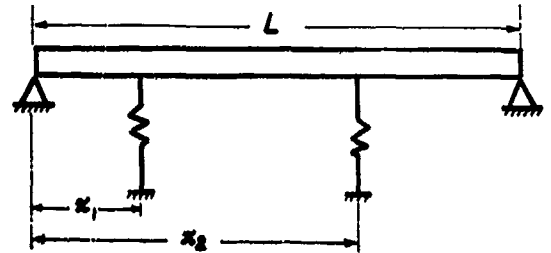
#### MAXIMUM ANTIRESONANT FREQUENCY CRITERION (MAFC)

For given sets of support locations, a near optimal set of locations is where the corresponding lowest antiresonant frequency is a maximum.

We will call this criterion the Maximum Antiresonant Frequency Criterion (MAFC). This criterion leads to the two optimal locations for rigid supports and to near optimal ones for flexible supports; the stiffer the spring rates, the better the criterion. To find the antiresonant frequency, one can either solve an eigenvalue problem of order  $(n-s)$  or solve the nonlinear Eq. (6).

#### NUMERICAL EXAMPLES

To illustrate the basic contention of the MAFC criterion, consider the simply supported beam of Fig. 1. The fundamental frequency of this beam is 15.71 Hz. It is desired to introduce two intermediate supports to increase the fundamental natural frequency to above 25 Hz. For this example it is practical to restrict the support locations to two possible sets of positions, say A ( $x_1 = .1L$ ,  $x_2 = 0.5L$ ) and B ( $x_1 = 0.34L$ ,  $x_2 = 0.67L$ ).



$$L = 2.54 \text{ m (100 in.)}$$

$$E = 69 \text{ GPa (10}^7 \text{ psi)}$$

$$\rho = 8748.73 \frac{\text{kg}}{\text{m}^3} \left( 0.01 \frac{\text{lb-sec}^2}{\text{in}^2} \right)$$

$$I = 4.1623 \times 10^{-6} \text{ m}^4 \text{ (10 in}^4 \text{)}$$

Fig. 1 A simply supported beam

For this case with two supports, we have

$$[\Delta K] = \begin{bmatrix} \Delta K_1 & 0 \\ 0 & \Delta K_2 \end{bmatrix} \quad (7)$$

and

$$[\hat{R}] = \begin{bmatrix} \hat{R}_{11} & \hat{R}_{12} \\ \hat{R}_{21} & \hat{R}_{22} \end{bmatrix} \quad (8)$$

It is convenient to calculate the elements  $\hat{R}_{ij}$  with a modal summation. Thus,

$$\hat{R}_{ij} = R(x_1, x_2) = \sum_{n=1}^{\infty} \frac{\phi_n(x_1)\phi_n(x_2)}{0_i(\omega_n^2 - \omega^2)} \quad (9)$$

where, for a simply supported beam,

$$\rho_2(x_1) = \sin \frac{\pi x}{L}$$

$$G_2 = 1/2 \rho L$$

$$\omega_1 = \frac{(1\pi^2)}{L^2} \sqrt{\frac{EI}{\rho}}$$

In the numerical calculation  $n = 20$  is used, or, in other words, 20 modes are used to evaluate the receptances in Eq. (9). The frequency determinant of Eq. (7) gives

$f_1^{(A)}$  = fundamental natural frequency for rigid supports at  $x_1 = 0.1L$ ,  $x_2 = 0.5L$   
 $f = 70.9$  Hz

$f_1^{(B)}$  = fundamental natural frequency for rigid supports at  $x_1 = 0.34L$ ,  $x_2 = 0.67L$   
 $= 180.1$  Hz

Since  $f_1^{(B)} > f_1^{(A)}$ , we conclude that the location pair B is more effective than location pair A in raising the fundamental frequency of the system.

To check the above proposition, we will compute the fundamental frequencies of the spring supported beam for the special case of equal spring rates. The results are summarized in Table 1. Alternatively, we can compute the required (equal) spring rates for both springs for given fundamental frequencies. The results are summarized in Table 2. We observe that to raise the fundamental frequency above 25 Hz, springs with rates of about  $1.23 \times 10^6$  N/m (7000 lb/in) are needed at location  $x_1 = 0.1L$  and  $x_2 = 0.5L$ , while less stiff springs with rates of  $0.88 \times 10^6$  N/m (5000 lb/in) are needed if they are located at  $x_1 = 0.34L$ ,  $x_2 = 0.67L$ .

As a second numerical example, consider the clamped-supported beam of Fig. 2 with an intermediate spring support. The fundamental frequency of this beam is plotted in Fig. 3 as a function of support spring locations and rates. From NAFPC, a near optimal location is determined to be  $x = 27.4$  in., the point of maximum antiresonant frequency. This is the optimal location for a rigid support. The optimal support diverges from  $x = 27.8$  as the stiffness of the support is decreased. However, note that the system with a spring support located at  $x = 27.8$  results in a system almost as good as the system with a spring located at the true optimal location.

#### CONCLUSION

In summary, a simple criterion has been derived that will allow a designer to determine

the relative effectiveness of possible sets of locations for placing vibration supports. This will narrow the design problem to that of determining the required stiffness to achieve a desired fundamental natural frequency.

TABLE 1  
Natural Frequencies for Simply Supported Beam  
with Two Equal Intermediate Springs

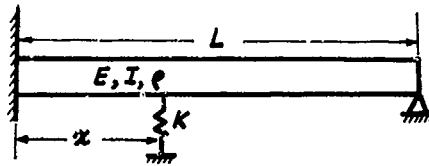
Spring Stiffness N/m	(lb/in.)	Fundamental Natural Frequency of the Supported System (Hz)	
		$x_1 = 0.1L$ $x_2 = 0.5L$	$x_1 = 0.34L$ $x_2 = 0.67L$
17513	(100)	15.88	15.95
87565	(500)	16.67	16.88
175130	(1000)	17.38	17.98
350268	(2000)	18.90	20.00
525390	(3000)	20.30	21.81
700520	(4000)	21.61	23.48
875650	(5000)	22.82	25.05
1751300	(10,000)	28.07	31.72
=		76.9	180.1

TABLE 2  
Required Spring Rate to Achieve Prescribed  
Natural Frequency

Fundamental Natural Frequency (Hz)	Required Spring Stiffness (lb/in) for Springs at	
	$x_1 = 0.1L$ N/m	$x_2 = 0.5L$ (lb/in)
16	29238	(166.95)
17	133608	(762.91)
18	244632	(1396.86)
19	362386	(2069.24)
20	486935	(2780.42)
25	1214360	(6934.07)
30	2125640	(12137.50)

Fundamental Natural Frequency (Hz)	Required Spring Stiffness (lb/in) for Springs at	
	$x_1 = 0.34L$ N/m	$x_2 = 0.67L$ (lb/in)
16	21220.5	(121.17)
17	948962.7	(533.09)
18	177135	(1011.45)
19	262047	(1496.3)
20	351610	(2007.71)
25	869482	(4964.78)
30	1505170	(8594.61)



$L = 50$  inch  
 $EI = 5 \times 10^6$  lb-in<sup>2</sup>  
 $\rho = 0.0005181$  lb-sec<sup>2</sup>/in  
 $x$  = spring location

Figure 2. Fixed supported beam with intermediate spring support.

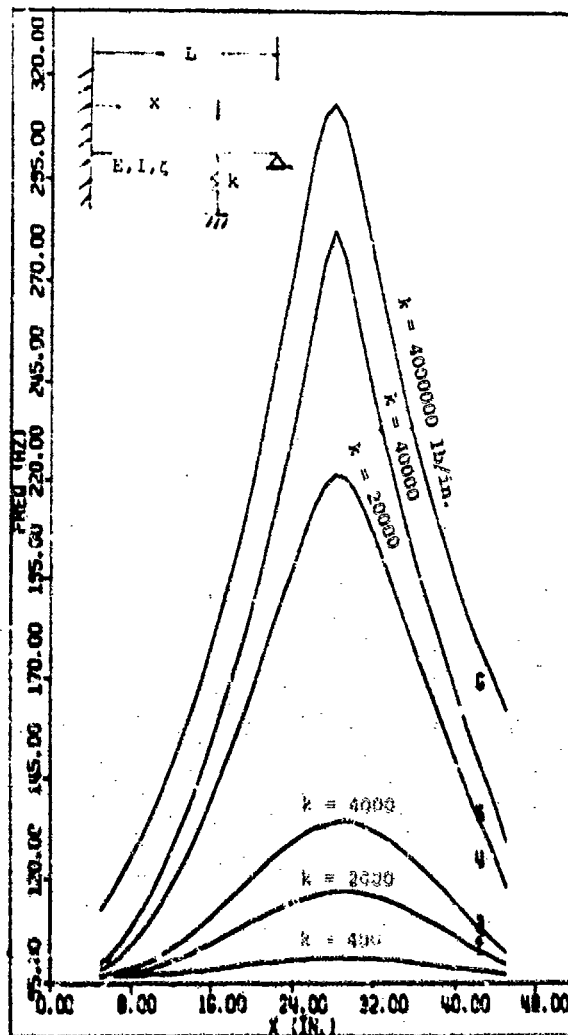


Figure 3. Variation of first natural frequency for different spring rate and location.

#### ACKNOWLEDGMENT

This work was supported by the Office of Naval Research, Arlington, Virginia. The assistance of Mr. G. Mayer of the University of Virginia for the second numerical example is acknowledged.

#### REFERENCES

1. P. Bezler, and J.R. Curreri, "Some Aspects of Vibration Control Support Designs," The Shock and Vibration Symposium Bulletin, The Shock and Vibration Information Center, No. 47, Part 2, Sept. 1977, pp. 1-3.
2. R.E.D. Bishop, and C.D. Johnson, "The Mechanics of Vibration", 1st ed., The University Press, Cambridge, 1960.
3. B.P. Wang, A.B. Palazzolo, and W.D. Pilkey, "Reanalysis, Modal Synthesis and Dynamic Design," Chapter 8, State of the Art Review of Finite Element Methods, edited by A. Noor and W. Pilkey, ASME, 1981.
4. B.P. Wang, and W.D. Pilkey, "Efficient Reanalysis of Locally Modified Structures," Proceedings of the First Chautauqua on Finite Element Modeling, 1980, Schaeffer Analysis.
5. B.P. Wang, and F.H. Chu, "Effective Dynamic Reanalysis of Large Structures," Shock and Vibration Bulletin, No. 51.
6. K.J. Bathe, and E.L. Wilson, Numerical Methods in Finite Element Analysis, 1st ed., Prentice Hall, New Jersey, 1976, p. 60.

## DYNAMIC BUCKLING OF PINNED COLUMNS

J. M. Ready

David W. Taylor Naval Ship R&D Center  
Bethesda, MD 20084

### ABSTRACT

To develop design guidance for foundations of shipboard equipment DTNSRDC conducted a series of dynamic tests on parametrically varied pinned columns. Tests showed that incipient buckling can occur at loads as low as 70 percent of the Euler buckling load. Applied dynamic loads of 50 percent of the Euler load do not appear to cause buckling when eccentricity is low. The tests also showed that columns can carry loads that are multiples of the Euler load provided the load duration is short compared to the fundamental bending period of the columns; otherwise the columns collapse. Columns subjected to dynamic compressive loads equal to the Euler load and of a duration equal to the period of the column are in imminent danger of collapse.

### INTRODUCTION

An underwater explosion (UNDEX) near a ship can induce dynamic compression loads in foundations of internal equipment mounted in the ship. This loading can trigger in the compression members a collapse mechanism called dynamic buckling. As used in this text, dynamic buckling is the collapse history of a column that bends in its fundamental mode. The expected increase in use of high strength steel (e.g. HY-130) in the structures of Navy ships can lead to a reduction of structural sections over that if HY-80 or HTS steel were used. This can occur when yield stress governs a design rather than a critical buckling stress. The reduced section may, in the case of columns, increase their susceptibility to buckle dynamically from the effects of an underwater shock loading on a ship.

David W. Taylor Naval Ship R&D Center (DTNSRDC) conducted a series of dynamic buckling tests, the purpose of which was to:

- Confirm some of the theoretical observations about dynamic buckling, e.g. long columns can withstand multiples of its Euler capacity for short periods of time;
- Determine circumstances, if any, in which dynamic buckling becomes a problem;
- Develop design guidelines.

### DIMENSIONAL ANALYSIS

To help design columns for dynamic buckling tests and to analyze test data a dimensional analysis was made to determine significant parameters involved in their dynamic behavior. A pinned column of rectangular section, having a measured offset at its midpoint, was conceived in which one end was vertically restrained and the other was free to rotate and to move vertically. It is idealized to that shown in Figure 1.

The variables involved in buckling are the applied load  $P$ , its duration  $\theta$ , the rise time of the loading  $t_r$ , the midpoint deflection  $y$ , and a characteristic of the column's bent shape, either the eccentricity  $y$ , or its radius of curvature. Other variables for the column include length  $L$ , radius of gyration  $r$ , fundamental period  $T$ , Euler load  $P_E$ , any static weight  $W$  on the column, and finally, the column area  $A$ . Variables accounting for material properties include density  $\rho$ , and modulus of elasticity  $E$ .

In the above listing, deflection, is a dependent variable. But duration  $\theta$  may also be a dependent variable because vertical motion of the end of the column may affect it. Hence,  $\theta$  will be a dependent variable in this analysis.

To these dependent variables a characteristic strain at the midpoint of the column can be added, if only one cross-sectional shape is to be investigated, as here in this case. In a general case, a characteristic of the cross-section, e.g., section modulus, must be included in the list of independent variables. The variables ( $\epsilon$ ,  $\theta$ ,  $y$ ) give rise to three independent nondimensional equations of which only one is shown below; the other two are similar. If we have accounted for all the variables that affect dynamic buckling, a functional equation appears as:

$$f(y, y_1, \ell, r, T, t_r, E, \rho, P, P_E, A, W) = 0 \quad (1)$$

Following the Buckingham Pi Theorem,<sup>1,2,3</sup> we have 12 variables and three dimensions, thus there are 9 dimensionless variables that affect dynamic buckling. After some manipulation, a nondimensional equation may be derived and it appears as:

$$y/y_1 = (\ell/r)^2 \cdot P_E/AE \psi(y_1/\ell, \ell/r, t_r/T, t_{rc}/\ell, P/P_E, W/P_E, A/\ell^2) \quad (2)$$

Note: acoustic velocity  $c_0 = (E/\rho)^{1/2}$

The deflection ratio  $y/y_1$ , the duration ratio  $\theta/T$ , or the characteristic midpoint strain could be used on the left side of this equation. Of the independent variables that are listed in equation 2,  $y_1/\ell$ ,  $\ell/r$ ,  $t_r/T$ ,  $t_{rc}/\ell$ ,  $A/\ell^2$  and  $P/P_E$  are judged to be the most important. The effect of the variable  $W/P_E$  is judged small for these tests. But static loads could have a significant effect on buckling history of a column; they lower the fundamental frequency, making the column slower to respond than it would otherwise. In these tests a static load came from spacers that had to be interposed between an applied load and the column. In the worst case of these tests, the effect of static load was estimated to be less than 10 percent of the response of the column with no initial loading.

#### TEST DESCRIPTION

##### APPARATUS

To do these tests the drop weight machine shown in Figure 2 was used. A 224 lb. weight was suspended above a column and then released. The weight rode between rails that guided its downward path. Between the top end of the column and the drop weight was a spacer, stop of which was a crushable styrofoam block. The styrofoam block was used to resolve the impact of the 224 lb. drop weight to a

constant force which was then transmitted down the spacer to the column below.

The test columns were made from bars having a rectangular cross-section and to which round bars of 3/4" diameter were welded breadth-wise at each end of a column. The post-test photographs of Figure 3 show the manner of the construction of the columns. When the columns were vertically placed in the machine the cross bars extended beyond the breadth of the column and into vertical guide channels located to either side of the column. The guide channels were welded in place in the machine, and since the cross bars close fit into the channels, they served to keep the ends of the column reasonably aligned, yet they permitted the top of the column to rotate and to move vertically in response to the drop weight.

#### DESCRIPTION OF COLUMN

The geometries and properties of all the columns are listed in Table 1. Note that preset eccentricities  $y_1$  of the columns were altered because of the weight of spacers on the columns; at first they did not appear significant and were not measured. However, later it seemed prudent to use altered values of eccentricities. So the altered eccentricities that resulted were calculated and are shown in Table 1A. These values were used in all subsequent calculations involving eccentricity.

The columns used in these tests were made of 6061-T6 aluminum. The test results should be equally applicable to other materials because of the parametric nature of the testing.

#### NUMBER OF TESTS AND LOAD CONDITIONS

For these tests a total of 9 columns were used of which three were nearly identical and the remaining 6 were parametrically varied according to equation 2. The columns were numbered 1 through 7; note that there were 3 No. 7 columns. Columns 1 through 6 were tested twice - one test with an applied load about 1/2 of their Euler capacity and another test using an applied load equal to the Euler capacity. Column 7 could only be tested once, since the drop weight itself would buckle the column. For this column (3 in number) loads of 1, 2 and 8 times their Euler capacities were applied.

The total number of tests was 17, encompassing load conditions of 1/10 to 8 times the Euler capacity of the columns with the bulk of the experiments done at load conditions of 1/2 and full Euler loads. For column 1 a repeatability test of 1/2 its Euler capacity was done. And column 6, a short, strong column, was tested to 1/10 of its Euler capacity.

in addition to the  $1/3$  and full Euler load tests. Note that these load conditions represent ideal values; actual load conditions were different. Table 2 identifies the tests and the ideal load conditions.

#### LOAD SHAPE

Static tests have shown that styrofoam when statically compressed to a certain stress will crush under a constant load. At about 50 percent strain, the styrofoam stiffens and the stress rises exponentially till complete compression obtains. Under the impact force from the 224 lb. drop weight a similar load shape, but varying in time, is obtained. For example, Figure 4 shows a typical acceleration history of the 224 pound mass as it crushes a styrofoam block for which the support was relatively stiff. The record shows a rise time (6 msec) in which acceleration reaches some value which then remains constant for a period of time, followed by a stiffening of the styrofoam which gives rise to accelerations much beyond the constant value.

Constant force crushing of styrofoam is a convenient property for use in these buckling tests. The loading and its effects are easily defined or characterized during the period in which acceleration, vis-a-vis force, is constant. And also, much of the theoretical work on dynamic buckling use constant forces on columns, though suddenly applied. The load shape for the buckling tests, however, is less than this ideal, since it has a finite rise time. This paper is concerned with the loading and its effects up to the time that this constant acceleration ends.

#### GROUPING OF COLUMNS

In the buckling tests the columns were divided into three groups, as shown in Table 3, such that eccentricity ( $y_1/\ell$ ), slenderness ( $\ell/r$ ) and stoutness ( $A/\ell^2$ ) ratios would be variables. Group I contains three columns while Groups II and III have two columns each. As Table 3 shows, however, only in the test series of eccentricity (Group I) was it possible to completely isolate eccentricity and keep the other non-dimensional variables constant. In Group II, it was not possible to isolate slenderness; the period ( $T$ ) of columns, appearing in the ratio  $T_0/\ell$ , also varied. And in Group III it was not possible to isolate stoutness ( $A/\ell^2$ ); the  $T_0/\ell$  and slenderness ratios also varied. Obviously, having more than one variable makes the correlation of data difficult. But when these "extra" variables come into play later on in this report, their effects are judged to be secondary or tertiary to column response.

#### INSTRUMENTATION

The instrumentation consisted of 2 strain gages, 2 displacement gages, 1 accelerometer and a timing signal. Two strain gages were mounted at the midpoint of each column; one gage measured a bending strain and the other measured axial compressive strain. See Figure 2.

Displacement meters were used to measure the lateral displacement of the mid-section and vertical displacement of the upper end of the columns. These meters can be seen in Figures 2.

An accelerometer was mounted to the side of the drop weight. See Figure 2.

#### TEST RESULTS

##### OSCILLOGRAPH RECORDS

Figures 5, 6 and 7 are typical records of the responses of a column to the impact of the drop weight. The responses in Figures 5 and 6 are for the nominal load condition of  $R = 1/2$  or for an applied load of  $1/2$  the Euler capacity of the test columns. For Figure 7 the applied load is about  $2 1/2$  times the drop weight or a nominal load condition of  $R = 1$ .

In Figures 5 and 6 we can see that the time at which the duration of flat acceleration ends, is signalled by a sinusoidal motion, and that prior to this sinusoidal action the lateral displacement reached a maximum. Note that axial strains are small compared to bending strains and also that their durations are short. In the case of the  $R = 1$  load condition, Figure 7 shows that bending strain, and the lateral and vertical displacements continue to rise beyond the period of flat acceleration. This is expected, since the applied load is more than the Euler load, and the column would therefore buckle.

Figure 8 is a collection of ten records that show response histories of several columns after impact by the drop weight. The plots were taken from oscillograph records and are shown here in non-dimensional form; response is in terms of deflection  $y/y_1$  and time in terms of  $t/T$  where  $t$  is the real time and  $T$  is the period of the column. Zero time for each plot was taken at the start of lateral motion, as was indicated in the oscillographs. The measured load conditions ranged from a low of  $R = 0.423$  to a high of  $R = 7.8$ . The plots indicate that deflections increase as loading increases; for loads less than 70 percent of the Euler load ( $R = 0.70$ ) the deflections reach a peak and then start to decline. Note that there appears to be a lag between response

of columns 1 and 5. These columns are identical except that the eccentricity for column 5 is larger than for column 1.

For loads greater than 70 percent of the Euler load the tendency to peak appears to diminish until  $R = 1.12$ , or the Euler load is exceeded by about 12 percent. Beyond this loading, deflections monotonically increase with time because the Euler load is exceeded.

The deflection histories of all of these records are foreshortened because acceleration did not remain constant for the entire test event; it became sinusoidal.

#### ACCELERATION DATA

Table 4 contains acceleration data including peaks, rise times and durations. Note that the load conditions ( $R$ ) when referred to in the text below, are nominal. The accelerations ranged from a low of 0.3g (Test 7A, column 7) to a high of 12.2g (Test 6C, column 6). The rise time and duration of these accelerations, decreased as applied loads increased. The rise time is about 10 msec when  $R = 1/2$  and 5 msec when  $R = 1.0$ . Column stiffnesses do not seem to affect this value.

Under load condition  $R = 1/2$ , the durations were, except for the test on column 6, greater than 50 msec; the durations ranged from a low of 27 msec to a high of 114 msec. As load increased, its duration decreased. For example when  $R = 1.0$  durations were generally less than 30 msec; the low was 7.5 msec and the high was 54 msec.

#### STRAIN DATA

Tables 5, 6, and 7 show the peak values of strains, lateral and vertical deflections and their corresponding rise times. These values are those that occurred within the duration of the flat response of the acceleration trace.

The axial strains were about a quarter of the bending strains that are shown in the tables. They range in value from 0 to a high of 1042  $\mu\text{in/in}$  (Test 5B, Column 3). Recall that yield for 6061-T8 occurs at about 3600  $\mu\text{in/in}$ . The measured strains increased as load increased and as stiffness increased. Unfortunately, in the case of column 6, a relatively stiff column, the axial gage was affected by bending of the column. The strains that are listed are those peaks that occurred early in the strain record; those that occurred later were probably affected by bending of the column themselves. In other words, the size of the gage was a large portion of the lateral dimension of the column; hence, bending, as well as axial strain, affected

the gage reading. Early on, when lateral deflection was small the axial gage gave a truer strain account than later.

In general, bending strains are more significant than axial strains; this is not surprising since the columns tend to be long and have pronounced eccentricities. Long columns buckle at relatively low compressive axial strains, and eccentricity easily induces bending strains. Values of bending strains ranged from a low of 312  $\mu\text{in/in}$  (Test 6A, column 6) to the extremely high 19,929  $\mu\text{in/in}$  (Test 6C, column 6). Rise times ranged from the very low 3.5 msec, (Test 6C, column 6) to the very high 75 msec, (Test 7A, column 7).

#### DEFLECTION DATA

Lateral deflections ranged from about zero (Test 6A, column 6) to a high of 3.34 in. (Test 7A, column 7). Their rise times were generally the same as those for peak bending strains. Vertical displacements are about 1/3 to 1/2 of the lateral deflections and have about the same rise times.

#### ANALYSIS OF NON-DIMENSIONAL VARIABLES

##### RESPONSE OF COLUMNS

Tables 4 through 7 contain the measured test data; it includes accelerations, strains, lateral and vertical displacements, rise times and durations. This data was converted to the non-dimensional variables of equation 2 and are shown in Tables 8, 9 and 10. The following section looks at each of the non-dimensional variables and tries to correlate each variable with responses of the columns. The responses that are used are lateral deflection  $y_m/y_1$  and bending strain  $\epsilon_b$ .

##### Load Ratio

Looking first at the load ratio  $R$ , the tables show that for nominal test condition  $R = 1/2$ , the actual loading ranged from a low of 0.623 to a high of 0.71. For nominal load condition  $R = 1$ , the actual loading ranged from a low of 0.92 to a high of 1.53.

Figure 9 shows a nonlinear dependency of response  $y/y_1$  and the applied load. In the case where  $R$  increases to 1 the data plot shows a decrease in  $y/y_1$ , but this is only significant for these tests, since durations are cut short by the buckling of the column itself. Note, again, that since the Euler load was exceeded, in time the column would completely buckle; obviously lateral deflections would be more than indicated here.

What is significant though, is that when  $R = 0.7$ , the onset of yield occurs (Figure 9A);



see Table 5 for the bending strain of column 7. At 90 percent of the Euler load strains greater than 5 times the yield strain occurred; see Table 6 for the bending strain of column 6. Clearly, then, a dynamic compression load less than the Euler capacity of a column can bring on an incipient buckling situation. Whether or not a column suffers catastrophic collapse depends in part, on the duration of that load, but more importantly on the energy absorption capacity of the columns while buckling, and lastly on the residual strength of the column after the dynamic load has dissipated. For example, a column may be able to absorb plastically a dynamic load but then it could reach a deflected shape such that the normal service loads could now continue the buckling motion.

#### Eccentricity Ratio

Looking at response data for columns 1, 4, and 5 for which their slenderness ratio ( $\ell/r$ ) is constant (312.5), Figures 10 and 11 show the variation in peak response ( $y_m/y_1$ ) as a function of eccentricity ( $y_1/\ell$ ). Figure 10 shows that under a loading  $R = 1/2$  the peak deflections of the columns decrease linearly, with a shallow slope as eccentricity increases, though the absolute value of lateral deflection increases; see Table 5. When  $R = 1.0$ , the response ratio also decreases with increasing eccentricity; see Figure 10. For this case it would appear that the response ratio should be more than shown, since the Euler load was attained. However, the durations were as much as seven times less here than when the load was  $R = 1/2$  (see Table 4). In other words, had the duration of the load been as long as in the condition when  $R = 1/2$ , we might reasonably expect deflections to be as high as seven times more than measured.

The  $y_m/y_1$  responses of all of the columns are plotted in Figure 11 as a function of eccentricity  $y_1/\ell$ . Figure 11 shows that the responses of columns 2, 3, 6 and 7 are scattered about the data curve for columns 1, 4, and 5. The scatter occurs because other variables affect their behavior.

Notice in Figure 11A that in the limit as  $y_1 \rightarrow 0$ ,  $y_m/y_1 \rightarrow \infty$ ; in other words the response would appear unbounded. In the case of an applied load greater than the Euler load this is reasonable. But when  $R = 1/2$  theory indicates that response is limited, not unbounded. If that indeed is true in our case, and there is no reason to suspect otherwise, then  $y_m = f(y_1)$ , such that when the  $y_1 = 0$ , the maximum lateral displacement  $\delta_h$  must also be zero. And if that is true, then a perfectly straight column can not buckle when subjected to  $1/2$  its Euler load. This assumes complete elasticity during the motion of the column. In other words, the column must be strong

enough to withstand elastically a deflection that is in theory twice the initial eccentricity.

Looking now at test data, Figure 11C shows for columns 1, 4 and 5 a plot of  $\delta_h$  vs.  $y_1$  which was taken from Tables 1A and 5. The plot of that data approaches zero as near as experiment allows. For small eccentricities the initial slope of of this curve is about  $\delta_h/y_1 = 0.83$ . The maximum midpoint deflection of a column is  $y_m$  and

$$y_m = \delta_h + y_1 \quad (3)$$

where  $y_1$  is the initial eccentricity

and  $\delta_h$  is the midpoint displacement of a column

Dividing equation 3 by  $y_1$  we have

$$y_m/y_1 = 1 + \delta_h/y_1 \quad (3A)$$

And substituting  $\delta_h/y_1 = 0.83$  into equation 3A we have

$$y_m/y_1 = 1.83 \quad (4)$$

In other words when  $y_1 \rightarrow 0$ ,  $y_m/y_1 \rightarrow 1.83$ . This value in the limit for small eccentricities supports the bound  $y_m/y_1 = 2$  derived in several related theoretical works.<sup>4-7</sup>

Though largely of academic interest, there is another bound but at the upper limit of eccentricity or,  $y_1/\ell = 1/2$ . At that point  $\delta_h$  is again zero, but now it is because the column is entirely bent over, and it has no lateral movement left. In this case  $\delta_h = 0$ , hence  $y_m/y_1 = 1$ .

In summary, eccentricity does play a role in the response of a column. At low eccentricities the response seems to be limited to about twice the initial eccentricity. As eccentricity goes to its upper limit of  $\ell/2$ , response decreases, or in the limit  $y_m/y_1 \rightarrow 1$ .

Bending strains for columns 1, 4, and 5 are shown in Table 5, 6, and 7; these values, after subtracting a calculated axial compression stress, are plotted in Figure 12. The strains are consistent with the previously shown deflection data. When  $R = 1/2$  the strains increase with increasing  $y_1/\ell$ . When  $R = 1.0$  the strains decrease as  $y_1/\ell$  increases; had the durations been as long here as when  $R = 1/2$ , then the strains would have been concomitantly increased. In fact, if the strains were increased by the ratio of the duration when  $R = 1.0$  and  $R = 1/2$ ,

respectively, then the strains would be in Figure 12 on a curve sloped in the same general direction as that when  $R = 1/2$ ; strains increase with increasing eccentricity

#### Slenderness Ratio ( $\ell/r$ )

Looking at the response data for Group II columns 2 and 4, Figure 13 shows the variation of response ( $y_m/y_1$ ) with slenderness ratio. For nominal load condition  $R = 1/2$  the response increases with increasing slenderness ratio; on the other hand, when  $R = 1.0$  the reverse appears. But as noted before, had the duration been as long for this condition as for when  $R = 1/2$  then the responses would have been more. Data for the remaining columns are plotted in Figure 13 and appear as scatter about the line drawn for columns 2 and 4. These figures indicate a functional relationship of response and slenderness ratio.

Figure 14 is a plot of bending strain against  $\ell/r$  ratio for Group II columns 2 and 4. The curves that are drawn are consistent in slope with deflection curves of Figure 12. In general, it seems reasonable to conclude that as  $\ell/r$  increases deflection and corresponding strain would increase; the values those deflections or strains take depend on the dynamic properties of columns, as measured by their period  $T$ .

#### Slenderness, Eccentricity and Onset of Yield

Figures 4 thru 14 have shown functional relationships of deflection and strain to the variations in eccentricity and slenderness ratio. These figures can be combined to show a relationship between response ( $y_m/y_1$ ), eccentricity, slenderness ratio, and the onset of yield in the column. For example, in a column with rectangular cross-section the bending moment ( $M_y$ ) for onset of yield is  $\sigma_y(bd^2/6)$  where  $b$  and  $d$  are cross-sectional dimensions and  $\sigma_y$  is the yield stress of the column material. If when  $R = 1/2$  the applied vertical load ( $P$ ) is the predominant force producing moment, the lateral deflection of the midpoint of the column at which the onset of yielding occurs may be calculated from  $M_y/P$ . Applying this to the Group I columns 1, 2, and 5, boundaries can be drawn which show at what deflections and eccentricities yielding occurs.

Figure 15 shows a series of linear boundaries that reflect various ideal yielding strengths for load condition  $R = 1/2$ . The deflection eccentricity curve of columns 1, 4, and 5, taken from Figure 10, is re-plotted here. The intersection of the yield boundaries with this curve indicates when yielding occurs. For example, the material for the test column has a yield strain of about  $\epsilon_y = 3600 \mu\text{in/in}$ . The intersection of the

3600  $\mu\text{in/in}$  strain boundary line and the column response line occurs at an eccentricity of about 9 percent. This is in fair agreement with a 7 percent eccentricity gained from extrapolating the strain test data in Figure 12.

From the trends indicated in Figure 15 we may conclude that columns of relatively short length, of moderately large eccentricity, say of up to 3 percent, and of moderate strength, say 30,000 psi, will not yield for loading condition  $R = 1/2$ . And they will not yield even if the load were suddenly applied. This experimental work supports similar indications of theoretical work in this respect.

In the case where  $R = 1.0$  a series of strain boundary curves are not as easily made as when  $R = 1/2$ . The bending moment that occurs at the midpoint of the column arises from not only the vertically applied load but also from horizontal inertial forces and a horizontal reaction at the support induced by the lateral motion of the column itself. A dynamic analysis of columns 1, 4, and 5 for load condition  $R = 1.2$  proved too crude for use in establishing a yield boundary. So, the experimental responses  $y_m/y_1$  were increased by the ratio of the yield strain to measured strain. The resulting approximate yield boundary is shown in Figure 16. This figure indicates for the actual load condition of these tests ( $R = 1.2$ ) that yielding would occur at about 0.6 percent eccentricity; this agrees with the extrapolated data in Figure 12 which indicates yielding at about 0.5 percent eccentricity.

Figures 17 and 18 relate bending strain to deflection  $y_m/y_1$ , eccentricity and slenderness of the test columns. Of the two data curves in Figure 18, one curve (where eccentricity is constant) shows for  $R = 1$  a precipitous rise in strain beginning at  $y_m/y_1 = 4$ . For comparison, the other curve (where  $\ell/r$  is constant, or 312), shows a much more gradual rise in strain as eccentricity is increased.

Figure 17 shows peak bending strains clustered vertically at about response  $y_m/y_1 = 1.9$  for load condition  $R = 1/2$ . Obviously, columns of insufficient strength, or of a cross-section other than rectangular, may yield even at dynamic loads  $1/2$  of their Euler capacity. The data also indicates that increasing eccentricity leads to increasing strains. This is consistent with previously shown data. The effects of slenderness are not apparent here.

#### Stoutness Ratio

Turning now to Group III columns 3 and 6, there are three variables so that any response

we see in Figure 23 that for nominal load condition  $R = 1/2$  the strains are scattered about the 2 percent eccentricity curve. The strains for column 1 (lowest in eccentricity) fall below the curve while the strains of columns 5 and 7 (eccentricities 3.9 and 2.6 percent, respectively) fall much above the curve. This is consistent with previous data. On the other hand, eccentricity is not a factor when the applied load is greater than the Euler load, or here when  $R = 1.2$ ; the columns were going to buckle anyway, regardless of the eccentricity.

#### Threshold of Buckling

In the case of UNDEX attack on ships experience has indicated that durations of the shock load from conventional explosives can last up to 6 msec for relatively low shock levels. Durations here are those of foundation motion of ship equipment; underwater shock wave durations are lower. Note further that 6 msec is an estimate of the upper bound of data from old ships; there is no similar data for modern ships. If 6 msec duration is reasonable for use in attaining design shock levels, then based on Figure 22B columns of rectangular cross-section should have periods greater than 6 msec. In other words, the lateral frequency should be no more than about 167 hertz, if columns are to remain elastic. If permanent set were allowed, then advantage could be taken of plasticity in the column section. But this is beyond the scope of this report.

The lateral frequency ( $f$ ) of a pinned, unloaded column is:

$$f = \frac{\pi}{2\ell} (r/\ell) c_0 \quad (7)$$

where  $\ell$  is the column length

$r/\ell$  is the inverse of slenderness ratio

and  $c_0$  is the acoustic velocity of the column material; for steel and aluminum  $c_0 = 196,500$  in/sec

Taking  $f = 167$  hertz as the maximum frequency a column may have and not buckle elastically, we may calculate a threshold for buckling as a function of slenderness ratio and the length of a column. This appears in Figure 24.

Columns whose frequencies are lower than 167 hertz fall above the solid curve and will not buckle. Those below the curve will buckle, if they experience an UNDEX load equal to its Euler capacity. The curve does not apply to UNDEX attacks from nuclear explosions; the durations from those explosions

can be much more than 6 msec. Note that these tests were performed on long columns whose axial strain were well below yield and whose slenderness ratios were greater than 90; this, coupled with a decided eccentricity, insured a bending failure in the fundamental mode of motion of the column.

Below are some further notes of caution and limitations regarding the buckling threshold of Figure 24. The curve assumes a material at least as strong as HY-80; that the applied load is no more than the Euler load; that axial yield strain does not obtain; that duration of the foundations motions is no more than 6 msec; that eccentricity is less than 2 percent; and that the cross-section is rectangular. Furthermore, the curve does not reflect strains brought on by the residual bending of the column. That is, the column may still have a lateral buckling velocity after the applied load has dissipated; this induces further strains that are not accounted for in these tests. Hence, this curve must be considered incomplete for load condition  $R = 1$ . Note again that static loads could seriously influence the dynamic buckling capacity of columns.

Finally with a very short column the predominant mode of failure is typically compression on the column section. Bending is of little or no concern, at least initially. In between the very short and the long columns the effect of compression and bending is a complicated mode of failure. Therefore, the results of these tests should be taken as tentative with respect to short columns.

#### COMPARISON OF THEORETICAL AND EXPERIMENTAL RESPONSE

Figure 25 is a plot of response ( $y_m/y_1$ ) to duration ratio ( $\theta/T$ ). When  $R = 1/2$  the responses reach a maximum of  $y_m/y_1 = 1.9$  at  $\theta/T = 0.75$ . As it happens, the points fall near a theoretical response line derived for a column subjected to a triangular, zero rise time loading pulse. Response data when  $R = 1$  is also plotted here, and it appears more or less as scatter to the high side of the theoretical response curve for a triangular pulse. And while there is no rigorous relationship between the test data and the theoretical curves in Figure 25A, the test data supports theory in that there is a maximum lateral deflection of a column when  $R = 1/2$ . Also it supports the rising slope of response when  $R = 1$ , as theory indicates in Figure 25A. However, reference 7, another work on a constant suddenly applied force on a column, indicated that a leveling off occurs when  $R = 1$ .

Figure 25B shows a plot of the test data scattered about a curve developed for a

there are three variables so that any response can be theoretically ascribed to any of the three. Figure 19 shows shallow sloped curves for the responses of these columns to changes in stoutness ratio  $A/\ell^2$ . The curves indicate that strain and deflections increase as  $A/\ell^2$  increases. But slenderness ratio also changed (188 to 90) and frequency changed from 83 to 269 hertz. Note that, when the responses ( $y_m/y_1$ ) for remaining columns (1, 2, 4, 5 and 7) are also plotted, all, except that for No. 7, are grouped near the response of column No. 3; see Figure 19A. Within this grouping the response is about the same despite the variations in their slenderness ratio (226 to 312) or frequencies (32 to 43 hertz), suggesting that the change in response between columns 3 and 6 are predominantly due to the changes in their  $A/\ell^2$  values and not in their  $\ell/r$  ratios or frequencies. Note also that eccentricity effects are low.

As to the response of column 7, Table 8 shows that the actual applied load on the column was 70 percent of its Euler capacity ( $R = 0.712$ ), and Table 4 shows that this load lasted 114 msec. For comparison, column 5 was loaded at about 45 percent of its Euler capacity and for a duration of 84.5 msec which is of course shorter than for column 7. If all things were linear and the load on column 7 was the same as on No. 5, then the response of column 7 might reasonably be expected to drop according to the load and duration ratios, or from  $y_m/y_1 = 4.15$  to about  $4.15 \times .45/0.712 \times 84.5/114$ , or  $y_m/y_1 = 1.9$ ; this is well within the grouping of columns 1 thru 5 in Figure 19A.

Figure 19B shows, for load conditions  $R = 1/2$ , the bending strains of columns 3 and 6 versus their  $A/\ell^2$  ratios. Just as deflections increase with increasing  $A/\ell^2$  ratios, here too strains increase but at a relatively slower rate than the deflections. In fact the strain curve in Figure 19B indicates that once past  $A/\ell^2 = 2.5 \times 10^{-4}$ , which is a relatively long and thin column, that bending strains rise very slowly. For the material of this test  $\epsilon_y = 3600 \text{ in/in}$ , and that value is reached when  $A/\ell^2 = 100 \times 10^{-4}$  which indicates a very short, stout column.

The strain data for the other columns show considerably more scatter than did appear in the deflection curve in Figure 19A. The scatter is undoubtedly due to the changes in the section properties of those columns.

Based on Figure 19 it seems stoutness has its most effect on deflection and bending strain when columns are relatively long. For relatively short columns it has little significance on bending strains.

## Time Ratios

This section looks at several nondimensional time variables. They are  $t_{c0}/\ell$ ,  $t_r/T$ , and  $\theta/T$ . The variables  $t_r/T$  and  $t_{c0}/\ell$  were obtained from equation 2 by inspection;  $\theta/T$  is also obtained by inspection after adding  $\theta$  to the list of significant physical variables.

Figures 20 and 21 show plots of the deflection responses  $y_m/y_1$  and the rise time variables  $t_{c0}/\ell$  and  $t_r/T$ . The figures indicate for load condition  $R = 1/2$  that  $y_m/y_1$  reaches a maximum of about 1.8 which is consistent with previously shown data. When the Euler load is exceeded, however, duration is a critical factor in what the maximum response of a column will be; obviously the longer the Euler load is exceeded the greater will be the deflection, regardless of the length of the rise time. Thus, the  $y_m/y_1$  vs. time curves in Figures 20 and 21 are misleading with respect to their general applicability to columns. They are valid only under conditions of these tests.

Since durations are significant, let us use for time the ratio of duration to period ( $\theta/T$ ) and for response use both deflection ( $y_m/y_1$ ) and bending strain. Figure 22A shows deflection against duration ratio for actual load conditions  $R = 0.55$  and  $R = 1.2$ ; the data is for columns 2, 3, 4 and 6; they have eccentricities of less than 2 percent. When  $R = 0.55$  the deflections are shown as leveling off to about  $y_m/y_1 = 2.0$  as duration increases to 6 times the period. When the Euler load is exceeded, or here  $R = 1.2$ , the deflections increase monotonically with increasing duration ratio. The usefulness of Figure 22A lies in its applicability to columns of any cross-section. But deflection alone does not indicate if a column is actually collapsing; strains would seem to be better in this respect.

Figure 22B shows bending strains against duration ratio for load condition  $R = 0.55$  and  $R = 1.2$ . In the figure we can see that when  $R = 0.55$  the strains appear to be leveling off to about 2000  $\mu\text{in/in}$  as duration increases to 6 times the period. On the other hand, when  $R = 1.2$  strains far in excess of yield obtain. That yield strain obtained was expected, since the Euler load was exceeded; but what is noteworthy is the great sensitivity of strain to relatively small changes in the ratio of duration to period. This agrees with theoretical work of references 5, 6 and 7 even though those works deal with other loading functions. The curve of Figure 22B suggests that to avoid a precipitous rise in strain, rectangular columns should have periods equal to or more than the duration of the loading.

If we re-plot Figure 22B to include other strain data, such as from columns 1, 5, and 7,

sinusoidal loading on a column.<sup>6</sup> And, in general one could conclude that this theoretical curve could be used with some confidence to predict motions of these columns when subjected to a triangular pulse of a finite rise time, having a peak equal to the Euler load of the column.

Figures 26 and 27 are comparisons between the experimental response histories of four of the seven test columns with those histories derived from theory. The theoretical equations were taken from reference 4 and are shown below:

$$y/y_1 = \frac{1-R \cos \omega t}{1-R} \quad R < 1 \quad (5)$$

$$y/y_1 = \frac{R \cosh(\omega t) - 1}{R-1} \quad R > 1 \quad (6)$$

where  $\omega$  is  $2\pi/T$

In the case of a load condition less than Euler load ( $R < 1$ ), the theoretical equation overestimates the actual response by a factor of about 2; note also that the peaks do not appear to be in phase probably because of the rise time in the test loads.

In the case of  $R > 1.0$ , theory usually overestimates test data but the phase appears about the same. Rise times were less here than when  $R = 1/2$ . Finally, theory and test data are approximately equal for a time up to about 10 percent of the period of an unloaded column.

#### DURATION OF LOAD

Figures 28 and 29 are plots of the period to duration ratio as a function of slenderness ratio ( $\ell/r$ ) and load ratio ( $R$ ). Values for period  $T$  and duration  $\theta$  were drawn from Tables 1 and 4, respectively. Figures 28 shows that duration was affected by the stiffness of the column. On the other hand, Figure 29 shows that duration can have various values for essentially the same load ratio; this means that duration depends on other factors besides  $R$ , such as slenderness ratio. In UNDEX attacks against Navy ships the duration of the applied load depends on the weapon and attack geometry.

#### CONCLUSIONS

1. From the evidence of theory and these experimental results, a pinned column subjected to a dynamic load equal to  $1/2$  the Euler capacity of the column will not buckle provided the column can elastically withstand

a lateral deflection twice the initial eccentricity. At zero eccentricity a column will not buckle.

2. Dynamic compression loads as low as 70 percent of the Euler capacity a column can effect yielding strains in a column, and hence bring on an incipient buckling condition.

3. A column subjected to a dynamic load equal to its Euler capacity must be considered in an a priori buckling situation. The seriousness of the situation may diminish as slenderness and as eccentricity increases. But to take advantage of these factors requires extensive data on duration of motions of foundations on modern ships when subjected to severe shock levels from conventional explosives. Having neither extensive nor certain data on durations, columns designed to carry a dynamic load equal to its Euler load invite collapse.

4. The theoretical work cited in this report have not been rigorously validated because the loading function in these tests have a rise time. However, the experimental curves developed for an applied load half the Euler capacity corroborate theoretical predictions on the lateral motions of buckling columns.

#### REFERENCES

1. Murphy, Glenn, "Similitude in Engineering", Ronald Press Co., New York 1950.
2. Buckingham, E., "Model Experiments and the Forms of Empirical Equations", ASME Transactions, Vol. 37, 1915.
3. Baker, W.E., et al., "Similarity Methods in Engineering Dynamics", Hayden Book Co., Rockville Park, New Jersey, 1978.
4. Meier, J.H., "On the Dynamics of Elastic Buckling", Journal of Aeronautical Sciences, Oct 1945.
5. Housner, George W., "Dynamic Behavior of Super Critically Loaded Struts", Journal of Engineering Mechanics Division, ASCE, Oct 1962.
6. Davidson, J.F., "Buckling of Struts Under Dynamic Loading", Journal of the Mechanics and Physics of Solids, Vol. 2, p. 54-66, 1953.
7. Koning, Carl and Josef Trub, "Impact Buckling of Thin Bars in the Elastic Range", NACA Tech Memo No. 748, June 1934.
8. "Shock Design of Shipboard Equipment, Dynamic Design Analysis Method", Department of Navy, Naval Ship Systems Command, NAVSHIPS 230-423-39, May 1961.

## DISCUSSION

Voice: In the present design environment many use a handbook and find the allowable static load on a column. But they are concerned with shock response, and they want it to be translated into stress based on the static reliability function. Did you say the dynamic load should be less than half of the standard static load?

Mr. Ready: If you design a column so that you allow only 50% of its Euler load, it probably won't buckle. You certainly have to look at its eccentricity and strength to know whether it is in a strained condition so that buckling can't take place. If you have a static weight on the column, it may withstand motion for a while, but that static weight may continue to collapse the column. This is a guide to steer your way through.

Voice: What was the pulse width of your dynamic load, the peak load?

Mr. Ready: The longest duration was about 120 milliseconds, and that was for 50% Euler load. That was the longest I could get. The durations would drop down to 4-6 milliseconds for greater loads.

Voice: Could you have higher loads for 20-30 milliseconds?

Mr. Ready: I could get a longer duration with the lower load. It was just in the characteristics of the styrofoam pad.

Voice: Is this to be used for design guidelines?

Mr. Ready: I don't know whether the Navy will officially adopt it.

Voice: What was the major reason for the higher prediction as opposed to the experimental results?

Mr. Ready: It was a different loading. I used a step pulse in the analysis. We used a ramp pulse in the test. It didn't make any difference on the long duration triangular pulse because they converged.

Mr. Haidekas (ONR): Would you comment on the preloading of the column?

Mr. Ready: I had it as one of the terms. I had  $W$  to account for static or dead weight on the column, but I didn't investigate that. I looked at the particular weight that I used. In my case, it made about a 10% difference compared to what it would have been with zero weight. You have to be careful if you are designing a column, with a static load; it can affect it.

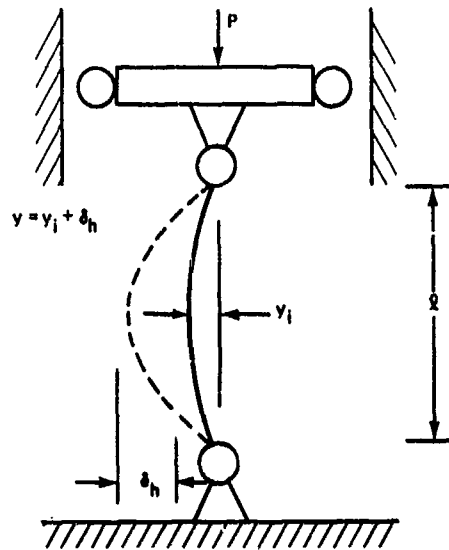


Figure 1 - Idealized Column

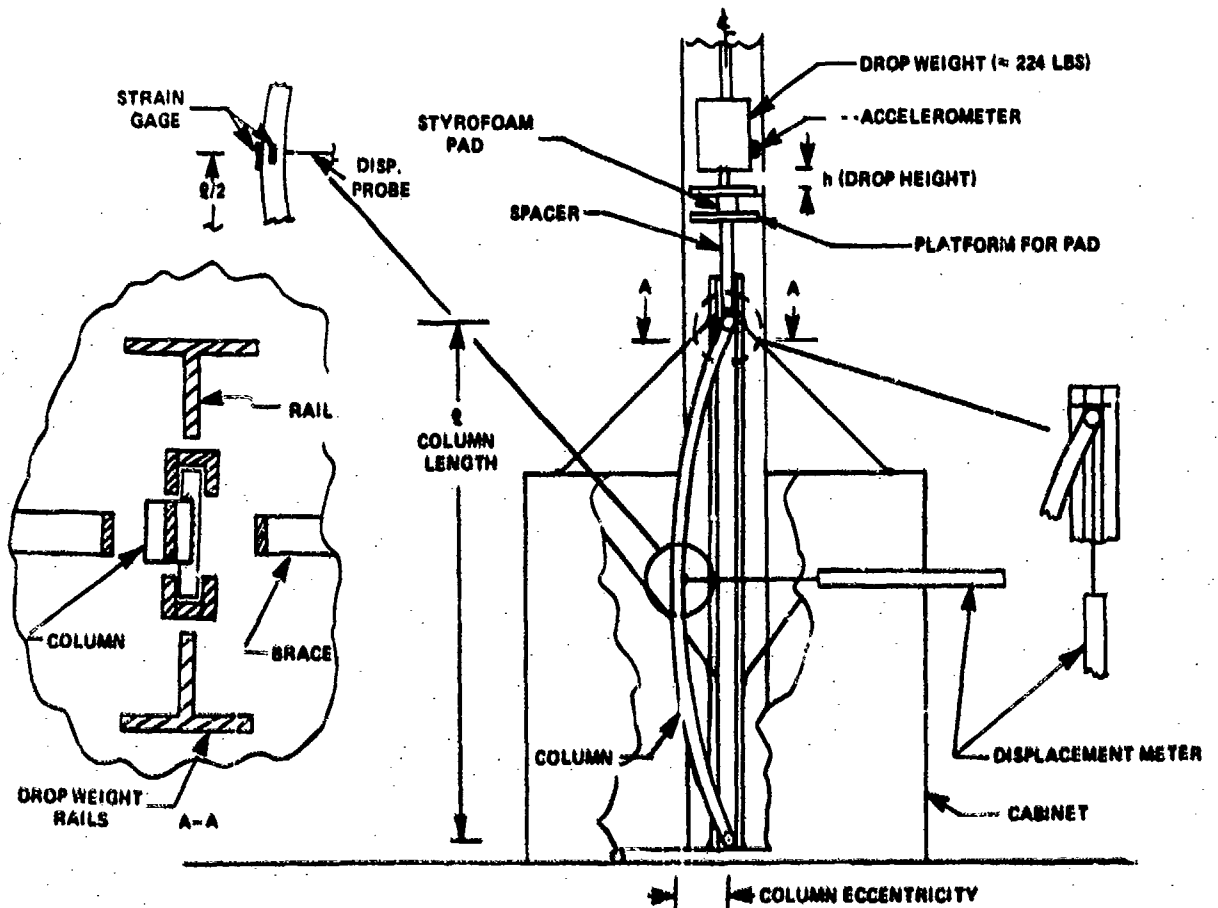


Figure 2 - Test Facility & Instrumentation

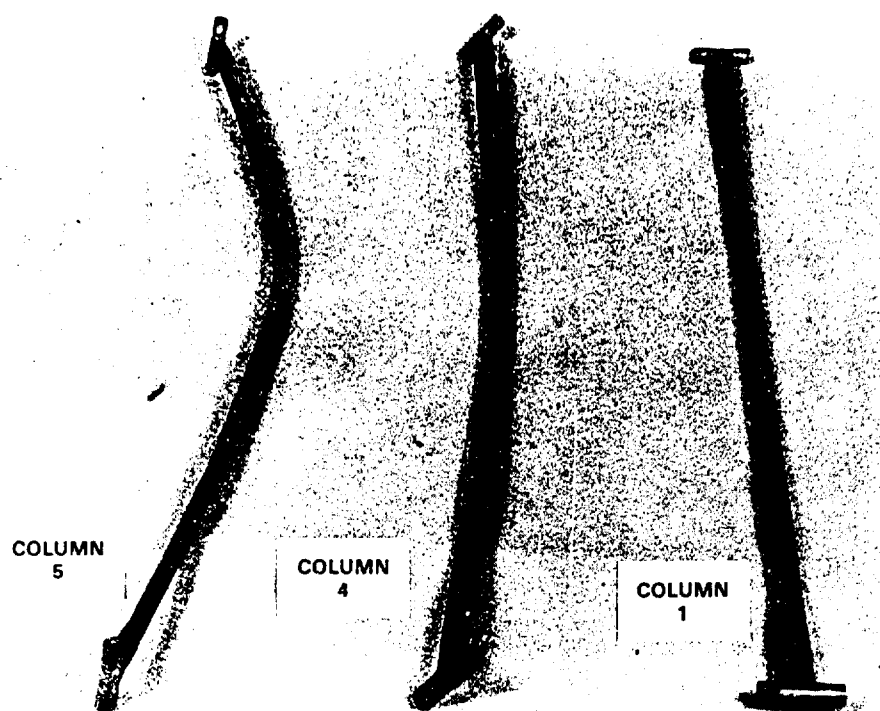


Figure 3a - Post Test Photograph of Columns

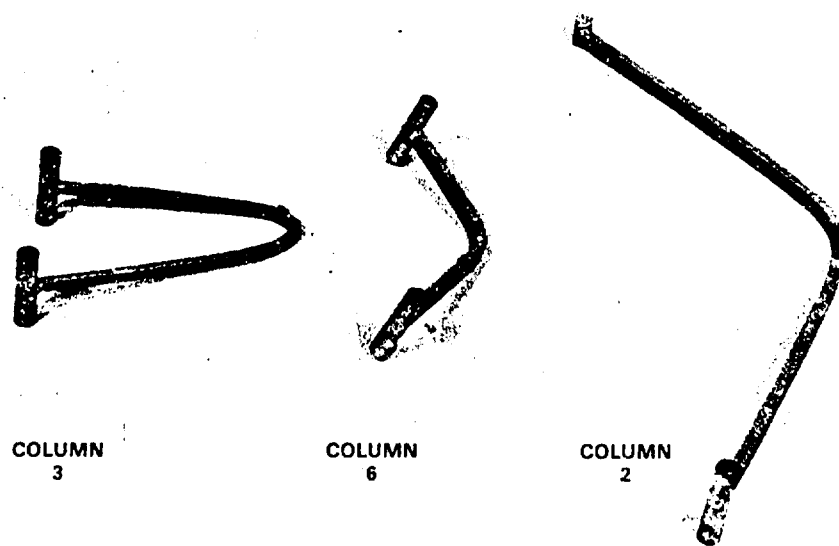


Figure 3b - Post Test Photograph of Columns (continued)



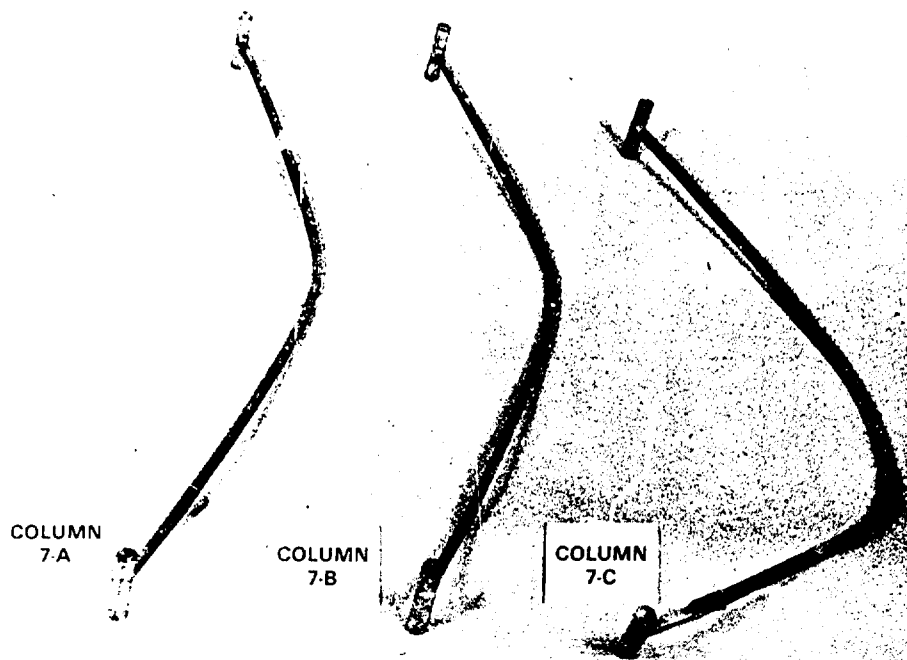


Figure 3c - Post Test Photograph of Columns (continued)

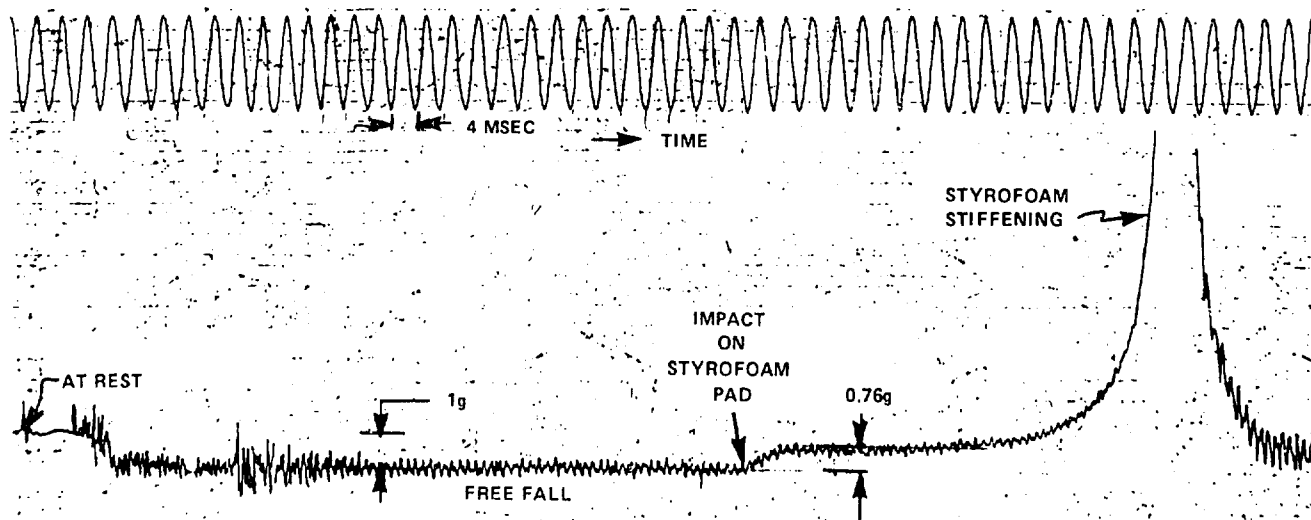


Figure 4 - Typical Acceleration History From Impact of Drop Weight on Crushable High Density ( $3.4 \text{ lb/ft}^3$ ) Styrofoam Block

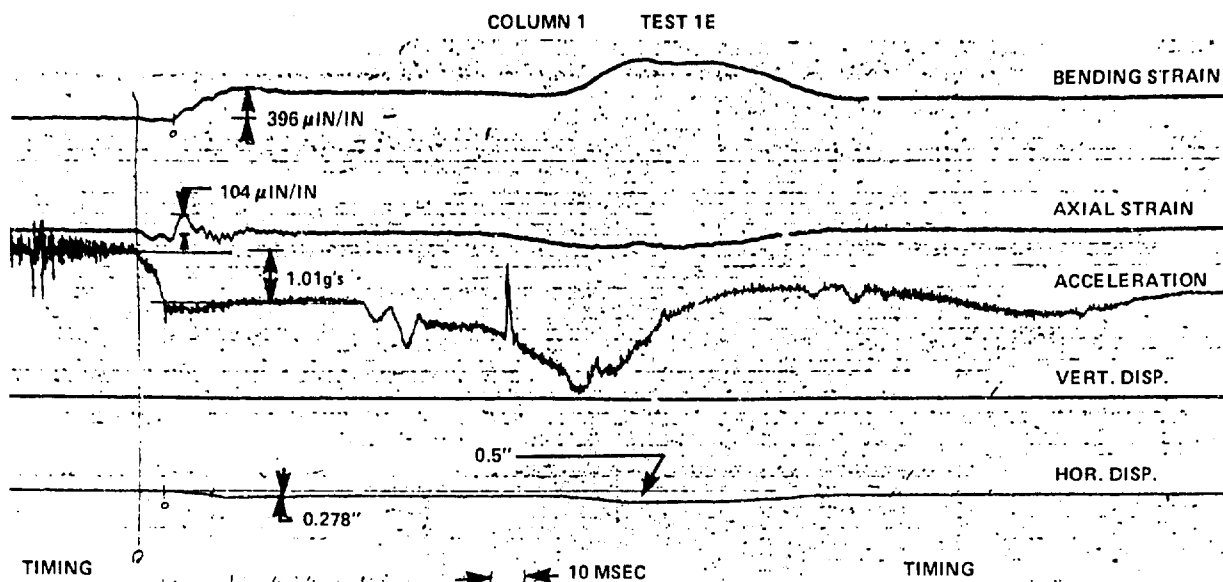


Figure 5 - Response Histories of Column 1 to Drop Weight  $R \approx 1/2$ , Test 1E

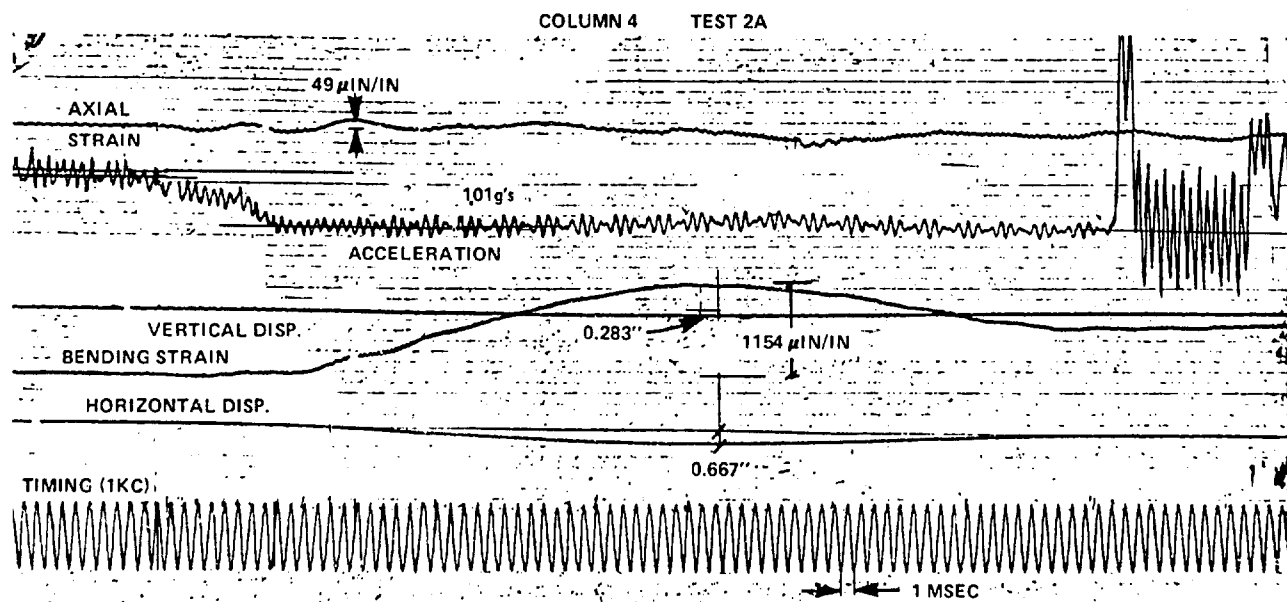


Figure 6 - Response Histories of Column 4 to Drop Weight  $R \approx 1/2$ , Test 2A

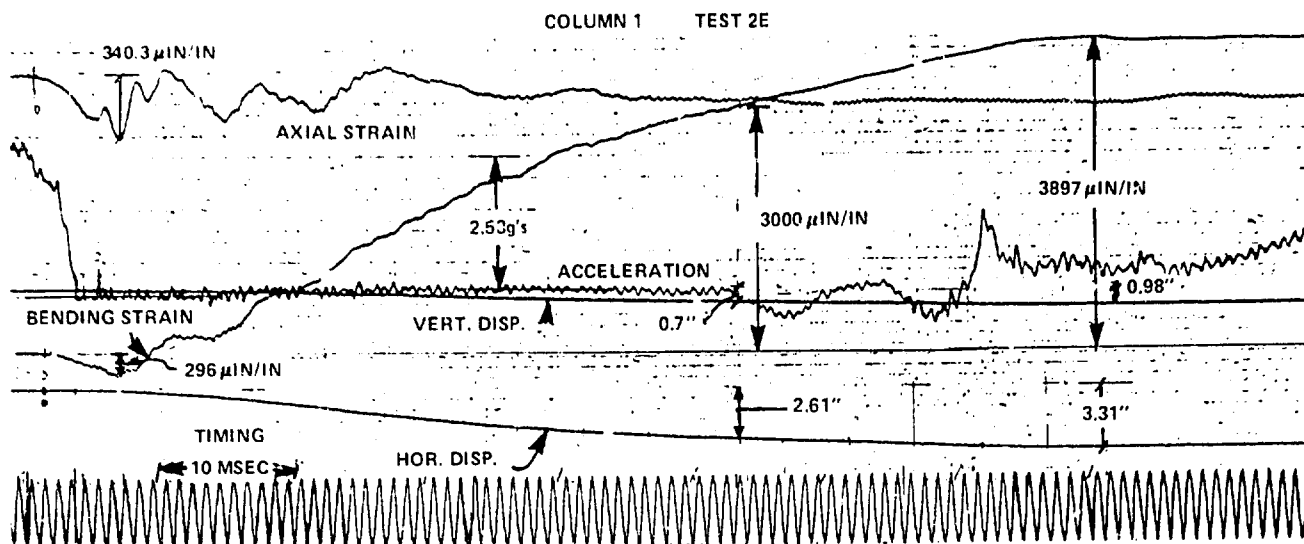


Figure 7 - Response Histories of Column 1 to Drop Weight  $R \approx 1$ , Test 2E

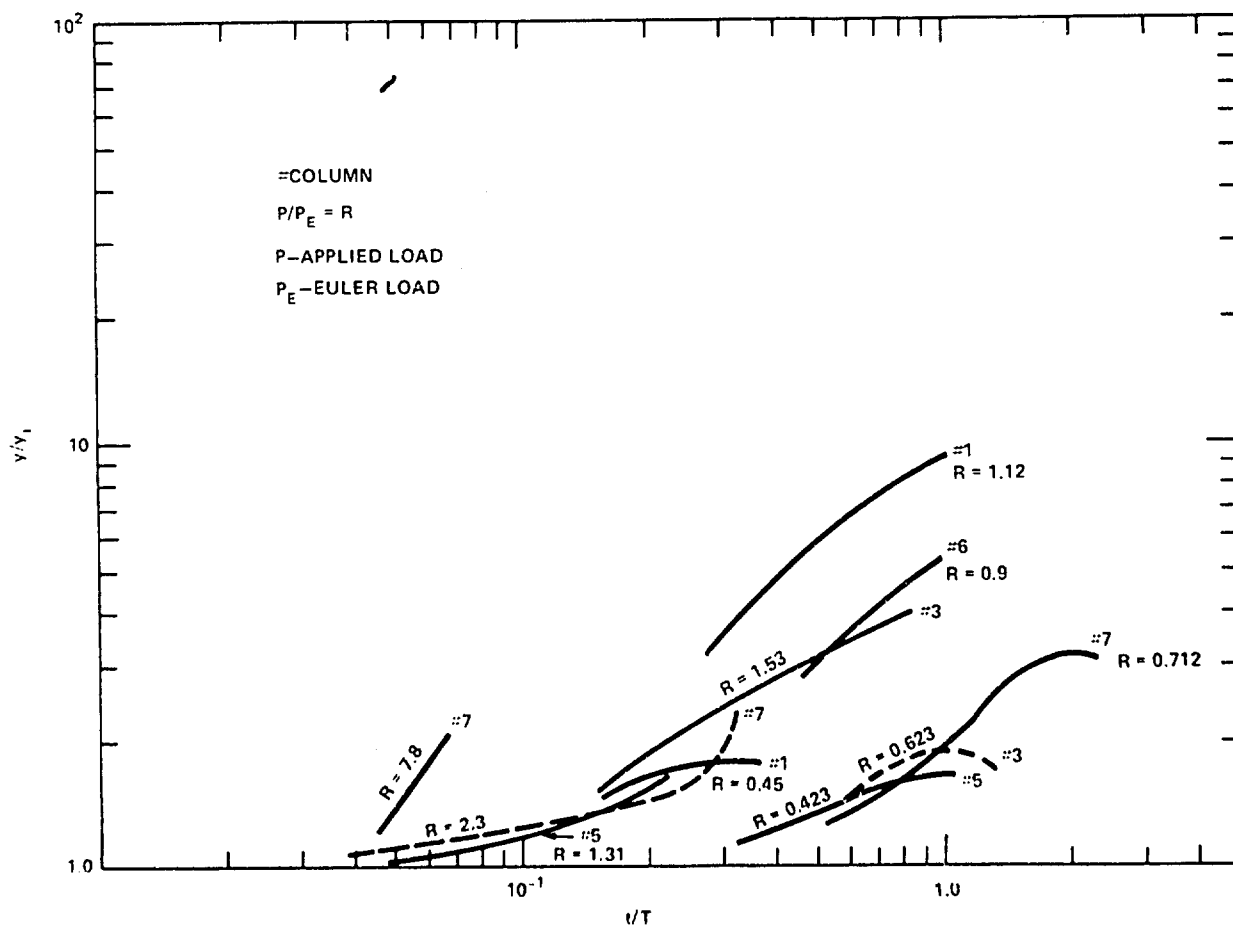


Figure 8 - Plots of Deflection Histories of Selected Columns

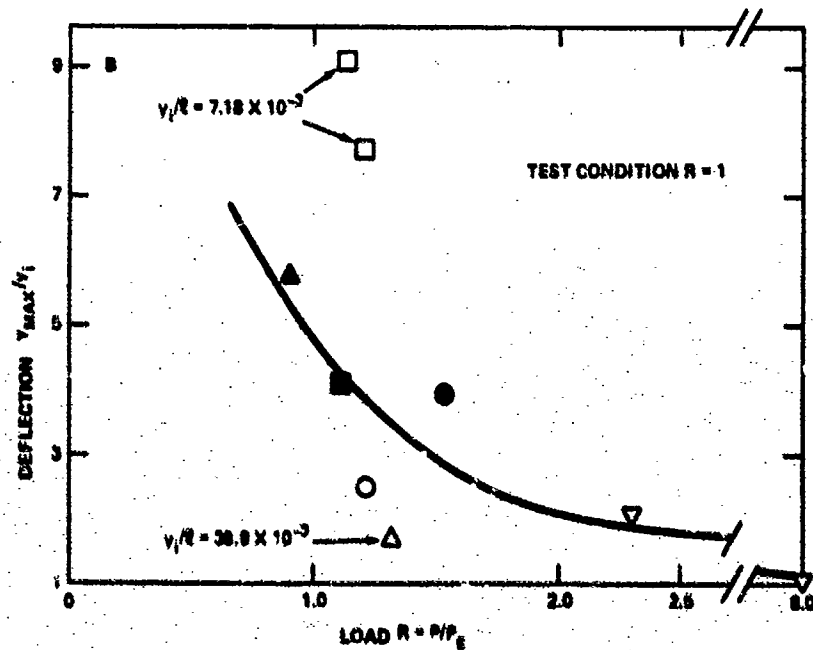
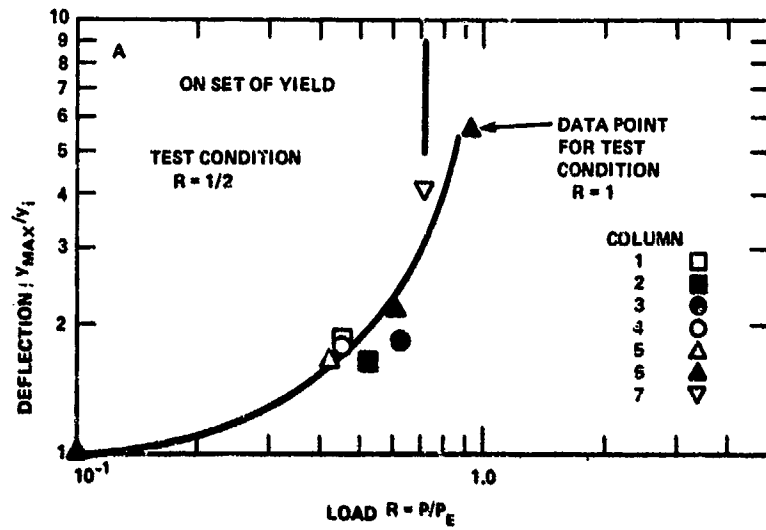


Figure 9 - Maximum Horizontal Deflection vs. Applied Load Ratio  $R$

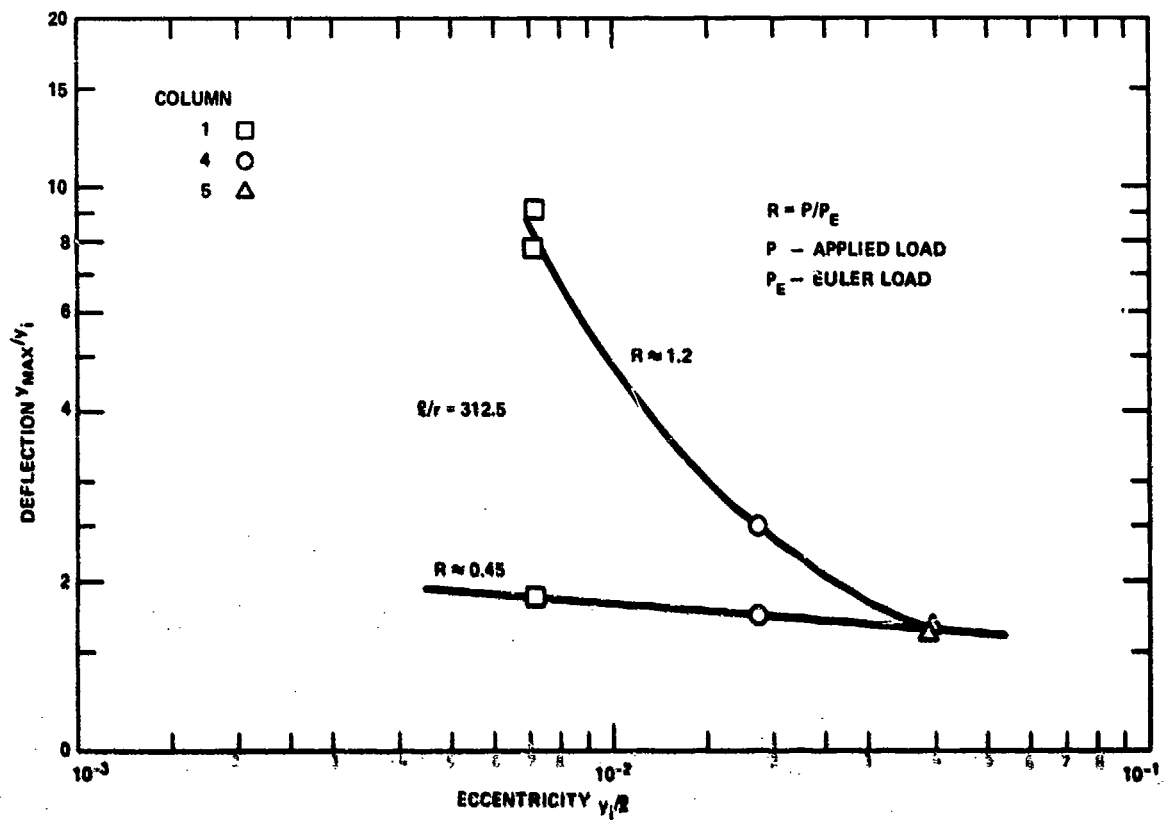


Figure 10 - Maximum Horizontal Column Responses vs. Eccentricity Ratio When  $\ell/r = 312.5$

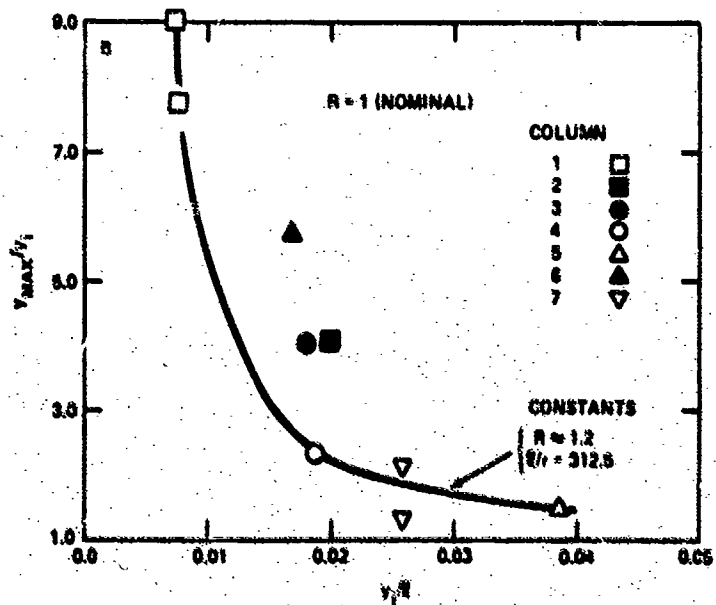
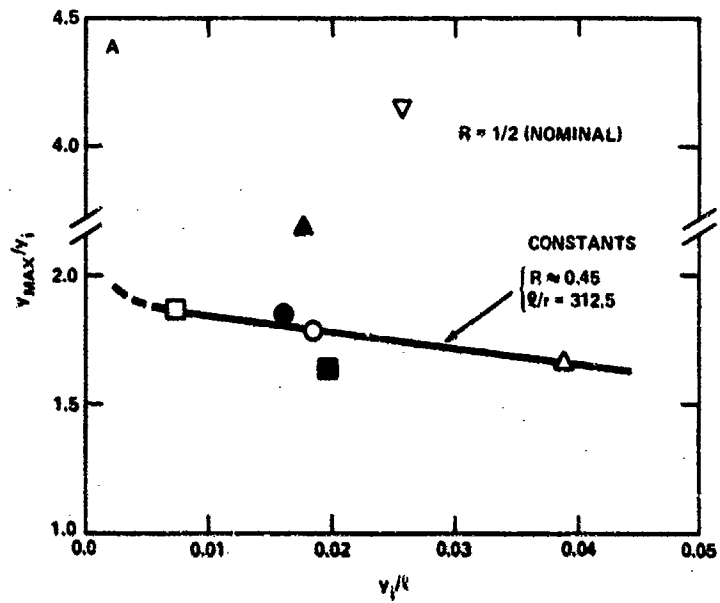


Figure 11. - Maximum Horizontal Column Responses vs. Eccentricity

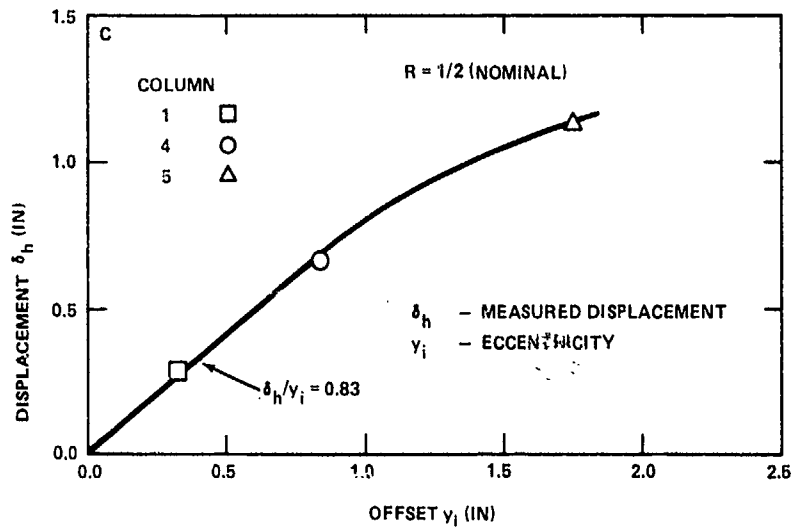


Figure 11 - Maximum Horizontal Column Responses vs. Eccentricity (continued)

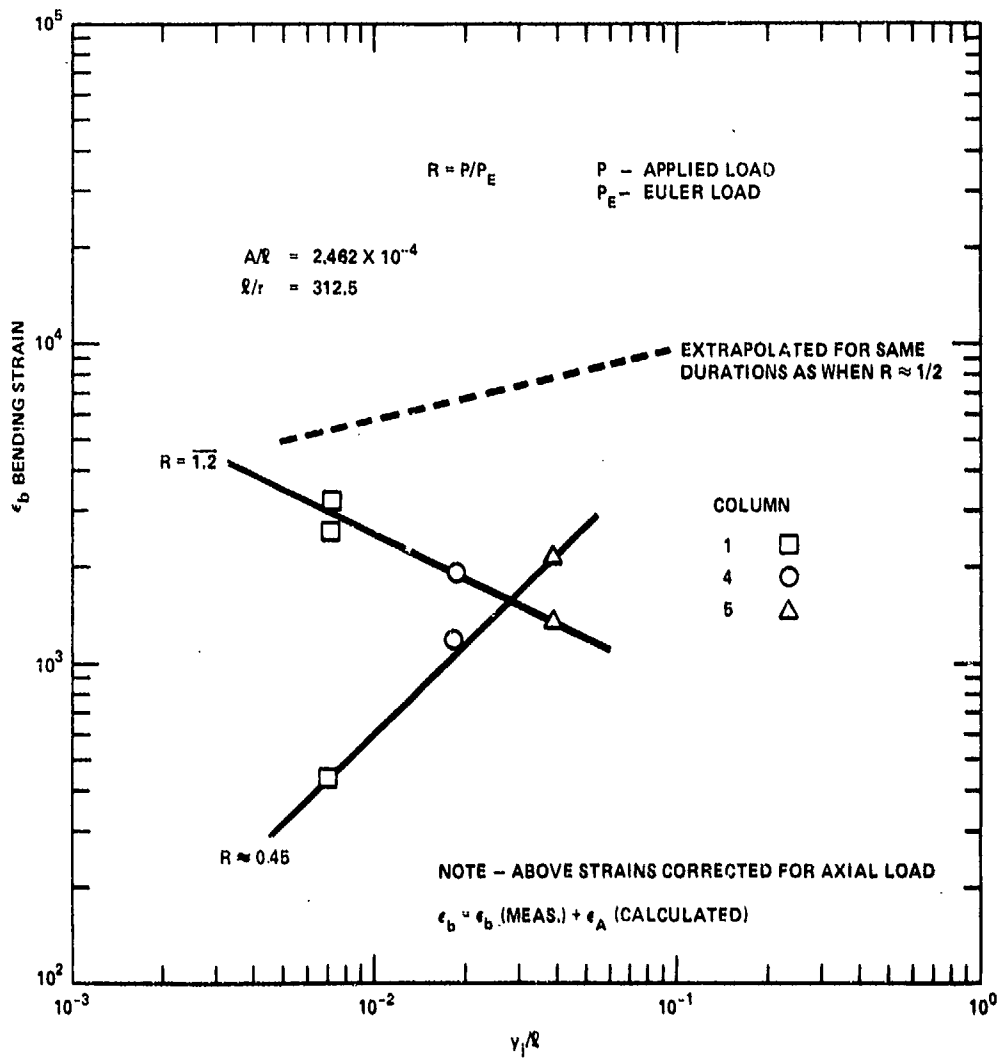


Figure 12 - Midpoint Strain vs. Eccentricity Ratio of Columns

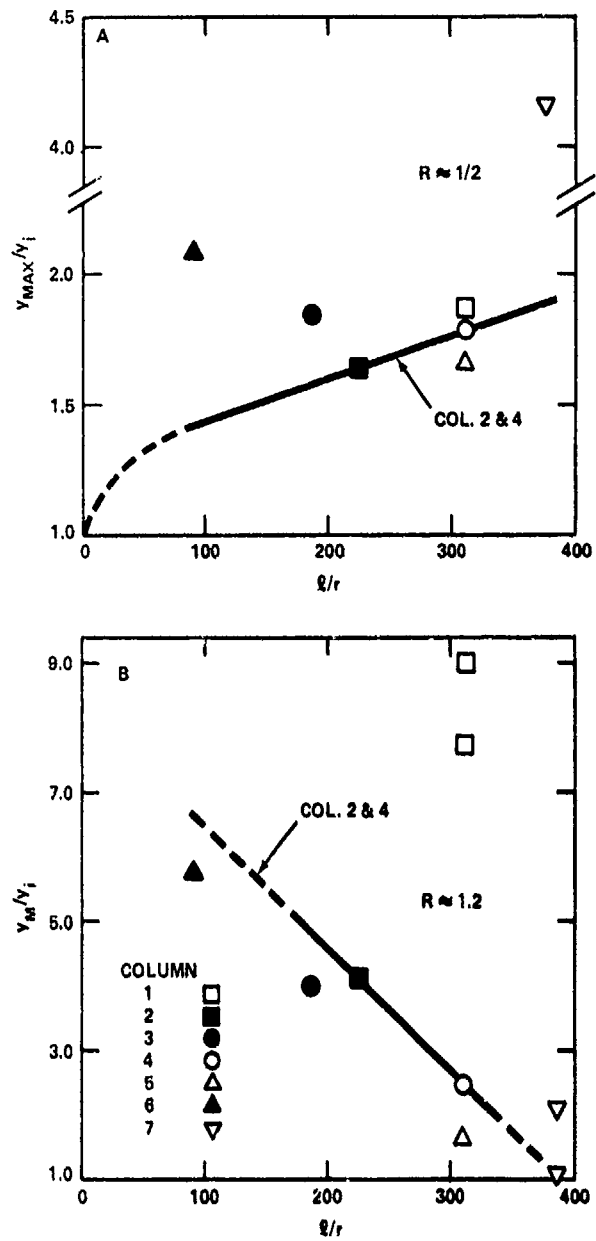


Figure 13 - Maximum Midpoint Horizontal Deflections vs. Slenderness Ratio



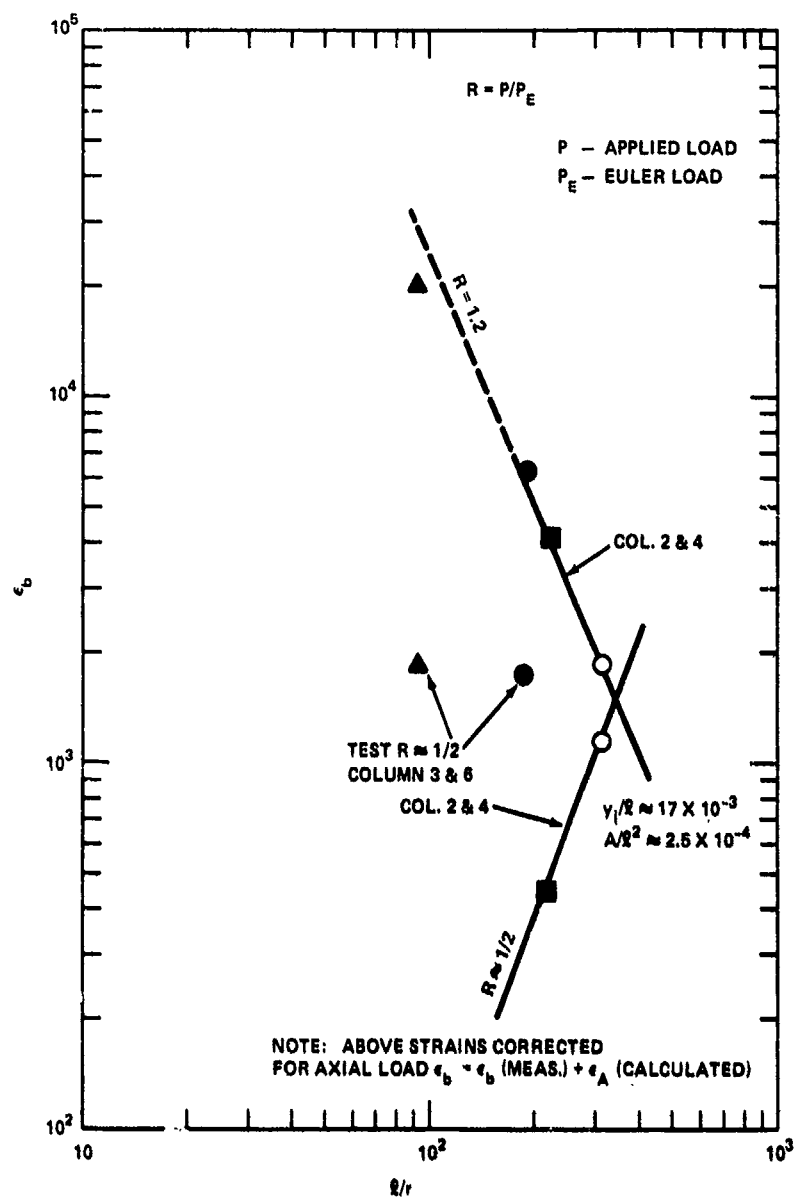


Figure 14 - Midpoint Bending Strain vs. Slenderness Ratio

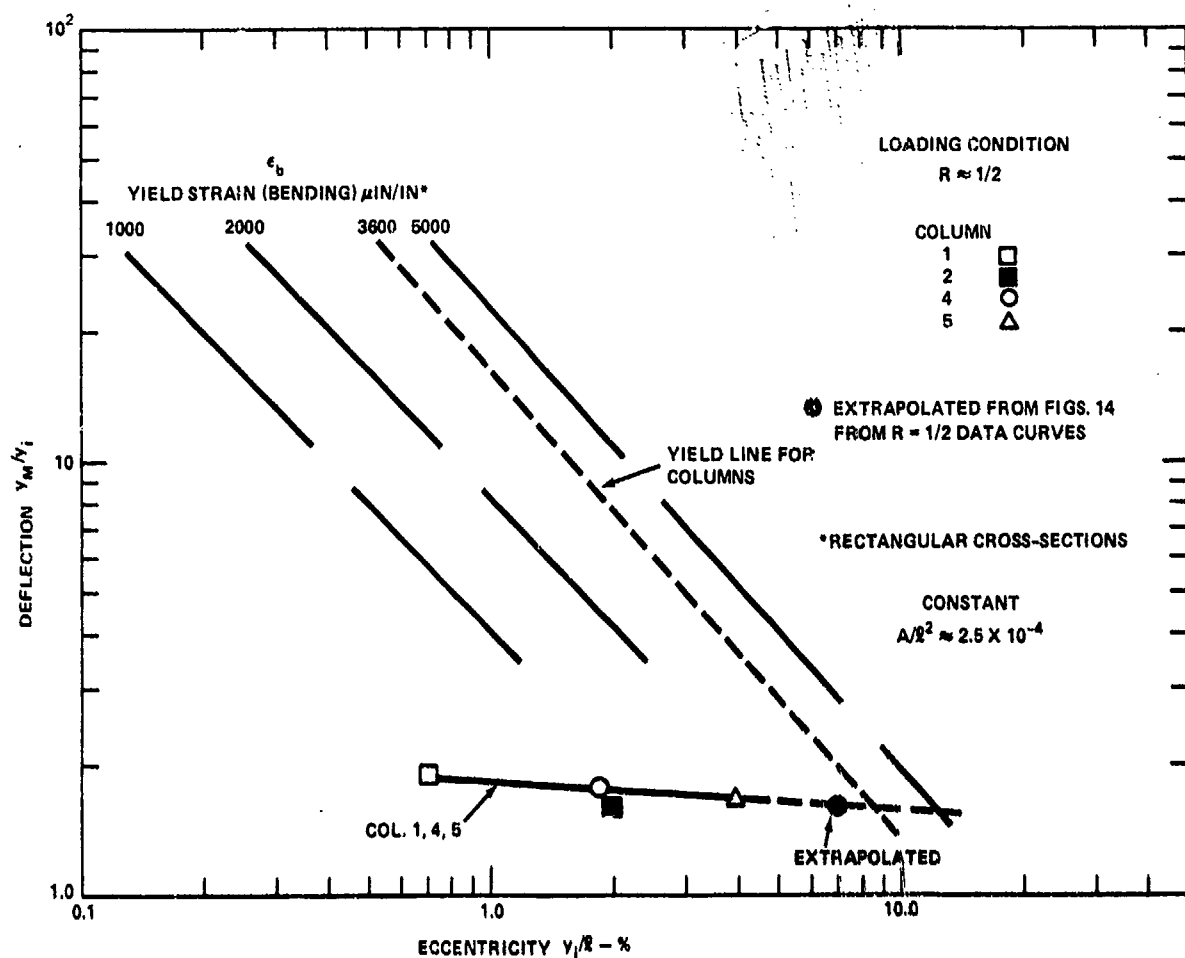


Figure 15 - Lateral Deflection Related to Eccentricity, Slenderness Ratio & Onset of Yielding -  $R \approx 1/2$

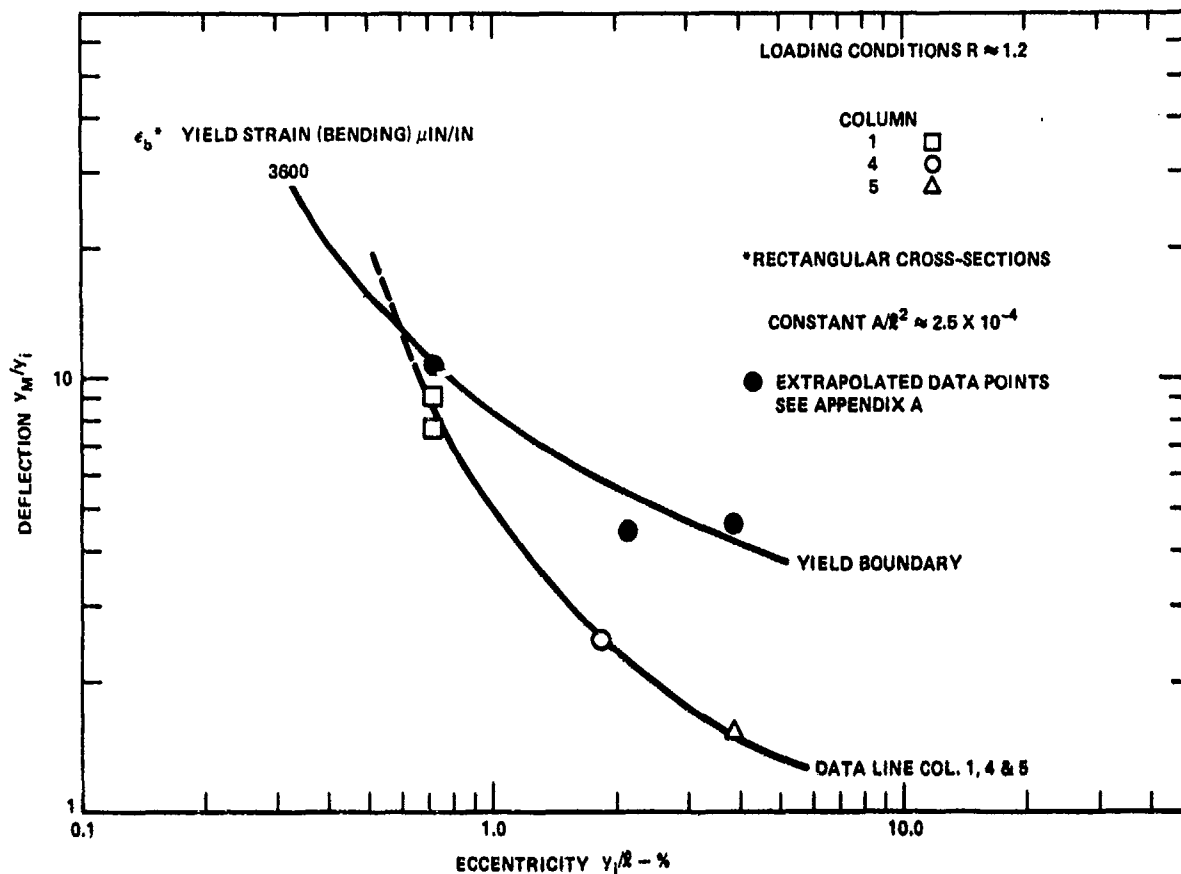


Figure 16 - Lateral Deflection Related to Eccentricity, Slenderness Ratio & Onset of Yielding -  $R \approx 1.2$

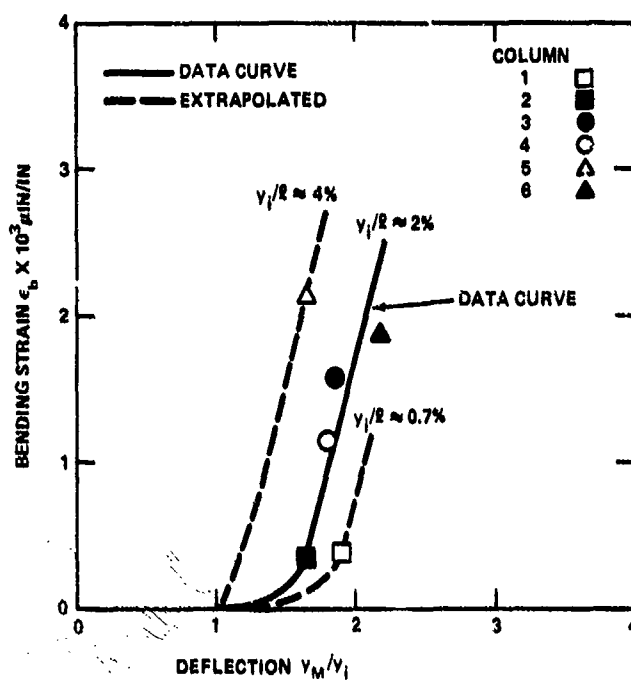


Figure 17 - Relationship of Strain to Response, Slenderness & Eccentricity of Columns when  $R \approx 1/2$

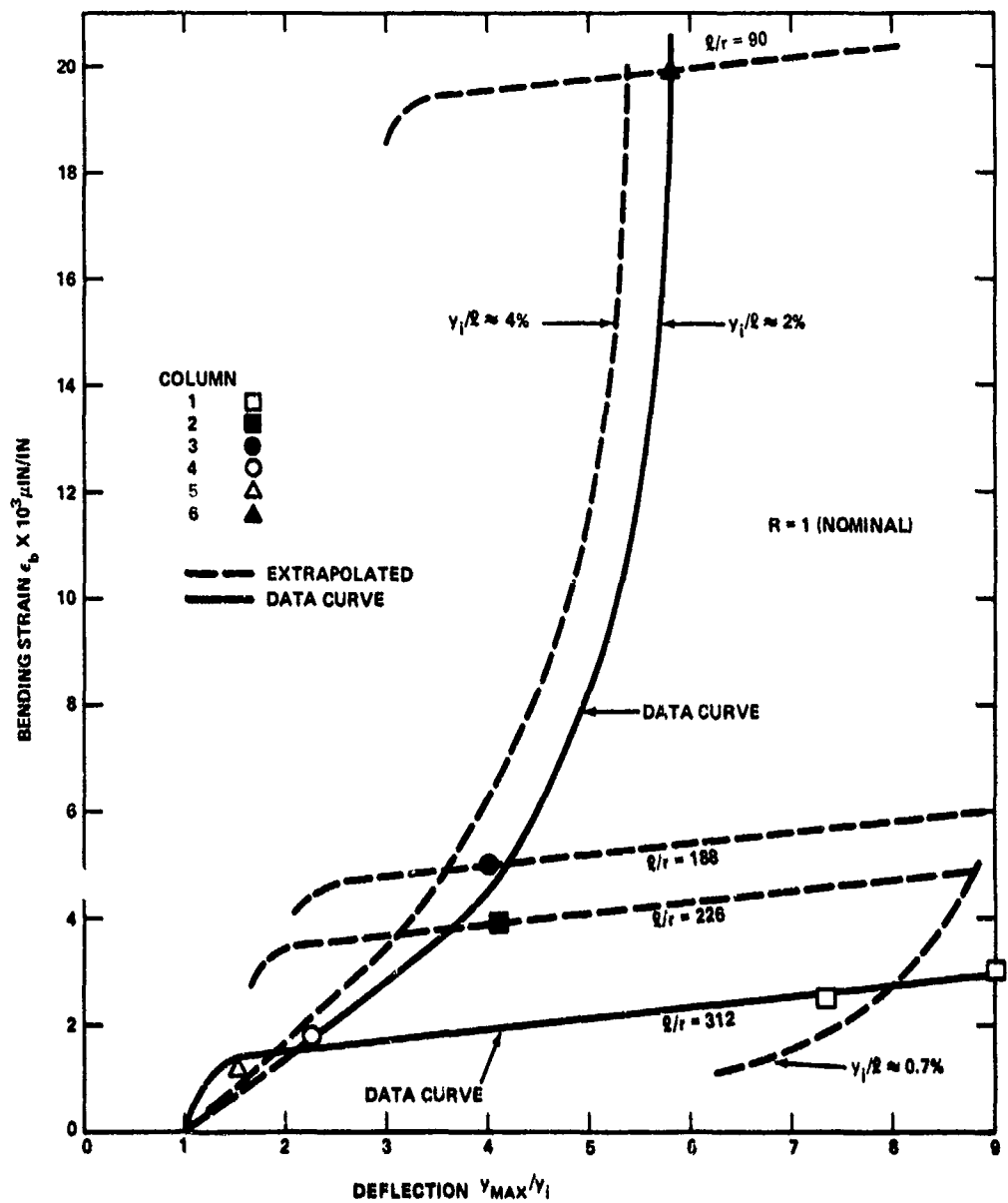


Figure 18 - Relationship of Strain to Response, Slenderness & Eccentricity of Columns when  $R \approx 1$

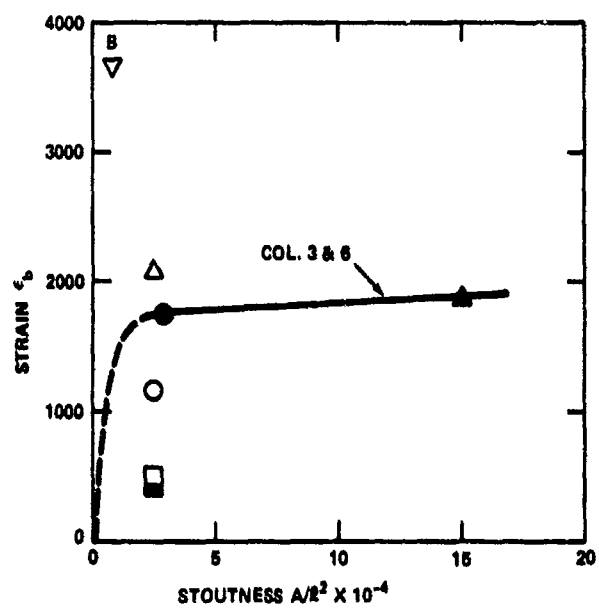
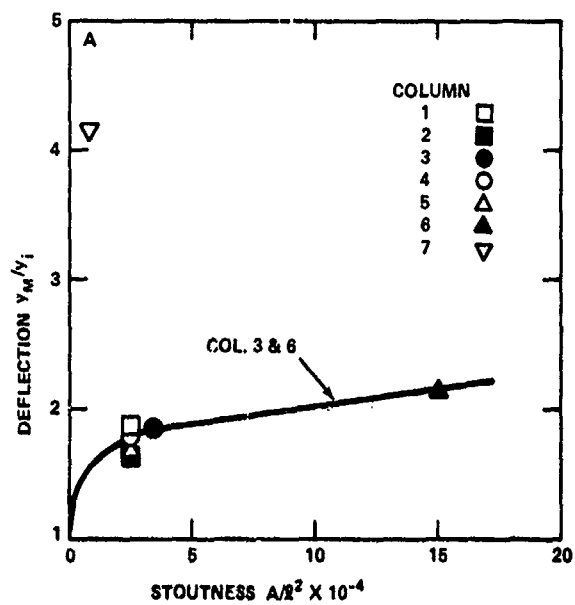


Figure 19 - Deflection & Strain Related to Stoutness Ratio,  $R = 1/2$

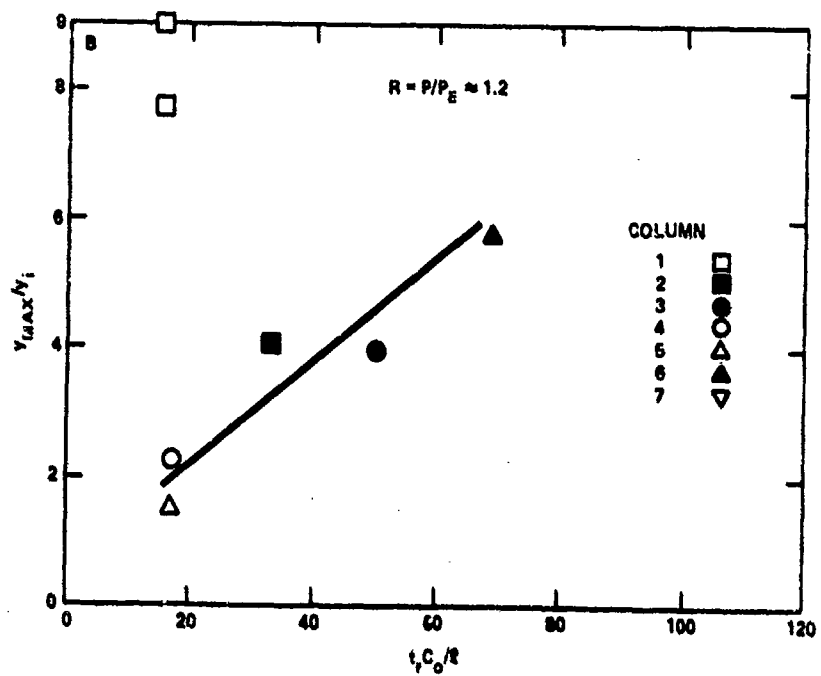
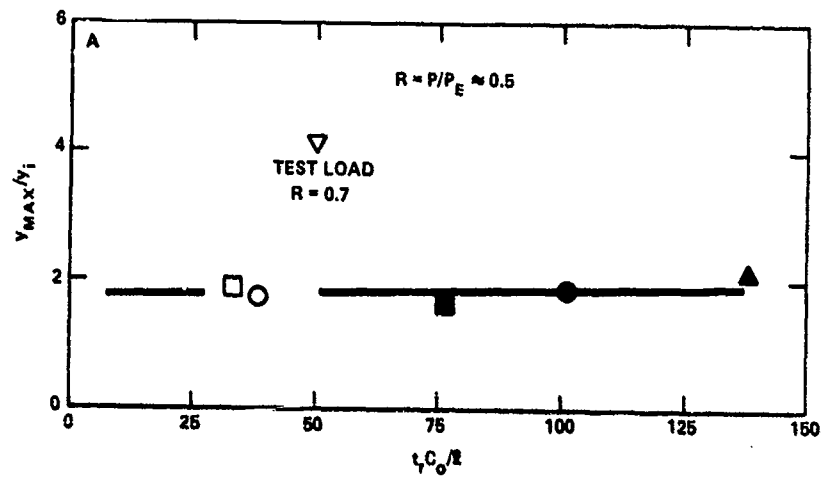


Figure 20 - Column Response vs. Rise Time Ratio

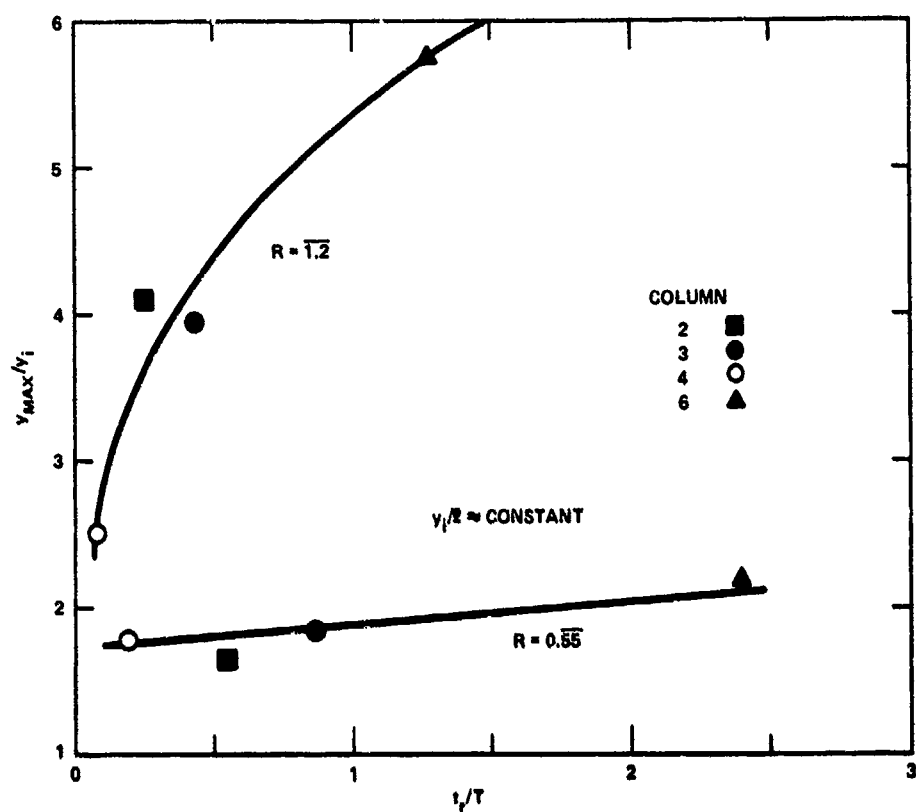


Figure 21 - Maximum Horizontal Deflections vs. Acceleration Rise Time

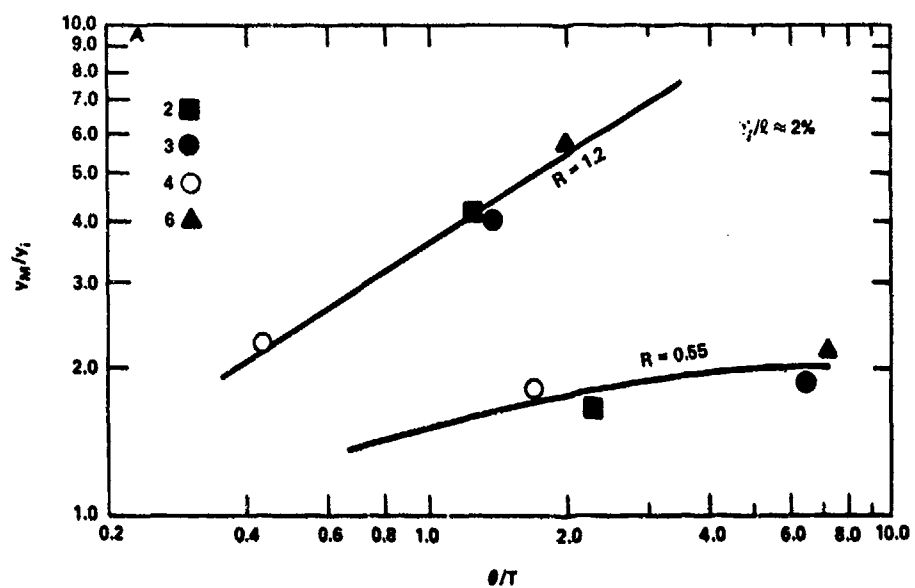


Figure 22 - Maximum Horizontal Deflection vs. Ratio Duration to Period ( $\theta/T$ )



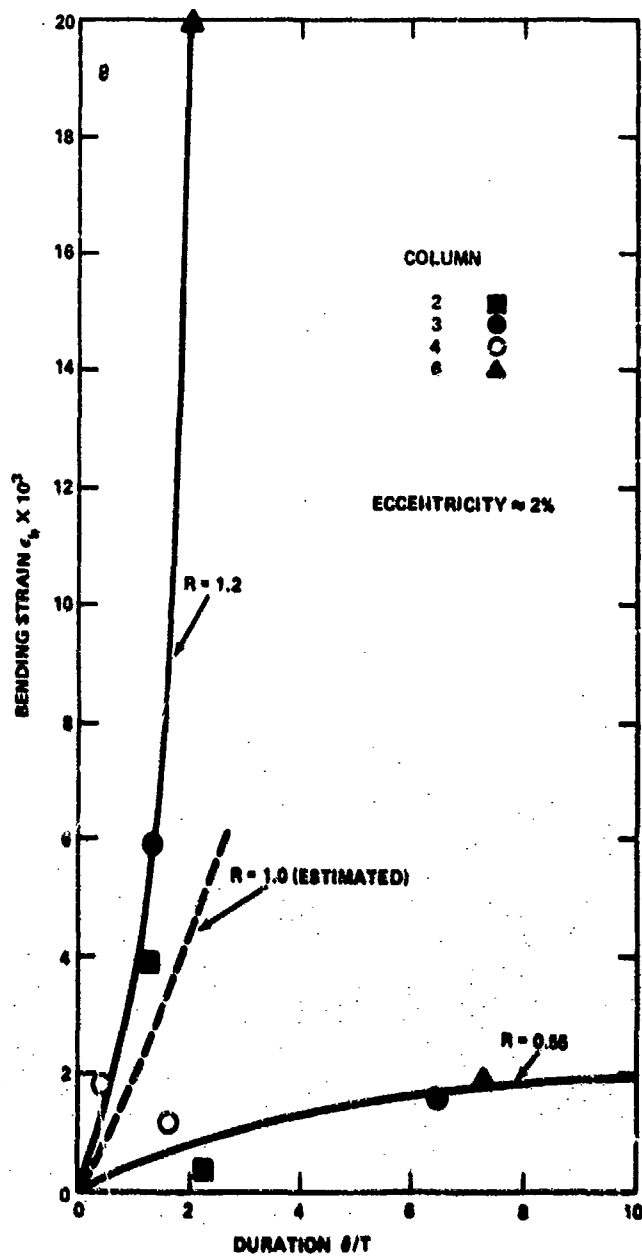


Figure 22 - Peak Bending Strains vs. Ratio Duration to Period ( $\theta/T$ )

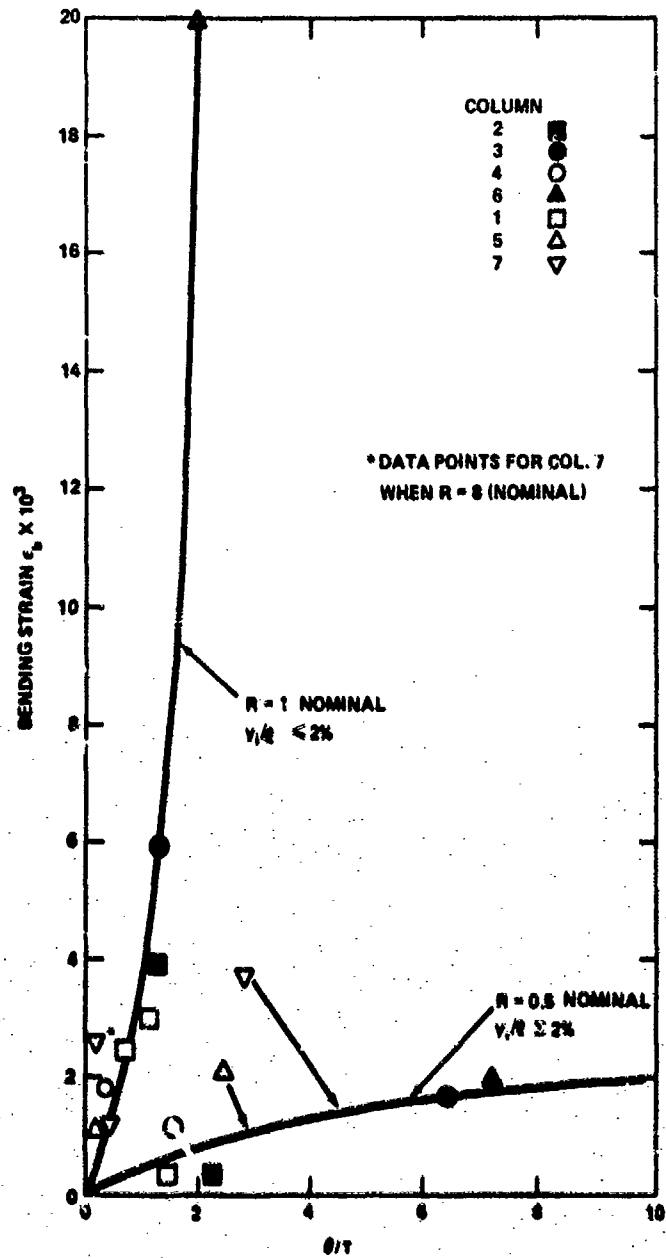


Figure 23 - Replot Figure 25 to Include All  $\theta/T$  and  $\epsilon_b$  Data

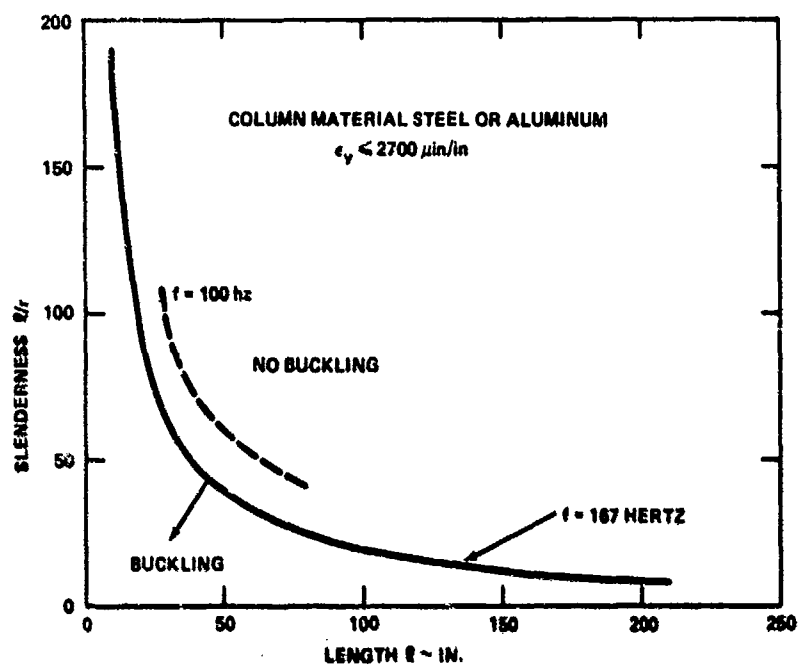


Figure 24 - Buckling Boundary as a Function of Slenderness Ratio & Column Length

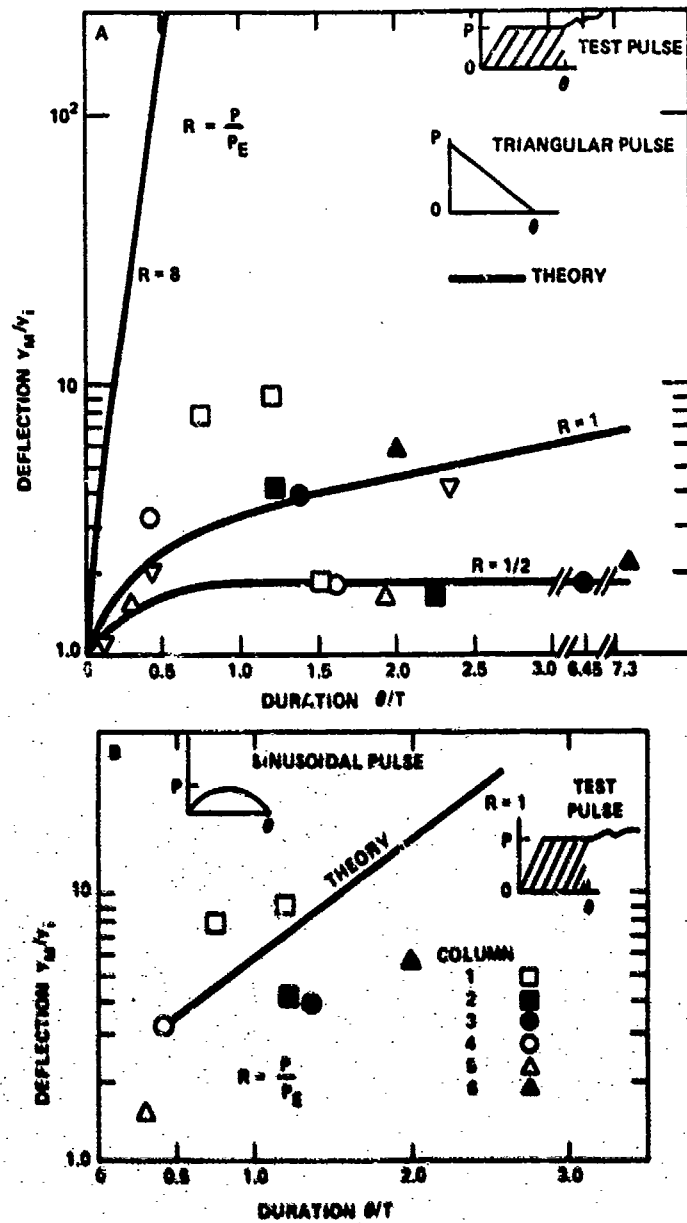


Figure 25 - Test Data Plotted Against Some Theoretical Columns

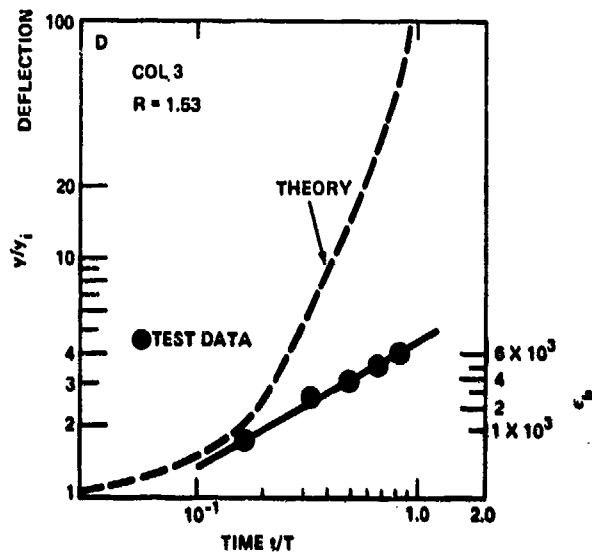
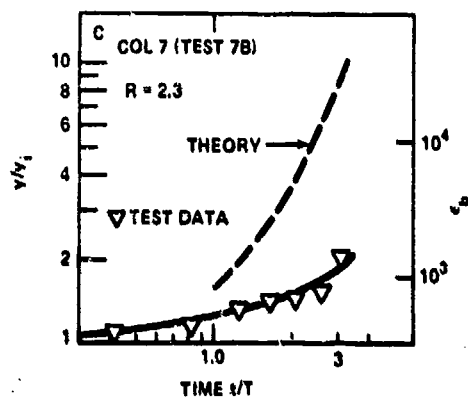
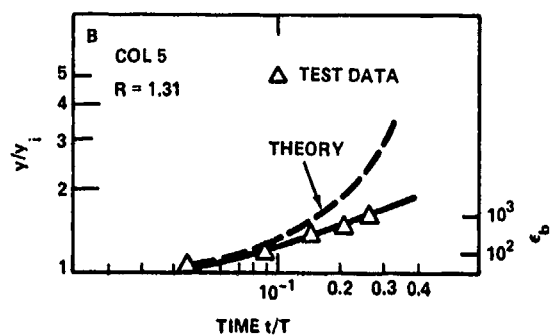
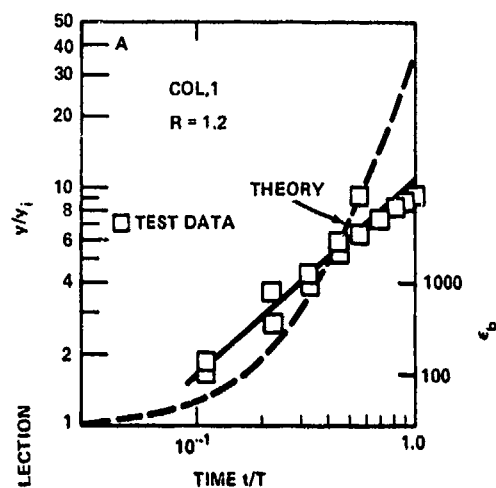


Figure 26 - Comparison of Horizontal Deflection vs. Time: Experiment  $R = 1$  (Nominal) (Ref. 5)

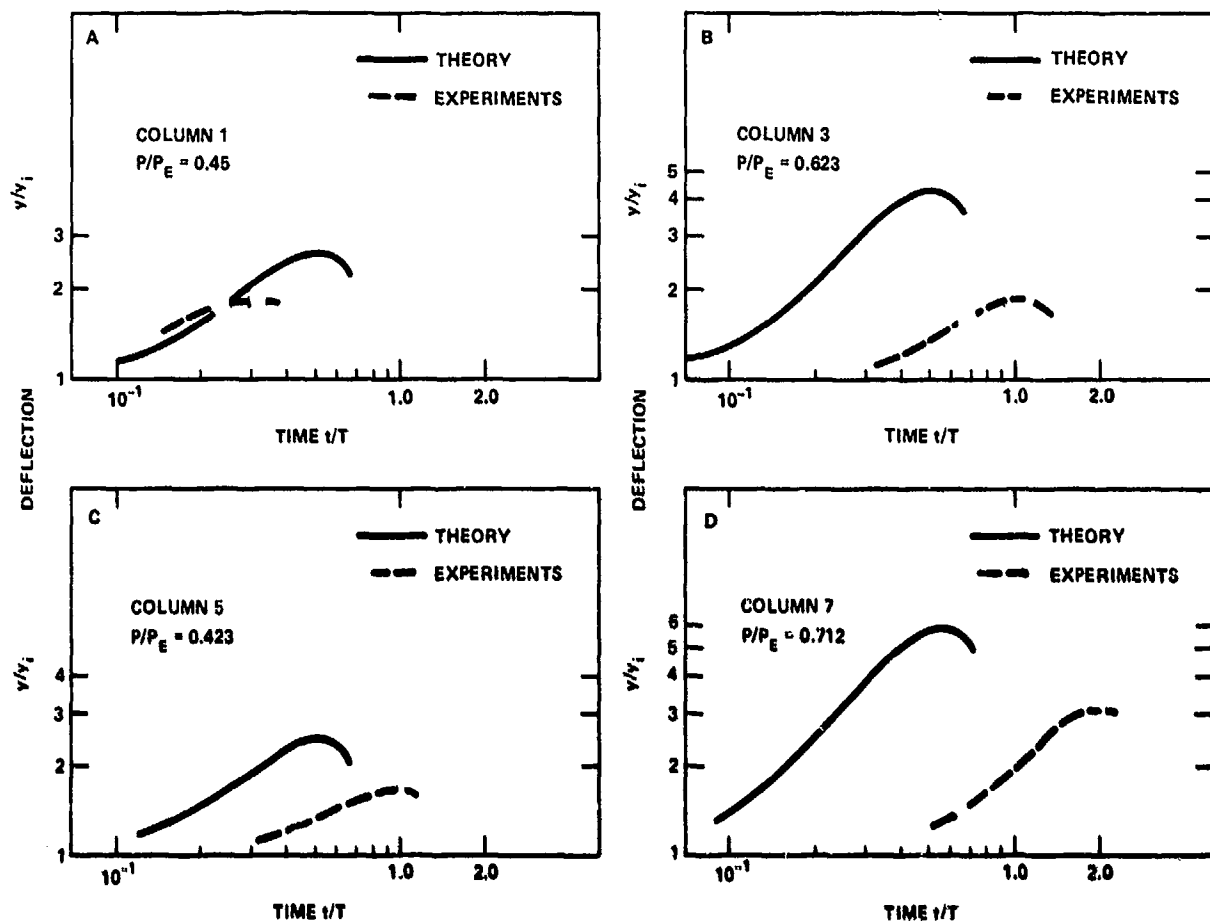


Figure 27 - Comparison of Horizontal Deflections vs. Time Ratio; From Theory & Experiment  $R = 1/2$  (Nominal) (Ref. 5)

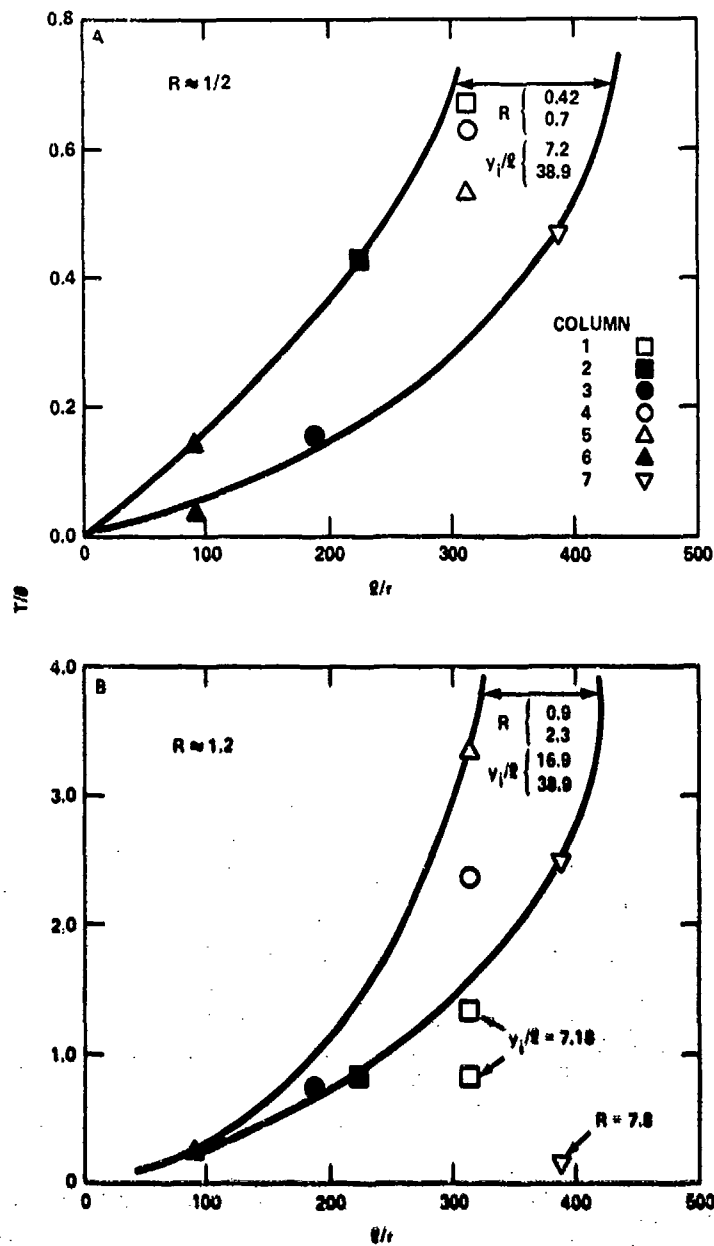


Figure 28 - Duration Ratio vs. Slenderness Ratio

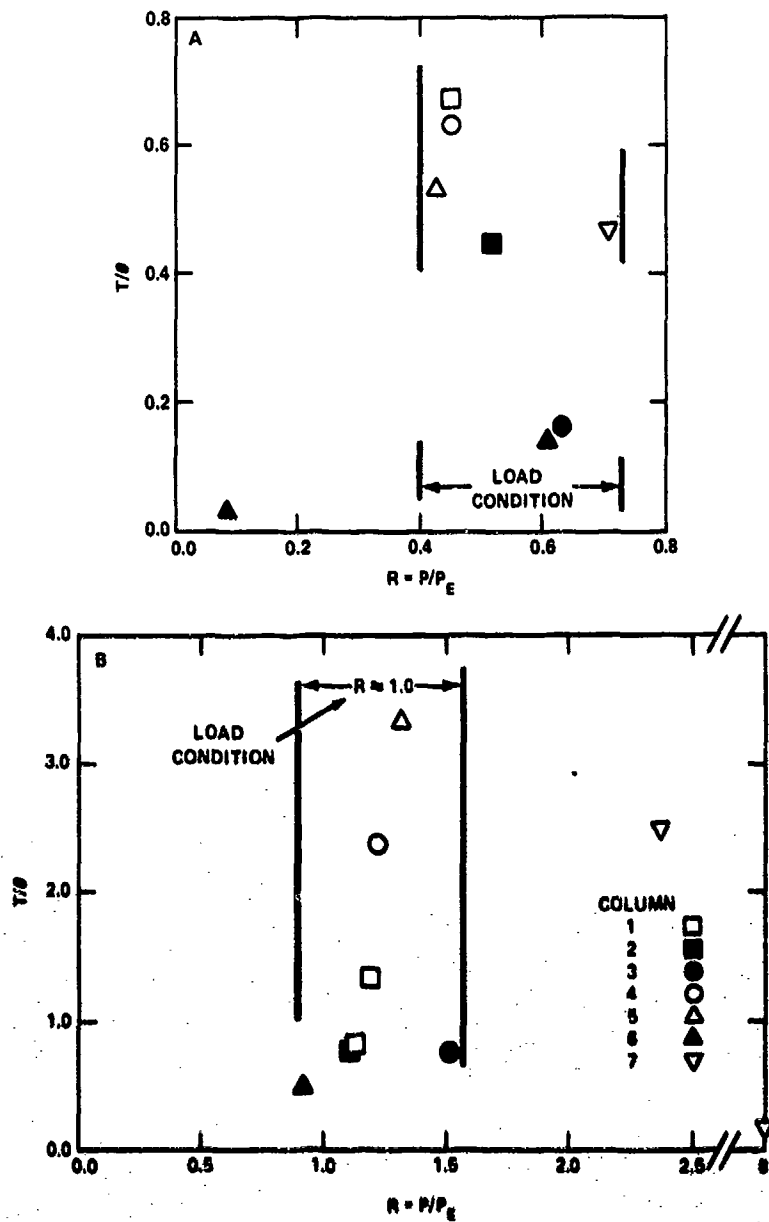


Figure 29 - Duration Ratio vs. Applied Load Ratio



TABLE 1 - COLUMN GEOMETRY AND PROPERTIES

Property	Column								
	1	2	3	4	5	6	7A*	7B*	7C*
Length (in.)	45.0625	32.625	20.375	45.0625	44.875	13.0625	40.875	40.875	40.875
Sides (in.)	1x1/2	1/2x1/2	3/8x3/8	1x1/2	1x1/2	1/2x1/2	3/8x3/8	3/8x3/8	3/8x3/8
Area (in. <sup>2</sup> )	0.5	0.25	0.1406	0.5	0.5	0.25	0.1406	0.1406	0.1406
Inertia (in. <sup>4</sup> )	0.01042	0.0052	0.00165	0.01042	0.01042	0.0052	0.00165	0.00165	0.0015
Radius Gyration (in.)	0.1443	0.1443	0.108	0.1443	0.1443	0.1443	0.108	0.108	0.108
Offset (in.)	0.3125	0.625	0.343	0.8125	1.6875	0.219	0.875	0.875	0.934
Frequency (hertz)	22.3	43.1	82.7	22.3	22.3	268.7	20.5	20.5	20.5
Euler Load (lb.)	506.5	482.2	392.2	506.5	506.5	2973.0	97.5	97.5	97.5
Slenderness Ratio	312.3	226.1	188.7	312.3	312.3	90.5	378.5	378.5	378.5
Eccentricity Ratio	0.00643	0.0192	0.0168	0.018	0.0376	0.01105	0.0214	0.0214	0.0228

\*Refers to Test Nos. 7A, 7B, 7C.

TABLE 1A - ALTERED COLUMN ECCENTRICITIES ( $y_i$ )

	Column							
	1	2	3	4	5	6	7*	7**
Static Load (lbs.)	17	17	30	17	17	30	17	17
$y_i$ (in.) Altered	0.3235	0.648	0.372	0.8405	1.7455	0.221	1.06	1.13

\*Test 7A and 7B.

\*\*Test 7C.

TABLE 2 - LISTING OF TESTS AND NOMINAL TEST CONDITIONS

COLUMN	TEST NUMBER		
	R* = 1/2	R* = 1.0	R* = Other
1	1E	2E	8 (R = 1.0)
2	4A	4B	
3	5A	5B	NA
4	2A	2B	NA
6	3A	3B	NA
6	6B	6C	6A (R = 1/10)
7	7A	NA	7B (R = 2) 7C (R = 8)

\*Nominal values of ratio of applied load (P) to column Euler Load ( $P_E$ ):  $R = P/P_E$ .

NA - Not Applicable.

TABLE 3 - COLUMNS GROUPED ACCORDING TO NON-DIMENSIONAL VARIABLES

GROUP I COLUMN	VARIABLES	CONSTANTS
1 4 5	$y_i/\ell$	$A/\ell^2, \ell/r, T_{c0}/\ell$
GROUP II COLUMN		
2 4	$\ell/r, T_{c0}/\ell$	$y_i/\ell, A/\ell^2$
GROUP III COLUMN		
3 6	$A/\ell^2, \ell/r, T_{c0}/\ell$	$y_i/\ell$

TABLE 4 - ACCELERATION DATA OF MASS IMPACTING ON COLUMNS

Column	$R^* = 1/2$			$R^* = 1$			$R = \text{Other}$		
	$A_0$	$t_r$	$\theta$	$A_0$	$t_r$	$\theta$	$A_0$	$t_r$	$\theta$
1	1.01	7.5	67.0	2.53	3.6	53.5	2.71	R = 1 5.3	33.5
2	1.12	12.7	52.0	2.38	5.5	28.5		NA	
3	1.09	10.5	78.0	2.67	5.2	18.5		NA	
4	1.01	8.7	71.5	2.75	3.7	18.9		NA	
5	0.98	12.0	84.5	2.98	3.9	13.5			
6	8.11	9.2	27.0	12.2	4.7	7.5	1.13	R = 1/10 9.4	98.5
7	0.31	10.4	114.0		NA		1.0	R = 2 8.8	21.6

Acceleration -  $A_0$  (g's)Rise Time -  $t_r$  (msec)Duration -  $\theta$  (msec)

\*Nominal Value of R

NA - Not Applicable

TABLE 5 - PEAK COLUMN STRAIN AND DISPLACEMENT DATA, R = 1/2 (NOMINAL)

Column	$\epsilon_A$	$t_r$	$\epsilon_b$	$t_r$	$\delta_h$	$t_r$	$\delta_v$	$t_r$
1	104	NA	396	19.5	0.28	35.0	0.0	NA
2	319	7.8	343	10.5	0.42	10.5	0.0	NA
3	128	6.8	1583	25.0	0.32	13.0	0.0	NA
4	49	NA	1154	27.0	0.67	26.0	0.28	26
5	48	2.0	2107	45.0	1.13	45.0	0.6	45
6	*	NA	1884**	9.0	0.26	20.0	0.12	20
7	201	5.5	3671	75.0	3.34	92.0	1.26	92

NOTE - Values listed above occur at time  $t \leq 0$ 

NA - Not Applicable

\*Gage effected by bending of column, calculated strain =  $P/AE = 727 \mu\text{in/in}$ \*\* $\epsilon_b = \epsilon_b (\text{Meas}) + \epsilon_{\text{axial}} (\text{calculated})$  $\epsilon_b = 1159 + 727 = 1884 \mu\text{in/in}$  $\epsilon_A$  - Axial strain  $\mu\text{in/in}$  (Comp.) $\epsilon_b$  - Bending Strain  $\mu\text{in/in}$  (Ten.) $\delta_h$  - Midpoint Displacement in $\delta_v$  - End Point Displacement in $t_r$  - Rise Time msec

TABLE 6 - PEAK COLUMN STRAIN AND DISPLACEMENT DATA R = 1 (NOMINAL)

Column	$\epsilon_A$	$t_r$	$\epsilon_b$	$t_r$	$\delta_h$	$t_r$	$\delta_v$	$t_r$
1	340	6.5	3000	51.5	2.61	51.5	0.70	51.5
2	914	4	3891	22.5	2.01	22.5	0.68	22.5
3	1042	2.5	5959	11.5	1.1	10.0	0.61	10.0
4	212	5.5	1800	11.5	1.06	11.5	0.0	0.0
5	125	4.8	1185	12.5	0.91	12.5	0.33	12.5
6	*	NA	19920	3.5	1.05	3.5	0.23	3.5

NOTE - Values listed above occur at time  $t \leq 0$ 

NA - Not Applicable

\* - Effected by bending in column

 $\epsilon_A$  - Axial strain  $\mu\text{in/in}$  (Comp.) $\epsilon_b$  - Bending Strain  $\mu\text{in/in}$  (Ten.) $\delta_h$  - Midpoint Displacement in $\delta_v$  - End Point Displacement in $t_r$  - Rise Time msec

TABLE 7 - PEAK COLUMN STRAIN AND DISPLACEMENT DATA R = OTHER

Column	R (Nom.)	$\epsilon_A$	$t_r$	$\epsilon_b$	$t_r$	$\delta_h$	$t_r$	$\delta_v$	$t_r$
1	1	169	4	2514	26.5	2.17	26.5	1.21	26.5
6	1/10	484	13	312	12.5	0.0	NA	0.0	NA
7	2	242	3	1183	21.5	1.15	13.0	0.39	13
	8	685	7	2622	7.0	0.03	1.0	0.0	NA

NOTE - Values listed above occur at time  $t \leq \theta$ 

NA - Not Applicable

 $\delta_h$  - Midpoint Displacement in. $\epsilon_A$  - Axial Strain  $\mu\text{in/in}$  $\delta_v$  - End Point Displacement in. $\epsilon_b$  - Bending Strain  $\mu\text{in/in}$  $t_r$  - Rise Time msec

TABLE 8 - LIST OF NON-DIMENSIONAL COLUMN VARIABLES R = 1/2

Column	$Y_{MAX}/V_i$	$v_i/\ell$	$(\ell/r)^2 \times P_E/AE$	$\ell/r$	$t_r^* c_o/\ell$	$t_r^*/T \times 10^{-3}$	R (Actual)	$A/\ell^2$	$\theta/T$
1	1.866	$7.18 \times 10^{-3}$	9.89	312.5	32.7	0.1673	0.45	$2.462 \times 10^{-4}$	1.52
2	1.644	$19.86 \times 10^{-3}$	9.86	226.1	76.48	0.538	0.52	$2.349 \times 10^{-4}$	2.25
3	1.849	$18.2 \times 11^{-3}$	9.93	188.7	101.25	0.8685	0.623	$3.38 \times 10^{-4}$	6.45
4	1.794	$18.65 \times 11^{-3}$	9.89	312.5	37.93	0.1786	0.45	$2.462 \times 10^{-4}$	1.62
5	1.647	$39.9 \times 11^{-3}$	9.89	312.5	52.54	0.2455	0.423	$2.483 \times 10^{-4}$	1.92
6	2.18	$16.92 \times 11^{-3}$	9.74	90.5	138.37	2.381	0.611	$1.465 \times 10^{-3}$	7.3
7	4.15	$25.93 \times 10^{-3}$	9.94	378.5	49.99	0.197	0.712	$8.415 \times 10^{-5}$	2.34

\* $t_r$  - refers to acceleration rise time.

TABLE 9 - LIST OF NON-DIMENSIONAL COLUMN VARIABLES R = 1

Column	$Y_{MAX}/V_i$	$v_i/\ell$	$(\ell/r)^2 \times P_E/AE$	$\ell/r$	$t_r^* c_o/\ell$	$t_r^*/T \times 10^{-3}$	R (Actual)	$A/\ell^2$	$\theta/T$
1	9.07			312.5	15.89	0.080	1.12		0.75
2	4.102			226.1	33.12	0.237	1.11		1.23
3	3.98	SEE TABLE 8		188.7	50.141	0.430	1.53	SEE TABLE 8	1.38
4	2.28			312.5	17.44	0.083	1.22		0.429
5	1.52			312.5	17.08	0.087	1.31		0.31
6	5.751			90.5	70.89	1.263	0.92		2.02

\* $t_r$  - refers to acceleration rise time.

TABLE 10 - LIST OF NON-DIMENSIONAL COLUMN VARIABLES R = OTHER

Column	$Y_{MAX}/V_i$	$v_i/\ell$	$(\ell/r)^2 \times P_E/AE$	$\ell/r$	$t_r^* c_o/\ell$	$t_r^*/T \times 10^{-3}$	R (Actual)	$A/\ell^2$	$\theta/T$
1	7.71	$7.18 \times 10^{-3}$	9.89	312.5	32.7	0.118	1.20	$2.462 \times 10^{-4}$	0.78
6	1.0	$16.92 \times 10^{-3}$	9.74	90.5	0.0	0.0	0.09	$1.48 \times 10^{-3}$	25.9
7	2.085	$25.93 \times 10^{-3}$	9.94	379.5	42.3	0.167	2.3	$8.41 \times 10^{-5}$	0.444
	1.03	$27.64 \times 10^{-3}$	9.94	378.5	28.7	0.114	7.8	$8.41 \times 10^{-5}$	0.125

\* $t_r$  - refers to acceleration rise time.

LARGE DEFLECTION RANDOM RESPONSE OF SYMMETRIC  
LAMINATED COMPOSITE PLATES

K. R. Wentz, D. B. Paul  
Air Force Wright Aeronautical Laboratories  
Wright-Patterson Air Force Base, Ohio

and

C. Mei  
Department of Mechanical Engineering and Mechanics  
Old Dominion University  
Norfolk, Virginia

Large amplitude response of symmetric laminated rectangular plates subjected to broadband random acoustic excitation is studied analytically. The boundary conditions considered are all the edges simply supported and all the edges clamped. The inplane edge conditions considered are immovable and movable for each of the above cases. Mean-square deflections, mean-square strains, and equivalent linear frequencies at various acoustic loadings are obtained for  $[0, \pm 45]_s$  and  $[0, \pm 45, 90]_s$  graphite-epoxy laminates. The analytical results are verified through comparison with experimental data. The results obtained can be used in the sonic fatigue design of composite aircraft panels.

#### INTRODUCTION

The need to improve sonic fatigue resistance of aircraft structures has become increasingly important as a result of military and commercial demands on current and future airplane designs. A significant number of theoretical [1-6] and experimental investigations [7-12] on the sonic fatigue design of aircraft structures have been undertaken during the past several years to help provide the needed reliability. The majority of analytical investigations to date have been formulated within the framework of linear or small-deflection structural theory. Test results [5, 7, 9-12] on various aircraft panels have shown that high noise levels in excess of 120 dB produce nonlinear behavior with large deflections. The linear analyses often predict the root-mean-square (RMS) deflection and RMS stresses well above those of the experiment, and the frequencies of vibration well below those of the experiment [5, 7, 9, 11, 12]. It is well known that the prediction of sonic fatigue life is based on RMS stress and predominant response frequency in conjunction with the stress versus cycle to failure (S-N) data. Therefore, the use of linear analyses results in a poor estimation of panel service life.

High strength and high modulus fiber-reinforced composite materials are under development for use on aircraft. Many of these composite structural components are exposed to high intensity noise fields and are therefore subject to sonic fatigue. In the present paper, the large deflection response of symmetric laminated rectangular panels subjected to broadband random acoustic excitation is studied analytically. The nonlinear equations of motion for symmetric laminates are derived in terms of a stress function,  $F$ , and a lateral displacement,  $W$ . Due to the complex nature of the problem, the study is restricted to single mode response. A deflection function representing the first mode is assumed. Corresponding to the assumed mode, a stress function satisfying the different inplane edge conditions is obtained by solving the compatibility equation. A modified Galerkin's method is then applied to the governing equation of motion to yield a nonlinear time-differential equation. Assuming that the excitation is Gaussian, the equivalent linearization method [13] is employed in order to linearize this equation. An iterative procedure is introduced to obtain RMS amplitude and equivalent linear (or nonlinear) frequency at various acoustic loadings for  $[0, \pm 45]_s$  and  $[0, \pm 45, 90]_s$  graphite-epoxy laminates. RMS strains are also obtained as functions of RMS amplitude and at locations of

interest. Solutions are developed for the out-of-plane boundary conditions of all edges simply supported (SSSS) and all edges clamped (CCCC). Two inplane edge conditions considered are immovable and movable for each of the above cases.

The accuracy of the analytical method is investigated thru a quantitative comparison with experimental data. Experimental response data for  $[0, \pm 45]_s$  graphite-epoxy laminates from a previous Air Force sponsored program are compared to the analytical results. The comparison demonstrates that a better correlation between theory and experiment is achieved when the large deflection effect is included in the formulation.

#### NOMENCLATURE

a, b	plate length and width
A, D	laminate stiffnesses
A*	inverted laminate stiffnesses
C <sub>1</sub> , C <sub>2</sub> , D <sub>1</sub> , D <sub>2</sub>	constants
err	error of linearization
E[q <sup>2</sup> ]	mean-square of q
E <sub>1</sub> , E <sub>2</sub>	Young's moduli in major (longitudinal) and minor (transverse) principal material directions
f	equivalent linear frequency in Hz
F	stress function
F <sub>ij</sub>	constants
G <sub>12</sub>	shear modulus
H	plate thickness
H(ω)	frequency response function
K	middle surface curvature
L	mathematical operator
m	mass coefficient
N	resultant bending moment
n	number of layers
N <sub>x</sub>	resultant normal force
N <sub>y</sub>	constant
p	pressure loading
q	modal amplitude or displacement
Q	reduced stiffness
Q̄	transformed, reduced stiffness
r	length-to-width ratio
R(τ)	autocorrelation function
S	nondimensional excitation spectral density parameter
S(ω)	spectral density function of excitation pressure p( )
t	time
u, v	displacements of middle surface
w	transverse deflection
x, y, z	coordinates
α	nonlinearity coefficient
α <sub>0</sub>	nondimensional nonlinearity coefficient
ε	strain
ζ	damping ratio, c/c <sub>c</sub>
θ	lamination angle
λ	nondimensional frequency parameter
ν	Poisson's ratio
ρ	plate mass density
σ	stress
σ(V, W)	function defined in equation (16)

ω	radian frequency
Ω	equivalent linear or nonlinear radian frequency

#### Subscripts

c	complementary solution
p	particular solution
x, y, z	corresponding directions
0	linear
1, 2	major, minor principal material directions

#### Superscripts

k	kth layer
T	transpose

#### EQUATIONS OF MOTION

In this section, the governing equations are derived for a symmetric, angle-ply, laminated, composite plate. Using the Kirchhoff hypothesis of classical thin-plate theory, the total strains can be expressed as

$$\begin{aligned}\epsilon_x &= \epsilon_x^0 + z K_x \\ \epsilon_y &= \epsilon_y^0 + z K_y \\ \epsilon_{xy} &= \epsilon_{xy}^0 + z K_{xy}\end{aligned}\quad (1)$$

The strains in the middle surface, considering Karman-type geometric nonlinearity, can be expressed as

$$\begin{aligned}\epsilon_x^0 &= u_{,x} + \frac{w_{,x}^2}{2} \\ \epsilon_y^0 &= v_{,y} + \frac{w_{,y}^2}{2} \\ \epsilon_{xy}^0 &= u_{,y} + v_{,x} + w_{,x} w_{,y}\end{aligned}\quad (2)$$

Assuming small slopes ( $w_{,x} \ll 1$  etc.) as well as the Kirchhoff hypothesis, the middle surface curvatures can be expressed as

$$\begin{aligned}K_x &= -w_{,xx} \\ K_y &= -w_{,yy} \\ K_{xy} &= -2w_{,xy}\end{aligned}\quad (3)$$

The plate equations are obtained by applying force equilibrium of an element of the kth layer of the laminate. Integrating these equations over the plate thickness h, neglecting inplane inertia and rotary inertia terms, and retaining those nonlinear terms in accordance with the von Karman assumptions, lead to the following equations of motion

$$N_{x,x} + N_{xy,y} = 0 \quad N_{xy,x} + N_{y,y} = 0 \quad (4)$$

# METHOD OF ANALYSIS

**SIMPLY SUPPORTED EDGES.** Consider a simply supported, rectangular, symmetric composite plate of dimensions  $a$ ,  $b$  with the origin located at the center of the plate. The boundary conditions are:

$$x = \pm a/2: W = 0$$

$$D_{11}W_{,xx} + D_{12}W_{,yy} + 2D_{16}W_{,xy} = 0$$

$$y = \pm b/2: W = 0$$

$$D_{12}W_{,xx} + D_{22}W_{,yy} + 2D_{26}W_{,xy} = 0 \quad (20)$$

For the inplane condition of zero shear stress at the edges, the deflection function is assumed as

$$W = q(t)h(\cos \frac{\pi x}{a})(\cos \frac{\pi y}{b}) \quad (21)$$

Substituting equation (21) for  $W$  in equation (18) and solving it, the stress function is obtained as

$$F = F_c + F_p \quad (22)$$

in which the particular solution is

$$F_p = -\frac{q^3 h^2 F^2}{32} (F_{10} \cos \frac{2\pi x}{a} + F_{01} \cos \frac{2\pi y}{b}) \quad (23)$$

where the constants  $F_{10}$  can be expressed in terms of the laminate stiffnesses as

$$F_{10} = \frac{1}{A_{11}^2}$$

$$F_{01} = \frac{1}{A_{22}^2}$$

$$r = \frac{a}{b} \quad (24)$$

The complementary solution  $F_c$  will now be obtained such that it satisfies boundary conditions. For movable edges, the inplane boundary conditions are

$$x = \pm a/2: F_{,xy} = 0$$

$$\int_{-b/2}^{b/2} F_{,yy} dy = 0$$

$$y = \pm b/2: F_{,xy} = 0$$

$$\int_{-a/2}^{a/2} F_{,xx} dx = 0 \quad (25)$$

By making use of these conditions, it can be shown that  $F_c$  is zero for movable inplane edges. Hence

$$F = F_p \quad (26)$$

With the assumed deflection  $W$  given by equation (21) and stress function  $F$  given by equation (23), equation (15) is then satisfied by applying a modified Galerkin's method:

$$\begin{aligned} & \iint [\rho h \ddot{W} + L_1 W - \phi(F, W) - p] W dx dy \\ & + \int_{-b/2}^{b/2} (M_x)_x = -a/2 (W_x)_x = -a/2 dy \\ & + \int_{-b/2}^{b/2} (M_x)_x = a/2 (W_x)_x = a/2 dy \\ & + \int_{-a/2}^{a/2} (M_y)_y = -b/2 (W_y)_y = -b/2 dx \\ & + \int_{-a/2}^{a/2} (M_y)_y = b/2 (W_y)_y = b/2 dx = 0 \end{aligned} \quad (27)$$

which yields a modal equation of the form

$$\ddot{q} + \omega_0^2 q + \beta_p q^3 = \frac{p(t)}{m} \quad (28)$$

and

$$\omega_0^2 = \Lambda_0^2 \frac{E_2 h^2}{\rho b^4}$$

$$\beta_p = \beta_p^0 \frac{E_2 h^2}{\rho b^4}$$

$$m = \frac{\pi^2 \rho h^2}{16} \quad (29)$$

$$\Lambda_0^2 = \frac{\pi^4}{E_2 h^3 r^2} (D_{11} + 2(D_{12} + 2D_{66})r^2 + D_{22}r^4)$$

$$\beta_p^0 = \frac{\pi^4}{16 E_2 h} (F_{10} + F_{01}) \quad (30)$$

where  $\omega_0$  is linear radian frequency,  $\beta_p$  is nonlinearity coefficient, and  $m$  is mass coefficient. The linear frequency  $\omega_0$  and nonlinearity coefficient  $\beta_p$  are nondimensional parameters.

For immovable edges, the inplane boundary conditions of zero shear stress and zero normal displacement at the four edges are

$$M_{x,xx} + 2M_{xy,xy} + M_{y,yy} + N_{x,xx} + 2N_{xy,xy} + N_{y,yy} + p = \rho h \ddot{w} \quad (5)$$

where  $N$  and  $M$  are resultant normal forces and resultant bending moments, respectively, defined in the usual manner of classical plate theory, and the average mass density of the laminate is defined by

$$\rho = \frac{1}{h} \int_{-h/2}^{h/2} \rho_0(k) dz \quad (6)$$

the distributed transverse load is simply

$$p = \sigma_z(k) \Big|_{-h/2}^{h/2} \quad (7)$$

The constitutive relation for a symmetric laminated composite plate is given by:

$$\begin{Bmatrix} N \\ M \end{Bmatrix} = \begin{bmatrix} A & 0 \\ 0 & D \end{bmatrix} \begin{Bmatrix} \epsilon^0 \\ \kappa \end{Bmatrix} \quad (8)$$

where

$$\begin{aligned} N^T &= (N_x \ N_y \ N_{xy}) \\ M^T &= (M_x \ M_y \ M_{xy}) \\ \epsilon^0 T &= (\epsilon_x^0 \ \epsilon_y^0 \ \epsilon_{xy}^0) \\ \kappa^T &= (\kappa_x \ \kappa_y \ \kappa_{xy}) \end{aligned} \quad (9)$$

and the laminate stiffnesses  $A$  and  $D$  are symmetric matrices defined by the relations:

$$(A_{ij}, D_{ij}) = \int_{-h/2}^{h/2} (1, z^2) \bar{Q}_{ij} dz \quad (10)$$

The  $\bar{Q}_{ij}$  are the transformed, reduced stiffness components [1, 13]. For the  $[0, \pm 45]$  and  $[0, \pm 45, 90]$  laminated plates it can be shown that

$$A_{16} = A_{26} = 0 \quad (11)$$

Nonvanishing elements of  $A$ ,  $D$  and  $\bar{Q}_{ij}$  are given in Reference 16. Equation (8) can be rewritten as:

$$\begin{Bmatrix} N \\ M \end{Bmatrix} = \begin{bmatrix} A^* & 0 \\ 0 & D \end{bmatrix} \begin{Bmatrix} \epsilon^0 \\ \kappa \end{Bmatrix} \quad (12)$$

where

$$A^* = A^{-1} \quad (13)$$

Nonvanishing components of the inverted laminate stiffness  $A^*$  are also given in Reference 16.

The Airy stress function  $F$  is defined such that

$$N^T = (F_{,yy} \ F_{,xx} \ -F_{,xy}) \quad (14)$$

Using equations (3), (9), (12) and (14) in equation (5) leads to the equation of motion in the transverse direction as

$$\rho h \ddot{w} + L_1 w - \phi(F, w) - p = 0 \quad (15)$$

where

$$\begin{aligned} L_1 &= D_{11} \frac{\partial^4}{\partial x^4} + 4D_{16} \frac{\partial^4}{\partial x^3 \partial y} + 2(D_{12} + 2D_{66}) \\ &\quad \frac{\partial^4}{\partial x^2 \partial y^2} + 4D_{26} \frac{\partial^4}{\partial x \partial y^3} + D_{22} \frac{\partial^4}{\partial y^4} \end{aligned}$$

$$\phi(F, w) = F_{,yy} w_{,xx} + F_{,xx} w_{,yy} - 2F_{,xy} w_{,xy} \quad (16)$$

The compatibility equation is derived from equation (2) and is written as

$$\epsilon_{x,yy}^0 + \epsilon_{y,xx}^0 - \epsilon_{xy,xy}^0 + \frac{1}{2} \phi(w, w) = 0 \quad (17)$$

Using equations (12) and (14) in equation (17), the compatibility equation in terms of  $F$  and  $w$  is given below

$$L_2 F + \frac{1}{2} \phi(w, w) = 0 \quad (18)$$

where

$$L_2 = A^* \frac{\partial^4}{\partial x^4} + (2A_{12}^* + A_{66}^*) \frac{\partial^4}{\partial x^2 \partial y^2} + A_{11}^* \frac{\partial^4}{\partial y^4} \quad (19)$$

Equations (15) and (18) are the governing equations which will be solved by employing modified Galerkin's approach and the equivalent linearization method.



$$x = \pm a/2: F_{,xy} = 0$$

$$\iint (\epsilon_x^0 - \frac{1}{2} W_{,x}^2) dx dy = 0$$

$$y = \pm b/2: F_{,xy} = 0$$

$$\iint (\epsilon_y^0 - \frac{1}{2} W_{,y}^2) dx dy = 0 \quad (31)$$

The complementary solution is assumed as

$$F_c = \bar{N} \frac{x^2}{2} + \bar{N} \frac{y^2}{2} \quad (32)$$

Upon using relations (12) and (21) and enforcing the conditions of equation (31),  $\bar{N}_x$ ,  $\bar{N}_y$ , and  $\bar{N}_{xy}$  in equation (32) are obtained as

$$\bar{N}_x = \frac{q^2 h^2 \pi^2}{8(A_{11}^* A_{22}^* - A_{12}^{*2})} \left( \frac{A_{22}^*}{a^2} - \frac{A_{12}^*}{b^2} \right)$$

$$\bar{N}_y = \frac{q^2 h^2 \pi^2}{8(A_{11}^* A_{22}^* - A_{12}^{*2})} \left( \frac{A_{11}^*}{b^2} - \frac{A_{12}^*}{a^2} \right) \quad (33)$$

The particular solution  $F_p$  has been obtained and given in equation (23). The total stress function, therefore, is  $F = F_c + F_p$  for immovable inplane edges. Substituting the stress function  $F$  and the deflection  $W$  in equation (27), the modal equation is obtained as follows

$$\ddot{q} + \omega_0^2 q + (\beta_p + \beta_c) q^3 = \frac{p(t)}{m} \quad (34)$$

where

$$\beta_c = \beta_c^* \frac{E_2 h^2}{\rho b^4}$$

$$\beta_c^* = \frac{\pi^4}{8 E_2 h r^4} \left( \frac{A_{22}^* - 2 A_{12}^* r^2 + A_{11}^* r^4}{A_{11}^* A_{22}^* - A_{12}^{*2}} \right) \quad (35)$$

The term  $\beta_c$  is an addition to the nonlinearity coefficient due to immovable inplane edges; the nonlinearity coefficient  $\beta_c^*$  is a nondimensional parameter. Equations (28) and (34) represent the undamped, large-amplitude, modal equations of simply supported rectangular, symmetric laminated, composite panels with movable and immovable inplane edges, respectively. This nonlinear modal equation will be solved by employing the method of equivalent linearization.

**CLAMPED EDGES.** The deflection function which satisfies the clamped condition on all four

edges of the plate is assumed as

$$W = \frac{q(t)h}{4} (1 + \cos \frac{2\pi x}{a})(1 + \cos \frac{2\pi y}{b}) \quad (36)$$

The clamped support is simply

$$x = \pm a/2: W = W_{,x} = 0$$

$$y = \pm b/2: W = W_{,y} = 0 \quad (37)$$

Introducing equation (36) in equation (18) and solving it, the stress function is obtained as follows

$$F = F_c + F_p \quad (38)$$

$$\begin{aligned} F_p = & \frac{q^2 h^2 \pi^2}{32} (F_{10} \cos \frac{2\pi x}{a} + F_{01} \cos \frac{2\pi y}{b} \\ & + F_{11} \cos \frac{2\pi x}{a} \cos \frac{2\pi y}{b} + F_{20} \cos \frac{4\pi x}{a} + F_{02} \cos \frac{4\pi y}{b} \\ & + F_{21} \cos \frac{4\pi x}{a} \cos \frac{2\pi y}{b} + F_{12} \cos \frac{2\pi x}{a} \cos \frac{4\pi y}{b}) \quad (39) \end{aligned}$$

where the constants  $F_{ij}$  can be expressed in terms of the laminate stiffnesses and the length-to-width ratio of the panel ( $r = a/b$ ) as

$$F_{10} = \frac{1}{A_{22}^*}$$

$$F_{01} = \frac{1}{A_{11}^* r^4}$$

$$F_{11} = \frac{2}{A_{22}^* + (2A_{12}^* + A_{66}^*) r^2 + A_{11}^* r^4}$$

$$F_{20} = \frac{1}{16 A_{22}^*}$$

$$F_{02} = \frac{1}{16 A_{11}^* r^4}$$

$$F_{21} = \frac{1}{16 A_{22}^* + 4(2A_{12}^* + A_{66}^*) r^2 + A_{11}^* r^4}$$

$$F_{12} = \frac{1}{A_{22}^* + 4(2A_{12}^* + A_{66}^*) r^2 + 16 A_{11}^* r^4} \quad (40)$$

It can be shown that for movable inplane edge conditions [eq. (25)],  $F_c = 0$ . Hence,

$$F = F_p \quad (41)$$

Introducing the expressions for  $W$  and  $F$ , equations (36) and (39), and applying Galerkin's method:

$$\iint [\rho h W + L_1 W - \phi(F, W) - p] W dx dy = 0$$

yields the modal equation

$$\ddot{q} + \omega_0^2 q + \beta_p q^3 = \frac{p(t)}{m} \quad (42)$$

where

$$\omega_0^2 = \lambda_0^2 \frac{E_2 h^2}{\rho b^4}$$

$$\beta_p = \beta_p^* \frac{E_2 h^2}{\rho b^4}$$

$$m = \frac{9 \rho h^2}{16} \quad (43)$$

$$\lambda_0^2 = \frac{16 \pi^4}{9 E_2 h^3 r^4} \left\{ 3 D_{11} + 2(D_{12} + 2 D_{66}) r^2 + 3 D_{22} r^4 \right\} \quad (44a)$$

$$\beta_p^* = \frac{\pi^4}{9 E_2 h} [F_{10} + F_{01} + F_{11} + F_{20} + F_{02} + \frac{1}{2} (F_{21} + F_{12})] \quad (44b)$$

in which  $\omega_0$  is linear radian frequency,  $\beta_p$  is the nonlinearity coefficient, and  $m$  is the mass coefficient. The linear frequency  $\lambda_0$  and nonlinearity coefficient  $\beta_p^*$  are both nondimensional parameters.

For the case of the clamped plate with immovable edges the complementary stress function is assumed as the form appearing in equation (32). Upon enforcing the inplane edge conditions [eq. (31)], it can be shown that the constants  $N_x$ ,  $N_y$ , and  $N_{xy}$  are obtained as

$$N_x = \frac{3 q^2 h^2 \pi^4}{32 (A_{11} A_{22} - A_{12}^2)} \left( \frac{A_{22}}{a^2} - \frac{A_{12}}{b^2} \right)$$

$$N_y = \frac{3 q^2 h^2 \pi^4}{32 (A_{11} A_{22} - A_{12}^2)} \left( \frac{A_{11}}{b^2} - \frac{A_{12}}{a^2} \right)$$

$$N_{xy} = 0 \quad (45)$$

Using equations (32), (36), and (39) and applying Galerkin's method yields the modal equation

$$\ddot{q} + \omega_0^2 q + (\beta_p + \beta_c) q^3 = \frac{p(t)}{m} \quad (46)$$

where the additional nonlinearity coefficient due to immovable inplane edges is

$$\beta_c = \beta_c^* \frac{E_2 h^2}{\rho b^4}$$

$$\beta_c^* = \frac{\pi^4}{8 E_2 h r^4} \left( \frac{A_{22} - 2 A_{12} r^2 + A_{11} r^4}{A_{11} A_{22} - A_{12}^2} \right) \quad (47)$$

Equations (42) and (46) represent the modal equations of undamped, clamped, rectangular, symmetric laminates undergoing large deflections with movable and immovable inplane edges, respectively.

**DAMPING FACTOR.** It is known that damping has a significant effect on the response of structures. The precise determination of the damping coefficient of a given structure, therefore, should be emphasized. Two methods commonly used for determining the damping characteristics of structures are the bandwidth method and the decay rate method. In the bandwidth method, the half-power bandwidth ( $= 2\zeta$ ) is measured at modal resonance. In the decay rate method, the logarithmic decrement ( $= 2\pi\zeta$ ) of decaying modal response traces is measured. The values of damping ratio  $\zeta$  ( $= c/c_c$ ) generally range from 0.005 to 0.05 for the common type of composite panel construction used in aircraft structures [4, 12, 17]. Once the damping ratio is determined from experiments or from existing data of similar construction, the modal equations [eqs. (28), (34), (42), and (46)] can be expressed in a general form as

$$\ddot{q} + 2\zeta\omega_0\dot{q} + \omega_0^2 q + \beta q^3 = \frac{p(t)}{m} \quad (48)$$

The method of equivalent linearization will be used to obtain an approximate RMS amplitude from equation (48).

**METHOD OF EQUIVALENT LINEARIZATION.** The basic idea of the equivalent linearization method [13, 18, and 19] can be obtained from the linearized equation

$$\ddot{q} + 2\zeta\omega_0\dot{q} + \Omega^2 q = \frac{p(t)}{m} \quad (49)$$

where  $\Omega$  is an equivalent linear or nonlinear frequency. The error of linearization, a random process, is

$$\text{err} = (\omega_0^2 - \Omega^2)q + \beta q^3 \quad (50)$$

which is simply the difference between equation (48) and equation (49). The method of attack is to minimize this error in a suitable way. The usual choice is to minimize the mean-square error  $E[\text{err}^2]$ , that is

$$\frac{\partial}{\partial \Omega^2} E[\text{err}^2] = 0 \quad (51)$$

If the acoustic pressure excitation  $p(t)$  is stationary Gaussian, is ergodic, and has a zero mean. Then the approximate displacement  $q$ , computed from the linearized equation eq. (49), is also Gaussian and approaches stationarity because the panel motion is stable. Substituting equation (50) into equation (51) and interchanging the order of differentiation and expectation yield

$$(\omega_0^2 - \Omega^2)E[q^2] + 8E[q^4] = 0 \quad (52)$$

which leads to the relation between the equivalent linear frequency and the mean-square displacement as

$$\Omega^2 = \omega_0^2 + 38E[q^2] \quad (53)$$

Dividing both sides of equation (53) by  $\frac{E_2 h^2}{\rho b^4}$  yields

$$\lambda^2 = \lambda_0^2 + 38^* E[q^2] \quad (54)$$

where  $\lambda^2$  is a nondimensional equivalent linear or nonlinear frequency parameter and  $E[q^2]$  is the maximum mean-square deflection of the laminated composite plate. The linear frequencies  $\lambda_0$  and nonlinearity coefficients  $38^*$  are given in equations (30), (35), (44), and (47) for different support conditions.

The mean-square response of modal amplitude from equation (49) is

$$E[q^2] = \int_0^\infty S(\omega) |H(\omega)|^2 d\omega \quad (55)$$

where  $S(\omega)$  is the PSD function of the excitation  $p(t)$ . The frequency response function  $H(\omega)$  is given by

$$H(\omega) = \frac{1}{m(\lambda_0^2 - \omega^2 + 2i\zeta\omega_0\omega)} \quad (56)$$

For lightly damped ( $\zeta \leq 0.05$ ) structures, the frequency response curves will be highly peaked at the equivalent linear frequency  $\Omega$  (not at  $\omega_0$  as in the small-deflection linear theory). The integration of equation (55) can be greatly simplified when the spectral density of the excitation is slowly varying in the neighborhood of  $\Omega$  and  $S(\Omega)$  can be treated as constant in the frequency band surrounding this nonlinear resonance peak  $\Omega$ ; then equation (55) yields

$$E[q^2] = \frac{\pi S(\Omega)}{4m^2 \zeta \omega_0 \Omega^2} \quad (57)$$

In practice, the PSD function is generally given in terms of the frequency  $f$  in Hz. To convert the above result one can substitute

$$\Omega = 2\pi f$$

$$S(\Omega) = \frac{S(f)}{2\pi} \quad (58)$$

into equation (57); then the mean-square peak deflection becomes

$$E[q^2] = \begin{cases} \frac{32S}{\pi^2 \zeta \lambda_0 \lambda^2}, & \text{for Simply Supported Edges} \\ \frac{32S}{81 \zeta \lambda_0 \lambda^2}, & \text{for Clamped Edges} \end{cases} \quad (59)$$

The PSD function  $S(f)/2\pi$  has the units  $(\text{Pa})^2/\text{Hz}$  or  $(\text{psi})^2/\text{Hz}$ , and  $S$  in equation (59) is a nondimensional, forcing excitation, spectral density parameter defined as

$$S = \frac{S(f)}{\rho^2 h^4 \left( \frac{E_2 h^2}{\rho b^4} \right)^{3/2}} \quad (60)$$

The equivalent linear frequency parameters  $\lambda^2$  in equation (59) can be determined through equation (54).

**SOLUTION PROCEDURE.** The mean-square displacement  $E[q^2]$  in equation (57) [or eq. (59)] is evaluated at the equivalent linear frequency  $\Omega$  (or  $\lambda$ ) which is in turn related to  $E[q^2]$  through equation (53) [or eq. (54)]. To determine the mean-square deflection, an iterative procedure is introduced. One can estimate the initial mean-square deflection  $E[q_0^2]$  using linear frequency  $\omega_0$  through equation (57) as

$$E[q_0^2] = \frac{\pi S(\omega_0)}{4m^2 \zeta \omega_0^3} \quad (61)$$

This initial estimate of  $E[q_0^2]$  is simply the mean-square displacement based on linear theory. It can now be used to obtain a refined estimate of  $\Omega_1$  through equation (53):  $\Omega_1^2 = \omega_0^2 + 38E[q_0^2]$ ; then  $E[q_1^2]$  is computed through equation (57) as

$$E[q_1^2] = \frac{\pi S(\Omega_1)}{4m^2 \zeta \omega_0 \Omega_1^2} \quad (62)$$

As the iterative process converges on the  $n$ th cycle, the relations

$$E[q_n^2] = \frac{\pi S(\Omega_n)}{4\pi^2 \omega_0^2 \Omega_n^2} = E[q_{n-1}^2]$$

$$\Omega_n^2 = \omega_0^2 + 3\beta E[q_{n-1}^2] = \Omega_{n-1}^2 \quad (63)$$

become satisfied. In the numerical results presented in the following section, convergence is considered achieved whenever the difference of the RMS deflections satisfy the relation

$$\left| \frac{\sqrt{E[q_n^2]} - \sqrt{E[q_{n-1}^2]}}{\sqrt{E[q_n^2]}} \right| \leq 10^{-3} \quad (64)$$

**STRAIN AND STRESS RESPONSE.** Once the RMS displacement is determined, the strains can be obtained from eqs. (1), (3), and (12). For simply supported, symmetric laminates with immovable inplane edges, the strains on the surface ( $z = h/2$ ) of the plate are given by

$$\begin{aligned} \frac{b^2}{h^2} \epsilon_x &= q \frac{\pi^2}{2} \cos \frac{\pi x}{a} \cos \frac{\pi y}{b} \\ &+ q^2 \frac{\pi^2}{8} \left[ \cos \frac{2\pi y}{b} + \frac{A_{12}^*}{A_{22}^*} r^2 \cos \frac{2\pi x}{a} + 1 \right] \end{aligned} \quad (65a)$$

$$\begin{aligned} \frac{b^2}{h^2} \epsilon_y &= q \frac{\pi^2}{2} \cos \frac{\pi x}{a} \cos \frac{\pi y}{b} \\ &+ q^2 \frac{\pi^2}{8} \left[ \frac{A_{12}^*}{A_{11}^* r^2} \cos \frac{2\pi y}{b} + \cos \frac{2\pi x}{a} + 1 \right] \end{aligned} \quad (65b)$$

$$\frac{b^2}{h^2} \epsilon_{xy} = q \left( -\frac{\pi^2}{r} \sin \frac{\pi x}{a} \sin \frac{\pi y}{b} \right) \quad (65c)$$

For movable inplane edges, the last term in equations (65a) and (65b) vanishes.

For clamped, symmetric laminates with immovable inplane edges, the strains on the surface of the plate are given by:

$$\begin{aligned} \frac{b^2}{h^2} \epsilon_x &= q \frac{\pi^2}{2} \left[ \frac{1}{2} \cos \frac{2\pi x}{a} (1 + \cos \frac{2\pi y}{b}) \right] \\ &+ q^2 \frac{\pi^2}{8} \left[ \frac{A_{12}^*}{A_{22}^*} \cos \frac{2\pi x}{a} + \frac{A_{12}^*}{4A_{22}^*} \cos \frac{4\pi x}{a} + \frac{1}{r^2} \cos \frac{2\pi y}{b} \right. \\ &+ \frac{1}{4r^2} \cos \frac{4\pi y}{b} + \frac{2(A_{12}^* + A_{11}^* r^2)}{A_{22}^* + (2A_{12}^* + A_{66}^*)r^2 + A_{11}^* r^4} \cos \frac{2\pi x}{a} \cos \frac{2\pi y}{b} \\ &+ \frac{4A_{12}^* + A_{11}^* r^2}{16A_{22}^* + 4(2A_{12}^* + A_{66}^*)r^2 + A_{11}^* r^4} \cos \frac{4\pi x}{a} \cos \frac{2\pi y}{b} \\ &\left. + \frac{A_{12}^* + 4A_{11}^* r^2}{A_{22}^* + 4(2A_{12}^* + A_{66}^*)r^2 + 16A_{11}^* r^4} \cos \frac{2\pi x}{a} \cos \frac{4\pi y}{b} + \frac{3}{4r^2} \right] \end{aligned} \quad (66a)$$

$$\begin{aligned} \frac{b^2}{h^2} \epsilon_y &= q \frac{\pi^2}{2} (1 + \cos \frac{2\pi x}{a}) \cos \frac{2\pi y}{b} \\ &+ q^2 \frac{\pi^2}{8} \left[ \cos \frac{2\pi x}{a} + \frac{A_{12}^*}{A_{11}^* r^2} \cos \frac{2\pi y}{b} \right. \\ &+ \frac{2(A_{12}^* + A_{11}^* r^2)}{A_{22}^* + (2A_{12}^* + A_{66}^*)r^2 + A_{11}^* r^4} \cos \frac{2\pi x}{a} \cos \frac{2\pi y}{b} \\ &+ \frac{1}{4} \cos \frac{4\pi x}{a} + \frac{A_{12}^*}{4A_{11}^* r^2} \cos \frac{4\pi y}{b} \\ &+ \frac{4A_{12}^* + A_{11}^* r^2}{16A_{22}^* + 4(2A_{12}^* + A_{66}^*)r^2 + A_{11}^* r^4} \cos \frac{4\pi x}{a} \cos \frac{2\pi y}{b} \\ &\left. + \frac{A_{12}^* + 4A_{11}^* r^2}{A_{22}^* + 4(2A_{12}^* + A_{66}^*)r^2 + 16A_{11}^* r^4} \cos \frac{2\pi x}{a} \cos \frac{4\pi y}{b} + \frac{3}{4} \right] \end{aligned} \quad (66b)$$

$$\begin{aligned} \frac{b^2}{h^2} \epsilon_{xy} &= q \frac{\pi^2}{r} (-\sin \frac{2\pi x}{a} \sin \frac{2\pi y}{b}) \\ &+ q^2 \frac{\pi^2}{8} \left[ \frac{2}{A_{22}^* + (2A_{12}^* + A_{66}^*)r^2 + A_{11}^* r^4} \right. \\ &\left. (\sin \frac{2\pi x}{a} \sin \frac{2\pi y}{b}) \right. \\ &+ \frac{2}{16A_{22}^* + 4(2A_{12}^* + A_{66}^*)r^2 + A_{11}^* r^4} \sin \frac{4\pi x}{a} \sin \frac{2\pi y}{b} \\ &\left. + \frac{2}{A_{22}^* + 4(2A_{12}^* + A_{66}^*)r^2 + 16A_{11}^* r^4} \sin \frac{2\pi x}{a} \sin \frac{4\pi y}{b} \right] \end{aligned} \quad (66c)$$

For movable inplane edges, the last term in equations (66a) and (66b) vanishes.

## RESULTS AND DISCUSSION

Due to the complications involved in including multiple modes in the analysis, only a single mode approximation was used in this study. The assumption for fundamental mode predominacy is admittedly over simplified; the conditions under which this is a valid approximation remain to be investigated. This single-mode approximation was first presented by Miles [20] and its use has become known as "Miles' single degree-of-freedom theory." This approximation is commonly used for all sonic fatigue analyses [2] and a simple model sometimes helps to give basic understanding of the problem.

Using the present formulation, nonlinear responses of symmetric laminated composite plates subjected to broadband, random acoustic excitation are studied. Both simply supported and clamped out-of-plane boundary conditions are considered. Two inplane edge conditions considered are immovable and movable. In the results presented, the excitation power spectral density function is considered constant or varying slowly with frequency in the vicinity of the equivalent linear frequency and a representative, graphite-epoxy with material properties:

$$E_1 = 17 \times 10^6 \text{ psi} \quad (117.9 \text{ GPa})$$

$$E_2 = 1.7 \times 10^6 \text{ psi} \quad (11.8 \text{ GPa})$$

$$G_{12} = 0.65 \times 10^6 \text{ psi} \quad (4.5 \text{ GPa})$$

$$D_{12} = 0.30$$

is used in all computations. Mean-square displacement, equivalent linear frequency, and mean-square strains are determined for  $[0, \pm 45]_s$  and  $[0, \pm 45, 90]_s$  graphite-epoxy laminates of different aspect ratios and damping ratios at various excitation spectral densities.

Figure 1 shows the maximum (center) mean-square deflection versus the spectral density parameter of excitation for square, simply-supported, symmetric composite plates with  $[0, \pm 45]_s$  and  $[0, \pm 45, 90]_s$  ply orientations and with a damping ratio of 0.02. The mean-square deflection of the immovable inplane edges case is less than that of the movable edges: that is, as the inplane edges are restrained, the plate becomes stiffer. Results of the mean-square deflection versus forcing spectral density based on small deflection theory are also shown.

Figure 2 shows the frequency parameter versus mean-square deflection for square, simply-supported, symmetric laminated composite plates with the above ply orientations for a damping ratio of 0.02. The frequency parameter corresponding to zero mean-square deflection is the frequency based on linear structural theory.

The normalized mean-square maximum strains at the center of the simply-supported square plate with a damping ratio of 0.02 are shown in figure 3. Results based on small deflection theory are also shown.

Figure 4 shows the maximum mean-square deflection as a function of the excitation spectral density parameter for square, clamped, symmetric composite plates with  $[0, \pm 45]_s$  and  $[0, \pm 45, 90]_s$  ply orientations. The mean-square deflection of clamped plates is generally somewhat less than that of the simply supported case. The results on small deflection theory are also presented.

Figure 5 shows the frequency parameter as a function of mean-square deflection of square clamped symmetric laminated composites with the above ply orientations. The frequency parameter corresponding to zero mean-square deflection is the frequency based on linear structural theory.

Figure 6 shows the normalized mean-square maximum strains at the edge of the clamped square plate with the above ply orientations and a damping ratio of 0.02.

The effects of aspect ratio on mean-square deflection are shown in Figure 7. The example is for a clamped symmetric laminated composite plate with a  $[0, \pm 45]_s$  ply orientation and a damping ratio of 0.02. It is clear from the figure that an increase of  $r$  will cause a "closing" of the curve. This occurs because as  $r$  increases the panel becomes less stiff, and the mean-square has to be finite.

Figure 8 shows the effects of aspect ratio on the maximum mean-square strain for clamped  $[0, \pm 45]_s$  laminated composite plates with a damping ratio of 0.02. The aspect ratios investigated are: 1 and 2.

Figure 9 shows the effects of damping ratio on the mean-square deflection for clamped  $[0, \pm 45]_s$  laminated composite plates with an aspect ratio of 1. It is clear from the figure that the precise determination of plate damping is important.

The accuracy of the analytical method is investigated thru a quantitative comparison with experimental response data for  $[0, \pm 45]_s$  graphite-epoxy laminates from a previous Air Force sponsored program. Details of the experimental program can be found in Reference 12. Table 1 lists the results of the comparison. Shown are the analytical and experimental strains versus level of excitation. The comparison demonstrates that a better correlation between theory and experiment is achieved when the large deflection effect is included in the formulation.

TABLE I  
RESULTS COMPARISON

OVERALL SOUND PRESSURE LEVEL dB	LOCATION	ANALYTICAL CLAMPED* $\mu$ in/in	EXPERIMENTAL $\mu$ in/in	
			#1	#2
139	SG 2	180	160	164
	SG 7	77	96	74
142	SG 2	230	210	190
	SG 7	95	110	100
145	SG 2	292	260	260
	SG 7	118	138	120
148	SG 2	371	310	310
	SG 7	144	164	136
151	SG 2	476	345	374
	SG 7	176	200	164

\*IMMOVABLE

#### CONCLUDING REMARKS

An analytical method is presented for determining large-amplitude response of symmetric, laminated, rectangular plates subjected to broadband, random, acoustic excitation. Governing equations in terms of stress function and deflection function are derived. The formulation is based on the Karman-type geometric non-linearity, a single-mode Galerkin approach, the equivalent linearization method, and an iterative procedure. Both simply supported and clamped support conditions with either immovable or movable inplane edges are considered. The large deflection theoretical formulation was verified through direct comparison with experimental results. Improvement over linear theory can be achieved when the large deflection effect is included in the formulation. The solutions developed herein may be used in the determination of RMS deflection, RMS stress/strain, and equivalent linear frequency, in conjunction with failure S-N data, may be used for the estimation of service life.

#### REFERENCES

1. Mei, C., "Response of Nonlinear Structural Panels Subjected to High Intensity Noise," AFWAL-TR-80-3018, WPAFB OH, Mar 1980
2. Rudder, F. F., Jr. and Plumblee, H. E., Jr., "Sonic Fatigue Design Guide for Military Aircraft," AFFDL-TR-74-112, WPAFB OH, May 1975
3. Volmir, A. S., "The Nonlinear Dynamics of Plates and Shells," Chapter X, AD-781338, Foreign Technology Division, WPAFB OH, Apr 1974
4. Thomson, A. G. R. and Lambert, R. F., "Acoustic Fatigue Design Data," AGARD-AG-162-Part I and II, NATO Advisory Group for Aero. Res. and Dev., 1972
5. Jacobs, L. D. and Lagerquist, D. R., "Finite Element Analysis of Complex Panel to Random Loads," AFFDL-TR-68-44, WPAFB OH, Oct 1968
6. Fox, H. L., Smith, P. W., Jr., Pyle, R. W. and Nayak, P. R., "Contributions to the Theory of Randomly Forced, Nonlinear, Multiple-Degree-of-Freedom, Coupled Mechanical Systems," AFFDL-TR-72-45, WPAFB OH, 1973
7. Holehouse, I., "Sonic Fatigue Design Techniques for Advanced Composite Aircraft Structures," AFWAL-TR-80-3019, WPAFB OH, Apr 1980
8. Wentz, K. R. and Wolfe, H. F., "Development of Random Fatigue Data for Adhesively Bonded and Weldbonded Structures Subjected to Dynamic Excitation," ASME J. Eng. Materials and Technology, Vol. 100, Jan 1978, pp. 70-76
9. Jacobson, M. J., "Sonic Fatigue Design Data for Bonded Aluminum Aircraft Structures," AFFDL-TR-77-45, WPAFB OH, Jun 1977
10. Van der Heyde, R. C. W. and Wolf, N. D., "Comparison of the Sonic Fatigue Characteristics of Four Structural Designs," AFFDL-TR-76-66, WPAFB OH, Sep 1976
11. Van der Heyde, R. C. W. and Smith, D. L., "Sonic Fatigue Resistance of Skin-Stringer Panels," AFFDL-TN-73-149-FYA, WPAFB OH, Apr 1974
12. Jacobson, M. J., "Advanced Composite Joints; Design and Acoustic Fatigue Characteristics," AFFDL-TR-71-126, WPAFB OH, Apr 1972
13. Caughey, T. K., "Equivalent Linearization Techniques," JASA, Vol. 35, 1963, pp. 1706-1711
14. Jones, R. M., Mechanics of Composite Materials, McGraw Hill, 1975
15. Tsai, S. W. and Hahn, H. T., Introduction to Composite Materials, Technomic Publishing, 1980
16. Wentz, K. R., Paul, D. B., Mei, Ch., "Large Deflection Random Response of Symmetric Laminated Composite Plates," AFWAL-TR-81-WPAFB OH, Feb 1982
17. Caughey, T. K., "Nonlinear Theory of Random Vibrations," in Advances in Applied Mechanics, Vol. 11, Yih, C. S. ed., Academic Press, 1971, pp. 209-253
18. Spanow, P. T. D. and Iwan, W. D., "On the Existence and Uniqueness of Solutions Generated by Equivalent Linearization," Int. J. Non-Linear Mechanics, Vol. 13, 1978, pp. 71-78
19. Rupert, C. L. and Wolf, N. D., "Sonic Fatigue and Response Tests of Boron Composite Panels," AFFDL-FYA-73-10, WPAFB OH, Jul 1973
20. Miles, J. W., "On Structural Fatigue Under Random Loading," J. Aeronaut. Sci., Vol. 21, Nov 1954, pp. 753-762

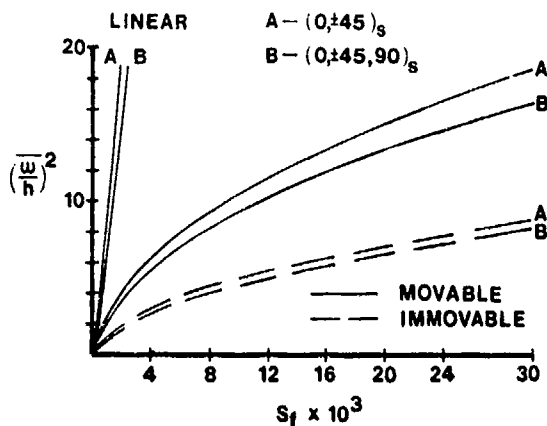


Fig. 1 - Mean-Square Deflection Versus Spectral Density Parameter of Excitation for Square Simply-Supported Symmetric Composite Plates,  $z = 0.020$

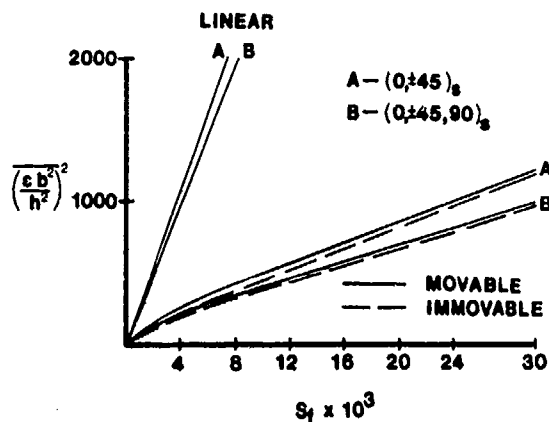


Fig. 3 - Maximum Mean-Square Strain Versus Spectral Density Parameter of Excitation for Square Simply-Supported Symmetric Laminated Composite Plates,  $z = 0.020$

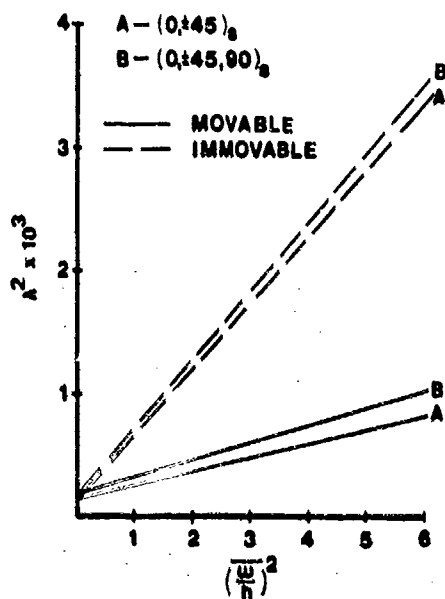


Fig. 2 - Frequency Parameter Versus Mean-Square Deflection for Square Simply-Supported Symmetric Laminated Composite Plates,  $z = 0.020$

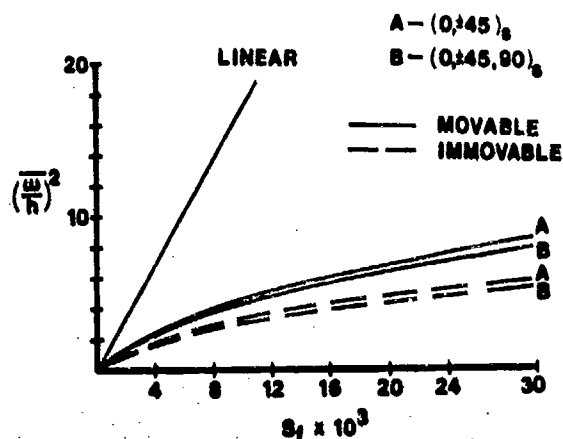


Fig. 4 - Mean-Square Deflection Versus Spectral Density Parameter of Excitation for Square Clamped Symmetric Composite Plates,  $z = 0.020$

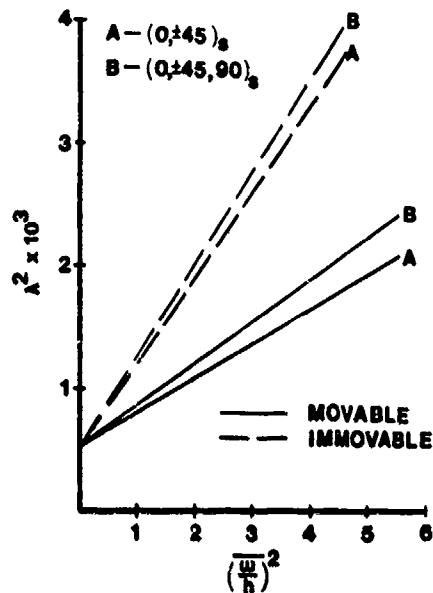


Fig. 5 - Frequency Parameter Versus Mean-Square Deflection for Square Clamped Symmetric Laminated Composite Plates,  $z = 0.020$

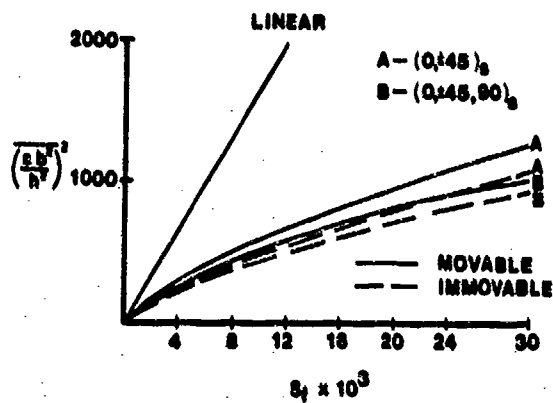


Fig. 6 - Maximum Mean-Square Strain Versus Spectral Density Parameter of Excitation for Square Clamped Symmetric Laminated Composite Plates,  $z = 0.020$

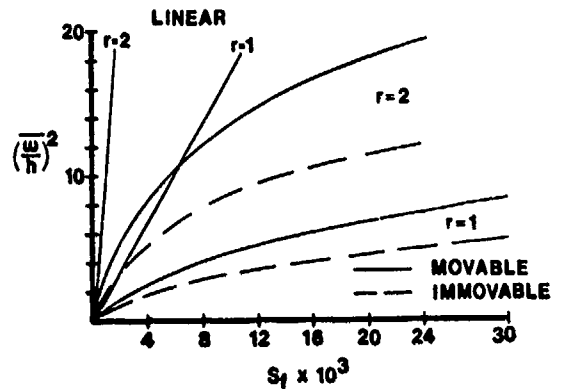


Fig. 7 - Effects of Aspect Ratio on Mean-Square Deflection for Clamped  $(0, \pm 45)_s$  Laminated Composite Plates,  $z = 0.020$

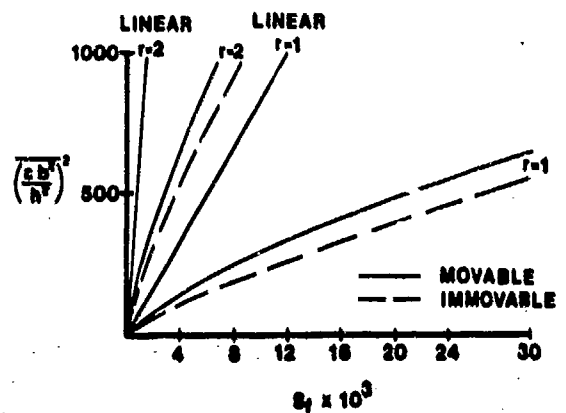


Fig. 8 - Effects of Aspect Ratio on Maximum Mean-Square Strain for Clamped  $(0, \pm 45)_s$  Laminated Composite Plates,  $z = 0.020$

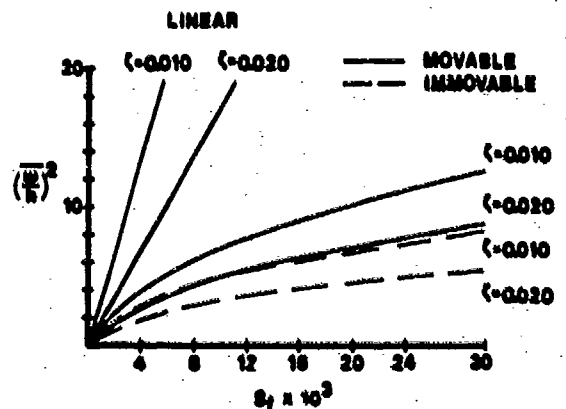


Fig. 9 - Effects of Damping Ratio on Mean-Square Deflection for Clamped  $(0, \pm 45)_s$  Laminated Composite Plates,  $r = 1$



## DISCUSSION

Voice: I'd like to comment that actually the life would be affected by much greater than two to one because the S/N curve is fairly flat. In other words, a small change in stress or strain gives a tremendous change in life. So it would be a tremendous difference between the linear prediction and your predictions here.

Voice: How many modes were excited significantly in your acoustic test?

Mr. Wentz: There was just really the one mode at the lower level for the panel that we looked at. And as you would increase the level 3DB at a time, more modes would come in to play arbitrarily. At the higher level, as each mode appears when you increase your excitation, the Q of the peak acts as a hard spring oscillator. The peaks just really broaden out, and this brings up another problem in trying to use linear damping theories to determine the damping; you can't use a bandwidth method since there are other factors.

Voice: You made your analytical calculations for the fundamental mode only?

Mr. Wentz: Yes.

Voice: Are you comparing the multi-mode test response with the single mode analytical predictions?

Mr. Wentz: Yes.

Voice: Was that part of the error?

Mr. Wentz: Yes, at the higher levels. We are in the process of incorporating multi-modal response and looking at various modes. You have some more complexities because you can't just assume one value of damping. You have a different damping ratio for each mode. So we are extending this work to try to be more accurate. We wanted to do a fundamental

analysis and see where we were.

Voice: I heard you mention that you have single mode response when you displayed the frequency response of the measurement.

Mr. Wentz: Yes.

Voice: How can you judge the modal response; there were so many peaks?

Mr. Wentz: There were peaks, but they were 25-30dB down in amplitude from the main response mode.

Voice: Was this a transfer function?

Mr. Wentz: No. This was a power spectral density function.

Voice: I think you would have better luck getting a transfer function in steel.

Mr. Wentz: Yes. Classically, in sonic fatigue we use the Miles single degree of freedom theory which just assumes that damage comes from the main fundamental response mode. There are other modes. There were other peaks, but at the lower levels. These peaks were at a level far enough down that they wouldn't affect the damage. At the higher levels, it was very broad.

Voice: Why is it so difficult? You might have some reasons. Why can't you get white noise excitation?

Mr. Wentz: There are noise generators that do a much better job.

Voice: Generally, not at those high levels.

Mr. Wentz: Yes, but I have seen a few spectra that are quite flat.

Voice: Better?

Mr. Wentz: Yes.

## DYNAMIC CHARACTERISTICS OF A NON-UNIFORM TORPEDO-LIKE HULL STRUCTURE

Azriel Harari  
Naval Underwater Systems Center  
Newport, Rhode Island 02840

The vibratory response of a torpedo-like structure is investigated here. The torpedo hull is characterized by a long cylindrical shell where the length-to-radius ratio is large. The cylindrical shell is built from several sections that may differ from each other in thickness and material properties. The response of the structure to various loading conditions is found and the results presented. Reduction of the vibration level of the torpedo hull at the frequency band of interest can be accomplished only after the response of the structure is well understood.

### INTRODUCTION

Self-noise is a major handicap to the operation of a torpedo because noise generated by vibratory sources on the structure interferes with the functioning of instruments attached to the shell. The excitations of the structure are due to various sources such as engine vibration, propeller shaft excitation, and hydrodynamic fluctuating forces on the shell. The torpedo shell is composed of several sections. The various segments of the torpedo hull may differ from each other structurally and can be made from different materials. Structural discontinuities such as stiffeners discontinuity and joint discontinuity were studied previously by the author.<sup>1,2,3</sup> Different geometric and material properties for the various sections and end plates are studied here. The structural discontinuities introduced by cylindrical sections of different geometric and material properties have an effect on the vibration of the hull and on the transmission of power along the shell. In order to treat and control the level of vibration, it is first required to know the dynamic response of the structure in the frequency band of interest. The response of the transducer array panel to vibratory forces on the structure is of particular interest. Constrained layered plates and shells can be used selectively for several sections of the hull to reduce the vibration level. In order to design the proper constrained layered cross section for the shell sections and plates, the predominant vibrational wavelengths, the near field solutions, and other characteristics of the shell vibration at the frequency band of interest must be known. The vibrational mode near the interface between the sections of different material properties is of particular interest. The analysis here considers a

cylindrical shell with end plates. The load is arbitrary and can be placed at any point on the shell or end plates. The various sections of the hull can have different structural and material properties. Since the primary interest of this paper is the shell vibration at high frequencies, fluid mass loading can be neglected. Radiation damping affects the magnitude of the vibrational modes but not the relative transfer impedance. The analysis conducted here is for the in-vacuo vibration of non-uniform cylindrical shells with end plates. For the sake of completeness and comparison the mode shapes for low frequencies and for uniform shells are also included.

### CYLINDRICAL SHELL ANALYSIS

Consider a thin cylindrical shell of thickness  $h$  and mean radius  $a$ . The midsurface of the shell is described in terms of an  $x, \theta$  coordinate system. The  $x$  coordinate is taken in the axial direction of the shell and the  $\theta$  coordinate in the circumferential direction. The components of the midsurface of the shell are designated by  $u, v, w$  (Fig. 1). The equations of shell motion governing  $u, v$ , and  $w$  are the Sanders-Koiter<sup>4,5</sup> shell equations. The equations are written as follows:

$$\begin{aligned} & u_{,\xi\xi} + \frac{1}{2}(1-\nu)(1+\frac{1}{2}b)u_{,\theta\theta} \\ & + \left[ \frac{1}{2}(1+\nu) - \frac{3}{8}(1-\nu)b \right] v_{,\xi\theta} \\ & - \frac{1}{2}(1-\nu)bw_{,\xi\theta} - \nu w_{,\xi\xi} \\ & - \rho(a^2/E)(1-\nu^2)\ddot{u} = 0, \end{aligned}$$

$$\begin{aligned}
& \left[ \frac{1}{2}(1 + \nu) - \frac{3}{8}(1 - \nu)b \right] u_{\xi\theta} \\
& + \frac{1}{2}(1 - \nu)(1 + \frac{3}{4}b)v_{\xi\xi} + (1 + b)v_{\theta\theta} \\
& + b(\frac{1}{2})(3 - \nu)w_{\xi\xi\theta} + bw_{\theta\theta\theta} - w_{\theta} \\
& - \rho(a^2/E)(1 - \nu^2)\ddot{V} = 0, \\
& - \nu u_{\xi} - b(\frac{1}{2})(1 - \nu)u_{\theta\theta\xi} \\
& + b(\frac{1}{2})(3 - \nu)v_{\xi\xi\theta} + bv_{\theta\theta\theta} - v_{\theta} \\
& + b(w_{\xi\xi\xi\xi} + w_{\theta\theta\theta\theta} + 2w_{\xi\xi\theta\theta}) + w \\
& + \rho(a^2/E)(1 - \nu^2)\ddot{W} = 0,
\end{aligned} \quad (1)$$

where

$$\begin{aligned}
\xi &= \frac{x}{a}, \quad (\cdot)_{\xi} \equiv \partial/\partial\xi, \quad (\cdot)_{\theta} \\
&\equiv \partial/\partial\theta, \quad (\cdot)' \equiv \partial/\partial t, \quad b = \frac{h^2}{12a^2}.
\end{aligned}$$

$E$  is Young's modulus, Poisson's ratio is denoted by  $\nu$ ,  $\rho$  is the mass density, and  $h$  is the thickness of the shell.

The displacements  $w$ ,  $u$ , and  $v$  may be expanded by Fourier series

$$\begin{aligned}
w(\xi, \theta, t) &= \sum_{n=0}^{\infty} w_n \cos(n\theta), \\
u(\xi, \theta, t) &= \sum_{n=0}^{\infty} u_n \cos(n\theta), \\
v(\xi, \theta, t) &= \sum_{n=0}^{\infty} v_n \sin(n\theta),
\end{aligned} \quad (2)$$

on the circumferential  $\theta$  coordinate direction. The solution is then sought in the following form:

$$\begin{aligned}
w_n(\xi, t) &= C_n \exp(i\omega t + P_n \xi), \\
u_n(\xi, t) &= C_n^* \exp(i\omega t + P_n \xi), \\
v_n(\xi, t) &= C_n^{**} \exp(i\omega t + P_n \xi),
\end{aligned} \quad (3)$$

where  $\omega$  is the circular frequency and where  $C_n$ ,  $C_n^*$ , and  $C_n^{**}$  are constants. Substituting Eqs. (2) and (3) in Eq. (1), one obtains three homogeneous algebraic equations on the constants  $C_n$ ,  $C_n^*$ ,  $C_n^{**}$ , the determinant of which when set to zero yields a fourth-order equation on  $P_n^2$ .

$$P^8 + A_3 P^6 + A_2 P^4 + A_1 P^2 + A_0 = 0 \quad (4)$$

Eight roots,

$$(P_{\kappa})_n = (\delta_{\kappa})_n + (\gamma_{\kappa})_n, \quad \kappa = 1, \dots, 8$$

are obtained, thus yielding eight independent solutions. Using Eq. (1), the constants  $C_n$  and  $C_n^{**}$  can be written in terms of constant  $C_n^*$ . Since the analysis is done for every  $n$  component separately, it is convenient to drop the subscript  $n$  from subsequent expression and discussion, with the understanding that the analysis is for particular  $n$  mode.  $\exp(i\omega t)$  is also omitted from all subsequent expressions.

The solution can be written now as:

$$\begin{aligned}
w &= c_1 e^{P_1 \xi} + c_2 e^{P_2 \xi} + \dots \\
&\quad + c_8 e^{P_8 \xi} \\
u &= c_1 \bar{u}(P_1) e^{P_1 \xi} + c_2 \bar{u}(P_2) e^{P_2 \xi} + \dots \\
&\quad + c_8 \bar{u}(P_8) e^{P_8 \xi} \\
v &= c_1 \bar{v}(P_1) e^{P_1 \xi} + c_2 \bar{v}(P_2) e^{P_2 \xi} + \dots \\
&\quad + c_8 \bar{v}(P_8) e^{P_8 \xi}
\end{aligned} \quad (5)$$

where  $\bar{u}$  and  $\bar{v}$  are functions of  $P_{\kappa}$ ,  $\omega$ , and the shell geometric and material properties.

Once the displacements are known, the stress-resultants can be obtained. The stress resultants associated with the boundary  $\xi = \text{constant}$  are as follows:

$$N_x, Q = -N_{x,x} - \frac{2}{a} N_{x\theta, \theta}$$

$$M = N_{x\theta} + \frac{3}{2a} N_{x\theta, \theta}, \text{ and } M_x,$$

$$\text{where } N_x = \frac{Eh}{(1-\nu^2)a} [u_{\xi} + \nu(u_{\theta\theta} - v)],$$

$$N_{x\theta} = \frac{1}{2} \frac{Eh}{(1-\nu)} \frac{1}{a} (v_{\xi} + u_{\theta}),$$

$$M_x = \frac{Eh^3}{12(1-\nu^2)} \frac{1}{a^2} \left[ \nu_{\xi\xi} + \nu(u_{\theta\theta} + v_{\theta}) \right],$$

$$M_{x\theta} = \frac{Eh^3}{12(1-\nu)} \frac{1}{a^2} \left[ \frac{3}{4} v_{\xi} + v_{\xi\theta} - \frac{u_{\theta}}{4} \right].$$

# CIRCULAR PLATE ANALYSIS

The solutions to the problem of bending and extensional vibration of plate are uncoupled and can be solved separately. The differential equation and solution for the normal displacement  $w$  of the plate are as follows:

$$\frac{Eh^3}{12(1-\nu^2)} \nabla^4 w + \rho h \frac{\partial^2 w}{\partial t^2} = 0 \quad (6)$$

$$w(r, \theta) = \sum_{n=0}^{\infty} w_n(r) \cos(n\theta) e^{i\omega t} \quad (7)$$

$$w_n = \left[ A J_n(kr) + B Y_n(kr) + C I_n(kr) + D K_n(kr) \right] \quad (8)$$

$$\text{where } k^4 = \frac{\rho \omega^2}{Eh^2} 12(1-\nu^2) \quad (9)$$

and  $A, B, C$  and  $D$  are constants.

The differential equation for the extensional vibration of the plate is as follows:

$$\mu \nabla^2 \underline{u} + (\lambda' + \mu) \nabla \nabla \cdot \underline{u} = \rho \underline{\ddot{u}} \quad (10)$$

where  $\underline{u}$  is the in-plane vector displacement and where

$$\lambda' = \frac{2\mu\lambda}{\lambda+2\mu}, \quad \lambda = \frac{E\nu}{(1+\nu)(1-2\nu)},$$

$$\mu = \frac{E}{2(1+\nu)}.$$

The scalar and cross product of Eq. (10) yields:

$$\nabla^2 (\nabla \cdot \underline{u}) = \frac{\rho}{E} (1-\nu^2) \frac{\partial^2}{\partial t^2} (\nabla \cdot \underline{u}), \quad (11)$$

$$\nabla^2 (\nabla \times \underline{u}) = \frac{\rho}{E} 2(1+\nu) \frac{\partial^2}{\partial t^2} (\nabla \times \underline{u}). \quad (12)$$

Substituting  $\underline{u} = \underline{u}^* e^{i\omega t}$  in Eqs. (11) and (12), one gets the following differential equation:

$$(\nabla^2 + k^2) (\nabla \cdot \underline{u}^*) = 0, \quad (13)$$

$$(\nabla^2 + k'^2) (\nabla \times \underline{u}^*) = 0, \quad (14)$$

$$\text{where } k^2 = \frac{\rho}{E} (1-\nu^2) \omega^2,$$

$$k'^2 = \frac{2\rho}{E} (1+\nu) \omega^2.$$

Let  $U$  and  $V$  be the components of the displacement vector in polar coordinates:  $\underline{u}^* = U\hat{e}_r + V\hat{e}_\theta$ . The displacement vector can be expanded, as before by Fourier series. The  $n$ th components of the displacement vector can be written as:

$$U_n = \tilde{U}_n \cos(n\theta), \quad V_n = \tilde{V}_n \sin(n\theta).$$

The solutions for  $\nabla \cdot \underline{u}^*$  and  $\nabla \times \underline{u}^*$  for the  $n$ th component of the displacements can be written as follows:

$$\begin{aligned} \frac{\partial U_n}{\partial r} + \frac{1}{r} U_n + \frac{1}{r} \frac{\partial V_n}{\partial \theta} \\ = \left[ A_1^* J_n(kr) + A_2^* Y_n(kr) \right] \cos n\theta, \\ \frac{\partial V_n}{\partial r} + \frac{1}{r} V_n - \frac{1}{r} \frac{\partial U_n}{\partial \theta} \\ = \left[ B_1^* J(k'r) + B_2^* Y_n(k'r) \right] \sin n\theta. \end{aligned} \quad (15)$$

From Eq. 15 the following expression for  $U_n$  and  $V_n$  can be obtained:

$$\begin{aligned} U_n = \left[ A_1 \frac{dJ_n(kr)}{dr} + A_2 \frac{dY_n(kr)}{dr} + B_1 n \frac{J_n(k'r)}{r} + \right. \\ \left. B_2 n \frac{Y_n(k'r)}{r} \right] \cos n\theta, \\ V_n = - \left[ A_1 n \frac{J_n(kr)}{r} + A_2 n \frac{Y_n(kr)}{r} + B_1 \frac{dJ_n(k'r)}{dr} + \right. \\ \left. B_2 \frac{dY_n(k'r)}{dr} \right] \sin n\theta. \end{aligned} \quad (16)$$

## FORCED VIBRATION

The structure is loaded by harmonic in time force acting on the cylindrical shell and end plates as shown in Fig. 1c. The load is expanded by Fourier series around the circumference. The cylindrical shell is segmented at the point along the shell where there is a change of thickness or material properties and at any point on the shell where the load is applied. The boundary condition imposed at the interface between the segments where no force is being applied is that the displacements and the stress-resultants be continuous across the interface.  $u^L = u^R =$

$$0, \quad u^L = u^R = 0, \quad v^L = v^R = 0, \quad w_x^L = w_x^R = 0,$$

$$Q^L = Q^R = 0, \quad N_x^L = N_x^R = 0, \quad N^L = N^R = 0,$$

$$M_x^L = M_x^R = 0 \text{ where the superscripts "L" and "R" refer to the segment to the left and to the right of the interface. The boundary condition at the point where the line force is applied is the same except for the discontinuity condition of the appropriate stress-resultant. For normal force, } Q^L - Q^R = F_1. \text{ For axial force on the cylindrical shell, } M_x^L - M_x^R = F_2, \text{ etc. The boundary condition between the cylindrical shell and the plate is similar to the one between the segments except that the}$$

appropriate elements of the shell and the plate have to be matched, i.e.,  $w_c = -u_p$ , etc., where the subscripts c and p refer to the cylindrical shell and the plate respectively.

The overall boundary condition results in a set of non-homogeneous algebraic equations for the constants  $c_i$ . The number of unknown constants is eight for every cylindrical segment and four for each end plate. If the load is on the end plate, the plate is segmented. The outer plate segment has eight constants, and the inner one has four constants. Once the constants are found, the displacements at any point on the structure can be found by using Eqs. (5) and (16).

#### NUMERICAL ANALYSIS

The analysis discussed here is applied to a cylindrical shell with end plates as shown in Fig. 2. The length-to-radius ratio is  $L/a = 12$ , and the thickness-to-radius ratio for the shell and end plates is  $h/a = 0.03$  except when indicated otherwise. The shaded shell sections shown in Figs. 2b and 2c can have different thickness and material properties. Poisson's ratio is equal to  $\nu = 0.3$ . The frequency parameter is  $\tau = \omega \sqrt{\frac{\rho}{E} (1-\nu^2)}$ .

The force parameter is  $\psi = \frac{P}{Ea} = 10^{-6}$  where P is

the magnitude of the harmonic in time line force applied uniformly on an arc b of the circumference ( $\frac{b}{a} = 0.1$ ). Only partial results are presented due to the large variety of cases. Frequency sweeps were conducted for several loading and structural configurations. The results are presented in Figs. 3-10. The normal displacement w and the axial (radial for the plate) displacement u are plotted separately on an outline figure of the structure. The combined deformation of the structure due to the displacements w and u is plotted only for a few cases as shown in Figs. 5a and 5b. This is because the different scales for the structure and the axial displacements frequently cause unacceptable distortion. The plotting scale is adjusted for every frequency parameter because the magnitude of the response can vary by a large magnitude for different values of the frequency parameter. The adjustment is made such that the plotted ordinate of the maximum displacement is a fixed value for all plots. The maximum displacement-to-radius ratio  $\frac{w_m}{a}$  and  $\frac{u_m}{a}$  are

typed below each figure for the cylindrical shell and the two end plates, where  $\frac{w_m}{a}$  is the

maximum displacement-to-radius ratio for the cylindrical shell and  $\frac{u_m}{a}$  is the maximum displacement-to-radius ratio for end plates. For  $n=0$ , v is uncoupled from w and u. The modes associated with v ( $n=0$ ) are pure torsional

modes and are not discussed here. Figs. 3-6 present the response of long uniform shell with end plates (Fig. 2) under various loading conditions. The location and direction of the exciting force, on the cylindrical shell or the end plates, are marked by an arrow on the outline of the structure. Figs. 7-10 present results where non-uniformity of thickness or material property were introduced. Figs. 3 and 4 show the axisymmetric  $n=0$  response of the structure. At low frequencies the response of the structure under normal force is limited to the close neighborhood of the force, Fig. 3a. As the frequency increases, the vibrational mode changes to an overall bending mode, Figs. 3c and 3d. Under axial force the shell response, at very low frequencies, is primarily translational, Fig. 4a. The mode changes to the first accordion mode of the shell and bending mode of the plate as the frequency increases, Fig. 4b. The response of the shell changes to an overall bending mode as the frequency gets higher, Figs. 4c and 4d. The value of the positive root for  $p^2$  increases with the frequency. The effects of the nearfield solution at high frequencies are thus limited to the close neighborhood of the force. At high frequencies the boundary conditions at the location of the force and between the shell and end plates do not have significant effect on the character of the mode shape, Figs. 3c, 3d, 4c, and 4d. Figs. 5a-5c show the  $n=1$  response of the shell to a normal line force. Figs. 6a-6c show the  $n=2$  response of the shell to a normal line force on the plate. The exciting force, for the examples shown in Figs. 7-10, is placed at the center of the shell, and non-uniformity such as change of thickness or material is made on part of the structure. Figs. 7a and 7b show the  $n=0$  response of the shell shown in Fig. 2b where the thickness-to-radius ratio for the shell section on the right side (shaded) is  $h/a=0.06$ , while the ratio for the rest of the structure is  $h/a=0.03$ . For intermediate and high frequencies, the nearfield solutions do not have any significant effect. As can be seen, the shell sections vibrate in two different wavelengths in accordance with the thickness of each section. Figs. 8a-8d show the  $n=0$  response of a hull where the thickness-to-radius ratio of the end plate on the right (Fig. 2c) is  $h/a=0.2$ , while the ratio for the rest of the structure is  $h/a=0.03$ . Figs. 9a-9d show the  $n=0,2$  response of a shell where the modulus of elasticity for the right segment (Fig. 2b) is three times the value for the rest of the structure. Thickness-to-radius ratio is  $h/a=0.03$  for the cylindrical shell and  $h/a=0.2$  for the end plates. Figs. 9a-9b show the  $n=0$  response, and Figs. 9c-9d show the  $n=2$  response. Figs. 10a-10d show the  $n=0,2$  response of a shell where the modulus of elasticity for the right segment (Fig. 2b) is half the value for the rest of the structure. The thickness-to-radius ratio is  $h/a=0.03$  for the cylindrical shell and  $h/a=0.2$  for the end plates. Figs.

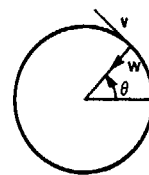
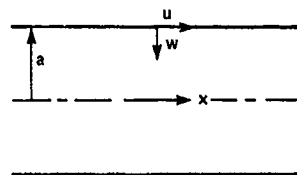
10a-10b show the  $n=0$  response, and Figs. 10c-10d show the  $n=2$  response.

#### CONCLUSIONS

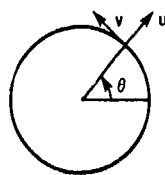
The dynamic response of a long cylindrical shell with end plates was found. The vibrational mode shapes for uniform and non-uniform shells are presented. Thickness and material non-uniformity were considered. The information obtained here can be used to control the vibration level at frequency bands of interest by introducing constrained layered end plates, constrained layered shell sections, material with damping properties, or by stiffening several sections of the structure.

#### REFERENCES

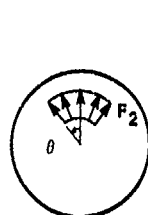
1. A. Harari, "Wave Propagation in a Cylindrical Shell with Joint Discontinuity," Shock and Vibration Bulletin, 48, Part 3, 1978.
2. A. Harari, "Wave Propagation in a Cylindrical Shell with Finite Regions of Structural Discontinuity," J. Acoust. Soc. Am., Vol. 62, No. 5, Nov. 1977.
3. A. Harari and M. L. Baron, "Analysis for the Dynamic Response of Stiffened Shells," Journal of Applied Mechanics, Dec. 1973.
4. J. L. Sanders, "An Improved First Approximation Theory for Thin Shells," NASA-TR-R24, 1959.
5. W. T. Koiter, "A Consistent First Approximation in the General Theory of Thin Elastic Shells," Proc. Symp. on Theory of Thin Elastic Shells (Delft, August 1957).



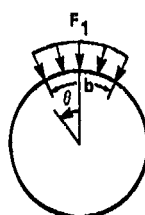
(a) CYLINDRICAL SHELL COORDINATES



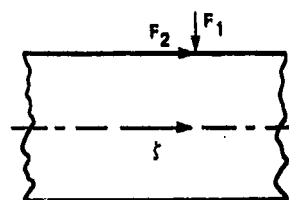
(b) PLATE COORDINATES



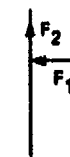
PLATE



SHELL



SHELL

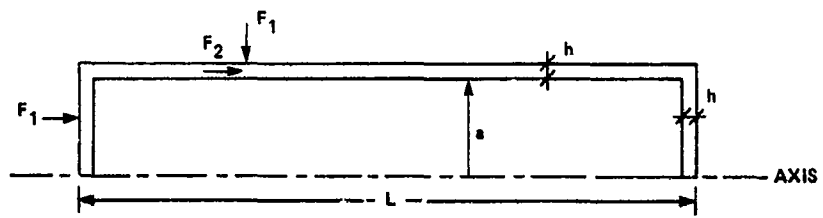


PLATE

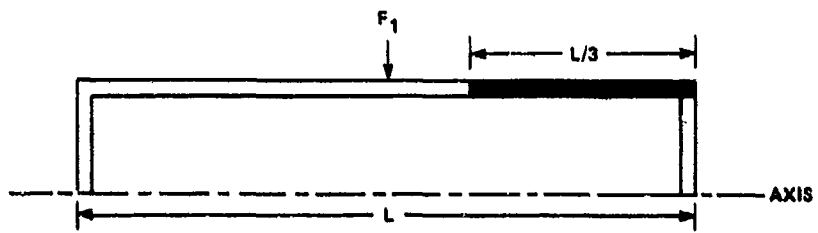
(c) FORCES ON SHELL AND PLATE

COORDINATE SYSTEM

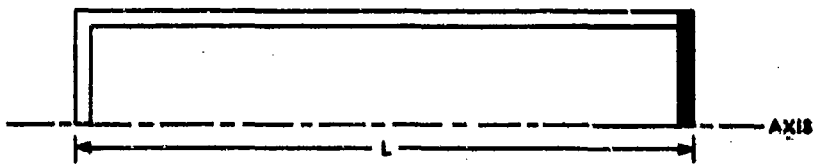
Fig. 1



(a)



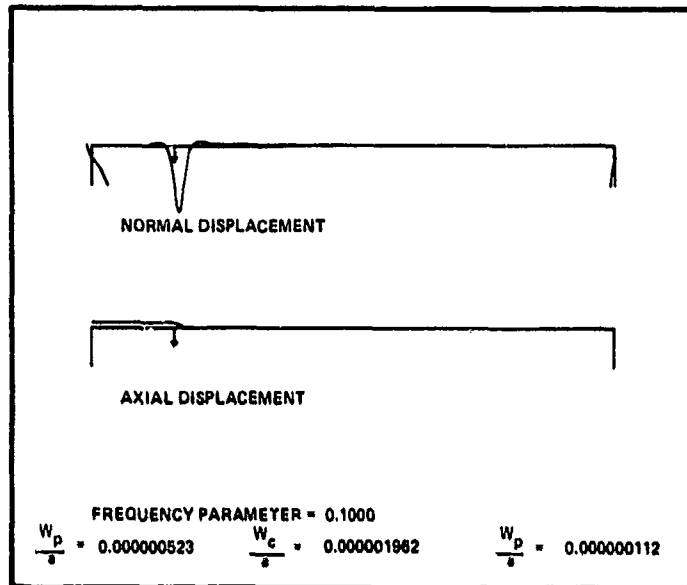
(b)



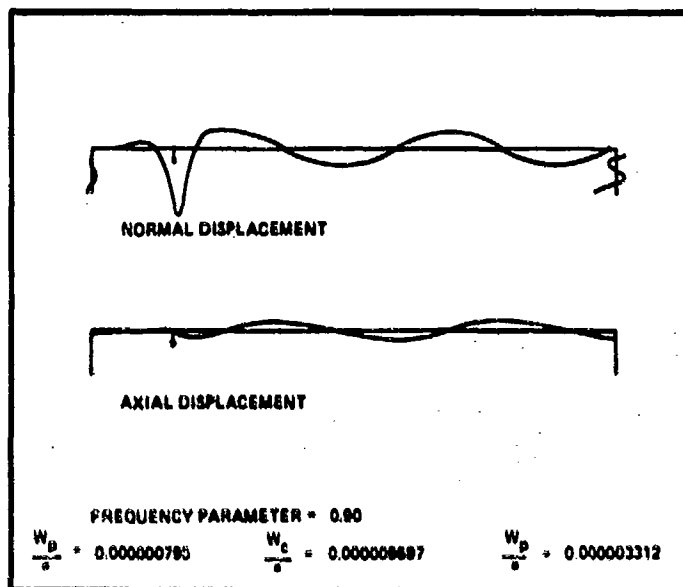
(c)

Fig. 2

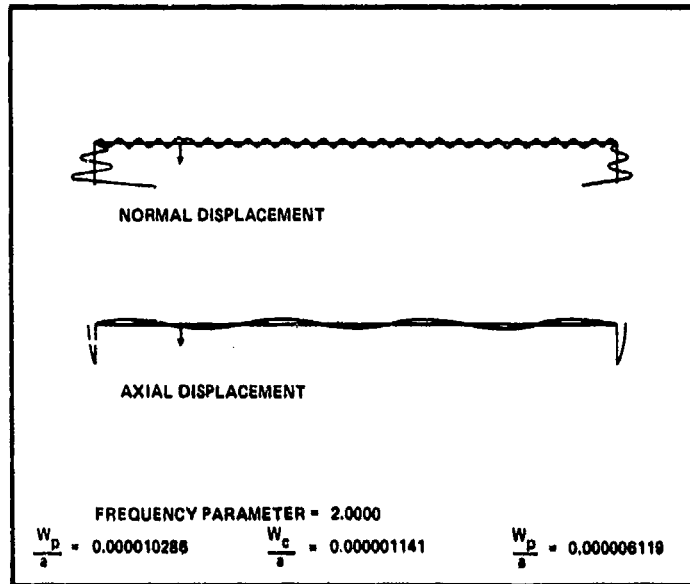




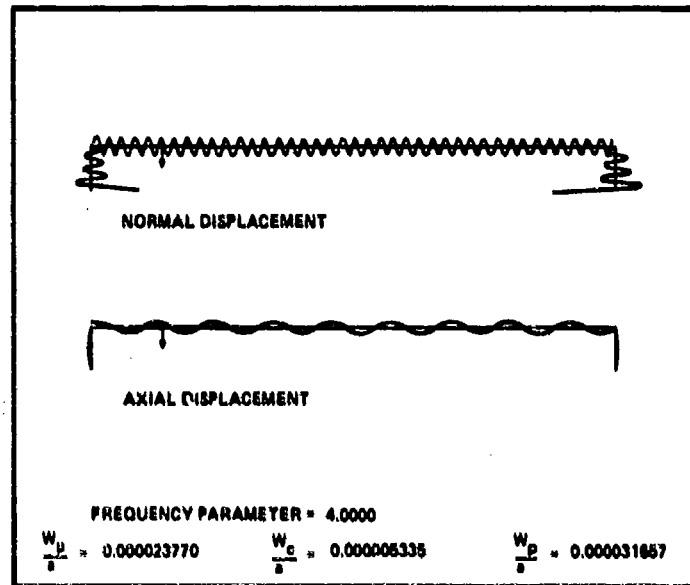
3a.



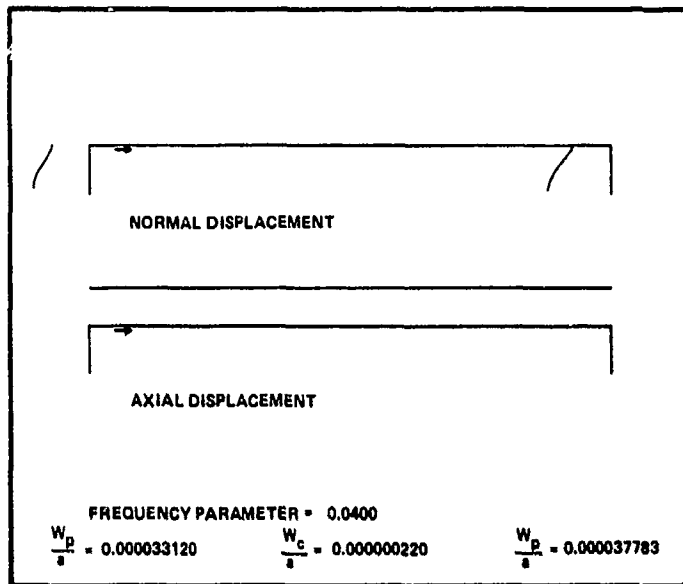
3b.



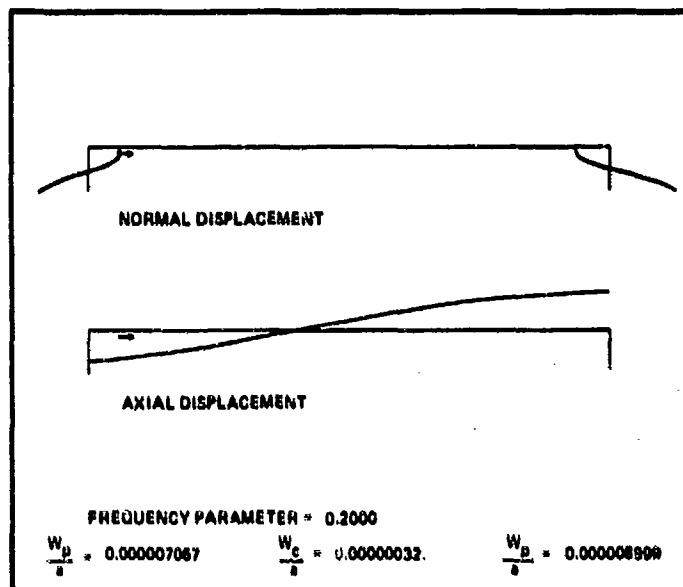
3c.



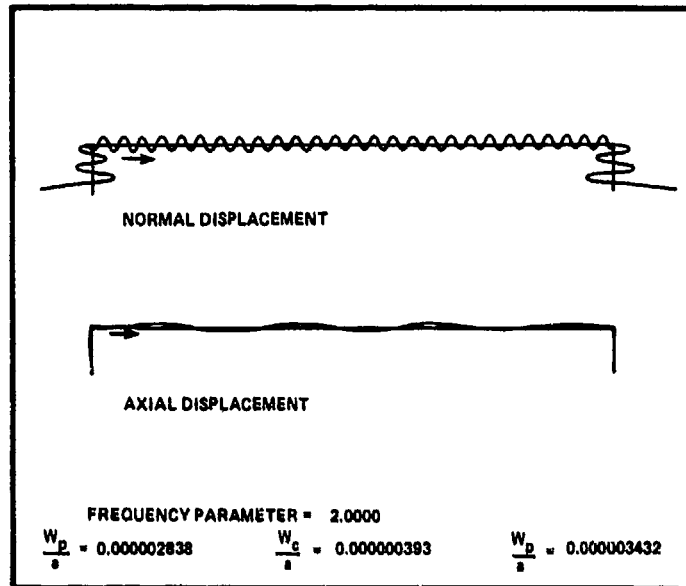
3d.



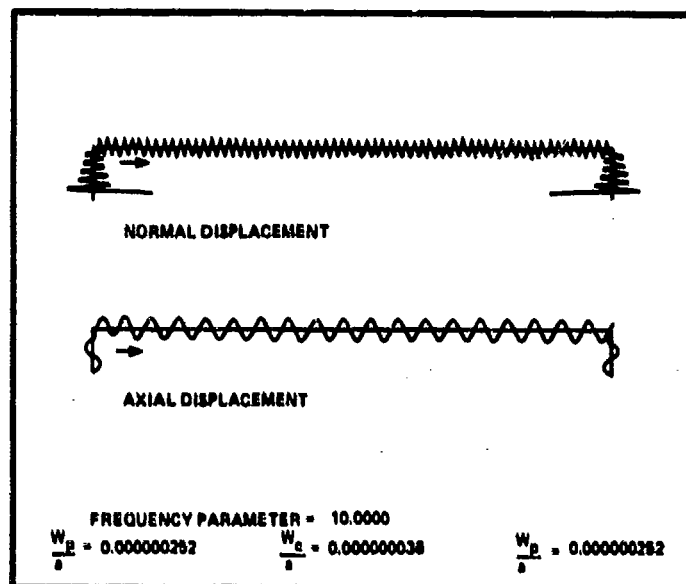
4a.



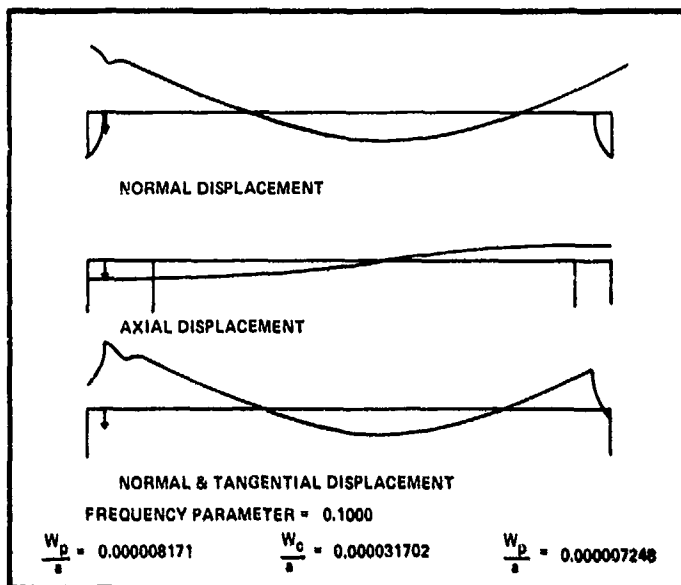
4b.



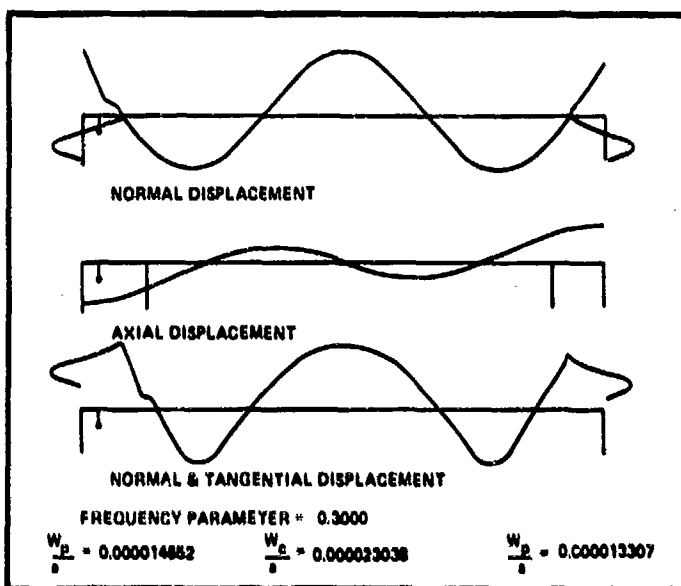
4c.



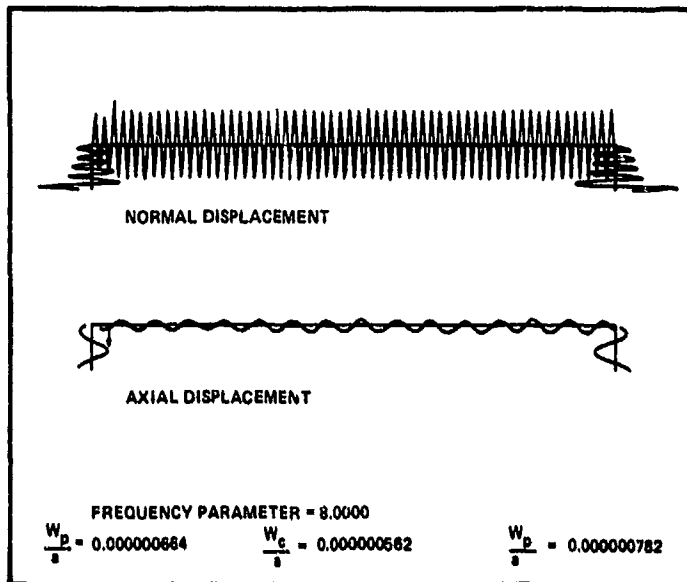
4d.



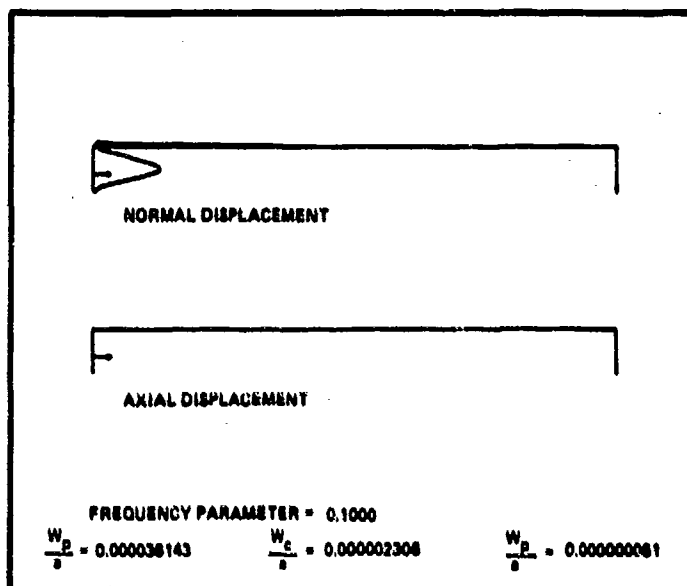
5a.



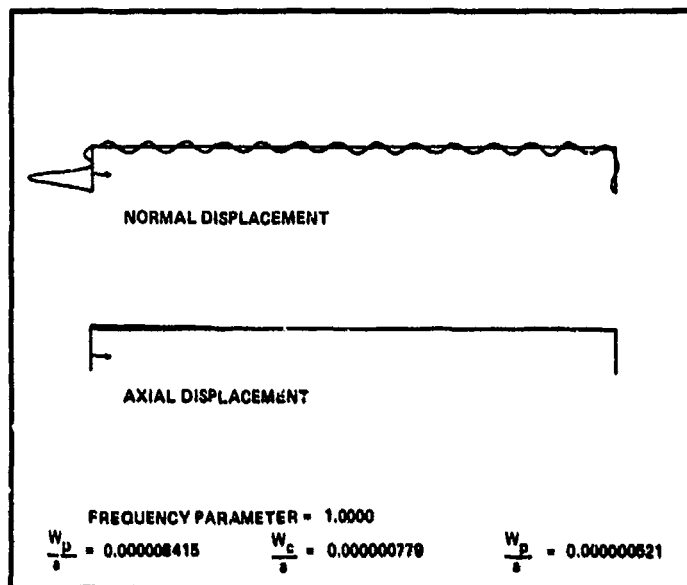
5b.



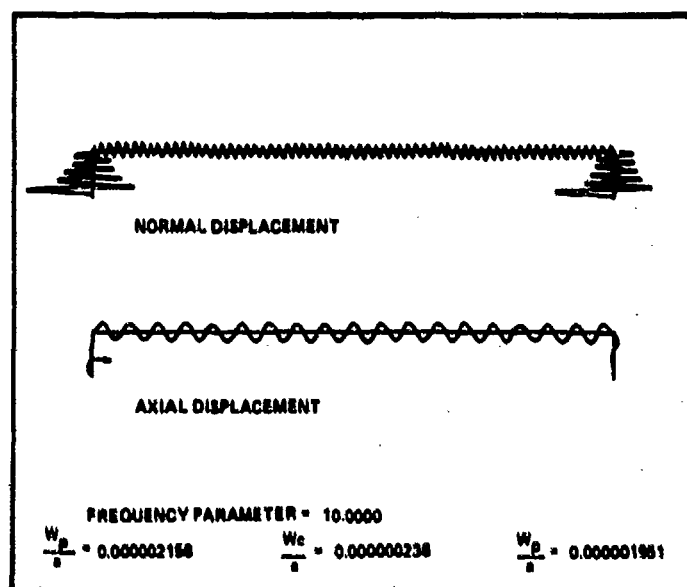
5a.



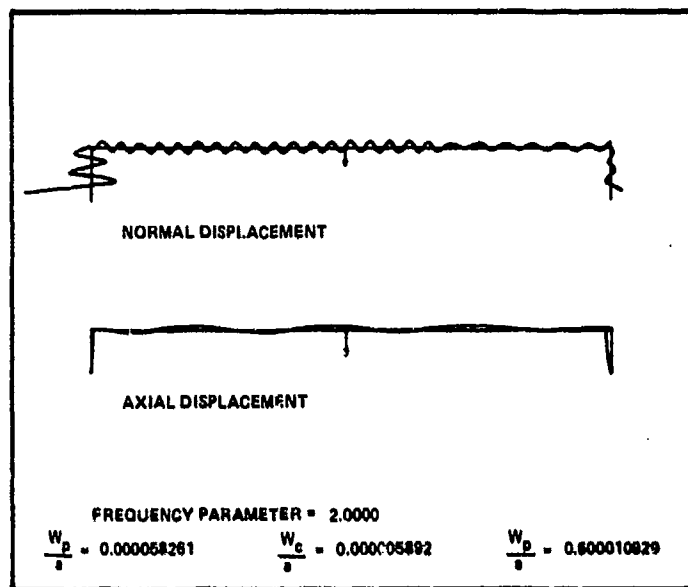
6a.



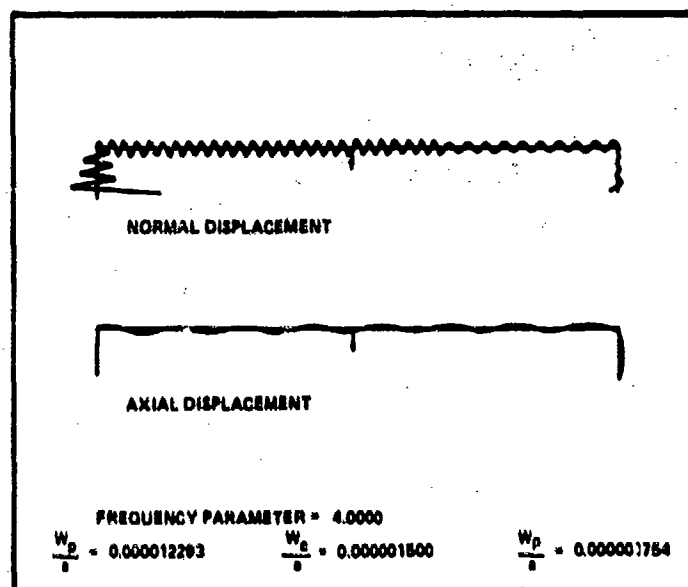
6b.



6c.

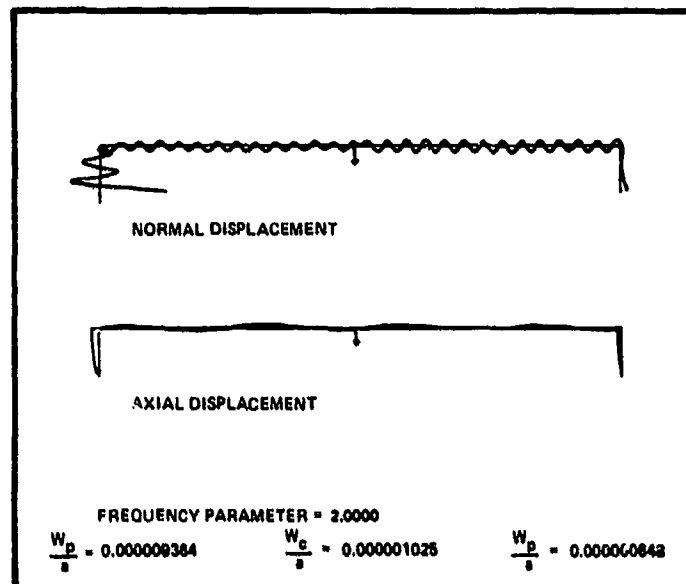


7a.

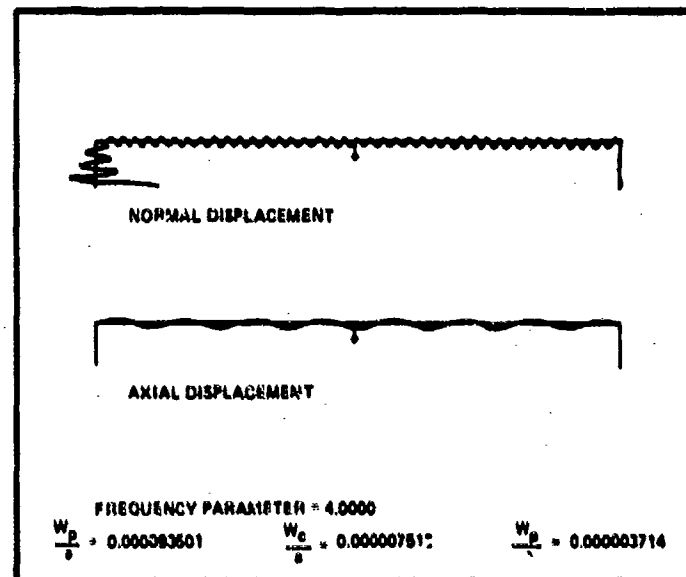


7b.

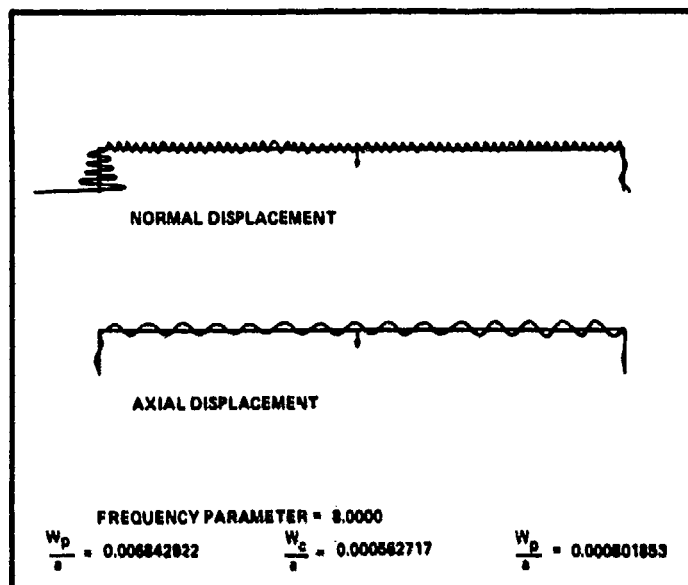




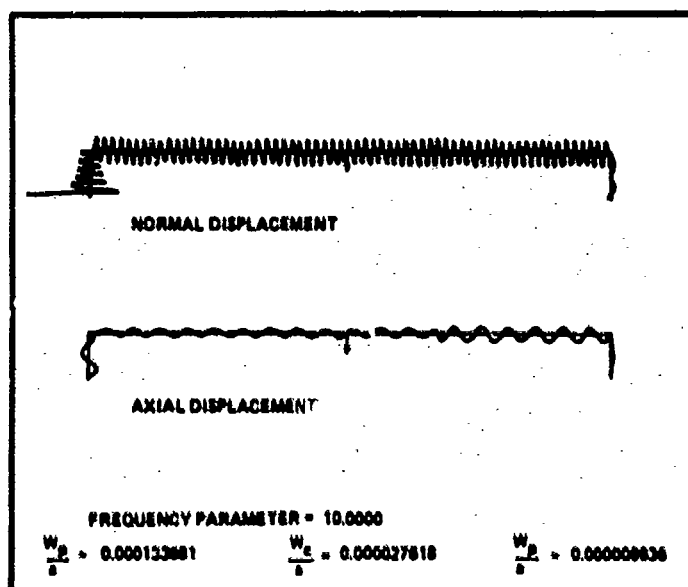
8a.



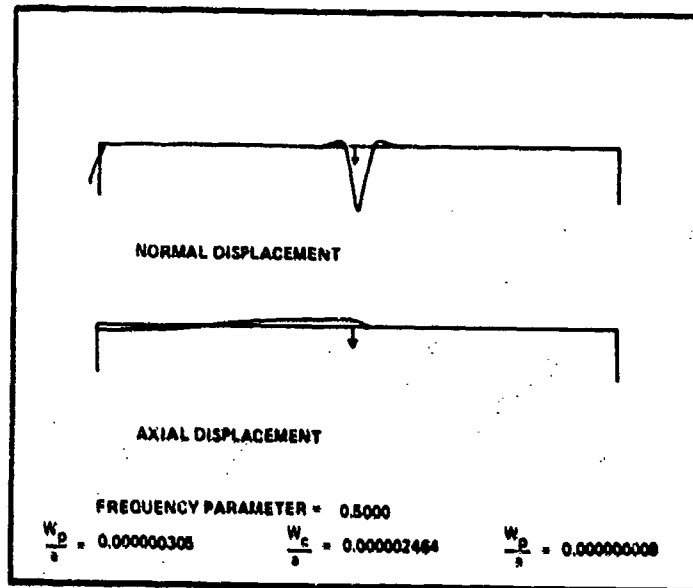
8b.



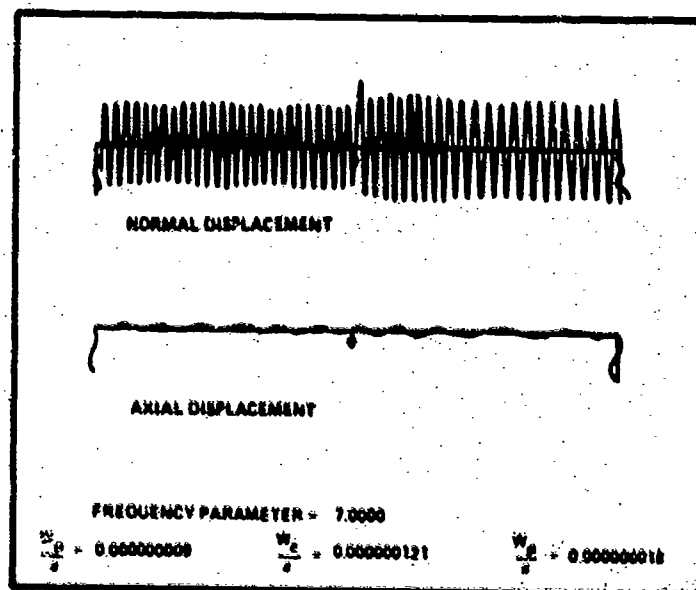
8c.



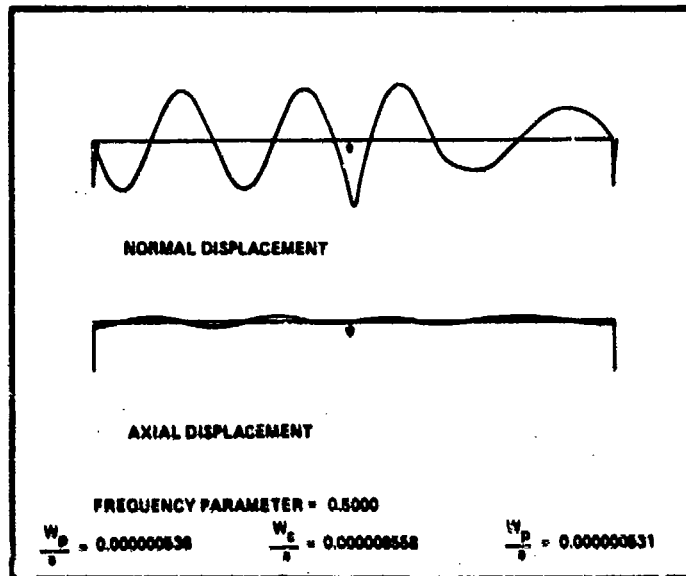
8d.



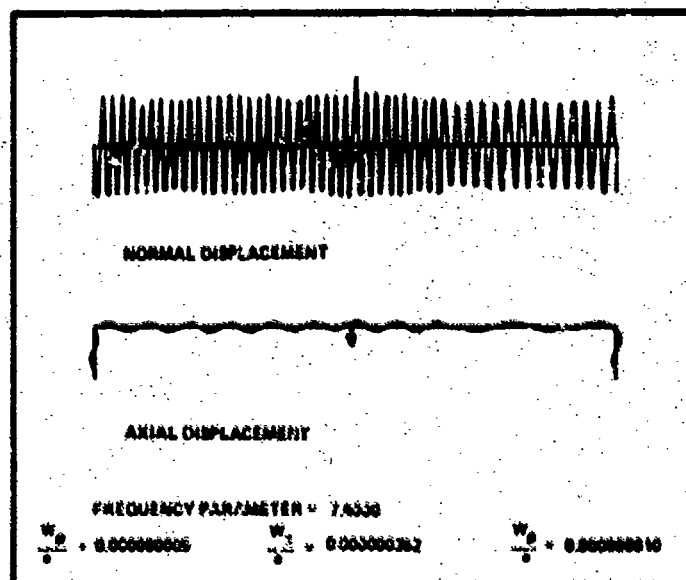
9a.



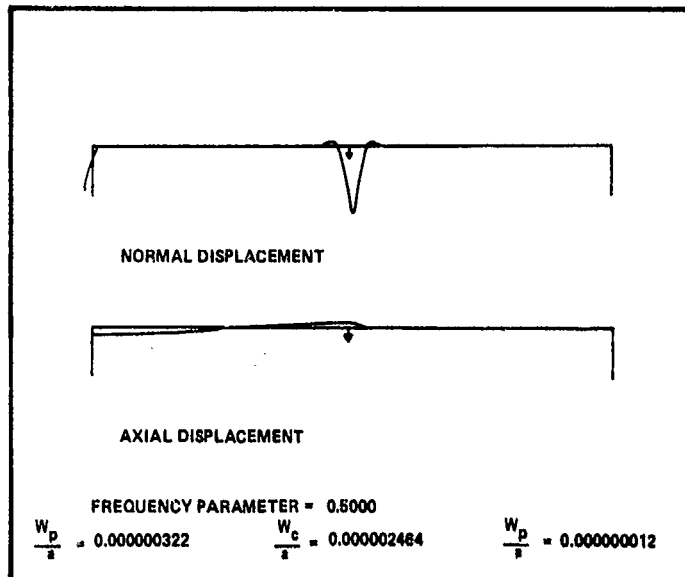
9b.



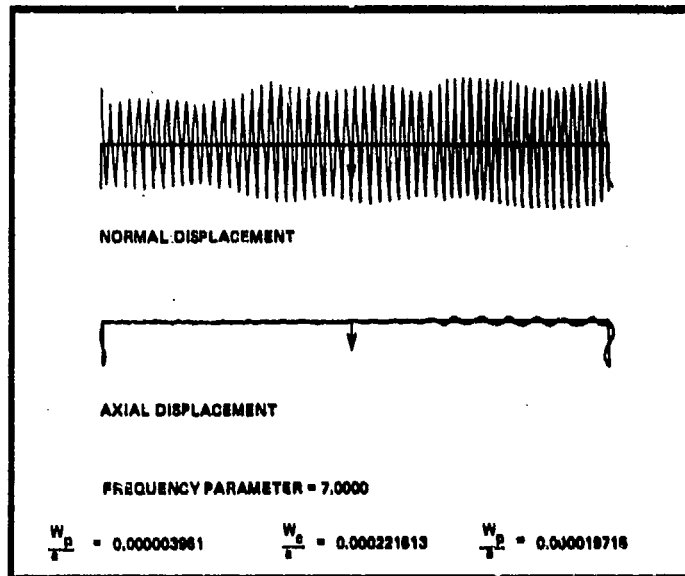
8a.



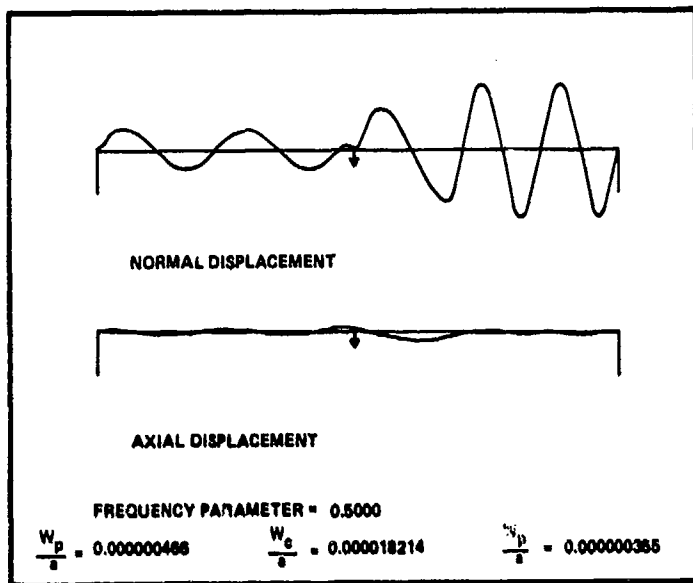
8a.



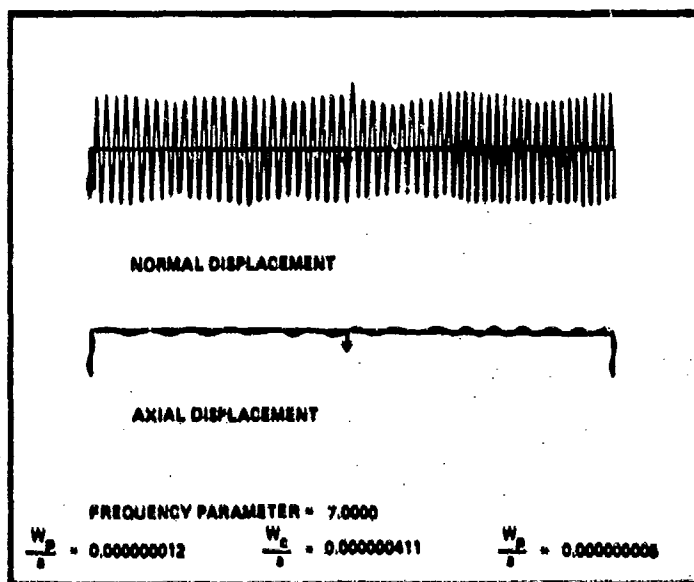
10a.



10b



10c.



10d.

# VIBRATION AND ACOUSTIC RADIATION FROM POINT EXCITED SPHERICAL SHELLS

Edmond H. Wong, Code 5134  
Naval Ocean Systems Center  
San Diego, CA 92152

and

Sabih I. Hayek  
The Pennsylvania State University  
University Park, PA 16802

## SUMMARY

The vibration and acoustic nearfield of thin aluminum spherical shells were investigated analytically and experimentally. Two such shells with thickness-to-radius ratios of  $6.4 \times 10^{-3}$  and  $13.4 \times 10^{-3}$  were excited by an impedance head at the apex, simulating a mechanical point excitation. The driving point admittance frequency spectra of the shells when excited in air were recorded and at each maximum, the mode shape at resonance was plotted. These measurements were repeated when the shell was suspended in a large water tank. The driving point admittance of the submerged shells was recorded. The mode shapes at resonance were plotted by use of a small hydrophone that measured the nearfield pressure of the vibrating shells. The measurements were carried to high frequencies ( $ka \approx 30$ ).

A parallel analytic prediction of the amplitude of the vibration, the nearfield and far-field pressures were made. Basically, a thin shell theory with bending terms was adapted for the equations of motion. For vibration in air or in vacuum, the solution was obtained by the normal mode approach. The predicted resonances were compared to the measured ones and found to agree within 5 percent for mode orders up to 32. For vibration of a submerged shell, an iterative technique was used to calculate the resonances of the submerged shells in water. The predicted resonances were also found to agree within 6 percent with the measurements.

To predict the mean-line of the driving point admittance, use of Skudrzyk's mean-line theorem was made. This theory requires the knowledge of the resonance density of vibrating spherical shells. Expressions for the resonance density of spherical shells were developed in the low, medium, and high frequency ranges. The predicted mean-line of the driving point admittance vibrating shell was within 3 dB of the measured mean-line.

## INTRODUCTION

The study of the vibration of a spherical shell submerged in an infinite acoustic fluid medium is the main objective of this paper, where the mechanical and acoustical energies are coupled by a fluid reaction [1]. The vibration of a spherical shell has been studied by many authors [2-9]. In a paper "On the Vibrations of a Spherical Shell," Lamb [2] has investigated a membrane spherical shell for axisymmetric vibration, and pointed out the existence of two infinite sets of normal modes. Baker [3] has expanded the work given by Lamb, and demonstrated experimentally the existence of normal modes predicted by the theory. Kalnins [4] studied the bending effects on the vibration of a spherical shell in vacuum, and labeled the lower branch as bending modes. Wilkinson [5] showed that there are three branches in the frequency spectrum when the equations of motion of closed spherical shells include the effects of transverse shear deformation and rotatory inertia.

Considering the vibration of a spherical shell submerged in a fluid medium, Junger [1] examined the sound scattering of a membrane elastic spherical shell, insonified by a plane acoustic wave. He concluded that the scattering field of all

elastic scatterers is the result of the rigid body scattering and radiation scattering. In another paper [6], he studied the same configuration but excited by a point force, where he demonstrated the radiation loading on an elastic shell. Hayek [7] studied the vibration of the forced, axisymmetric spherical shell in the light of the bending theory in an acoustic medium. He concluded that the resonance frequency is sensitive to the parameter  $(h/a)$ , especially for large mode numbers  $n$ , and the resonance frequency increases as  $n$  increases, no matter how small is the ratio  $(h/a)$ . Lauchle [8] extended the work of Junger, and demonstrated the interaction of a spherical acoustic wave with an elastic spherical shell in fluid media. Skudrzyk [9] has developed approximate expressions for the resonances of a spherical shell and new expressions for the forced vibration amplitudes.

## THE EQUATIONS OF MOTION

In this section, the dynamical response of an excited elastic shell is considered where the applied forces, the displacements, etc., are time-dependent. To derive the equations of motion for a vibrating shell, Hamilton's variational principle is applied. The variational integral requires expres-

sions for the kinetic energy  $T$  and the strain energy  $\bar{V}$  of the system as well as the external forces as derived from a potential function  $Q$ . Hamilton's principle states that:

$$\delta \int_{t_1}^{t_2} (T - \bar{V} + Q) dt = 0, \quad (1)$$

where  $t_1$  and  $t_2$  are the initial and final time states, respectively, of the system. The symbol  $\delta$  represents differential variation. Substituting the strain and kinetic energies and the potential function into Equation (1) one obtains the coupled equations of motion of a spherical shell in terms of time harmonic displacements  $U$  and  $W$ , see Figure 1:

$$L_{uu}U + L_{uw}W = (1 - \nu^2)\Omega^2U \quad (2)$$

and

$$L_{wu}U + L_{ww}W = (1 - \nu^2)\Omega^2W - \frac{1 - \nu^2}{Eh} a^2 (P_i + P_r), \quad (3)$$

where the operators  $L_{uu}$ ,  $L_{uw}$ ,  $L_{wu}$ ,  $L_{ww}$  are given by:

$$L_{uu} = -(1 + \beta) \left\{ (1 - \eta^2)^{1/2} \frac{d^2}{d\eta^2} (1 - \eta^2)^{1/2} + (1 - \nu) \right\}, \quad (4)$$

$$L_{uw} = (1 - \eta^2)^{1/2} \left[ \beta(1 - \nu) \frac{d}{d\eta} - (1 + \nu) \frac{d}{d\eta} + \beta \frac{d}{d\eta} \nabla^2 \right], \quad (5)$$

$$L_{wu} = -[\beta(1 - \nu) - (1 + \nu)] \frac{d}{d\eta} (1 - \eta^2)^{1/2} - \beta \nabla^2 \frac{d}{d\eta} (1 - \eta^2)^{1/2} \quad (6)$$

and

$$L_{ww} = \beta \nabla^4 + \beta(1 - \nu) \nabla^2 + 2(1 + \nu), \quad (7)$$

where

$$\nabla^2 = \frac{d}{d\eta} (1 - \eta^2) \frac{d}{d\eta}, \quad \eta = \cos \theta,$$

$$\Omega^2 = \rho_s \omega^2 a^2 / E = \frac{\omega^2}{\omega_r^2} \text{ is the normalized frequency,}$$

$$\omega_r = \frac{C_b}{a} \text{ is the ring frequency}$$

$$C_b = \sqrt{\frac{E}{\rho_s}}, \quad \beta = (h^2/a^2)/12, \quad (8)$$

and  $\nu$  is the Poisson's ratio,  $E$  is the Young's modulus,  $a$  is the radius of the shell,  $U$  and  $W$  are the tangential and radial displacements,  $P_i$  is the applied radial force, and  $P_r$  is the acoustic surface pressure.

For this problem, the tangential and radial displacements can be expressed in terms of Legendre polynomial of degree  $n$  as follows:

$$U(\eta) = \sum_{n=0}^{\infty} U_n (1 - \eta^2)^{1/2} \frac{dP_n(\eta)}{d\eta}, \quad (9)$$

$$W(\eta) = \sum_{n=0}^{\infty} W_n P_n(\eta),$$

and

$$P_i = \sum_{n=0}^{\infty} P_{in} P_n(\eta), \quad P_r = \sum_{n=0}^{\infty} P_{rn} P_n(\eta). \quad (10)$$

Then, on substitution of these two equations into Equations (2) and (3), one obtains two algebraic equations in terms of  $U_n$  and  $W_n$ :

$$\left\{ (1 - \nu^2)\Omega^2 - (1 + \beta)[\lambda_n - (1 - \nu)] \right\} U_n + \left\{ \beta[\lambda_n - (1 - \nu)] + (1 + \nu) \right\} W_n = 0 \quad (11)$$

and

$$\begin{aligned} & [\lambda_n(\beta(1 - \nu) - (1 + \nu)) - \beta\lambda_n^2] U_n + [\beta\lambda_n^2 \\ & - \beta(1 - \nu)\lambda_n + 2(1 + \nu) - (1 - \nu^2)\Omega^2] W_n \\ & = -\frac{1 - \nu^2}{Eh} a^2 (P_{in} + P_{rn}), \end{aligned} \quad (12)$$

where  $\lambda_n = n(n + 1)$ ,  $P_{in}$  and  $P_{rn}$  represent the modal applied and reactive pressures, respectively.

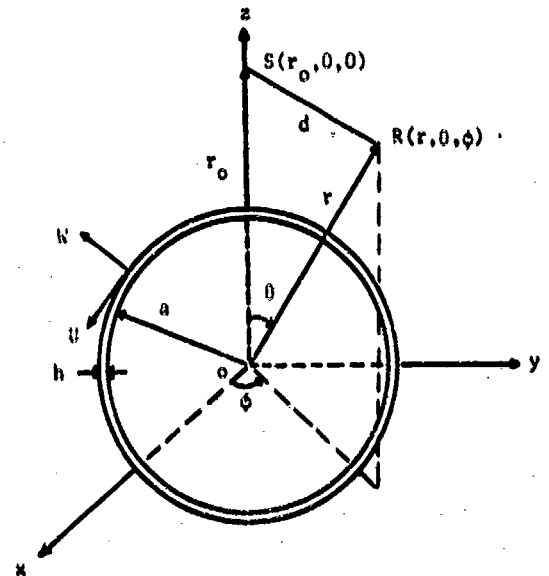


Fig. 1 - Configuration of the spherical shell in the spherical coordinate system



## NATURAL FREQUENCIES IN VACUO AND IN FLUID

The natural frequencies of a free vibration in vacuo are the roots of the following equations:

$$\begin{aligned} (1 - \nu^2)^2 \Omega^4 - [\beta \lambda_n^2 + (1 + \beta \nu) \lambda_n + (1 + 3\nu) \\ - \beta (1 - \nu)] (1 - \nu^2) \Omega^2 + \beta \lambda_n^3 - 4\beta \lambda_n^2 + [\beta(5 - \nu^2) \\ + (1 - \nu^2)] \lambda_n - 2(1 + \beta)(1 - \nu^2) = 0 \end{aligned} \quad (13)$$

This is a quadratic equation in  $\Omega^2$  with only two distinct positive roots for each mode number  $n$ . The larger root of each mode belongs to the upper branch, and denoted by  $\Omega_h$ . The smaller root,  $\Omega_l$ , belongs to the lower branch. The roots  $\Omega_{hn}$  and  $\Omega_{ln}$  are the natural frequencies of the spherical shell. For  $n = 0$ , there is only one positive real root:

$$\Omega_{ho}^2 = \frac{2}{1 - \nu}$$

This frequency represents purely radial motion, which is referred to as the "breathing mode." This mode's elastic energy is due to extensional deformation only because the shell vibrates only in the radial direction, and the radius of curvature of the shell remains constant. The natural frequencies of duralumin shells of radius  $a = 8$  inches and thickness  $h = 0.1069$  inch ( $h/a = 0.0134$ ) and  $h = 0.0514$  inch ( $h/a = 0.0064$ ) were computed and plotted in Figure 2. Both shells are considered

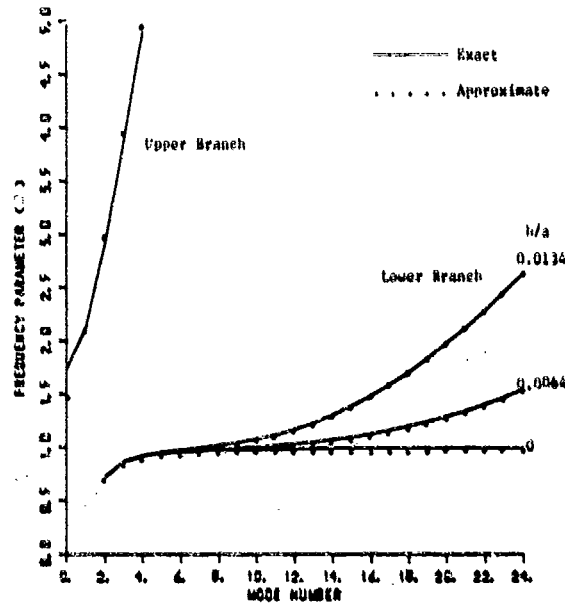


Fig. 2 - Dimensionless frequency  $\Omega$  for various modes when spherical shells are excited in vacuo

as thin shells for shell theory of deformation, but will be referred to as "thick" and "thin" shell, respectively. It is clear that the natural frequencies of the lower branch for membrane theory,  $\beta = 0$ , are independent of the shell's thickness, while the natural frequencies of bending modes, for  $\beta > 0$ , vary with the thickness. However, the upper branch frequencies do not change significantly with  $\beta$ . For a thin shell, where the ratio  $h/a$  is very small such as the ratio 0.0064 shown in Figure 2, the membrane theory may be applicable at low frequencies or for small values of the mode number. It is interesting to note that  $\Omega$  approaches unity when the mode number goes to infinity for  $\beta = 0$ . Different asymptotic approximations to the roots of Equation (13) were obtained as follows:

$$\Omega_{ln}^2 \approx \frac{\lambda_n - 2}{\lambda_n + 1 + 3\nu}, \quad \Omega < 1, \quad (14a)$$

$$\Omega_{ln}^2 \approx \frac{\beta \lambda_n^2}{1 - \nu^2} + 1, \quad \Omega > 1 \quad (14b)$$

and

$$\Omega_{hn}^2 \approx \frac{\lambda_n + 1 + 3\nu}{1 - \nu^2}, \quad n \geq 0. \quad (14c)$$

For a thick shell ( $h = 0.1069$ " or thin shell ( $h = 0.0514$ " ), Equations (14b) and (14c) predict the natural frequencies with 10% accuracy for  $n \geq 6$  for the lower branch and  $n \geq 3$  for the upper branch. These approximations are better than those given by Feit and Junger [10] which eliminates the unity in Equation (14b). The unity in the formula for the lower branch represents the membrane energy and the first term represents the bending energy. Thus, neglecting this factor, the 10% accuracy can only be obtained for  $n \geq 20$  for the lower branch. If  $n$  is large enough, the unity can be neglected and the shell resonances approach those of a plate of equivalent surface, i.e., the shell resonances fall in the so-called "plate range," where the curvature effects are no longer important. When  $\Omega < 1$ , the lower branch roots given by Equation (14a) are within 5% for  $n \leq 10$ . These frequencies are shown in Figure 2.

The modal mechanical impedance of a spherical shell for a radially applied force can be obtained by setting  $P_{rn} = 0$  in Eq. (12). The mechanical impedance is

$$Z_{mn} = \frac{P_{in}}{W_n} = \frac{P_{in}}{-i \omega W_n} = -\frac{i E h}{(1 - \nu^2) \omega a} \frac{N_n}{D_n}, \quad (15)$$

where

$$\begin{aligned} N_n = (1 - \nu^2)^2 \Omega^4 - [\beta \lambda_n^2 + (1 + \beta \nu) \lambda_n \\ + 1 + 3\nu - \beta (1 - \nu)] (1 - \nu^2) \Omega^2 + \beta \lambda_n^3 - 4\beta \lambda_n^2 \\ + [\beta(5 - \nu^2) + (1 - \nu^2)] \lambda_n - 2(1 + \beta)(1 - \nu^2), \end{aligned}$$

and

$$D_n = -(1+\beta)\lambda_n + (1-\nu)(1+\beta) + (1-\nu^2)\Omega^2$$

When  $\beta = 0$ ,  $Z_{mn}$  reduces to the modal mechanical impedance of a membrane shell [8]. The modal ratio of the tangential to radial displacement amplitude  $U_n/W_n$  is obtained from Equation (11) as follows:

$$\frac{U_n}{W_n} = \frac{\beta[\lambda_n - (1-\nu)] + (1+\nu)}{(1+\beta)[\lambda_n - (1-\nu)] - (1-\nu^2)\Omega^2} \quad (16)$$

which depends on the excitation frequency  $\Omega$ .

To obtain the resonances of a shell submerged in a fluid, one can write the equations of motion in terms of generalized coordinates. The displacements  $u$  and  $w$  are expressed in terms of generalized coordinates as follows:

$$u = \sum \bar{U}_n(\theta) q_n(t)$$

and

$$w = \sum \bar{W}_n(\theta) q_n(t)$$

where  $\bar{U}_n$  and  $\bar{W}_n$  are the mode shapes of the tangential and the radial component of the displacement and  $q_n(t)$  are the generalized coordinates.

The equation of motion on the generalized coordinates becomes:

$$\ddot{q}_n + \frac{\frac{K}{\mu} + \frac{r_{an}}{\mu S_n}}{1 + \frac{M_{an}}{\mu S_n}} \dot{q}_n + \frac{\omega_n^2}{1 + \frac{M_{an}}{\mu S_n}} q_n = \frac{\int_{-1}^{+1} \bar{W}_n P_{in} d\eta}{\left(1 + \frac{M_{an}}{\mu S_n}\right) \left(\frac{2}{2n+1}\right) \mu S_n} \quad (17)$$

where  $K$  represents the damping factor,  $r_{an}$  and  $M_{an}$  are the resistive and reactive components of the modal acoustic impedance  $Z_{an}$

$$Z_{an} = i\omega c \frac{h^{(1)}(ka)}{h_n^{(1)}(ka)} = r_{an} - i\omega M_{an} \quad (18)$$

$\mu$  is the surface mass density and  $S_n$  is a shape factor which appears in the modal mass  $M_n$ :

$$M_n = \frac{4\pi a^2 \mu}{2n+1} \left[ \lambda_n \left( \frac{U_n}{W_n} \right)^2 + 1 \right] = \frac{M}{2n+1} S_n \quad (19)$$

with  $S_n = \lambda_n (U_n/W_n)^2 + 1$  and  $M$  is the total mass of the shell. For a freely vibrating shell in an acoustic medium, let  $q_n = A_n \exp(-i\omega_n t)$ , with the natural frequency of the submerged shell being  $\omega_n$ , in Equation (17), which results in an expression for  $\omega_n$  as:

$$\bar{\omega}_n^2 = \frac{\omega_n^2}{1 + \frac{M_{an}}{\mu S_n}} = \frac{\omega_n^2}{1 + M_R} \quad (20)$$

where  $\omega_n$  is the natural frequency in vacuo, and the factor,  $M_R = M_{an}/\mu S_n$ , represents the ratio of the additional fluid virtual mass to the unloaded shell modal mass.

It is evident from Equation (20) that the resonant frequency of a submerged shell is affected by the virtual mass,  $M_{an}$ , and the modal mass,  $M_n = \mu S_n$ . In other words, it is determined by the mass loading factor,  $M_R$ . The virtual mass, which is a function of the frequency, adds to the inertia of the shell. The contribution of this mass to the total mass of the system depends on the acoustic characteristic impedance  $\rho c$ . The modal normalized acoustic resistance,  $r_{an}/\rho c$ , and reactance,  $M_{an}/\rho a$ , are computed from Equation (18) and plotted in Figures 3 and 4, vs the nondimensional frequency  $ka$ , respectively. The modal reactance increases with frequency and then decreases rapidly toward zero as the frequency increases. It means that the virtual mass is low at high frequencies. The normalized modal acoustic resistance increases from zero to peak value before it reaches its asymptotic value of unity for high frequencies.

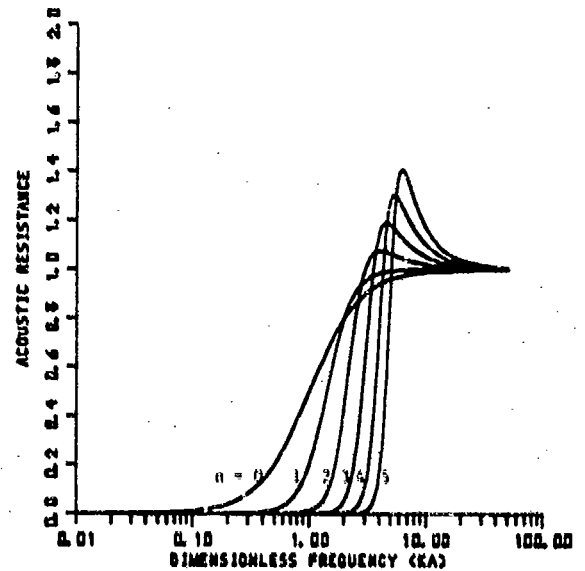


Fig. 3 - Normalized acoustic resistance curves,  $\text{Re}(Z_a)/\rho c$

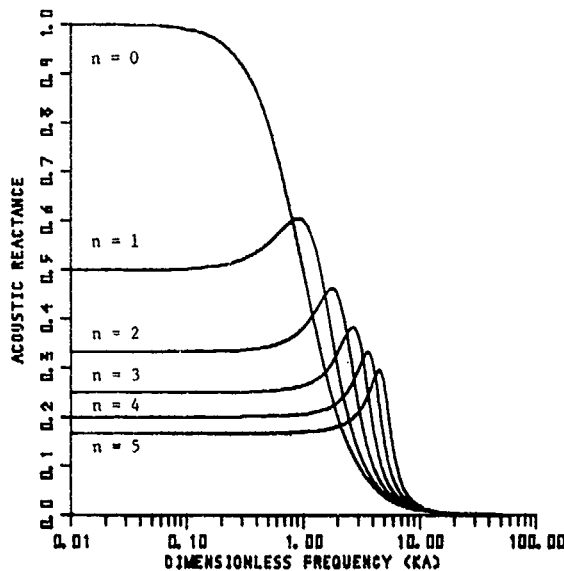


Fig. 4 - Normalized acoustic reactance curves,  $I_m(Z_a)/\rho a$

The natural frequencies of a submerged shell  $\bar{\omega}_n$  are obtained from Equation (20) by use of an iteration technique, since the natural frequencies in vacuo,  $\omega_n$ , are already known. These are plotted in Figures 5 and 6 for the upper and lower branches. It is evident that the submerged shell natural frequencies of the lower branch are lower than those for a shell in vacuo (or in air). For the light fluid (air) loading, the mass loading factor,  $M_R$ , is negligible and hence the resonances in air are very close to those in vacuo. For the heavy fluid (water) loading, the mass loading factor,  $M_R$ ,

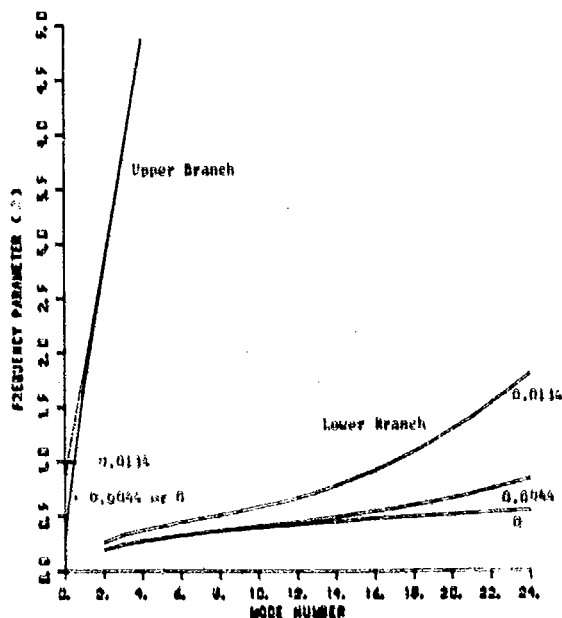


Fig. 5 - Dimensionless frequency  $\Omega$  for various modes when spherical shells are excited in water

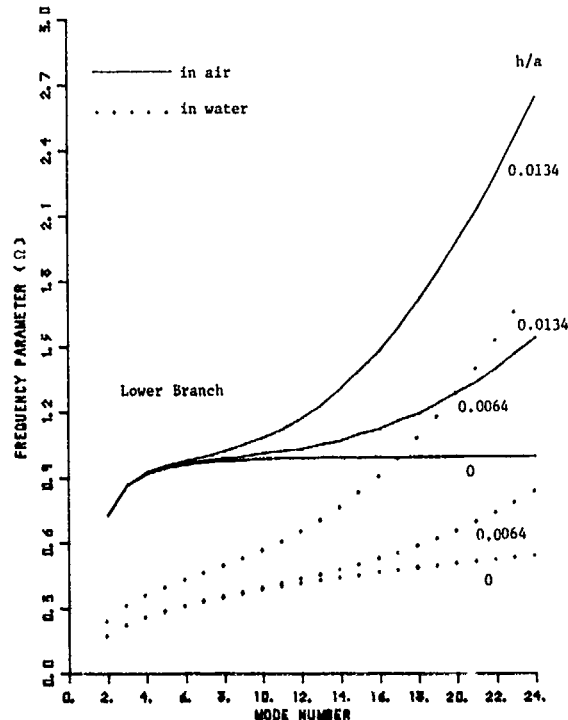


Fig. 6 - Dimensionless frequency  $\Omega$  for various modes. Comparison of spherical shells in water with that in air

increases up to four times the mass of the shell for the mode shapes of the primarily radial modes of the lower branch ( $U_n/W_n \ll 1$  (strong fluid coupling) except that ( $U_n/W_n = 1$  ( $\Omega_1 = 0$ ) for the first mode. Thus, the natural frequencies in water are reduced significantly for the lower branch at low mode numbers. However, when  $M_R$  decreases to less than unity for high mode orders of the lower branch (higher frequencies), the natural frequencies in water are slightly decreased from those in air. For the mode shapes of the upper branch, which are primarily tangential ( $U_n/W_n < 1$  (weak fluid coupling), the virtual mass of the accelerated fluid is negligible.

#### THE RESONANCE DENSITY OF SPHERICAL SHELLS AND THE MEAN LINE OF THE DRIVING POINT ADMITTANCE

In order to obtain an approximation of the shell's characteristic admittance, a study of the spherical shell's resonance density is necessary. The resonance density [11] is defined as:

$$\frac{1}{E_n} = \frac{dn}{d\omega}$$

$$= \frac{n}{C_b} \frac{dn}{d\Omega} \quad (21)$$

where  $\omega$  is the resonant angular frequency and  $C_b = (E/\rho_s)^{1/2}$ .

By differentiating Equation (13) with respect to mode number  $n$ , the resonance density is expressed as:

$$\frac{dn}{d\Omega} \cong \Omega \frac{4(1-\nu^2)\Omega^2 - 2c_n}{a_n\Omega^2 - b_n}, \quad (22)$$

where

$$a_n = (2n+1)(1+\nu\beta + 2\beta\lambda_n^2),$$

$$b_n = \frac{(2n+1)[3\beta\lambda_n^2 - 8\beta\lambda_n + \beta(5-\nu^2) + (1-\nu^2)]}{(1-\nu^2)},$$

and

$$c_n = 1 + 3\nu - \beta(1-\nu) + \lambda_n(1+\nu\beta) + \beta\lambda_n^2.$$

At low frequencies or in the membrane range  $\Omega < 1$ , the parameters in Equation (22) can be approximated as follows:

$$a_n \approx (2n+1),$$

$$b_n \approx (2n+1)$$

and

$$c_n \approx (1 + 3\nu + \lambda_n). \quad (23)$$

Then, Equation (23) with  $n$  and  $\lambda_n$  substituted for Equation (14a) can be expressed approximately as:

$$\frac{dn}{d\Omega} \approx \frac{2\sqrt{2}\Omega}{(1-\Omega^2)\sqrt{1-\Omega^4}}, \quad \Omega < 1, \quad (24)$$

which is independent of the shell thickness, because it is for the membrane range. In the membrane range, the resonance density increases as  $\Omega$  increases [see Equation (24)]. The resonance density reaches a maximum [see Equations (22) and (23)] when  $\Omega$  is given by:

$$\Omega^2 \approx \frac{3\beta\lambda_n^2}{1-\nu^2} + 1. \quad (25)$$

Thus, the maximum resonance density is given by:

$$\frac{dn}{d\Omega} \approx 0.433/\beta^{1/2}.$$

It is quite clear that, in general, the maximum point is not at  $\Omega = 1$  except for a membrane shell, when  $\beta = 0$ . Due to introduction of the term  $\beta\lambda_n^2$ , the maximum occurs at  $\Omega > 1$ . Actually, the resonance density is an inverse slope of the frequency curves shown in Figure 6.

Thick shells' natural frequencies differ from the membrane mode at a higher frequency than thin shells. The take-off point from the membrane curve in Figure 6 is the maximum point of the resonance density. Therefore, it is

expected that the maximum point of the resonance density is closer to unity as the thickness of the shell decreases and that the peak becomes higher (see Figures 7 and 8). For frequencies above  $\Omega = 1$ , the resonance density decreases slowly with frequency.

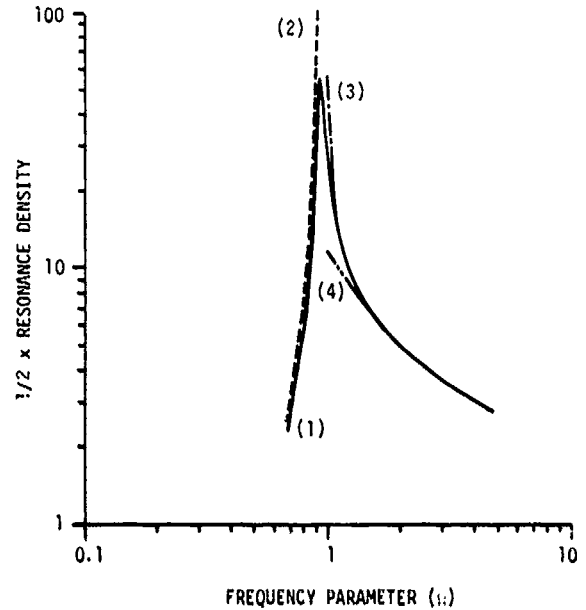


Fig. 7 - Resonance density of a spherical shell,  $h = 0.0514''$ , in vacuo

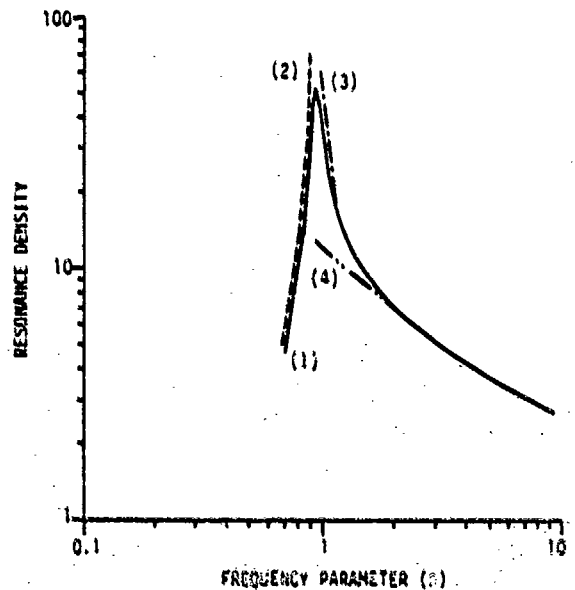


Fig. 8 - Resonance density of a spherical shell,  $h = 0.1069''$ , in vacuo

At high frequencies,  $\Omega \gg 1$  when the resonances approach the plate range, it is convenient to use the asymptotic form. By differentiating Equation (14b), the resonance density for a spherical shell becomes:

$$\frac{dn}{d\Omega} \approx \frac{1}{2} \left( \frac{1-\nu^2}{\beta} \right)^{1/4} \frac{1}{\Omega^{1/2} \left( 1 - \frac{1}{\Omega^2} \right)^{3/4}} \quad \text{for } \Omega > 1, \quad (26a)$$

and, in the plate range, becomes:

$$\frac{dn}{d\Omega} \approx \frac{1}{2} \left( \frac{1-\nu^2}{\beta} \right)^{1/4} \frac{1}{\Omega^{1/2}} \quad \text{for } \Omega \gg 1, \quad (26b)$$

with a maximum value given by:

$$\frac{dn}{d\Omega} \approx 0.433/\beta^{1/2}. \quad (26c)$$

Figures 7 and 8 show the resonance density of the two spherical shells in vacuo. Curves (1), (2), (3), and (4) represent, respectively, the resonance density for the exact [Equation (22)], the low frequency approximation [Equation (24)], the density for midrange frequencies' approximation [Equation (26a)], and the high frequency plate range [Equation (26b)]. The maximum point in the resonance density spectrum separates the resonances into membrane range and plate range. Resonances between those two ranges are in the so-called "coupling range." The segment of Curve (1) for  $\Omega > 1.5$  matches with that of Curve (4) for the plate range, and Curve (3) matches Curve (1) down to  $\Omega \approx 1$ . Curve (2) matches with Curve (1) up to  $\Omega = 1.0$ . In the membrane range, both shells have the same resonance density [see Equation (24)]. The higher resonance density of the thin shell implies that it has a higher response when one considers the driving point admittance (DPA) because the mean value of the DPA [11] is:

$$Y_c = \frac{\pi}{2E_n M_n} \quad (27)$$

where  $M_n$  is the modal mass of the spherical shell [Equation (19)]. Figure 9 shows the mean value of the DPA of the shells. For  $\Omega > 1$ ,

$$Y_c = \frac{\pi a}{4C_b M_n} \frac{\left( \frac{1-\nu^2}{\beta} \right)^{1/4}}{\Omega^{1/2} \left( 1 - \frac{1}{\Omega^2} \right)^{3/4}} \quad (28)$$

and

$$Y_c \approx (8\alpha^2 \rho_s h)^{-1} \quad \text{for } \Omega \gg 1. \quad (29)$$

When  $\Omega < 1$ ,  $E_n$  in Equation (27) is replaced by  $\Delta\omega$  because the shell does not have many modes in the membrane range, and also, a 3 dB is added to Equation (28) due to the imaginary part of the mean value of the DPA (see

Reference 11). Thus,

$$Y_c = \frac{2(n+1)}{8\alpha^2 \rho_s h \sqrt{3(1-\nu^2)} \Delta\Omega}, \quad \Omega < 1, \quad (30)$$

where  $\Delta\Omega = (\omega_{n+1} - \omega_n) / \omega_r$

$$\text{and } \alpha^4 = \frac{Eh^2}{12\rho_s(1-\nu^2)}.$$

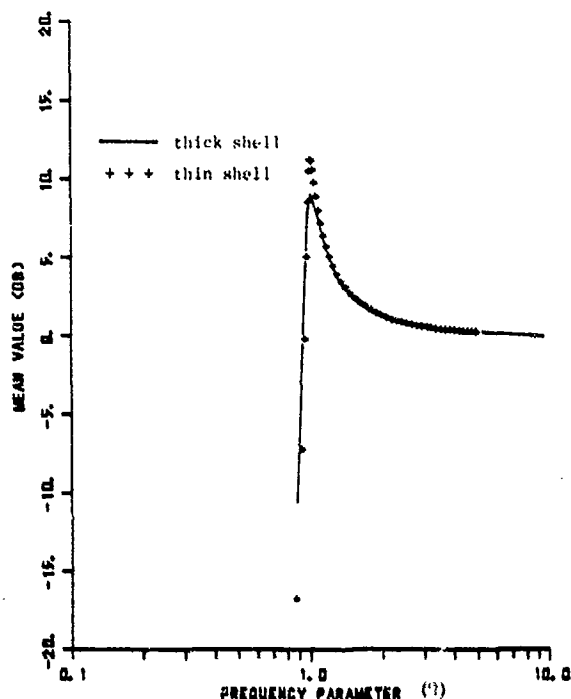


Fig. 9 = Mean value of the driving point admittance of spherical shells in vacuo

## THE POINT EXCITED VIBRATION OF A SHELL

The response of a point excited shell in an acoustic medium is analyzed in this section. The fluid pressure  $P_{rn}$  in Equation (12) is no longer assumed to be zero. Since the radiated acoustic pressure  $P_{rn}$  is an outgoing wave, it can be expressed in terms of the spherical Hankel function of first kind and order  $n$ . Therefore,

$$P_r(r, \eta) = \sum_{n=0}^{\infty} \{ \text{co}[h_n(kr)/h'_n(ka)] \} \hat{W}_n P_n(\eta) \quad (31)$$

$$= \sum_{n=0}^{\infty} Z_{an} [h_n(kr)/h_n(ka)] \hat{W}_n P_n(\eta).$$

where  $Z_{an} = i\rho c [h_n(ka)/h'_n(ka)]$  is defined as the acoustic radiation impedance.

The radial velocity is expressed in terms of the applied force and the total impedance of the shell by

$$\dot{W}_n = P_{in}/Z_n \quad (32)$$

where  $Z_n$  is the modal impedance of a submerged shell.

The driving point admittance and the response pressure field are examined first. Consider a unit concentrated force which can be described by:

$$P_i = (1/4\pi a^2) \sum_{n=0}^{\infty} (2n+1) P_n(\eta) \\ = \sum_{n=0}^{\infty} P_{in} P_n(\eta) \quad (33)$$

From Equation (32), the modal velocity of the shell in an acoustic medium is given by:

$$\dot{W}_n = \frac{2n+1}{4\pi a^2 Z_n} \quad (34)$$

The radial velocity of the submerged shell is given:

$$\dot{W} = \sum_{n=0}^{\infty} (2n+1) P_n(\eta)/(4\pi a^2 Z_n) \quad (35)$$

The driving point admittance (DPA) is defined as the ratio of the radial velocity of the shell to the applied force at that particular point. The DPA is obtained directly by setting  $\eta = 1$  [ $P_n(1) = 1$ ] in Equations (33) and (35) and taking the ratio,

$$Y_d = \frac{\sum_{n=0}^{\infty} \frac{2n+1}{Z_n}}{4\pi a^2} \quad (36)$$

Finally, substituting Equation (34) for  $\dot{W}_n$  into Equation (31), the pressure field of a submerged shell is:

$$p_d(r, \eta) = \frac{1}{4\pi a^2} \sum_{n=0}^{\infty} (2n+1) \frac{Z_{an}}{Z_n} \frac{h_n(kr)}{h_n(ka)} P_n(\eta) \quad (37)$$

At resonance, the imaginary part of the total impedance  $Z_n$  is equal to zero. Then,  $Z_n$  reduces to the sum of the internal damping  $r_{sn}$  of the shell and the acoustic resistance  $r_{an}$ , where  $r_{an} = \text{Real} [i\rho c h_n(ka)/h'_n(ka)]$ . The modal impedance of a submerged shell is expressed conveniently as:

$$Z_n(\omega) = Z_{an} + Z_{mn} \\ = [r_{mn} + r_{an}(\omega)] + i[M_{mn}(\omega) - \omega M_{an}(\omega)]$$

where  $Z_{mn} = r_{mn} + iM_{mn}$  and  $Z_{an} = r_{an} - i\omega M_{an}$ , for mode number  $n = 0, 1, 2, \dots$

## NUMERICAL RESULTS

Calculations are made for two different duralumin spherical shells when submerged in air and water. The physical properties of the shell material, fluid, and the dimensions of the shells are listed in Table 1.

TABLE 1  
PHYSICAL PROPERTIES OF A DURALUMIN  
SPHERICAL SHELL AND ACOUSTIC MEDIA

Thickness (h)	0.0514", 0.1069"
Radius (a)	8"
Young's Modulus (E)	$1.037 \times 10^7$ psi
Poisson's Ratio ( $\nu$ )	0.335
Mass Density of the Shell ( $\rho_s$ )	$2.649 \times 10^{-4}$ lb. sec. <sup>2</sup> /in. <sup>4</sup>
Mass Density of Air ( $\rho$ )	$1.15 \times 10^{-7}$ lb. sec. <sup>2</sup> /in. <sup>4</sup>
Mass Density of Water ( $\rho$ )	$9.645 \times 10^{-5}$ lb. sec. <sup>2</sup> /in. <sup>4</sup>
Velocity of Sound in Air (c)	$1.356 \times 10^4$ in./sec.
Velocity of Sound in Water (c)	$6 \times 10^4$ in./sec.
( $ra$ ) <sub>air</sub>	$14.59 \times \Omega$
( $ka$ ) <sub>water</sub>	$330 \times 10^{-2} \times \Omega$
( $\rho c$ ) <sub>water</sub>	$5.79$ lb. sec./in. <sup>3</sup>
( $\rho c$ ) <sub>air</sub>	$1.56 \times 10^{-3}$ lb. sec./in. <sup>3</sup>

The frequency spectra of the driving point admittance (DPA) for point excited spherical shells were calculated with structural damping factor  $6 \times 10^{-4}$  (except  $6 \times 10^{-3}$  in Figures 11 and 12) for duralumin. For vibration in air, the normalized acoustic resistance at the resonance frequency of each mode was found to be dominant. On the other hand, when the shell is vibrating in water, the structural damping was found to be dominant because the normalized modal acoustic resistance was negligible at the resonance frequency of each mode.

The amplitude of the normalized DPA for the two duralumin shells tested were computed and plotted in Figures 10 to 14. The DPA was normalized to that for a point driven infinite plate having the same thickness, as given in Eq. (29). The low frequency behavior is dominated by the mass of the shell. Thus, for the non-normalized DPA, the thin shell should be approximately 6 dB higher. However, when one normalizes with DPA of a plate with the same thickness, the normalization is proportional to  $h^{-2}$ , so that the normalization causes a 12 dB increase in the DPA of a thick shell, so the net change of the normalized admittance is 6 dB increase for the thick shell. The minimum response for frequencies less than the first resonance corresponds to the first anti-resonance between the rigid body frequency ( $\Omega_1 = 0$ ) and the first resonance ( $\Omega_2$ ). Thus, for frequencies below the first anti-resonance, the motion at the center of gravity of the freely suspended shell is governed by a term  $Y_0 = 1/Z_0 = 1/\omega M$ , where  $M$  is the total mass of the shell. Therefore, the slope of the response is 6 dB per octave. For classical shells, the resonances are well-spaced, and the resonant response shows distinct peaks in Figures 10, 11, and 12, which is not evident for the membrane theory.

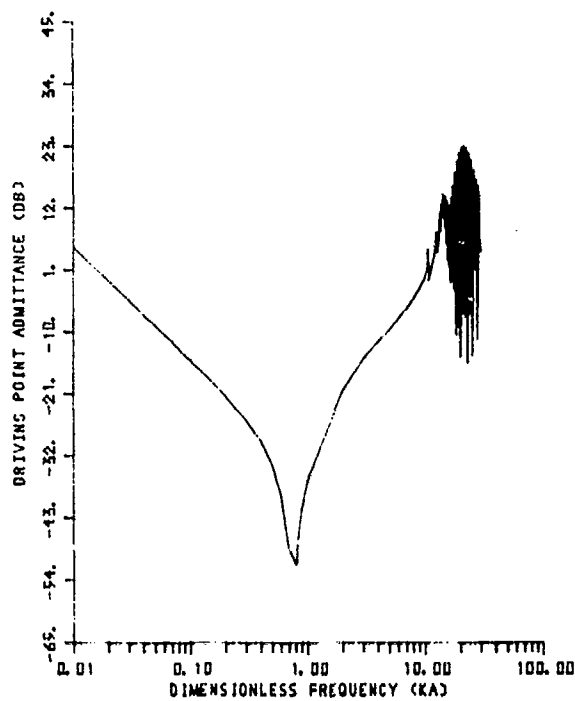


Fig. 10 - DPA of a classical shell with thickness  $h = 0.0514''$  in air

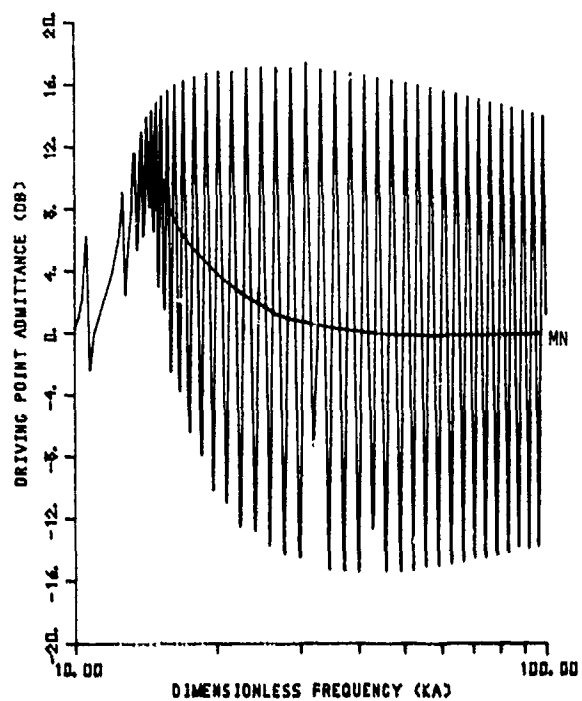


Fig. 12 - DPA of a classical shell with thickness  $0.0169''$  in air,  $10 \leq ka \leq 100$

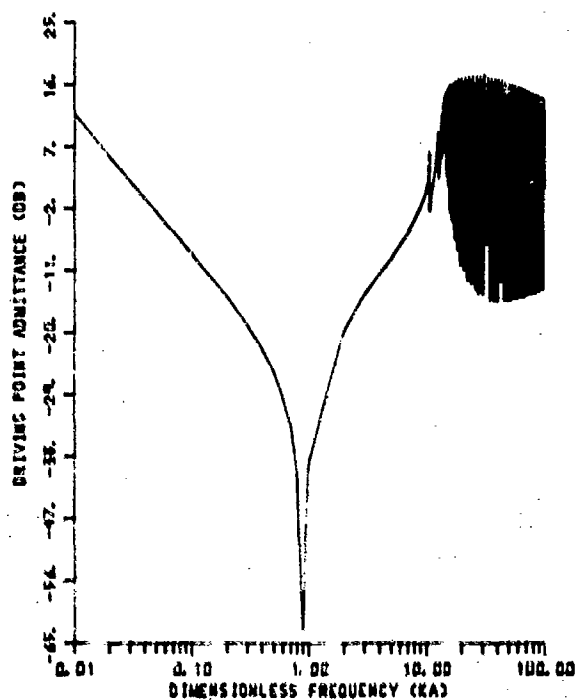


Fig. 11 - DPA of a classical shell with thickness  $h = 0.1069''$  in air,  $0.01 \leq ka \leq 100$

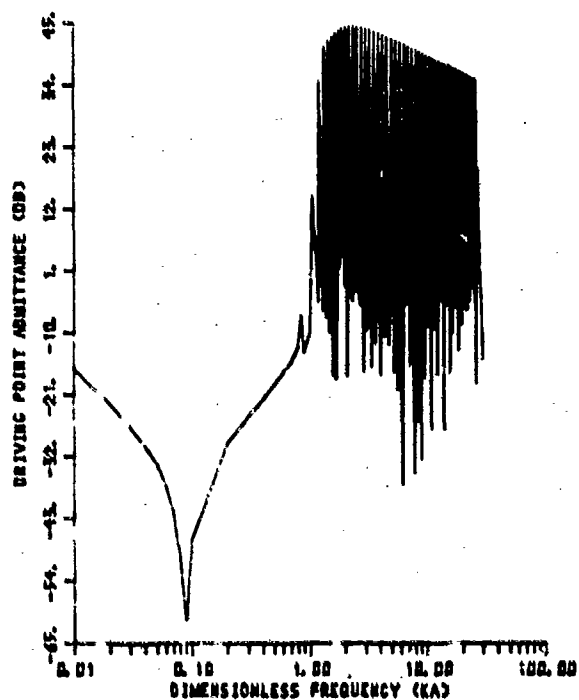


Fig. 13 - DPA of a classical shell with thickness  $h = 0.0514''$  in water

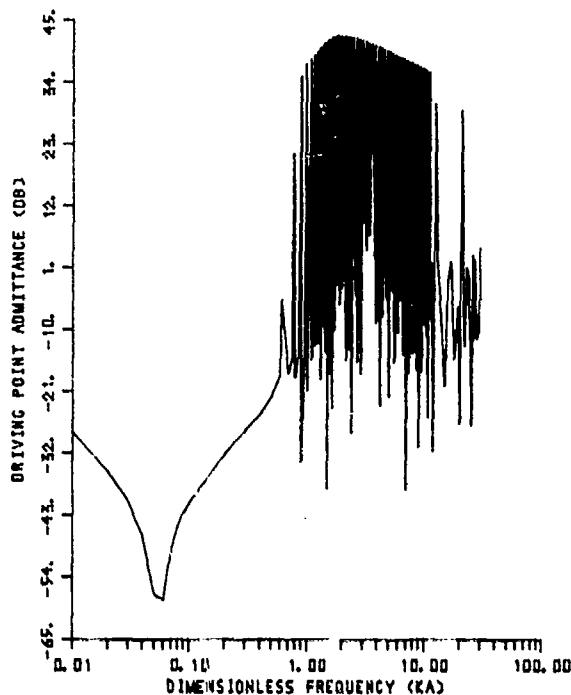


Fig. 14 - DPA of a classical shell with thickness  $h = 0.1069$ " in water

For vibration in water, the shell exhibits a similar behavior in the low frequency range, except that the DPA is much lower in water than in air. This is explained by the fact that the virtual mass of the displaced acoustic medium at low frequencies is negligible in air when compared to the mass of the shell but is much higher than the mass of the shell vibrating in water. Thus, since the admittance below the first resonance is  $1/\omega M$ ,  $M$  being the total mass being vibrated, the admittance in air is much higher than that in water. However, the admittance of the shell at resonances is lower in air than in water because of the previously explained behavior of the modal admittances in air and in water.

The minimum point in Figures 10 through 14 will shift due to the position of the first resonance. The position of the first resonance of the shell in air is the same for all shell thicknesses, so that the anti-resonance does not shift. However, the first resonance of the shells submerged in water is almost one-tenth of that in air, so that the location of the anti-resonance shifts down accordingly.

In vacuo or air, the mean value of the DPA for a shell will approach asymptotically the value of the impedance of

an infinite plate. The result is shown in Figure 12 when the line MN in the resonant spectrum is the predicted mean value computed by Equation (27). The resonant mean value is in excellent agreement with the line MN, but the predicted mean value in the first few modes of the membrane range fails to agree. This is because there are so few resonances in the membrane range.

The mean value method can also be used to predict the mean value of the DPA of a shell in water. However, it has to overcome the difficulty due to the introduction of the virtual mass in the equation of motion. At very high frequencies, the mean value of the DPA of a submerged shell again approaches the unloaded infinite plate value.

#### GENERAL EXPERIMENTAL APPROACH

The resonance frequency measurements were performed for both 14-gauge (actual thickness  $h = 0.0514$  inch) and 8-gauge (actual thickness  $h = 0.1069$  inch) thick spherical shells. The directivity pattern measurements were taken on the 8-gauge shell. Each of these shells is 16 inches in diameter and is constructed of duralumin material. The spherical shells were fabricated from two hemispherical shells welded at the equator and the weld's ground smooth.

The experimental measurements were carried out in the anechoic chamber at the Water Tunnel Building and the anechoic water tank at the Applied Science Building of the Pennsylvania State University. The anechoic chamber was built initially in support of this experimental program to investigate the fluid loading effects on elastic structures. It has internal dimensions of  $11 \times 12 \times 18$  feet. The sound absorbing walls are composed primarily of rock-wool fiberglass insulation, air voids, and wood frame members. It is considered as a semi-anechoic for frequencies less than 1 kHz and moderately anechoic for higher frequencies. The water-filled anechoic tank, which is 12 feet long, 4 feet wide, and 11 feet deep, is lined with Insulcrete wedges. Between 20 and 30 kHz, the tank is better than 90 percent absorbent. The absorption falls off rapidly below 20 kHz. The spherical shells were located near the center of the tank or the chamber. The source and receiver were placed on a horizontal plane through the center of the shell perpendicular to the walls of the tank or the chamber.

The resonances of spherical shells were measured by plotting the frequency response and the modal pattern. A continuous sinusoidal wave was applied to the shaker to excite the shell in both water and air. A schematic diagram of the test set-up is shown in Figure 15.



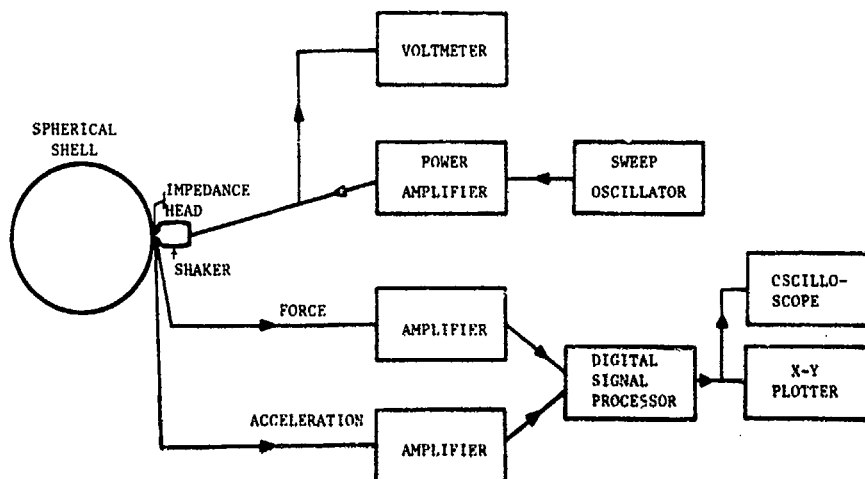


Fig. 15 - Operational set-up of the driving point inertance measurement

### EXPERIMENTAL RESULTS

The driving point admittance in air of the thin and thick shells are shown in Figures 16a - 17b, respectively. Both shells exhibit an antiresonance in the low frequency range as was predicted earlier and shown in Figures 10 and 11. In the higher frequency range, the measured resonances are the peaks of the admittance. These resonance frequencies were identified by the measurements of the mode shape by use of an accelerometer and shown in Figures 18 and 19, for the two shells. The difference between the predicted and the measured resonance frequencies is small for most of the measured mode orders. The good agreement occurred in spite of the nonuniformity of the shell's thickness and the existence of the weld between the two hemispheres making up each spherical shell.

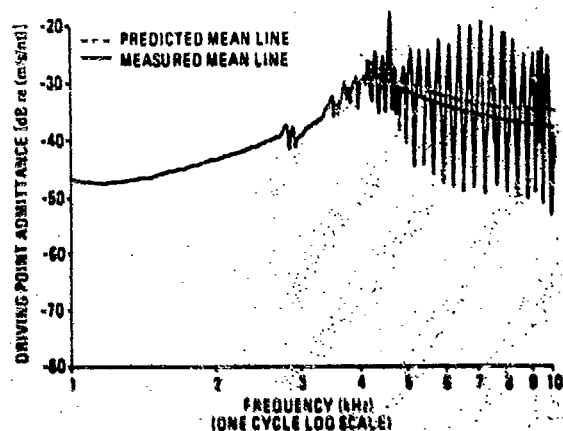


Fig. 16b - Measured driving point admittance of a duralumin spherical shell with thickness  $h = 0.0514$ " in air

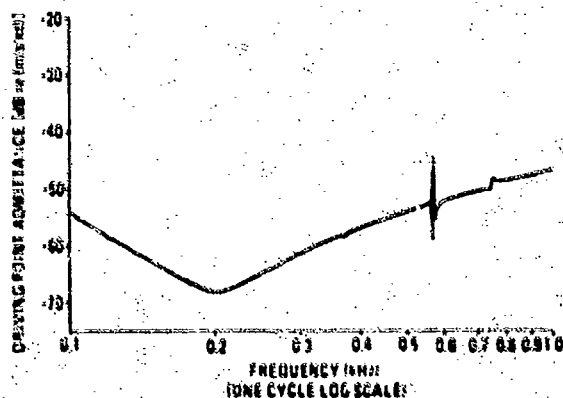


Fig. 16a - Measured driving point admittance of a duralumin spherical shell with thickness  $h = 0.0514$ " in air

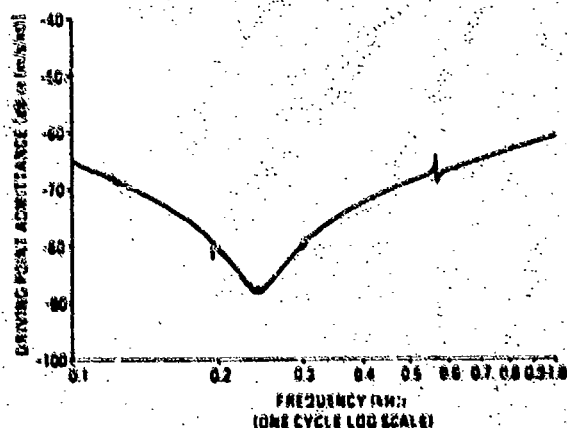


Fig. 17a - Measured driving point admittance of a duralumin spherical shell with thickness  $h = 0.1069$ " in air

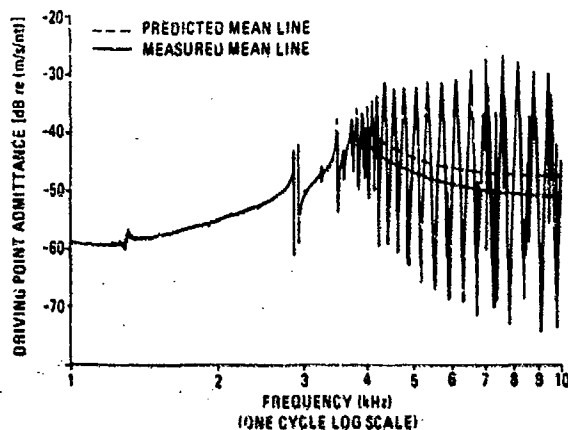


Fig. 17b - Measured driving point admittance of a duralumin spherical shell with thickness  $h = 0.1069''$  in air

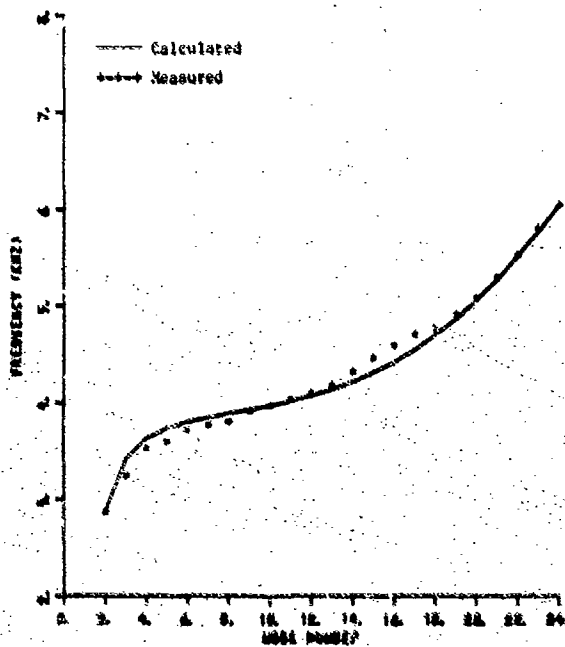


Fig. 18 - Resonant frequencies of a duralumin spherical shell with thickness  $h = 0.0514''$  in air

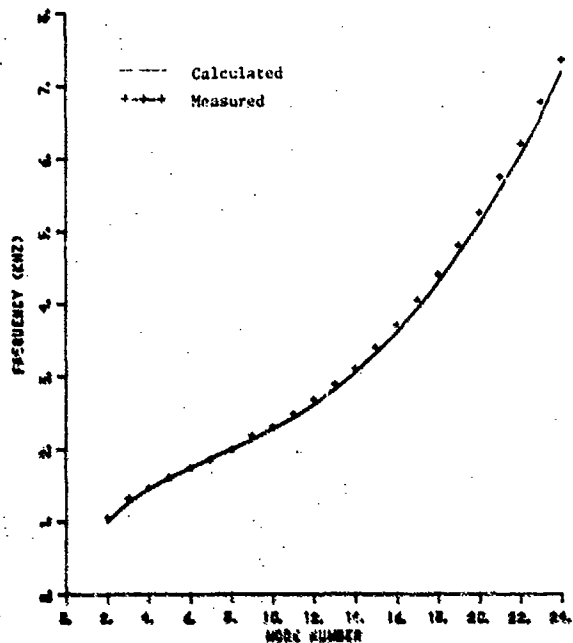


Fig. 19 - Resonant frequencies of a duralumin spherical shell with thickness  $h = .1069''$  in air

The measured resonance frequencies for submerged shells in water were obtained from the peaks in the driving point impedance shown in Figures 20 and 21 for the thin and thick shells, respectively. The measured resonances, as identified by the measured mode shape, are shown in Figures 22 and 23, respectively, for thin and thick shells. The agreement between the measured and predicted resonances again is very good.

It should be noted that the good agreement between the predicted and measured resonance frequencies was attained only after a thorough measurement of the thickness of the shell was made. The manufacturer has supplied us with nominal thicknesses of 8-gauge and 14-gauge for the two shells. However, it has been found that the 8-gauge and the 14-gauge shells actually have thicknesses of 0.1069 inch and 0.0514 inch, respectively. This drop in thickness of two gauges has been confirmed by ultrasonic measurement.

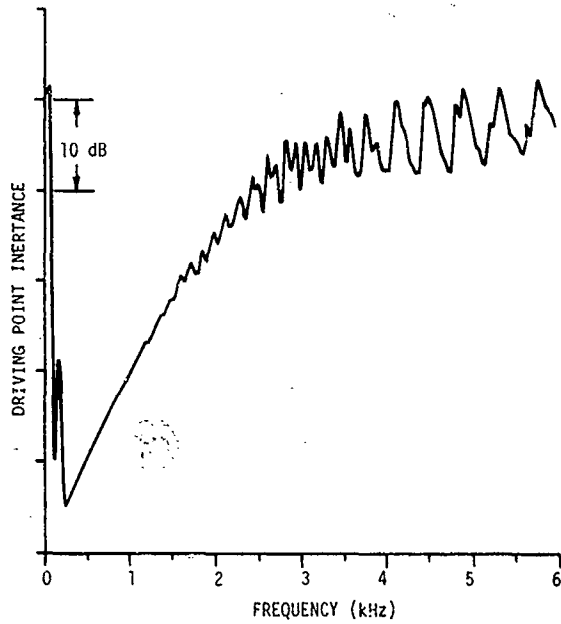


Fig. 20 - Measured driving point inertance of a duralumin spherical shell with thickness  $h = 0.0514$ " in water

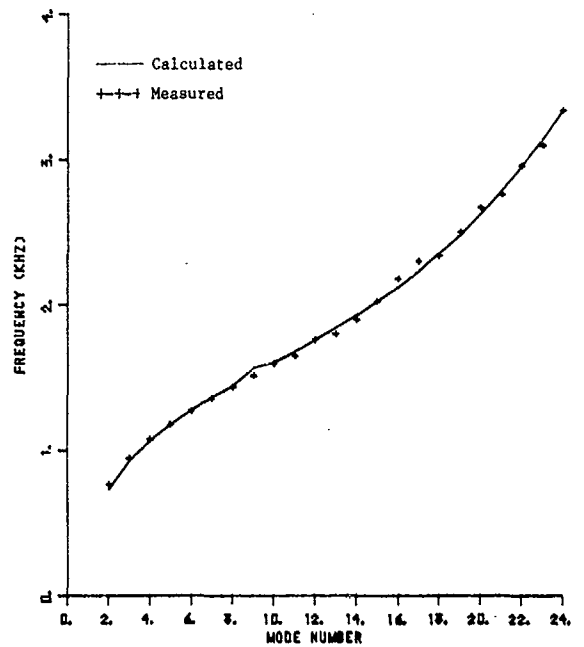


Fig. 22 - Resonant frequencies of a duralumin spherical shell with thickness  $h = 0.0514$ " in water

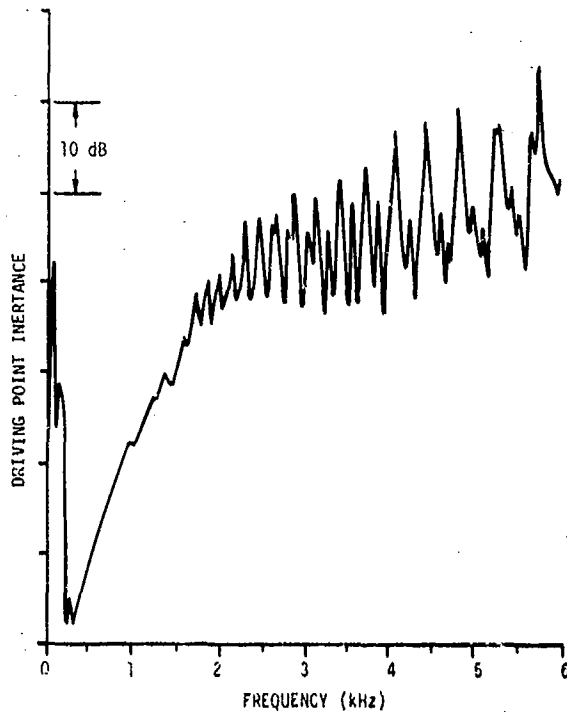


Fig. 21 - Measured driving point inertance of a duralumin spherical shell with thickness  $h = 0.1069$ " in water

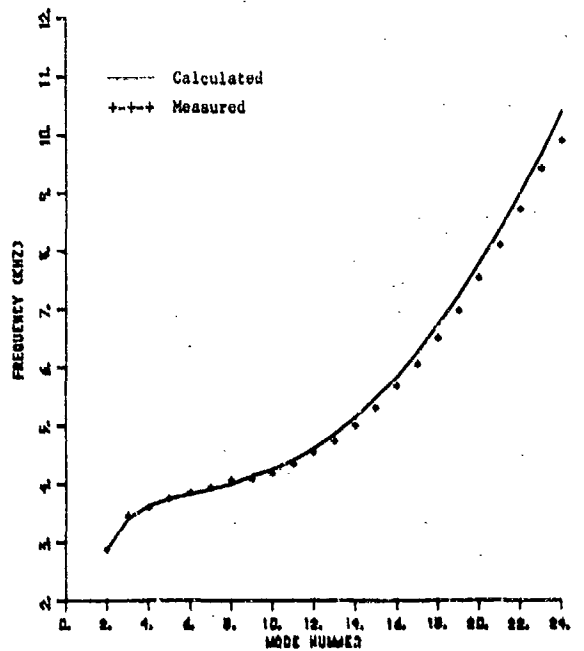


Fig. 23 - Resonant frequencies of a duralumin spherical shell with thickness  $h = 0.1069$ " in water

## CONCLUSION

The analytical and experimental study of the vibration response of point excited shells in air and in water indicates that the bending theory of deformation of shells is adequate for the frequency range of interest,  $ka \leq 30$ . Furthermore, the influence of shear deformation and rotatory inertia was found to be negligible for frequencies up to  $ka = 30$ .

The method for computing the natural frequencies of a submerged shell by use of generalized coordinates and the iteration method proved to be accurate, when one compares the predicted vs measured resonances. The resonances of a submerged shell were shown to be influenced heavily by the virtual mass of the displaced fluid in most of the frequency range under investigation, even though in the high frequency range, this influence disappears. The mode shapes at resonance for vibration in air and in water were found to be identical, as predicted.

## ACKNOWLEDGMENTS

The authors acknowledge the financial support of the Naval Sea Systems Command for the conduct of this study through a contract with the Applied Research Laboratory, the Pennsylvania State University, and the support of the Naval Ocean Systems Center, Code 5134 for assistance and encouragement. The authors also thank Drs. E. J. Skudrzyk and W. F. King III for many valuable discussions.

## REFERENCES

1. Junger, M. C., "Sound Scattering by Thin Elastic Shells," *J. Acoust. Soc. Amer.* **24**, 366-373 (1952).
2. Lamb, H., "On the Vibrations of Spherical Shells," *Proc. London Math. Soc.* **14**, 50-56 (1882).
3. Baker, W. E., "Axisymmetric Modes of Vibration of Thin Spherical Shell," *J. Acoust. Soc. Amer.* **33**, 1749-1758 (1961).
4. Kalnins, A., "Effects of Bending on Vibrations of Spherical Shells," *J. Acoust. Soc. Amer.* **36**, 74-81 (1964).
5. Wilkinson, J. P., "Natural Frequencies of Closed Spherical Shells," *J. Acoust. Soc. Amer.* **38**, 367-368 (1965).
6. Junger, M. C., "Vibrations of Elastic Shells in a Fluid Medium and the Associated Radiation of Sound," *J. Appl. Mech.* **19**, 439-445 (1952).
7. Hayek, S., "Vibration of a Spherical Shell in an Acoustic Medium," *J. Acoust. Soc. Amer.* **40**, 342-348 (1966).
8. Lauchle, G. C., "Interaction of a Spherical Acoustical Wave with an Elastic Spherical Shell," *J. Sound Vib.* **44**, 37-46 (1976).
9. Skudrzyk, E. J., "The Thin Spherical Shells as the Prototype of a Vibration with Coupled Modes, Exact Solution, Model Response and Mean-Value Prediction," *J. Acoust. Soc. Amer.* **70**(1), 1-9 (1981).
10. Felt, D., and Junger, M. C., "High Frequency Response of an Elastic Spherical Shell," *J. Appl. Mech.* **36**, 859-864 (1969).
11. Skudrzyk, E. J. *Simple and Complex Vibratory System*, The Pennsylvania State University Press, University Park, PA. 1968.

## DAMPING OF SHALLOW-BURIED STRUCTURES

### DUE TO SOIL-STRUCTURE INTERACTION

Felix S. Wong and Paul Weidlinger  
Weidlinger Associates  
Menlo Park, California and New York, New York

Damping of the motion of buried structures is derived based on the mechanics of dynamic soil-structure interaction. The interplay between the structural motion and the soil loading on the structure results directly in the damping of the structural motion. The derivation is illustrated by an example of a horizontal slab embedded in an elastic soil medium.

#### INTRODUCTION

It is the current practice to obtain hardness levels of shallow-buried structures from analyses using an undamped SDOF elastic-plastic model. Results of recent and past tests on buried structures have shown that these analyses underpredict the lethal overpressure; a number of fully-buried structures have retained their protective capability at airblast overpressures higher than their predicted collapse load [1,2]. This is illustrated in Fig. 1 which is taken from [1]. The undamped SDOF calculation results shown in the figure use currently accepted procedures for modifying the period to account for soil cover; calculation for the roof load includes attenuation of the overpressure with depth, but no damping and soil-structure interaction effects.

In an attempt to explain the apparent over-conservatism in current methods, Kiger and Balsara [2] retained the SDOF approach but suggested that a high damping ratio should be used to account for energy loss. (The load-deflection relationship obtained from static tests of the same soil-structure configuration was also used to account for "arching.") They indicated that a 20 percent damped SDOF model could accurately predict the permanent deflection of the roof element.

The need for higher damping was also suggested by Windham [3], and by Wojcik and Isenberg [4]. The latter attributed the damping to the radiation of energy away from the structure. Elastic finite element analyses were conducted and damping was assessed by the log decrement of peak displacement in successive cycles.

An analytical derivation of damping for this class of buried structures is given in this paper. The derivation is based on the mechanics

of dynamic soil-structure interaction. As stress waves in the soil strike a soil-structure interface, they give rise to scattered and transmitted waves. The transmitted waves impart particle velocities to the structure; motion of the structure imparts rarefaction waves to the soil, and loading exerted by the soil on the structure is lessened or relieved. This phenomenon, referred to as dynamic soil-structure interaction, is seen to lead to the high damping in structural motion.

The scope of the work is limited to elastic soil-structure configurations in order to clarify the origin of the damping due to soil-structure interaction. The actual interaction process is, of course, much more complex and involves inelastic properties of the soil and nonlinear interface conditions. Analytical solutions are difficult to obtain and numerical methods must be used. However, the basic mechanisms of reflection of the soil stress waves at the soil-structure interface, the relief of the interface load due to motion of the structure away from the soil, and the resultant damping in the structural motion remain the same as those illustrated herein.

#### DYNAMIC SOIL-STRUCTURE INTERACTION

The coupling between loading and structural response can be illustrated by referring to Fig. 2 which is a characteristic diagram of one-dimensional elastic wave interaction between a 6m layer of soil and a concrete slab 1.5m thick. When the incident compressive wave first reaches the soil-concrete interface (point A), it is reflected as well as transmitted. In this example, about 80% of it is reflected and 180% transmitted according to the following equations:

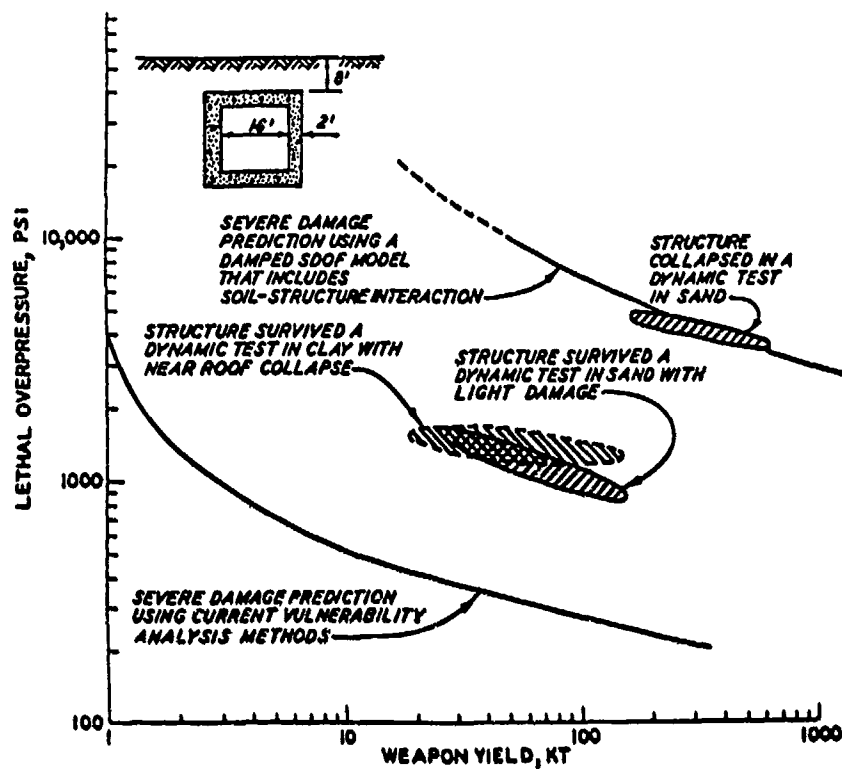


Figure 1. Recent test results of model protective structures [1].

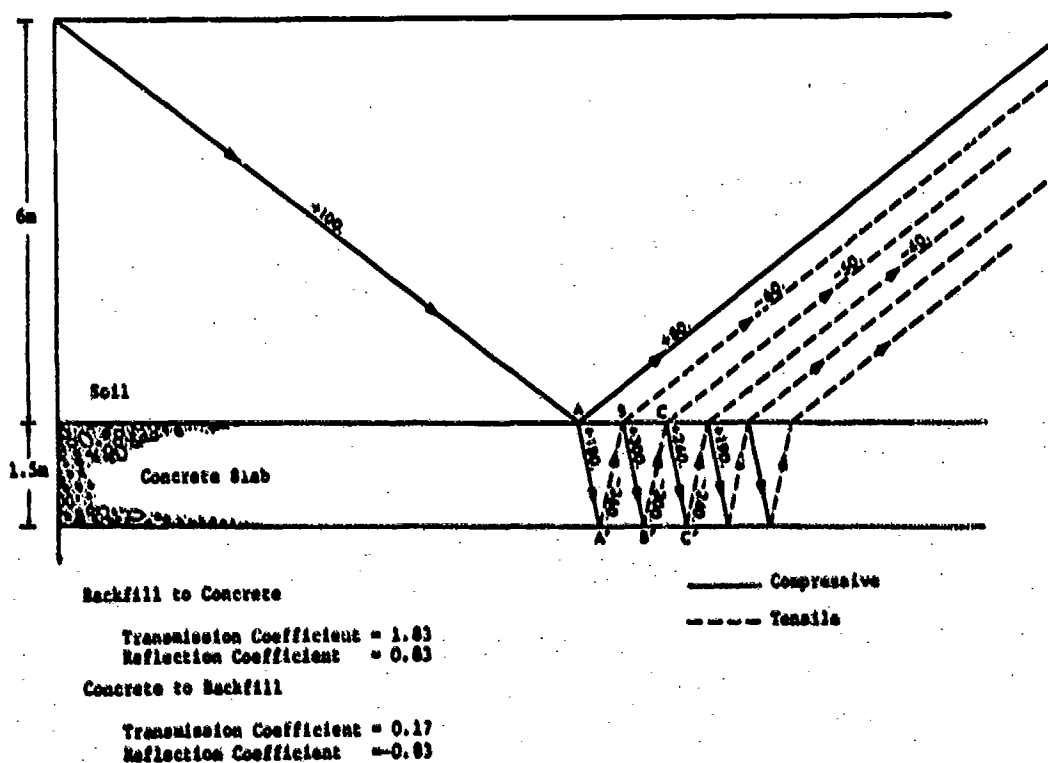


Figure 2. Characteristic diagram, one-dimensional elastic wave interaction.

$$\sigma_T = \frac{2\rho_c c_c}{\rho_c c_c + \rho_s c_s} \sigma_I \quad (1)$$

$$\sigma_R = \frac{\rho_c c_c - \rho_s c_s}{\rho_c c_c + \rho_s c_s} \sigma_I \quad (2)$$

where  $\sigma_I$ ,  $\sigma_T$ ,  $\sigma_R$  are the incident, transmitted and reflected stress components, respectively;  $\rho_c c_c$  is the acoustic impedance of concrete and  $\rho_s c_s$  that of soil;  $\rho$  is the mass density of the material and  $c$  its dilatational wavespeed [5]. Hence for a 100 MPa incident wave, the transmitted wave is 180 MPa. The transmitted wave is reflected at the free edge (point A') as a tensile wave, denoted by a dotted line, of magnitude -360 MPa. Upon encountering the interface, the -360 MPa wave in turn is reflected as a compressive wave of magnitude 300 MPa and transmitted as a tensile wave of magnitude -61 MPa. The reverberation process within the concrete continues as the wave goes from B to B', from C to C', etc.

This multiple wave reflection/refraction phenomenon is well-known. When the applied incident wave has a constant magnitude of 100 MPa, i.e. a step load, the stress at the soil-concrete interface is  $100 + 80 = 180$  MPa at

point A,  $100 + 80 - 60 = 120$  MPa at point B,  $100 + 80 - 60 - 50 = 70$  MPa at point C and so on. Hence, in two transit times across the thickness of the concrete slab, the initial peak of 180 MPa has dropped to 120 MPa, in four transit times to 70 MPa and so on.

When the applied load is not a step but decays with time and has a finite duration, the decay of the interface stress depends on the load duration. Some results for a triangular pulse are given in Fig. 3. Two observations regarding the interface stress can be made. The initial amplification of the interface stress depends on the impedance ratio across the interface. Secondly, this amplification is short-lived. In 2 to 4 transit times across the concrete, the layer will have attained the velocity that it should due to the action of the interface stress and begin to move away from the soil. This motion generates rarefaction or relief waves into the soil, thus relieving the loading on the concrete layer.

This observation is elementary but crucial to the understanding of soil-structure interaction: SSI is intimately connected to motion of the structure relative to soil. When structural motion is in the direction of (in phase with) the soil or free-field motion, it relieves the interface load. Similarly, when structural

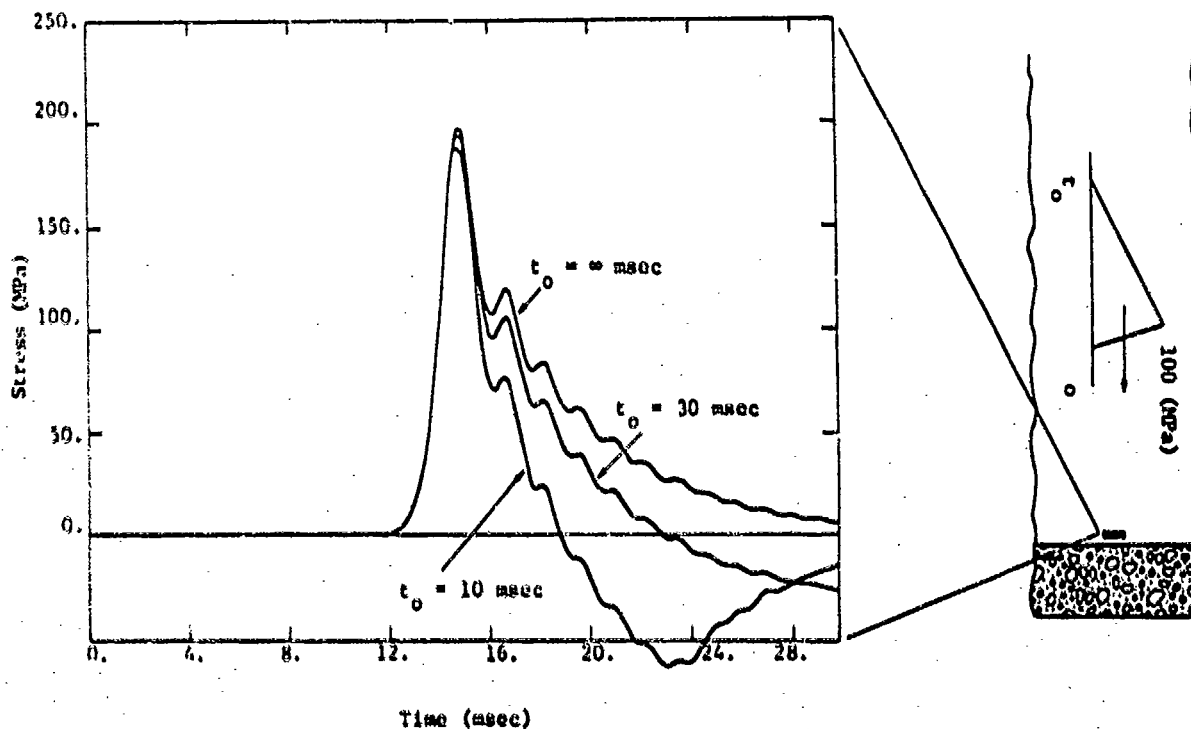


Figure 3. Interaction stress-time history as a function of incident-pulse duration.

motion is against (out-of-phase with) the soil motion, the interface load is enhanced.

For one-dimensional situations, this observation can be summarized quite simply as follows. From wave propagation results such as those given in Fig. 2, the relief (or enhancement) in interface stress,  $\bar{\sigma}$ , due to motion of the concrete layer,  $v$ , is given by

$$\bar{\sigma} = -\rho c v \quad (3)$$

when  $v$  is positive in the direction of free-field wave propagation, and  $\rho c$  is the impedance of soil noted earlier. Positive  $\bar{\sigma}$  means it is compressive, i.e. when motion is out-of-phase with the free-field motion and negative  $\bar{\sigma}$  means it is tensile, i.e. when motion is in-phase with the free field. It will be shown that this simple representation of soil-structure interaction leads to the damping in a class of buried structures where the SSI is basically planar.

#### SSI AND STRUCTURAL DAMPING

The response  $Z$  of a structure buried in a medium subjected to a known free-field excitation can be represented by

$$M\ddot{Z} + KZ = \sigma_I \quad (4)$$

where  $M$  is the mass matrix,  $K$  the stiffness matrix, both of dimension  $N$  by  $N$ ,  $N$  being the number of degrees of freedom.  $\sigma_I$ , a vector of dimension  $N$ , represents the interaction pressure (unit tributary area is implied) and can be written as

$$\sigma_I = \sigma_F + \sigma_R \quad (5)$$

where  $\sigma_R$  is the reflected (or radiated) pressure at the interface, and  $\sigma_F$  the free-field excitation.

Assuming that the reflected pressure at early time can be approximated by the plane wave relationship Eq. (3), the reflected pressure can be expressed as

$$\sigma_R = \rho_s c_s U_R \quad (6)$$

where  $\rho_s$  is the mass density of the soil,  $c_s$  is its P-wave velocity and  $U_R$  the reflected particle velocity.

The reflected particle velocity can also be written as

$$U_R = U_F + \dot{Z} \quad (7)$$

where  $U_F$  is the free-field particle velocity and  $\dot{Z}$  is the velocity of the structure at the interface. Combining Eqs. (6) and (7) gives

$$\sigma_R = \rho_s c_s U_F - \rho_s c_s \dot{Z} \quad (8)$$

and since

$$\sigma_F = \rho_s c_s U_F, \quad (9)$$

Eq. (4) may now be expressed as

$$M\ddot{Z} + \rho_s c_s \dot{Z} + KZ = 2\sigma_F. \quad (10)$$

Eq. (10) expresses the response  $Z$  in terms of  $\sigma_F$ , the free-field excitation. Since  $\sigma_F$  is independent of the response of the structure  $Z$ , the problem of soil-structure interaction as given by Eq. (10) is uncoupled; the free-field excitation can be analyzed first and separately from the structural motion analysis which follows. The effect of SSI is represented by a viscous damping term,  $\rho_s c_s \dot{Z}$ , which depends on the properties of the medium. It is this damping which (a) incorporates the SSI effect on the loading perceived by the structure and (b) effectively decouples the analysis of the structure from its surrounding medium.

The relationship expressed in Eqs. (6) and (9) is based on one-dimensional wave propagation considerations. For two-dimensional problems with simple geometries such as rectangular plane box structures, the relationship is an approximation. The assumption that the reflection process is (at least) initially plane has been extensively tested by finite element models for various span-depth ratios of the structure. The error involved in such applications is illustrated in Fig. 4 where the SSI loadings on a slab with a span of 6m obtained from two-dimensional finite element analysis and using the approximation Eq. (10) are compared.

Fig. 5 compares the corresponding structure motion time histories. The highly damped nature of the velocity response is apparent. Furthermore, by comparing Figs. 4 and 5, the relief and enhancement of the SSI load corresponding to the phasing of the structure and soil motions are clearly illustrated.

#### MODAL DAMPING

In modal analysis the generalized damping  $C_k^*$  in the  $k$ th mode is given by

$$C_k^* = \phi_k^T C \phi_k \quad (11)$$

where  $\phi_k$  is the  $k$ th mode shape vector and the superscript  $T$  indicates its transpose. Similarly, the generalized mass is given by

$$M_k^* = \phi_k^T M \phi_k \quad (12)$$

and the  $k$ th damping ratio is

$$\zeta_k = \frac{C_k^*}{2\omega_k M_k^*} \quad (13)$$



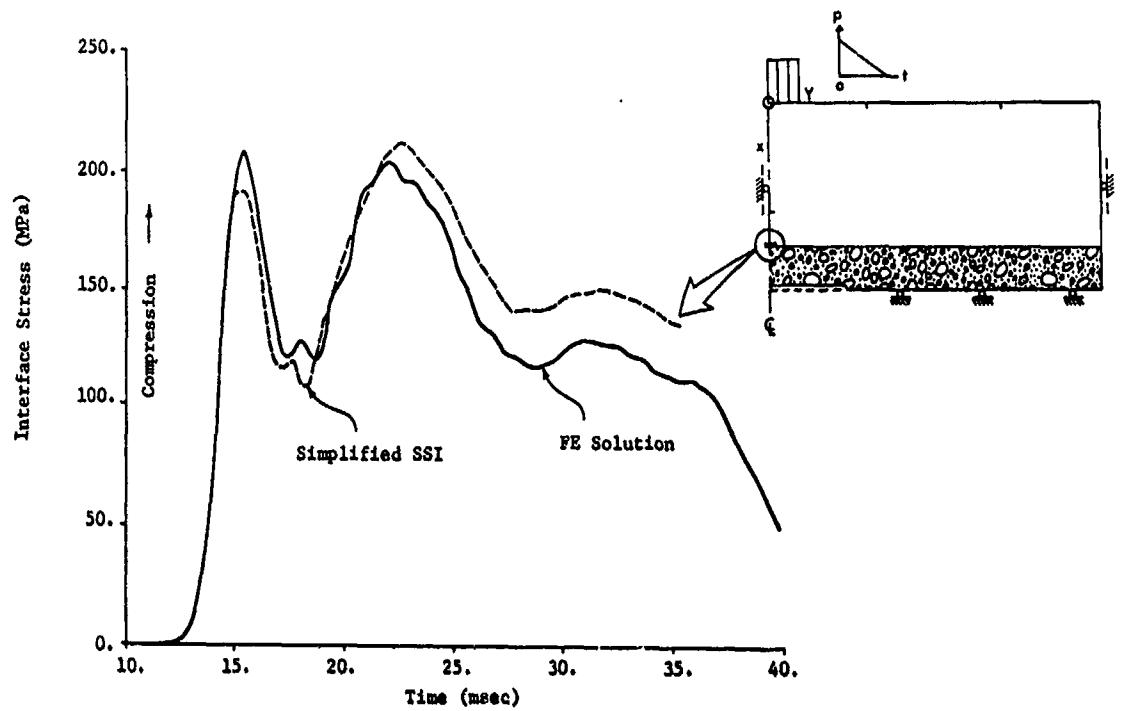


Figure 4. Comparison of FE calculation results and simplified SSI solution, nominal span = 6m, mid-span interface stress.

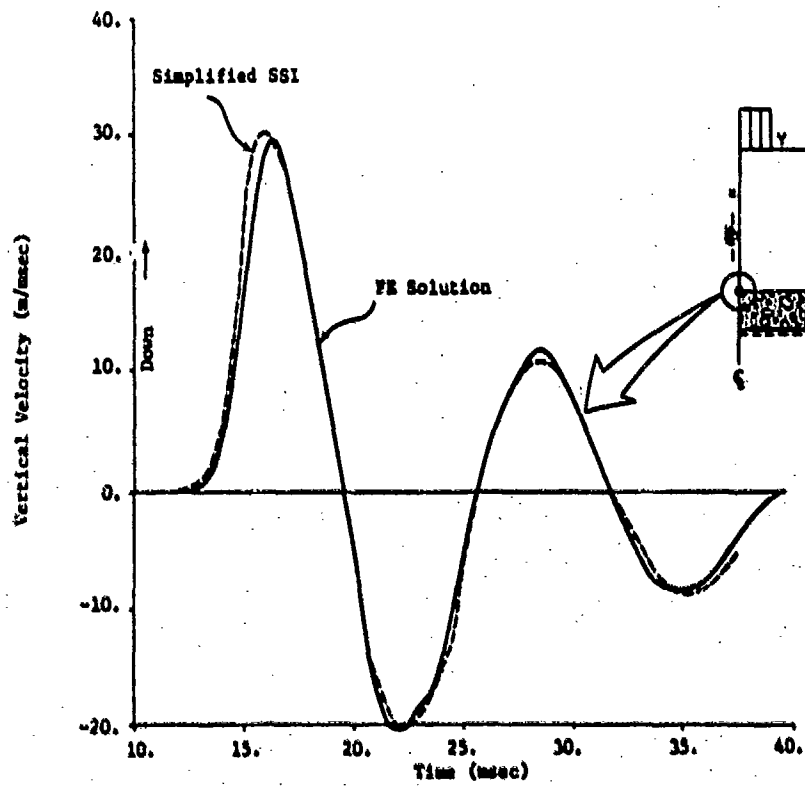


Figure 5. Comparison of FE calculation results and simplified SSI solution, nominal span = 6m, mid-span velocity.

where  $\omega_k$  is the  $k$ th modal frequency.

Specializing to Eq. (10), the modal damping due to SSI is

$$\xi_k = \frac{\rho_s c_s}{\rho_c d_c} \frac{1}{2\omega_k} \quad (14)$$

since both the damping coefficient  $C = \rho_m c_m$  and the mass of the roof structure with constant thickness  $d_c$  and density  $\rho_c$ , are constant.

Eq. (14) states that the modal damping due to SSI effect is inversely proportional to the modal frequency and unit mass of the structure, but is directly proportional to the acoustic impedance of the medium. Alternately, multiplying and dividing the righthand side of Eq. (14) by  $c_c$ , the wavespeed of the roof material, gives

$$\xi_k = \frac{\rho_s c_s}{\rho_c c_c} \cdot \frac{c_c}{d_c} \cdot \frac{1}{2\omega_k} \quad (15)$$

Recalling  $\omega_k = 2\pi/T_k$ , where  $T_k$  is the period of the  $k$ th mode, Eq. (15) becomes

$$\xi_k = \frac{1}{4\pi} \frac{\rho_s c_s}{\rho_c c_c} \frac{T_k}{T_c} \quad (16)$$

where  $T_c = d_c/c_c$  is the transit time of the roof. Hence, the modal damping due to SSI effect is proportional to the soil-structure impedance ratio and the ratio of modal period to transit time in the structure.

## CONCLUSIONS

Dynamic soil-structure interaction for buried structures is a complex phenomenon. We have considered a simplified subset of this

class of problems to delineate the relationship between dynamic SSI and damping of the structural motion. Damping is shown to be a direct result of the interaction mechanism.

Damping comes also from other sources: dissipation in the soil due to hysteresis, energy loss due to interface friction and damping internal to the structure. By considering elastic soil/structure configurations, we have eliminated these sources in the present study in order to concentrate on perhaps the largest contributor to damping in protective structures, and to illustrate its origin.

## REFERENCES

- [1] Kiger, S. A. and J. P. Balsara, "Results of Recent Hardened Structures Research," the 100th Symposium on Weapons Effects on Protective Structures, Mannheim, Germany, November 14-16, 1978.
- [2] Kiger, S. A., "Vulnerability of Shallow-Buried Structures," Defense Nuclear Agency, Strategic Structures Division Biennial Review Conference, SRI International, Menlo Park, CA, March 20-22, 1979.
- [3] Windham, J. E. and J. O. Curtis, "Effect of Backfill Properties and Airblast Variations on the External Loads Delivered to Buried Box Structures," Technical Report, U.S. Army Engineer Waterways Experiment Station, April 1977.
- [4] Wojcik, G. L. and J. Isenberg, "Effects of Radiation Damping on Vibration of a Shallow-Buried Rectangular Structure," DNA 4600F, Weidinger Associates for Defense Nuclear Agency, April 1978.
- [5] Kolsky, H., Stress Waves in Solids, Dover Publication, 1963.